technische universität
dortmund

Dissertation

Nonlinear Optical Functionalities of VO_2- and GaN-based Nanocomposites

submitted in partial fulfillment of the
requirements for the degree of

Dr. rer. nat.

to the Institute of Physics of the
TU Dortmund University, Germany

by

Jan Mundry

Dortmund, April 2022

Erster Gutachter:	Prof. Dr. Markus Betz	(Technische Universität Dortmund)
Zweiter Gutachter:	Prof. Dr. Donat Josef As	(Universität Paderborn)

Datum der Einreichung:	08.04.2022
Datum der Disputation:	14.06.2022

Contents

1 Introduction and Overview of the Thesis 1

Part I - VO_2 Nanocrystals 5

2 Vanadium Dioxide (VO_2) Nanocrystals (NCs) 7
- 2.1 The Insulator to Metal Phase Transition (IMT) of VO_2 10
- 2.2 Fabrication Process of VO_2 NCs 15
- 2.3 Optical Properties of VO_2 NCs 17
- 2.4 Thermally Induced IMT with Hysteresis in VO_2 NCs 20
- 2.5 Optically Induced IMT with Hysteresis in VO_2 NCs 24

3 Thermochromic and Photochromic Etalon Based on VO_2 Nanocrystals 27
- 3.1 Optics of Multilayer Systems 28
- 3.1.1 Resonator Optics 28
- 3.1.2 Transfer Matrix Method 31
- 3.2 Optical Etalon with VO_2 NC Layer 35
- 3.2.1 Simulation of the Etalon’s Optical Response 42

4 Nonlinearities of the Two Individual Phases of VO_2 NCs 47
- 4.1 Open Aperture Z-Scan Technique 48
- 4.2 Saturable and Reverse Saturable Absorption in VO_2 NCs 52

5 Conclusions and Outlook Part I 61

Part II - Hexagonal GaN/AlN Superlattice 65

6 GaN/AlN Heterostructures 67
- 6.1 Introduction to Quantum Wells 70
- 6.2 Fabrication Process and Energy Levels of the GaN/AlN Superlattice 75
- 6.3 Control Measurements of the Fabrication Process 81

7 Ultrafast (Inter Miniband) Carrier Dynamics in a GaN/AlN Superlattice 87
7.1 Time-resolved Pump-Probe Spectroscopy and Experimental Setup 88
7.2 Degenerate Pump-Probe Spectroscopy 92
7.3 Non-Degenerate Pump-Probe Spectroscopy 98

8 A Nonlinear Metasurface Based on a Superlattice and Plasmonic Antennas 105
8.1 Introduction to Nonlinear Optics and Nanoplasmonics 107
8.1.1 Nonlinear Optics 107
8.1.2 Nanoplasmonics 109
8.2 Preparation and Linear Optical Properties of the Metasurface 114
8.3 Experimental Approach for SHG/THG 117
8.4 Characterization of the Nonlinear Response from the Metasurface 118
8.4.1 Power Dependence 118
8.4.2 Polarization Dependence 122
8.4.3 Influence of the Antenna Periodicity 124

9 Conclusions and Outlook Part II 129

Bibliography 133

List of Publications 157

Conference Contributions 157

Acknowledgements 159

Chapter 1

Introduction and Overview of the Thesis

The term nanotechnology describes the precise manipulation of matter on the atomic and (supra-)molecular scale for the industrial fabrication of macroscale devices. Defined by the National Nanotechnology Initiative, the structural size of such nanoscale objects ranges between 1 nm and 100 nm in at least one dimension [Dre86]. This spatial definition reflects the fact that interface properties play an ever greater role compared to the bulk properties of the material. The confinement of charge carriers on the nanoscale eventually leads to the evolution of dominant quantum mechanical effects that must gradually be taken into account as the dimension of the structure shrinks. In particular, the length scales in nanotechnology strongly determine the properties of an object [NH12, KAP15].

Nanotechnology has become one of the most innovative branches of modern science by combining all fields of research and cross-linking different disciplines [Ram16]. By now, a broad range in science focusses on the size-induced functionalities including molecular biology, organic chemistry, micro and molecular engineering, surface science, semiconductor physics, nanoelectronics and many more. The associated research and applications in each field are equally diverse and range from the development of new nanoscale materials and their industrial fabrication methods to molecular self-assembly and nanorobotics. A detailed overview of the development of nanotechnology can be found in the following review [BAT20].

The question of the origin of nanotechnology is often asked. Although this term dates back to the second half of the 20th century, it also encompasses manufacturing methods that have very early roots. Even the ancient Romans unknowingly used metal nanoparticles in glass art, exploiting their optical properties to create remarkable color effects. The size and shape of the metal nanoparticles influence the visible colors. A piece of Roman glass art on display in the British Museum in London - the Beaker of Lycurgus - is a fascinating example of these color effects [TBM22]. From the outside, the cup appears green. But when illuminated from the inside, the cup looks ruby red - except for King Lycurgus, who appears in purple. The cause of this bi-color effect (dichroism) is the presence of nanoscale particles of silver, gold and copper up to a size of 100 nm incorporated into the glass matrix.

It took many centuries for physicist Richard P. Feynman’s visionary speech “There is plenty of room at the bottom” in 1959 at the Californian Institute of Technology to herald the modern age of nanotechnology [Fey60]. It is often considered as the cornerstone for the development of nanotechnology since Feynman spoke of how it would in principle be possible to build matter atom by atom. The term nanotechnology itself was first used by the Japanese professor Norio Taniguchi in 1974 [TAK74]. He described nanotechnology as the modification of materials as “nanotechnology mainly consists of the processing of separation, consolidation, and deformation of materials by one atom or one molecule”. Finally the development of the scanning tunneling microscope by Gerd Binnig and Heinrich Rohrer allowed the high quality imaging of structures in the nanometer range and even to conduct experiments with individual atoms [BR82]. These visions of the early pioneers are still the driving force for many scientists today to focus on the development of nanotechnology.

After many years of dedicated research, nanotechnology is considerably improving many fields in research and industry. The rapidly growing benefit in electronic and information technology based on modern nanoscale devices and applications is only one specific example that is present in daily life. Today's society would be unthinkable without the wealth of (handheld) smart devices. All major advances in computing are mainly related to faster and smaller chips that can handle and store the continuously growing amount of information. Transistors, the basic electronic switches that all modern computers are based on have gradually been downsized to the lower end of the nanoscale. From a typical size of 130 nm to 250 nm manufactured at the turn of the century, 7 nm to 10 nm transistors based on silicon are now widespread technology [Pee00]. Intel’s roadmap for the current decade even foresees the dawn of the angstrom era and future devices are envisioned to dive deeper and deeper in the quantum realm [Int22]. Expectedly, science has recently brushed the bitter limit of the famous Moore’s law [Moo98] by presenting a graphene transistor with a gate length of only 0.34 nm (approximately the size of a single carbon atom) [WTS22].

Beside this maybe last node for Moore’s law, at least one more chance of improvement remains: Photonic integrated circuits featuring small scale designs that are especially anticipated for single-chip applications [CD10]. To this end, the established all-electric transfer and processing of information are progressively replaced by electro-optical or all-optical devices. High-speed data transfer on a global scale featuring tremendous bitrates in optical fibers became a key component for the maintenance of daily life [Agr10, RFN13]. Therefore, sophisticated devices based on highly efficient light-matter interaction gain more and more importance, not only in fundamental research but also in industrial application. Photonics, the general term of this research branch, offers intrinsic benefits over electronic circuit solutions: A weak light-light interaction allows higher multiplexing rates and superior speed for data transfer combined with low power losses and greatly reduced heat dissipation that minimizes the overall power consumption [CCH07, CD10].

The typical wavelength rage in which optical fibers in photonic applications operate spans from 800 nm to 1650 nm [Agr10]. This so called telecom wavelength regime is based on the material-specific transmission range and dispersion properties of silica-based optical fibers. Located at approximately 1550 nm wavelength the conventional C-band of erbium-doped fibers features a shifted zero-dispersion wavelength towards the minimum-loss window allowing for optimal data transfer. The use of such optical fibers and networks as well as the flow of data to linked electronic circuits require a distinct modulation and demodulation of the optical signals [CD10]. In order to satisfy the demand for high transfer rates, this interconnection must even function at high frequencies. Proper laser sources that feed these optical networks are equally indispensable and subject to constant optimization.

Overview of the Thesis

This thesis presents fundamental research and concepts for active photonic elements operating in the telecom wavelength regime. The aim of the study is to determine the characteristics of the investigated nanostructures and to evaluate the implementation of the proposed materials in photonic research or in potential optical devices. The examined photonic elements are envisioned to pave the way towards an improved generation and modulation of optical signals. The application of such photonic elements is based on their ability to alter the properties of light by a distinct change of its intensity and/or wavelength. Although this work presents two completely different material systems, both are linked by common characteristics: The optical properties of the nanocrystals introduced in the first part and the superlattice structures presented in the second part are based on their nanoscopic origin. In addition, the light-matter interaction of both material systems can be custom-tailored at the nanoscale to be used in the aspired telecom wavelength regime [LFH04, Dav98].

In the first part of this thesis the optical properties as well as the photonic application of vanadium dioxide (VO_2) nanocrystals (NCs) are studied. VO_2 exhibits an easily accessible insulator-to-metal phase transition (IMT) near ambient temperatures [Mor59]. Upon excitation it undergoes an atomic rearrangement that is accompanied by a substantial modification of the complex dielectric function [VBB68]. Chapter 2 is dedicated to the characterization of the unique optical properties of VO_2 NCs that are specifically designed for the telecom wavelength regime.

Chapter 3 demonstrates a moderate-finesse etalon containing a sub-wavelength layer of VO_2 NCs. When VO_2 undergoes the IMT, the near-infrared transmission peaks are expected to markedly shift in their spectral position and peak transmissivity due to the substantial change of the dielectric function. Both heat deposition and ultrafast optical excitation are considered to actively control the etalon’s functionality. Transfer matrix simulations of the layered structure including the actual dielectric properties of the VO_2 NCs are performed to review the experimental findings.

Much less is known about the nonlinear optical properties of VO_2 beyond the established IMT. To this end the nonlinear optical response of a thin film of VO_2 NCs is investigated with open aperture z-scans involving femtosecond near-infrared pulses in chapter 4. Nonlinearities like saturable absorption are essential for e.g. mode-locked near-infrared lasers. Saturable absorbers based on custom-tailored VO_2 NCs would definitely benefit from a wide spectral tunability offered by NC-based materials.

In the second part of this thesis, a semiconductor heterostructure based on ultranarrow hexagonal GaN/AlN multi-quantum wells (MQWs) is investigated. Specifically, it is a planar layered stacking of alternated nanometer-thin sheets of GaN and AlN. As discussed in the context of chapter 6, energy levels emerge due to the confinement of charge carriers in the potential landscape [Dav98]. The tailored inter-miniband (IMB) transition between these levels is characterized in terms of its linear and ultrafast nonlinear optical properties. In particular, the central energy and energetic width of the IMB transition are analyzed. Furthermore the time-scales of the electron relaxation are examined using the established pump-probe scheme. Degenerate (chapter 7.2) and non-degenerate (chapter 7.3) experiments are carried out in order to get an insight into the electron dynamics for different excitation photon energies.

The following chapter 8 reports on a new type of nonlinear metasurface taking advantage of these telecom-range IMB transitions. The heterostructure is functionalized with an array of plasmonic antennas featuring cross-polarized resonances at these near-infrared wavelengths and their second harmonic. The focus of the investigation is on the generation of substantial second harmonic at normal incidence and the condition for free-space radiation perpendicular to the surface.

Part I

VO_2 Nanocrystals

Chapter 2

Vanadium Dioxide (VO_2) Nanocrystals

Transition-metal oxides steadily attract the interest of researchers, especially because some of them show an abrupt and sometimes enormous change in some of their physical properties when undergoing a phase transition at a certain, material-specific, critical temperature (T_c). Vanadium dioxide (VO_2) as one representative of the vanadium oxide family (principal oxides: VO, VO_2, V_2O_3 and V_2O_5) exhibits an easily accessible insulator-to-metal phase transition (IMT) near ambient temperatures ($T_c \approx 68°C$ for bulk crystals), firstly reported by F. J. Morin in 1959 [Mor59]. Since this discovery many experimental and theoretical studies as well as applications have evolved. But from all vanadium oxides[1], VO_2 is the most appealing one for room temperature applications due to its low critical temperature of the phase transition.

Upon heating [Mor59], the application of external stress [BLC15], electronical [JKS13] or optical [JZK14] excitation VO_2 undergoes an atomic rearrangement from a monoclinic to a tetragonal lattice. This reversible first-order phase transition features a strongly altered band structure. It is accompanied by a substantial modification of the complex dielectric function and a marked change of the DC electrical conductivity by about five orders of magnitude [VBB68, TJT98]. In general, VO_2 exhibits insulating properties at room temperature while the high temperature phase above T_c can be described by a metal-like character. Emerging from the altered complex dielectric function during the IMT, tremendous changes of the optical properties, especially in the near infrared (NIR) range, make VO_2 interesting for modern photonic applications in the telecom wavelength range [VBB68]. In the state of an insulator, VO_2 tends to some degree to transparency and switches to great opacity with reduced transmission and altered refractive index when being driven through the IMT to the metallic phase. The physical background of the IMT and the associated transition mechanisms, as well as the crystallographic material properties of both phases are outlined in the following chapters.

The optical performance of VO_2 opens the gate for the development of many functional applications outside of the broad field of photonics such as flexible foils and coated glass for

---

[1] Only VO_2, V_2O_3, V_2O_5 and Magnéli phases show an IMT [DNJ96, Mor59, SE04].

energy building efficiency [CJL19], thermochromic and electrochromic coatings for smart windows [Gra16] or light sensors and detectors for broadband photo detection [RKM03, SLK09, KNZ20]. Moreover, many other areas like electronics and electrical circuit-engineering benefit from the marked change of the DC electrical conductivity during the IMT. The progress of recent applied research covers, e.g., transistors [STA15] and so-called memristors[2] for memory devices and artificial intelligent architectures [DKC09, LMH19, ZS15].

In the course of the years, VO_2 thin-films and nanocrystals (NC) have been extensively studied due to their unique size effect and the possibility to tailor the light-matter interaction at the nanoscale [NH12, KAP15]. The ongoing technological development actually grants a multitude of techniques to produce NCs from many different materials with specific shapes and sizes [ZCX20, WLK16]. In comparison to bulk crystals or thin films, VO_2 NCs feature broad near-infrared plasmonic[3] resonances in the telecom regime with specific characteristics depending on their size, shape and the host matrix material [LHB02]. Notably, a substantial change of the complex refractive index during the IMT characterizes the optical properties of the VO_2 NCs. Shrinking VO_2 to the nanoscale leads to the evolution of a wide IMT-hysteresis featuring a supercooled metallic state in the cooling-down process that persists to temperatures (far) below T_c [CKK11, SZB14]. Therefore, VO_2 NC based structures are envisioned for applications such as switchable optical elements [CKK11, SKL12] and the optical control of the phase of light [SZB14]. Furthermore, nanothermochromic diffraction gratings [YBG13] and other planar optical elements like optically defined lenses have been realized [ZWK12, RCS05]. More recent work incorporates VO_2 into hybrid structures involving, e.g., photonic crystals and waveguides [RRH20, TCW16].

In the first part of this thesis, VO_2 NCs embedded into a fused silica host matrix are studied. Specifically, the thermally induced IMT with its effect on the optical transmissivity is examined in a wide spectral range to sufficiently resolve the plasmonic resonance of the metallic NCs. Furthermore, VO_2 NCs exhibit a broad hysteresis compared to bulk crystals that is examined with thermal and all-optical means. The VO_2 NC sample used in the course of this thesis is characterized be a uniquely broad hysteresis that outmatches the experimental findings of other nanoscopic VO_2 systems reported so far in literature [JZK14, ZWK12].

In the following section, a novel optical functionality of VO_2 NCs which is mainly related to the change of the real part of the dielectric function during the IMT is demonstrated. In particular, a sub-wavelength thick layer of VO_2 NCs embedded into fused silica is introduced into an optical cavity, creating a moderate-finesse etalon. When these NCs are driven through the IMT by either heating or optical excitation, a pronounced spectral shift of the near-infrared modes transmitted through the etalon is observed due to the substantial change of the complex

---

[2] Memristor: A portmanteau of memory and resistor.

[3] Plasmons are the quantized fluctuations of the charge carrier density. Further information is provided in the context of chapter 8.1.2.

refractive index during the IMT. Remarkably, spectral shifts of about one linewidth can be achieved. Transfer matrix simulations of the etalon are compared with the experimental findings, pointing towards a huge impact of the layer thickness and location of the NC layer with respect to the node/anti-node pattern of the optical resonator.

Much less is known about the nonlinear optical properties of VO_2 beyond the IMT. Z-scan experiments in bulk and nanoscale VO_2 have shown that effective nonlinear optical coefficients extracted for femtosecond pulses at 800 nm are mostly related to an optically induced phase transition rather than to an intrinsic optical nonlinearity of the two individual phases [LHF04]. For this reason, in the last chapter of part I the nonlinear optical response of a thin film of ion beam synthesized VO_2 nanocrystals is thoroughly investigated by the open aperture z-scan technique involving femtosecond near-infrared pulses. Remarkably, VO_2 NCs in their high-temperature phase show a pronounced saturable absorption or reverse saturable absorption for slightly off-resonant wavelengths. A quantitative analysis of multiple z-scan traces using a phenomenological model based on nonlinear and/or saturable absorption reveal high equivalent two-photon absorption coefficients and saturation intensities linked to the plasmonic resonances of the metallic VO_2 NCs. As this resonance can be custom tailored by, e.g., the NCs' size and host material, the present results hold promise to achieve widely adjustable and large optical nonlinearities in the near-infrared, suitable for applications such as saturable absorbers to mode-locked lasers.

2.1 The Insulator to Metal Phase Transition (IMT) of VO_2

At a critical temperature ($T_c \approx 68°C$ for bulk crystals) VO_2 undergoes a reversible first-order phase transition from an insulating to a metallic state, accompanied by a structural rearrangement of the lattice as well as a strong altering of the band structure. Although this transition was already discovered in 1959 by F. J. Morin [Mor59], the physics of this transition is still under ongoing discussion and will remain a topic of future research. Numerous approaches and theories have been published in the past, but none of the models describes all experimental findings in a unified way. This chapter addresses the basic material properties of both solid phases of VO_2 and provides a brief introduction to the physical background of the IMT. It should be mentioned that a detailed physical explanation of the IMT is not required for the understanding of the experiments presented in this thesis, since the application-related research in the first part and the examination of both individual phases beyond the IMT in the second part are not adversely affected by a potentially altering theory of the IMT. Moreover this thesis does not contribute to the complex description of the IMT itself. The interested reader may consult the references provided in this section for further information.

Vanadium[4] is a transition-metal with the atomic number 23, indicated by the symbol V and located in the 5th group of the periodic table of the elements. A typical characteristic of a transition metal is the exhibition of two or more oxidation states. In addition to the oxidation numbers 2, 3, 4 and 5 in compounds $V0$, V_20_3, $V0_2$ and V_20_5, Magnéli phases V_n0_{2n-1} ($n=3$-8), as well as Wadsley phases $V_{2n}0_{5n-2}$ exist. Complexes of the form V_n0_{2n+1} ($n=3$, 4, 6) have also been found in bulk material [DNJ96]. The compounds $V0_2$, V_20_3, V_20_5, and the Magnéli phases, with the exception of V_70_{13}, undergo temperature-dependent IMTs [DNJ96, Mor59, SE04]. The most appealing vanadium oxide for technological (room temperature) application remains VO_2 due to its low critical temperature of the IMT.

The first approach to explain the IMT in VO_2 by a fundamental and widely accepted theory was provided by J.B. Goodenough in 1971, in the framework of crystal field and molecular orbital theory [Goo71]. To facilitate the explanation of the reversible IMT and, in particular, the formation of the insulating phase, the illustration of this mechanism starts with the metallic, high-temperature phase above T_c. This metallic phase features a tetragonal body-centered (rutile) unit cell. The V atom has two 4s and three 3d-electrons in its electron shell whereas only four electrons are required for the bonding to the O-atom, leaving one 3d-electron. Therefore, the

---

[4] Vanadium in Old Icelandic "Vana-dís", a name of Freyja, the North Germanic goddess of beauty. The naming originates from the colorful appearance of some natural vanadium compounds [Sef31].

V^{4+} ion with its 3d electron is located in the center of an octahedron, formed by six O^{2-} ions. This high-temperature rutile crystal structure of VO_2 is illustrated in Fig. 2.1(a). As a consequence of this arrangement, the 5-fold degenerate 3d levels of vanadium split into the two-fold degenerate e_g and the three-fold degenerate t_{2g} levels. The e_g orbitals point in the direction of the oxygen and form σ and σ^* bands under hybridization with the 2p orbitals from the oxygen. The t_{2g} orbitals, pointing between the oxygen ligands, form the π and π^* bands, as well as the $d_{||}$ band, which is in turn created from the vanadium $3d_{xy}$ orbitals and orientated along the rutile c_R-axis [CFN96]. A schematic illustration of the band structure is depicted in Fig. 2.2(c). In this model, the metallic character above the transition temperature originates from the overlap of the $d_{||}$ and π^* bands at the Fermi level. Consequently, the partial filling of these two bands gives rise to a moderate DC electrical conductivity of the metallic phase featuring a fairly high resistivity[5] of $\rho_{metallic}=10^{-5}\text{-}10^{-6}\,\Omega m$. Nevertheless, Coulomb repulsion inhibits the conductivity from being as good as in, e.g., noble metals ($\rho_{silver}=1.6\cdot10^{-8}\,\Omega m$ [Mat79]) [QBC07]. Here in the case of metallic VO_2, the oxygen atoms separate the weakly bound valance electrons, thus, the overlap integral of the electron wave functions is diminished and the electrical conductivity is therefore reduced. From the electrical engineering point of view, the most striking property of the IMT is the negative differential resistance (NDR) of the order of about 10^5 ($\rho_{insulating}=0.1\text{-}1\,\Omega m$) when the electrical device made from VO_2 goes through the IMT [LMH19].

At ambient pressure, if the temperature drops below T_c, the lattice structure changes to a monoclinic crystal system, featuring a change of the unit cell dimensions by up to 1% [Eye02, KN79]. While small dislocations of the vanadium atoms along the c_R-axis happen, the positions of the oxygen atoms, forming the octahedron, remain nearly unchanged. Additionally, V-V pairing occurs, causing the formation of V-V dimers with slightly shortened bond length and a tilting away from the c_R-axis [BYZ07], as shown in Fig. 2.1(b). Owing to the strong V-V dimerization, the π^* band shifts above the Fermi level and the $d_{||}$ band splits into an empty higher-energy band (antibonding states) and a filled lower-energy band (bonding states). The resulting electronic band structure is schematically depicted in Fig. 2.1(d). Crystal field splitting and/or electron-electron repulsion support the formation of this band splitting, giving rise to its insulating 1D orbital character. Due to the fact that this band structure resembles a semiconductor with a band gap of $E_g\approx0.65\,eV$ (cf. Fig. 2.1(d)), the low-temperature insulating phase is often referred to as semiconducting or semi-insulating phase.

---

[5] In an ideal case, the resistivity ρ is defined as the electrical resistance of a uniform specimen of the material multiplied by its cross-section and divided by its length.

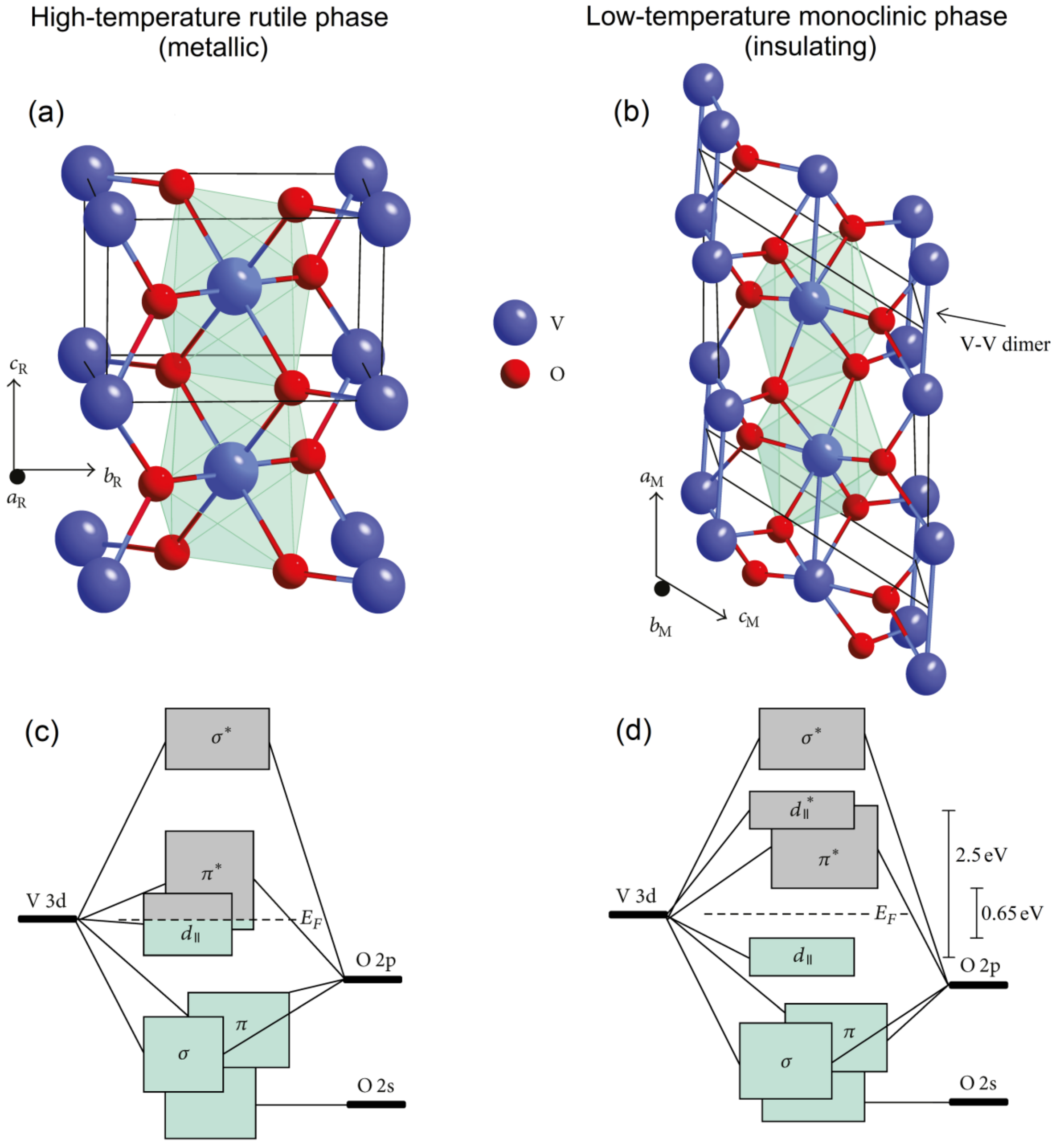

Fig. 2.1: Schematic of the crystal structures of (a) the high-temperature ($T>T_c$) tetragonal/rutile and (b) the low-temperature ($T<T_c$) monoclinic phase of VO_2. The rutile phase with regular octahedrons exhibits uniform distances between V ions, while the monoclinic phase with distorted octahedrons exhibits alternating distances between V ions due to V-V dimerization. Schematic illustrations of the electronic band structures highlight the differences between (c) the rutile and (d) the monoclinic phase. The metallic character in (c) originates from a partial filling of the $d_{\|}$ and π^* band at the Fermi level E_F (dashed line). The insulating behavior in (d) is caused by a splitting of the $d_{\|}$ band and a shift of the π^* band to higher energies due to the V-V dimerization and tilting of the V-V dimers, leading to a band gap at E_F. Taken and adapted from [HCS15].

Goodenough’s theory of the high-temperature rutile phase has been widely accepted up to date, while the isolating phase still lacks from an all-embracing and optimal description. The presented model illustrates the results of many experiments in an adequate way, but nevertheless, it is not able to explain, e.g., the experimentally determined large splitting of the $d_{||}$ band ($E_g \approx 2.5\,eV$, cf. Fig. 2.1(d)) [SST90, AGF91]. Band calculations for the $SrTi0_3$ system, which is similar to $V0_2$ in terms of the ion arrangement and lattice spacing, give a value of only about 1 eV [KL64].

Due to the fairly strong correlation of the electrons in the VO_2 system, the electron-electron interactions are complex and can neither be explained by Bloch theory with unbound electrons forming an electron gas, nor can they be described by a tight binding model with isolated, localized and tightly bound electrons. Established research sees the cause of the IMT rather in electron-electron interactions and/or electron-phonon interactions, in the sense of the more modern Mott-Hubbard or Peierls model [ZM75, PL80, GFE77]. There is experimental and theoretical evidence for both the Mott-Hubbard [ZM75, PL80, RLP94, WHX14] and the Peierls [Goo71, WSA94, CDC04, BPL05, PKE11] model. In 1994 Wentzcovitch et al. published the article "VO_2: Peierls or Mott-Hubbard? A view from band theory" [WSA94]. On the basis of local density approximations (LDA) a Mott-Hubbard insulator, where Coulomb interactions are dominant, was ruled out for the semiconducting phase of VO_2 and a Peierls insulator, where the structural change (tilting and dimerization) is responsible for the $d_{||}$ band splitting, was favorited. However, recent studies have shown that the low temperature phase of VO_2 is more Mott-Hubbard-like. This has been attributed to the appearance of additional insulating intermediate (metal-like) phases during the IMT, which are formed under tensile stresses [BLC15, ABC12], by doping [MWR72] or photo-induced [TBC16]. The appearance of this phases cannot be explained by Peierls theory alone [PCK13, RLP94]. The results of NMR ^{51}V studies [BGK00] suggest that the IMT of $V0_2$ is a transition of the type $2V^{4+}$ <-> V^{3+}+V^{5+}, i.e., that two structurally and chemically distinct vanadium ions exist in the low-temperature phase. The topic of “competing” explanations for the origin of the IMT, including a detailed overview of the theoretical development up to the turn of the millennium, is discussed in detail by Eyert [Eye02].

At the frontline of present research, many authors synergize both models to explain the IMT by an “orbital-assisted Mott-Peierls transition” [HHT05] or a so called “Peierls-assisted orbital selection Mott instability” [WRH12]. To further unravel the Mott-Peierls intrigue in VO_2, dynamical mean-field theory (DMFT) recently revealed the theoretical existence of a distorted transient metal phase that intrudes between the low-temperature insulating and the high-temperature metal phase [GAF20], according with the experimental evidence of a monoclinic metallic phase [MCT14, TBC16].

A promising experimental approach to a profound understanding of the complex mechanisms of the IMT is the time resolved optical pump-probe spectroscopy with a temporal resolution of sub-picoseconds. This technique allows for a separate observation of electronic and structural contributions to the IMT and, additionally, allows to distinguish their respective timescales. In comparison to a thermally induced IMT, caused by an elevated lattice temperature, a raised Fermi level and an increased electron density in the upper bands, on the other hand an optically induced IMT, initiated by photo carrier injection, happens on timescales of less than 200 fs [CDC04, PKE11, WHX14, RCS05, CJH15]. Photo-doping of VO_2 in the insulating, low temperature state depletes the d-symmetry valence band, while populating the π band, followed by an immediate band gap collapse. The electrons attain a transient, hot Fermi distribution with an electron temperature way above the lattice temperature. The final structural transition happens during a lattice thermalization via electron-phonon scattering that occurs on timescales of 10 ps-100 ps [MCT14, WFW13, KEH07].

In summary, none of the theoretical models presented and discussed in the past are able to explain all experimental results of the IMT in a unified way. Therefore, the IMT in VO_2 remains a very complex and partly unsolved problem in theoretical physics leading to ongoing research to determine the delicate interplay of the structural and electronic degrees of freedom.

Considering the optical experiments presented in the context of this thesis, a more detailed theoretical explanation of the IMT itself is not necessarily required. In the first experimental part, the functionality of the application-related integration of a sub-wavelength layer of VO_2 nanocrystals (NCs) in an optical resonator is based on the pure existence of a thermally and optically excitable IMT with unequal optical properties of the two solid phases. In the second part, the examination of both individual phases beyond the IMT is, just in the same way, not adversely affected by a potentially altering theory of the IMT. More importantly, the optical response of the two solid phases of the VO_2 NCs sample, utilized in the context of this thesis, is clarified in the conduct of the next chapters. Starting with the fabrication process of VO_2 NCs by ion beam implantation in fused silica, the focus will be laid on the altering complex refractive index and the IMT-related absorptive resonance in the near infrared spectral range. This overall tunable light-matter interaction in the telecom wavelength regime is highly suitable for photonic application and research.

2.2 Fabrication Process of VO_2 NCs

The technological development in the course of the last decades actually grants a multitude of techniques for the synthesis of artificially grown thin films and NCs with specific sizes or shapes made from many different materials [ZCX20, WLK16][6]. For most technological applications, thin films of polycrystalline VO_2 are necessary. Large single crystals are unsuitable because they cannot withstand the mechanical stress caused by the IMT and break after a few switching cycles. On the other hand, polycrystalline thin films can be reversibly switched without much degradation due to aging. In comparison to bulk crystals or thin films, VO_2 NCs feature broad near-infrared plasmonic resonances in the telecom regime with specific characteristics depending on their size, shape and the host matrix material [LHB02]. Furthermore, shrinking VO_2 to the nanoscale leads to the evolution of a wide IMT-hysteresis featuring a supercooled metallic state below T_c. Additionally, nanoscopic VO_2 profits from a highly crystalline structure and, at the same time, an increased stability to the mechanical stress from the IMT due to the small particle size. A long-term durability is clearly favorable for applications and devices based on VO_2 NCs.

Traditionally, gas-phase-based preparation methods (e.g., physical vapor deposition (PVD) [VCZ19], chemical vapor deposition (CVD) [MPB05, BPB09], sputtering [BCF02], pulsed laser deposition (PLD) [TKU10, WMY99] and sol-gel deposition [DNJ96]) have been practiced. The fabrication of high quality and single crystalline VO_2 thin films or NCs often relies on ion beam synthesis including a thermal annealing step [GB96]. In comparison to the preparation via the gas or liquid phase method, a uniform particle size and neat distribution of stoichiometric VO_2 NCs can be achieved by controlling the ratio of V and O ions during the implantation and the annealing temperature [LHB02]. This technique allows to tailor the light-matter interaction at the nanoscale by adjusting the specific fabrication parameters. Gea et al. [GB96] first demonstrated this technique and Lopez et al. [LHB02, LFH04] systematically studied the impact of different implantation and annealing parameters on the formation of the NCs and their optical properties. These relations will be explained in more detail in the next chapter while the fabrication process itself is addressed in the following section.

The sample used in this thesis is fabricated in the group "Nanoscale Functional Oxides" led by Prof. Dr. Helmut Karl at the University of Augsburg. The VO_2 NCs are synthesized by sequential implantation of vanadium ($9 \cdot 10^{16}$ atoms/cm² at 100 keV implantation energy) and oxygen ($1.8 \cdot 10^{17}$ atoms/cm² at 32 keV implantation energy) into a 500 µm thick fused silica (SiO_2) substrate with lateral dimensions of 10 mm x 10 mm (cf. Fig. 2.2(a)) [ZWK12]. These doses lead to a stoichiometric growth of VO_2, since they differ in an exact factor of 2, referring to the

---

[6] In addition to the specific references given in this chapter, these two references provide a good overview on the different fabrication methods.

stoichiometry of VO_2. The implantation energy, however, defines the penetration depth of the ions into the host material. The above mentioned values were selected to ensure a superposition of both the vanadium- and oxygen-implant distributions at the same depth in the near-surface region of the fused silica host. The formation of roughly spherical NCs with an average diameter of 100 nm and a lateral spacing of about 60 nm happens during a subsequent rapid (10 minutes) annealing step at a temperature of 1000°C. To protect the sample from oxidation, the annealing takes place in a high-purity flowing argon atmosphere [KDS09]. Specifically, a dense layer of isolated VO_2 nanocrystals (areal density $\sim 10^{10}\,\mathrm{cm}^{-2}$) is located about 100 nm below the surface of the SiO_2 host matrix. These values were estimated from a transmission electron micrograph (TEM) such as the example in Fig. 2.2(b). A high resolution TEM picture of a single NC is shown in Fig. 2.2(c). The good and homogenous crystal quality of the nanocrystal can be identified by the regular stripe-patterned structure. As a result, the NCs are well protected from the environment so that they do not suffer from potential detriments like oxidation or hydrophilicity. From the results of Raman spectroscopy the group of Prof. Dr. Karl could exclude a significant amount of other vanadium oxide phases such as V_2O_5. Accordingly, the results of this thesis can be attributed to the phase of VO_2.

It should be noted that the VO_2 NC samples investigated in this thesis slightly differ in the processing parameters. Consequently, the resulting average NC diameter and the optical properties show minor variations. However, the effects on any of the main conclusions drawn below are negligible. In the case that the NCs show a non-negligible deviation of the mentioned properties, this is pointed out separately.

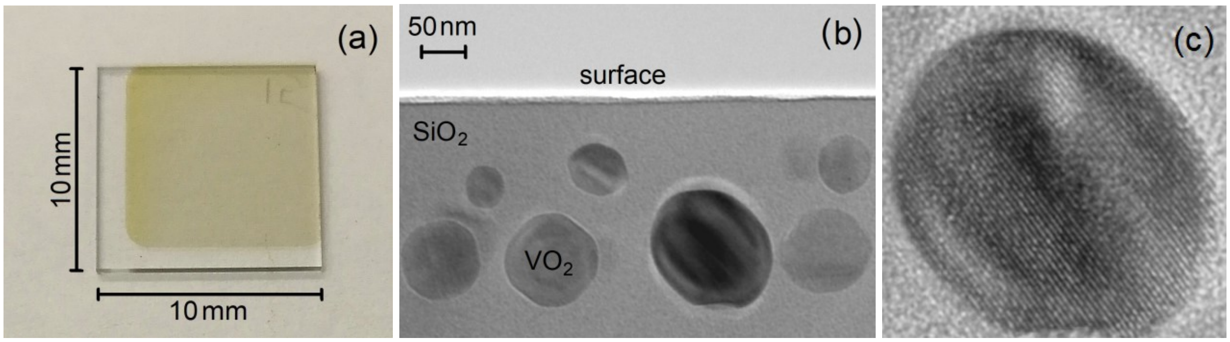

Fig. 2.2: (a) Photograph of the VO_2 nanocrystal (NC) sample. The yellowish area on the transparent piece of fused silica (SiO_2) originates from the implanted VO_2 NCs. (b) Cross-section transmission electron microscope (TEM) image of ion beam synthesized VO_2 NCs embedded into a SiO_2 matrix. (c) High resolution TEM image of one single VO_2 NC. The good and homogenous crystal quality is visualized by the regular stripe-patterned structure.

2.3 Optical Properties of VO_2 NCs

Upon heating and/or optical excitation, VO_2 undergoes an abrupt structural insulator-to-metal transition (IMT), accompanied by a marked change of the complex dielectric function especially in the telecom window [VBB68, TJT98]. This phenomena can be directly seen from the strongly deviating linear optical properties of the two solid phases, emerging from an altered complex refractive index during the IMT. To characterize the VO_2-NC sample used in the course of this thesis, the group of Prof. Dr. Karl performed spectral ellipsometry[7] to determine the real part n and the imaginary park k of the complex refractive index $\tilde{n} = n + ik$. Specifically, the contribution of the VO_2 NC layer has to be isolated in order to identify its individual optical properties without detrimental impact of the host material. For this purpose, the VO_2 NC sample is mounted on a temperature-controlled holder inside a “Sentech SE 850 (FT-IR)” ellipsometry unit that is operated by the software “SpectraRay 3”. In the analysis of the raw ellipsometry data, the NC layer is modeled as a thin layer of an effective medium[8] with spherical particles embedded into SiO_2 [Str98]. The dielectric function of VO_2 is included based on an established model with three Lorentz oscillators [KJN07]. Note that the sample used for the ellipsometry analysis has a different layer structure compared to the sample presented in chapter 2.2. Specifically, a 200 nm SiO_2 layer, serving as host matrix for the VO_2 NCs, was deposited on top of a Si wafer. The parameters of the substrate (Si+SiO2) were determined before the implantation of the VO_2 NCs to finally isolate the optical response of the VO_2 NC layer.

Fig. 2.3(a) and (b) display results for the complex refractive index as determined by ellipsometry. Close to room temperature, in the state of an insulator, VO_2 exhibits a rather flat spectral response in the near infrared (NIR) wavelength range, featuring a nearly constant complex refractive index of $n \approx 1.65$ and $k \approx 0.05 - 0.1$ (cf. blue lines in Fig. 2.3(a), (b)). According to the moderate extinction coefficient k, sub-micrometer layers of VO_2 tend to some degree to transparency. These optical properties are comparable to those from thin films with an equivalent thickness compared to the diameter of the NCs [TJT98]. Heating up the sample above T_c induces the IMT and the metallic VO_2 NCs switch to great opacity with reduced transmission and altered refractive index (cf. red lines in Fig. 2.3(a), (b)). Now the metallic phase features a Mie-type absorptive resonance as expected for roughly spherical, metallic NCs [RCS05, LFH04]. It is characterized by an increased imaginary part k and a dispersive signature in the real part n of the complex refractive index, as seen from Fig. 2.3(a), (b). This observation stands in agreement with the Kramers-Kronig-relation, assuming an absorptive resonance (see Ref. [Men01], p. 88).

---

[7] For an introduction to ellipsometry and further information see Ref. [Yeh88].

[8] Bruggemann type, see Ref. [Str98] for further information.

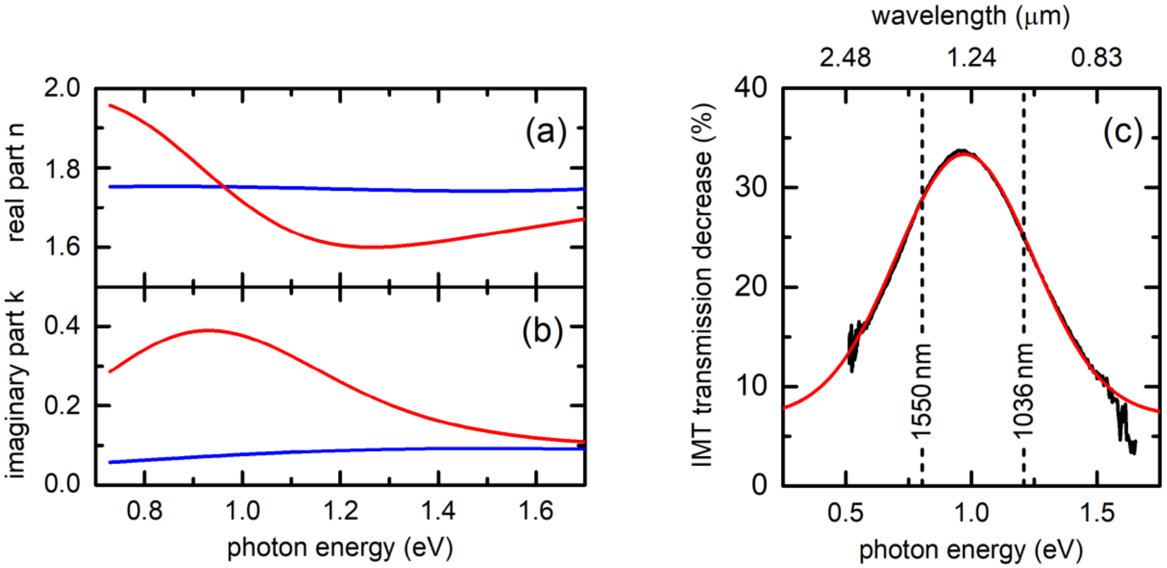

Fig. 2.3: (a) Real and (b) imaginary part of the complex refractive index of VO_2 NCs in SiO_2 as determined by spectral ellipsometry for different sample temperatures. Blue: 28°C (insulating), red: 100°C (metallic). (c) Spectrally resolved optical transmission decrease related to the phase transition from insulating to metallic VO_2 NCs. The red line is a Gaussian fit to the data. The dashed lines indicate typical laser lines utilized for the experimental analysis in the remainder of this thesis.

In comparison to bulk crystals, the dielectrically confined geometry of the spherical metallic VO_2 NCs allows electromagnetic dipole resonances, originating from the collective oscillation of the electron plasma. External light can couple to these resonances, leading to the characteristic, absorptive profile as depicted in Fig. 2.3(b). In general, Mie-theory describes the elastic scattering of electromagnetic waves at spherical particles whose diameter d is slightly smaller or in the same order of magnitude as the wavelength λ of the radiation (see Ref. [Men01] p. 145). In the limit of much smaller or much larger particles, accurate approximations like Rayleight scattering ($d \ll \lambda$) or classical elastic scattering theory ($d \gg \lambda$) are applied, respectively. Nevertheless, Mie scattering theory has no upper particle size limitation and does not refer to an independent physical theory or law. It rather suggests situations, where the above mentioned approximations do not lead to adequate results and more sophisticated solutions to Maxwell's equations are inevitable. Specifically, the Mie solutions take the form of an infinite series of spherical multipole partial waves respecting the boundary conditions of the spherical surface of the particles.

To further characterize this Mie-type, absorptive resonance, spectrally resolved transmission measurements at normal incidence are performed by the author. Therefore, the VO_2 NC sample is clamped to a temperature-controlled holder (Covesion Oven PV10 and Controller OC1) and illuminated by a commercial broadband white light source (Thorlabs SLS201). The analyzing unit consists of a monochromator (Andor Shamrock 193i, grating: 150 lines/mm) that is equipped with an external, biased, extended InGaAs photodiode (Thorlabs

DET05D) to record the transmission signal S through the sample. Fig. 2.3(c) shows the spectrally resolved data for the reduction of the transmissivity in the supercooled metallic state[9] when compared to the insulating state, both at a temperature of 60°C. The visualized IMT transmission decrease is calculated as $1\text{-}S_{metallic}/S_{insulating}$. Owing to an increased imaginary part k, governed by a strong plasmonic resonance in the metallic VO_2 NCs, the reduction of the transmission[10] due to the IMT is as high as 34%. Considering the relatively small effective interaction length[11] of about 25 nm in the partially filled VO_2 NC layer (cf. Fig. 2.2(b)), the IMT-induced change of the light-matter interaction is remarkably strong. This observation refers to an increase of the absorption coefficient by $\Delta\alpha_{IMT} \approx 1.7 \cdot 10^5\,cm^{-1}$. Similar values for VO_2 nanospheres characterized by $\Delta\alpha_{IMT} = 5 \cdot 10^4\,cm^{-1}$ can be found in literature [CRS06]. In contrast, the response of thin films and bulk crystals is dominated by the collapse of the optical bandgap at long wavelengths and by the appearance of the absorptive plasma edge at ~800 nm, leading to smaller changes of the absorption coefficient of only $\Delta\alpha \approx 1 \cdot 10^4\,cm^{-1}$ in the NIR wavelength range [CRS06].

The spectrum in Fig. 2.3(c) is well reproduced by a Gaussian curve (cf. red line) with a central photon energy of 0.97 eV and a full width at half maximum of 0.64 eV. Similar Gaussian-shaped Mie-type resonances from ion-beam implanted VO_2 NCs can be found in literature as well [CRS06]. The spectral position of this resonance and the characteristics of the hysteresis[8] can be tailored during the fabrication process via e.g. the particle's dimension, shape and the host matrix material [KDS09, LFH04, ZCX20, LNG10]. The geometrical properties of the NCs strongly depend on the annealing parameters. In general, increasing the annealing time and temperature leads to larger NCs that show more red-shifted resonances compared to smaller NCs. Accordingly, the light-matter interaction can be tailored at the nanoscale, allowing to shift the resonance, e.g., from the NIR [CRS06] to the visible [LFH04] wavelength regime by reducing the NC's diameter.

Note that the experimental results presented in this chapter, and in the remainder of this thesis, combine the optical answer of ~10^4 NCs that are probed simultaneously in the focal spot of the light beam. Consequently, a distribution of NCs with different diameters is addressed at once (cf. Fig. 2.2(b)).

---

[9] VO_2 NCs feature a broad hysteresis behavior when driven through the IMT. Upon cooling a supercooled metallic phase persists up to room temperature. Further information is provided in chapter 2.4.

[10] The reduction of the transmitted intensity is governed by an increased absorption. Owing to an altered real part of the refractive index, the change of transmission calculated by Fresnel equations for normal incidence leads to less than 2% change in reflectivity of the VO_2 NC layer.

[11] The effective interaction length of about 25 nm can be estimated from the NC's average diameter of 100 nm and the lateral spacing of about 60 nm.

2.4 Thermally Induced IMT with Hysteresis in VO_2 NCs

In 1959 F. J. Morin discovered and firstly reported the IMT in VO_2 bulk crystals and, in particular, highlighted the (unexpected)[12] appearance of a narrow thermal hysteresis in the performed electrical conductivity measurements [Mor59]. In this context, the term hysteresis refers to a separation of the two critical temperatures that mark the transition points to the neighboring solid phase. Specifically, the insulator-to-metal phase transitions upon heating occurs at a higher temperature compared to the backwards metal-to-insulator transition upon cooling. The relatively narrow hysteresis in VO_2 bulk shows a width in the order of only a few Kelvin [Mor59], but shrinking VO_2 to the nanoscale leads to the evolution of a much wider IMT-hysteresis featuring a supercooled metallic state in the cooling-down process. For thin films, the width of the hysteresis reaches about 10 K and NCs of high structural quality exhibit a broad hysteresis of 30-50 K with a supercooled metallic state that persists almost down to ambient temperatures [ALS12]. The first technical application of this IMT-hysteresis was reported in the early 1970s in the context of optical storage devices [Roa71, Smi73] and it is actually envisioned for memristors in modern memory networks [DKC09, LMH19, ZS15]. In this chapter, the physical background of the hysteresis and its appearance in nanoscopic VO_2 is discussed briefly. Furthermore, the characteristic of the IMT-hysteresis in the utilized VO_2 NC sample is examined with thermal and, in the following chapter, with all-optical means.

Phases are generally defined as the states of a macroscopic system in the thermal equilibrium. Thereby, the macroscopic observables deviate in different phases. A well-known example of phase transitions is the changes of the aggregate state (solid - liquid - gas). From the thermodynamic point of view, a transition between two solid phases, as well as the mentioned change of the aggregate state, is defined as a first-order phase transition. It can be triggered by a variation of, e.g., the lattice temperature or other parameters that alter the Gibbs free energy of the phases[13]. In general, different phases exhibit different internal energies and entropies and, consequently, a different course of Gibbs free energy. Accordingly, the critical temperature T_c marks the transition point at which both phases feature the same Gibbs free energy (the intersection of the two Gibbs free energy curves of both phases). In the case of VO_2, the insulating phase features the lowest Gibbs free energy for temperatures below T_c. Upon heating, as the temperature rises above T_c, the minimum is now in the metallic phase and the IMT occurs.

---

[12] "Finding a hysteresis about the Néel transition seems a little unusual" [Mor59].

[13] $G(p,T)=U+pV-TS$ (G = Gibbs free energy, U = internal energy, p = pressure, V = volume, T = temperature, S = entropy)

The origin of the hysteresis is a finite energy barrier between the two phases that has to be overcome in order to induce the phase transition. Additional energy has to be added to (insulator-to-metal) or subtracted from (metal-to-insulator) the system to reach the neighboring Gibbs free energy minimum, i.e., to trigger the phase transition. The energetic barrier can be overcome by sufficient heating or cooling of the system or by nucleation. The latter is usually a stochastic process and occurs spontaneously, but preferentially at impurities (intentional: doping, unintentional: dirt), roughness, grain boundaries or by the application of strain. At these nucleation sites the energy barrier height is reduced due to a modification of the Gibbs free energy potentials. Nucleation commonly initiates the process of forming a new thermodynamic phase in a first-order phase transitions [Sea14]. A well-known example for this process is the boiling and freezing of water that starts at impurities (minerals/salt/dirt) or at the boundaries to the container. Pure water in a cup with smooth surfaces can be heated up to temperatures above 100°C and stays liquid in a so called superheated condition. Likewise, pure water remains in a supercooled liquid state[14], when being cooled down slowly in a perfect container. Upon stirring or shaking the water freezes to ice.

In order to demonstrate the thermal hysteresis, the transmission of a weak 1036 nm laser[15] beam at normal incidence is recorded when the VO_2 NCs are heated and cooled through the phase transition. For this purpose, the VO_2 NC sample is clamped to a temperature-controlled holder (Covesion Oven PV10 with additional Peltier element for cooling and Controller OC1). Note that the given temperature refers to the fused silica (SiO_2) substrate temperature that, in turn, equals the VO_2 lattice temperature for a sufficiently slow heating or cooling process. The transmitted laser beam is measured using an InGaAs photodiode and lock-in detection. Considering a laser spot diameter of about 100 μm (measured with a scanning slit beam profiler (Thorlabs BP104-IR)), an ensemble of roughly 10^5 NCs is probed simultaneously.

Fig. 2.4 shows the probe transmission for increasing (blue) and decreasing (red) sample temperature. The data is normalized to the signal strength at the beginning of the heating cycle at 0°C. Upon heating the signal strength remains nearly constant until the IMT occurs at a critical temperature of $T_c \approx 80$°C, featuring a sharp drop in transmission. The phase transition comes along with a reduction of the transmission by as much as ~22%, in line with the ellipsometry and Mie resonance data (cf. Fig. 2.3). Further heating leads to a plateau, indicative for a complete switching of the entire NC ensemble to the metallic phase. When the sample is cooled down again, a supercooled metallic state persists until the transition back to the insulating state happens close to ambient temperatures. Specifically, the metal-to-insulator transition begins at approximately 40°C, leading to a remarkably broad width of the hysteresis of $\Delta T \approx 55$°C. This

---

[14] Scientists have reached a new low in the cooling of liquid water, hitting -45°C [KSP17].

[15] Note that the width of the hysteresis is not affected from the choice of the laser wavelength. However the transmission decrease is subject to the resonance shown in Fig. 2.3(c).

observed width exceeds the values reported in literature for nanoscopic VO_2 systems that are fabricated outside of the group of Prof. Dr. Karl [ALS12, DLF09, ZWW14, JZK14].

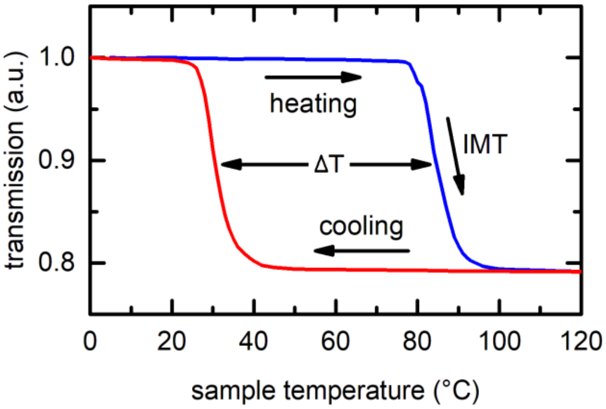

Fig. 2.4: Thermally induced IMT and hysteresis cycle recorded by tracking the 1036 nm probe transmission for increasing (blue line) and decreasing (red line) sample temperature. The IMT from insulating to metallic VO_2 is triggered at a critical temperature of $T_c \approx 80°C$. Upon cooling, a supercooled metallic state persists almost to room temperature.

In contrast to bulk material or thin films, spherical VO_2 nanoparticles implanted into a host matrix undergo a broader hysteresis. Furthermore, VO_2 NCs embedded into fused silica show an even wider hysteresis than those hosted in sapphire [GBB99]. In the course of the optical investigations, the high transmissivity of the host matrix material SiO_2 in the infrared range, guaranteed by the large band gap of SiO_2 of 8 eV [Lau80], as well as the absence of defacing birefringence (sapphire) or a strongly altering refractive index are beneficial. The sharpness and width of the hysteresis [GB97], as well as the critical transition temperatures of the reversible IMT [TBC16, ABC12, WWC09, CGF10] depend on the tensions between the substrate and the VO_2 NCs [NHH89]. Vanadium dioxide has a relatively high thermal coefficient of linear expansion along the c_R-axis ($2.8 \cdot 10^{-5} K^{-1}$) [Hea73] compared to the (fairly low) one of SiO_2 ($0.5 \cdot 10^{-6} K^{-1}$)[16]. Consequently, a change of the microstructure's temperature induces local strain fields, especially at the phase boundaries. In general, internal or external stress leads to modifications of the unit cell dimensions of VO_2 favoring one or the other crystallographic phase in a certain temperature range. Specifically, the V-V dimerization along the rutile c_R-axis is affected [TBC16, CGF10]. An explicit connection between the bonding length of the V atoms and the transition temperature were found [MUH02, SZM14]. Considering Gibbs free energy mentioned above, applying stress to the VO_2 NCs increases the energy barrier between the two solid phases, leading to a widened hysteresis.

---

[16] The thermal coefficient of linear expansion of synthetic sapphire (Al_2O_3) is $6.66 \cdot 10^{-6} K^{-1}$ (parallel to optical axis) and $5 \cdot 10^{-6} K^{-1}$ (perpendicular to optical axis) [Mol21]. Therefore, an Al_2O_3 host material applies less stress on the VO_2 NCs upon heating/cooling compared to a SiO_2 host.

The broad hysteresis is also related to the high structural quality of the NCs (cf. Fig. 2.2(c)) [ALS12, CWD19]. In particular, NCs with a small volume and a good crystal quality feature a reduced probability of finding nucleation sites (impurity, vacancy or grain boundary). This spherical single domain character protects the NCs from nucleation, hampering the structural phase transition. Spontaneous nucleation from fluctuations in the potential energies still remains. As a result, the critical temperature for the IMT is raised, as well as the back-switching temperature to the insulating phase is lowered, leading to a wide hysteresis. In general, small NCs [LFH04, ALS12] with outstanding crystal quality [ZWW14, SLF04] feature the broadest hysteresis. On the other hand, intentional doping of VO_2 allows for precise tailoring of the IMT and hysteresis width. Starting at a maximum width in the undoped case the hysteresis loop can be closed systematically by increasing the doping concentration. In parallel the critical temperature declines [KDS09]. Therefore, these thermal properties of the VO_2 can be modified in a certain range to fit specific applications' requirements. As an example, thermochromic window coatings benefit from a reduced T_c close to ambient temperature. An overview of the technological progress can be found in Ref. [WLK16].

The above mentioned considerations allow to rate the quality of the present NC sample based on the observed hysteresis. The results of electron microscopy (cf. Fig. 2.2(b))) and the temperature range of about 10°C, over which the IMT is seen point to a relatively broad distribution of NC sizes. Nevertheless, the notably wide hysteresis shown in Fig. 2.4 confirms the high structural quality of the fabricated NCs as seen in Fig. 2.2(c).

As already mentioned in the previous paragraphs, optical excitation of the IMT by, e.g. continuous wave (cw) laser light, is an alternative to a thermally induced phase transition. This mechanism, mainly based on an elevated nominal lattice temperature due to photon absorption, will be addressed in the next section.

2.5 Optically Induced IMT with Hysteresis in VO_2 NCs

The reversible first order phase transition in VO_2 can be controlled by a variety of excitation methods. Besides heating [Mor59], the application of external stress [BLC15] or electronical excitation [JKS13], optical pumping can also trigger the IMT [JZK14]. In the present chapter, the optically induced IMT and the appearing hysteresis in VO_2 NCs are investigated by all-optical means. Furthermore the term hysteresis will be explained with respect to the optical excitation process. Finally the mechanism behind the optical induced IMT will be clarified briefly. Note that the sample examined in this section is identical to the one used for the thermal experiments in chapter 2.4.

Analogue to the procedure in the previous chapter the VO_2 NC sample is mounted on a temperature-controlled holder (Covesion Oven PV10 with additional Peltier element for cooling and Controller OC1) to keep it at room temperature (20 °C). The momentary phase of the VO_2 NCs and the hysteresis are recorded by tracking the transmission of a weak 1036 nm laser beam through the sample. This probe beam is focused onto the sample surface at normal incidence and features a beam diameter of ~30 μm at full width of half maximum (FWHM). This value is measured with a commercial scanning slit beam profiler (Thorlabs BP104-IR). The transmitted probe intensity is recorded using an InGaAs photodiode and lock-in detection. Instead of a thermal excitation, an all-optical approach is used to drive the VO_2 NCs through the phase transition and back to the insulating state by increasing and decreasing the pump laser power. For this purpose, a 532 nm cw pump laser (Changchun New Industries MGL-H-532-500) is focused onto the sample surface, illuminating a spot with a diameter of roughly 90 μm (FWHM). Both beams, the pump and the probe beam are aligned to illuminate concentric spots at the sample's surface. The spatial distribution of the pump laser intensity features a Gaussian shape[17] in x- and y-direction leading to a non-uniform heat deposition in the illuminated area. In order to rule out potentially detrimental effects occurring from the complex temporal heat dissipation dynamics in the sample, two measures are performed: First of all, the spot diameter of the probe laser is chosen to be only a third of the pump laser spot diameter. Due to this restriction, the probed area is illuminated with nearly homogenous pump intensity and is less affected by heat dissipation dynamics outside the pump spot. Secondly, to ensure a thermal equilibrium at the probe spot, the change in pump power is carried out sufficiently slowly.

---

[17] The scanning slit beam profiler provides a xy-intensity-plot of the laser beam, revealing the Gaussian beam shape.

To accurately define the pump laser power, a half-wave plate and a polarizing beam splitter cube (PBSC) are inserted in the beam path. By rotating the half-wave plate, the polarization angle of the linearly polarized pump beam is rotated and the ratio of the transmitted power through the PBSC is changed, respectively. By using a motorized rotational holder, the pump beam's power can be adjusted continuously with respect to the rotation angle of the half-wave plate. This is done in order to simultaneously monitor the momentary pump irradiance and the probe transmission. A reference table, associating the rotation angle of the half wave plate with the pump laser power was created by using a commercial power meter (Thorlabs PM100A and S130C).

Fig. 2.5 displays the relative probe transmission for increasing and decreasing pump irradiance. All data points are normalized to the probe signal strength in absence of the pump beam. At the beginning of the hysteresis loop, the signal features a plateau. Increasing the pump power leads to a barely visible slope, indicative for only a few NCs that switch to the metallic state. At a threshold of ~2.75 kW/cm² pump irradiance a relatively sharp drop of the transmitted intensity displays the optically induced IMT caused by a local temperature increase of $T > T_c$ in the pumped area. Further increasing of the pump power does not alter the signal strength as all probed NCs are in the metallic state. Upon decreasing of the pump irradiance, a supercooled metallic state persists until the metal-to-insulator transition happens at ~0.75 kW/cm². At a sample temperature of 20°C, a broad and fully reversible hysteresis is found. As expected, the shape of the optically pumped hysteresis resembles the thermal hysteresis shown in Fig. 2.4, yet with switched x-axis labeling. For an elevated or reduced sample temperature the hysteresis shifts horizontally to a lower or higher pump irradiance, respectively [JZK14]. The shape (width, height, slopes) of the hysteresis remains unchanged. This behavior suggests that the optically induced phase transition, in turn, is somewhat based on a thermal excitation. The absorbed pump laser light mainly deposits heat in a two-step process: Photo carriers are injected by optical pumping of insulating VO_2 leading to a band gap collapse. On timescales of less than 200 fs the electrons attain a transient, hot Fermi distribution with an electron temperature way above the lattice temperature [CDC04, PKE11, WHX14, RCS05, CJH15]. The second step is a lattice thermalization via electron-phonon scattering that occurs on timescales of picoseconds [MCT14, WFW13, KEH07]. Upon a certain pump irradiance, the lattice temperature rises above the critical temperature of the phase transition T_c and, thereby, switches the illuminated NCs to the metallic phase.

Nevertheless, the question remains to what extent the IMT is triggered by optical injection of carriers, since time resolved pump-probe measurements give hints towards the absence of a structural bottleneck in the transition process. The ultrafast band structure renormalization is caused by photoexcitation of carriers from localized vanadium 3d valence states (~40 - 60 fs), strongly changing the optical properties before a significant hot-carrier relaxation (phonon bottleneck) occurs (~200 fs) [CJH15, WHX14]. Since the detection timescales of the experiments performed by the author greatly exceed those of the two-step transition process, a generalization to an optically pumped and thermally executed excitation, in other words, laser-induced heating, for simplicity's sake is valid.

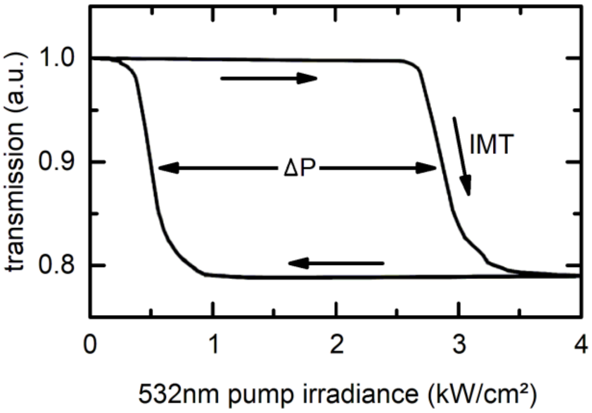

Fig. 2.5: Optically pumped hysteresis loop of VO_2 NCs featuring the insulator-to-metal and reverse metal-to-insulator phase transition by tracking a 1036 nm probe transmission for continuous change of the pump irradiance.

The approach to optically define metallic VO_2 patterns in an unstructured sample opens up the opportunity to design macroscopic, as well as microscopic optical elements. Using a commercial cw laser source with a build-in TTL trigger mode or an external time-controlled shutter allows for a fast and precise control of the transition between the two phases of VO_2. Thereby, the area of the optical excitation is subject to the finite laser spot and spatial patterns of insulating and metallic VO_2 can be created selectively with all-optical means. Optically imprinted reconfigurable photonic elements, designed by spatial illumination of a VO_2 NC sample have been demonstrated by Jostmeier et al. [JZK14]. This way, the photonic elements are independent of doping or local argon bombardment [JMZ16] used for permanent deactivation of the IMT.

In contrast to optical elements that have to be defined by a time consuming imprinting process, the integration of a single layer of VO_2 NCs into standard optical elements allows for a fast and reversible altering of the transmission properties by switching in between the two phases of the VO_2 layer. To demonstrate this concept, a moderate-finesse etalon containing a sub-wavelength layer of VO_2 NCs is introduced and investigated in the following chapter.

Chapter 3

Thermochromic and Photochromic Etalon Based on VO_2 Nanocrystals

The active, fast and precise modulation of light is the bedrock of modern photonics. Instead of relying on mechanical components like a chopper or shutter, an actively tunable material changes its essential optical properties motionless and on demand by an external trigger mechanism. A typical example for this kind of device is, e.g., an electro-optic modulator (EOM) in which a signal-controlled element, exhibiting an electro-optic effect, is used to modulate a beam of light. This modulation can be imposed on the polarization, phase, frequency and amplitude of the light beam. In this context, phase changing materials such as VO_2 are subject to extensive research, since they exhibit strong nonlinear modifications of their optical properties when undergoing the (structural) phase transition.

The marked change in optical and electrical properties during the IMT is a promising tool for modern photonic applications of VO_2. Vanadium dioxide based structures are suitable for applications such as switchable optical elements and optical memories [Roa71]. As an example, it has been shown that the dielectric contrast between the insulating and the metallic phase of VO_2-nanocrystals (NCs) defines nanothermochromic diffraction gratings [ZWK12]. More recently, other planar optical elements such as optically defined lenses have been realized [SBV14, JZK14].

In this chapter a novel optical functionality of VO_2 NCs which is mainly related to the change of the dielectric function during the IMT is demonstrated. In particular, a sub-wavelength layer of VO_2 NCs is embedded into a moderate-finesse etalon. When these NCs are driven through the IMT by either heating or optical excitation, a pronounced spectral shift as well as a transmission change of the near-infrared modes transmitted through the etalon is expected due to the substantial change of the complex refractive index. Both heat deposition and optical excitation permit to actively control the etalon’s functionality. Remarkably, spectral shifts of about one linewidth can be achieved. In agreement with transfer matrix simulations these spectral shifts strongly depend on the thickness as well as on the location of the sub-wavelength thick VO_2 NC layer with respect to the node/anti-node pattern of the optical resonator.

3.1 Optics of Multilayer Systems

3.1.1 Resonator Optics

An optical resonator confines and stores light with certain resonance frequencies in between its reflective boundaries. The easiest approach for such a resonator is a plane-parallel (Fabry-Pérot) etalon, consisting of two opposing broadband and highly reflective flat mirrors as depicted in Fig. 3.1(a). In particular, this classical Fabry-Pérot resonator was used for the first ruby laser, developed in 1960 by Theodore Maiman [Tow07]. Wrapped around an active medium, it serves as an optical "container" for the generation and amplification of laser light. Nowadays, the semiconductor crystal (active medium) in a laser diode is bounded by parallel surfaces, creating a small-volume Fabry-Pérot cavity. In general, the geometric properties of the resonator determine the frequency (wavelength) and the spatial distribution of the laser beam. In addition to laser applications, such an etalon is used as a spectrum analyzer or an interference filter with specific spectral transmission properties.

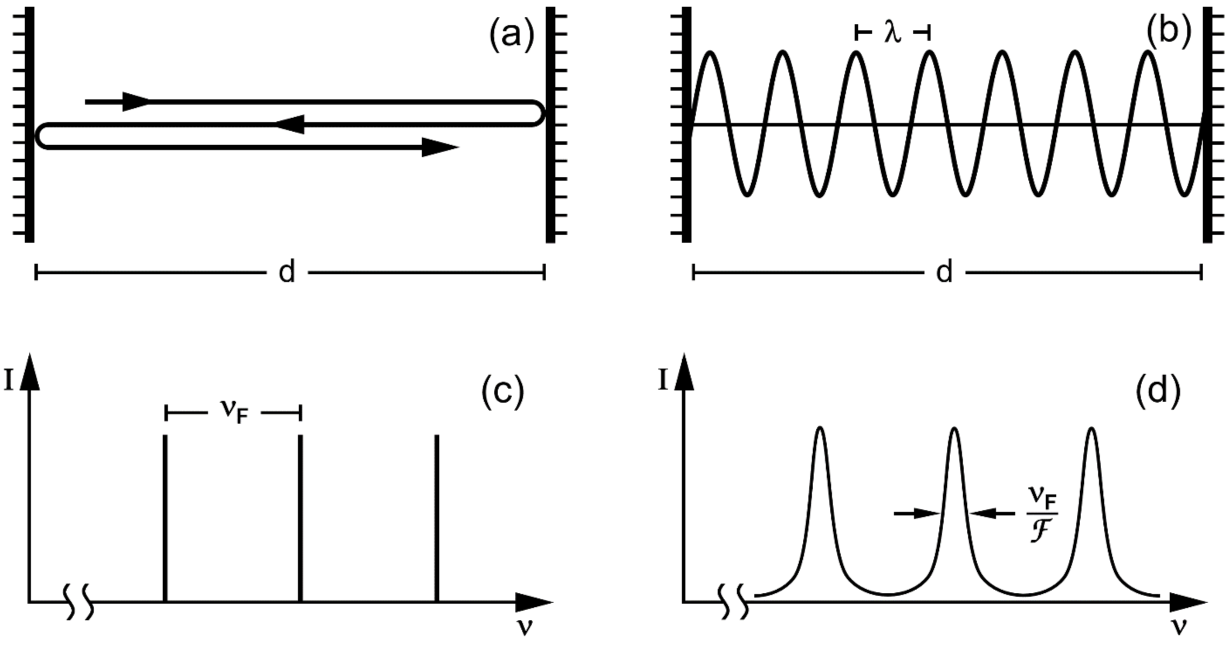

Fig. 3.1: (a) Light rays being reflected perpendicular to the mirrors back and forth without escaping the two-mirror planar Fabry-Pérot etalon. (b) Complex amplitude of a resonator mode ($q = 14$). (c) Resonator frequencies of a lossless etalon. In the steady state only light waves at the precise resonator frequencies are allowed. (d) A lossy resonator sustains waves at all frequencies. The attenuation resulting from destructive interference increases at frequencies away from the resonance.

Generally speaking, an optical resonator consists of a sequence of optical elements through which light repeatedly passes and on whose surfaces a part of the light is reflected. A complete revolution in the resonator ends at the same place as it began. Therefore, the corresponding mathematical matrix that describes one revolution has the determinant 1. Inside the resonator the light is modified (reflected, transmitted, absorbed and/or amplified and phase shifted) each time it passes through a specific (active) medium. In the case of a laser, the light is coupled out through one partially transparent mirror of the resonator.

In the following section the optical modes and the response of a simple etalon constructed of two parallel flat mirrors separated by the distance d (geometrical length of the resonator) are examined. This etalon will be considered as one-dimensional ideal resonator whose mirrors are lossless (cf. Fig. 3.1(a)). Subsequently, the effect of losses is introduced. The following brief introduction to a simple resonator is based on chapter 9 of Ref. [ST91]. The interested reader is encouraged to consult the book for further information about even more complex, higher dimension resonator types.

A monochromatic wave of frequency ν has the following wave function that represents the transverse component of the electric field:

$$u(\boldsymbol{r},t) = \mathrm{Re}\{U(\boldsymbol{r})\exp(i2\pi\nu t)\} \tag{3.1}$$

U(**r**) is the complex amplitude at position **r** within the resonator (cf. Fig. 3.1 (b)) that satisfies the Helmholtz equation:

$$\nabla^2 U + k^2 U = 0 \qquad \text{with} \qquad k = \frac{2\pi\nu}{c} \tag{3.2}$$

Note that k is the wavenumber and $c=c_0/n$ is the speed of light in the medium embedded between the mirrors (with refractive index n of the medium). The basic solutions of the Helmholtz equation, subject to the appropriate boundary conditions[18] of the planar-mirror etalon are the modes of the resonator. The following simple expression for a standing wave with amplitude A solves the Helmholtz equation:

$$U(\boldsymbol{r}) = A\sin(k_q z) \qquad \text{with} \qquad k_q = \frac{q\pi}{d} \tag{3.3}$$

---

[18] The transverse components of the electric field vanish at the surfaces of the mirrors, leading to U(**r**)=0 at these planes. The position vector **r** is reduced to the scalar *z* (z=0…d), referring to the 1D longitudinal position inside the resonator.

Therefore, the wavenumber k_q, with an integer q, is restricted to discrete values and, consequently, the resonance frequencies ν_q, which will constructively interfere to the longitudinal resonator modes are restricted as well:

$$\upsilon_q = \frac{ck}{2\pi} = q\frac{c}{2d} \tag{3.4}$$

As shown in Fig. 3.1(c) adjacent resonance frequencies ν_q are separated by a constant frequency difference, called the free spectral range ν_F:

$$\upsilon_F = \frac{c}{2d} \tag{3.5}$$

The corresponding resonance wavelengths (in the medium) are calculated by:

$$\lambda_q = \frac{c}{\upsilon_q} = \frac{2d}{q} \tag{3.6}$$

Note that at resonance condition, the length of the resonator $d=q\lambda/2$, is an integer multiple of half of the wavelength (cf. Fig. 3.1(b)).

The strict condition on the frequencies of the optical waves that are permitted inside the resonator is relaxed when the cavity has additional losses (cf. Fig. 3.1 panel (c) versus panel (d)). The main principal source of loss can be attributed to the mirror's imperfect reflectance $R_i<1$. Partially transmitting mirrors are often used to permit light to enter and/or escape from the cavity. Furthermore the finite size of the mirrors causes a fraction of the light to leak around the mirrors and, thereby, to get lost. Losses that originate from the absorptive behavior of the embedded materials can be expressed via an exponential round-trip power attenuation factor including the absorption coefficient α_i and the thickness of the layer d_i of the different materials inside the cavity. The overall intensity attenuation factor μ including the mirror's reflectance R_i is therefore:

$$\mu^2 = R_1R_2\exp\left(-2\sum_i \alpha_i d_i\right) \tag{3.7}$$

Following a wave in its excursion between the two mirrors of an ideal etalon (cf. Fig. 3.1(a)), results in an infinite sum of phasors with a constant phase difference imparted by each single propagation round trip. Introducing losses to the ideal resonator leads to phasors with unequal magnitude where two consecutive phasors show a magnitude ratio equal to the round-trip amplitude attenuation factor μ. The net result of all round trips is a superposition of an infinite number of waves that are separated by equal phase shifts, but with reduced amplitudes. On the basis of this consideration, the total transmission, or so called spectral response of the etalon can then be described as followed:

$$I = \frac{I_0}{(1-\mu)^2 + 4\mu \sin^2\left(\frac{2\pi\delta}{\lambda}\right)} \qquad \text{and} \qquad I_{\max} = \frac{I_0}{(1-\mu)^2} \tag{3.8}$$

Here, I_0 is the intensity of the initial wave. To consider a dispersive material, δ defines the optical path length with respect to the different media inside the resonator:

$$\delta = \sum_i d_i n_i \tag{3.9}$$

From the above equation it is clear that in the case of a vacuum filled resonator ($n = 1$) the optical path length is the same as the geometrical length. The typical quality factor of a cavity is the finesse $\mathcal{F}$. It is fully determined by the resonator losses and is independent of the resonator length:

$$\mathcal{F} = \frac{\pi\sqrt{\mu}}{1-\mu} \tag{3.10}$$

3.1.2 Transfer Matrix Method

A more sophisticated technique to calculate the optical response of a stratified medium, e.g. an optical resonator, is the transfer-matrix method [KS02]. This formalism is the central method with which the theoretical description of reflection and transmission properties of any multilayer system can be achieved. Specifically, it is used to analyze the propagation of electromagnetic, as well as acoustic waves, through a stacking of layers made from different materials. Theoretical descriptions of the various resonance phenomena, such as guided and quasi-guided optical waves or surface-plasmon modes in (multi-)layer structures, emerge from this method [WYC16, AGG17]. Furthermore, the transfer matrices offer the possibility to calculate the optical fields in a multilayer and to treat continuous refractive index profiles [MJD05, WYC16]. Dielectric mirrors and anti-reflective coatings can be simulated prior to the fabrication and (partially)[19] unknown layered structures can be analyzed.

---

[19] It is mandatory to know some basic information about the structure: For each layer the thickness or the refractive index have to be known.

In this sub-section, the essential contents of the transfer-matrix method for the optical analysis of stratified media are illustrated. The description is based on a transition of a plane wave of a given frequency propagating through a stack of N layers at normal incidence[20] (z-direction) as depicted in Fig. 3.2. This transition is described by Fresnel's formulae, which link the reflected or transmitted field amplitude to the incident amplitude at each of the N+1 interfaces. In order to satisfy the Helmholtz equation (3.2) for a layered system, the electric field within one layer with index i is represented as the superposition of a left- and right-traveling wave with wave number k_{zi}:

$$E_i(z) = E_i^r e^{ik_{zi}z} + E_i^l e^{-ik_{zi}z} \tag{3.11}$$

Here, E^r stands for the amplitudes of the component running in the positive z-direction (right) and E^l for the amplitude of the component running in the negative z-direction (left). According to Fig. 3.2, the partial waves to the right of the interface i-j are marked with a prime.

Based on the continuity conditions for electromagnetic fields across boundaries[21], a linear transformation can be derived [Yeh88] which links the amplitude vectors on the left and right of an interface by the 2x2 transition matrix (so called refraction/transmission matrix of the interface) $\mathbf{D}_{ij}$:

$$\begin{pmatrix} E_i^r \\ E_i^l \end{pmatrix} = \frac{1}{t_{ij}} \begin{bmatrix} 1 & r_{ij} \\ r_{ij} & 1 \end{bmatrix} \begin{pmatrix} E'^r_j \\ E'^l_j \end{pmatrix} = \mathbf{D}_i^{-1}\mathbf{D}_j \begin{pmatrix} E'^r_j \\ E'^l_j \end{pmatrix} = \mathbf{D}_{ij} \begin{pmatrix} E'^r_j \\ E'^l_j \end{pmatrix} \tag{3.12}$$

Here, $\mathbf{D}_{ij}$ is a product of 2x2 dynamical matrices $\mathbf{D}_i$ and $\mathbf{D}_j$ in sequence, each representing one side of an interface. They can be expressed in terms of the Fresnel transmission and reflection coefficients t_{ij} and r_{ij} (for normal incidence):

$$t_{ij} = \frac{2n_i}{n_i + n_j} \qquad \text{and} \qquad r_{ij} = \frac{n_i - n_j}{n_i + n_j} \tag{3.13}$$

---

[20] The description can be generalized to deal with incidence at an angle (polarization has to be considered), absorbing media, gradient or inhomogeneous refractive index media and media with magnetic properties. Surface properties, e.g. roughness, can be treated as well.

[21] In general, the tangential component of the electric field strength E and the normal component of the magnetic flux density B are continuous across an interface. Furthermore, the normal component of the electric displacement D has a step of surface charge on the interface surface and the tangential component of the magnetic field strength H shows a step of surface current density.

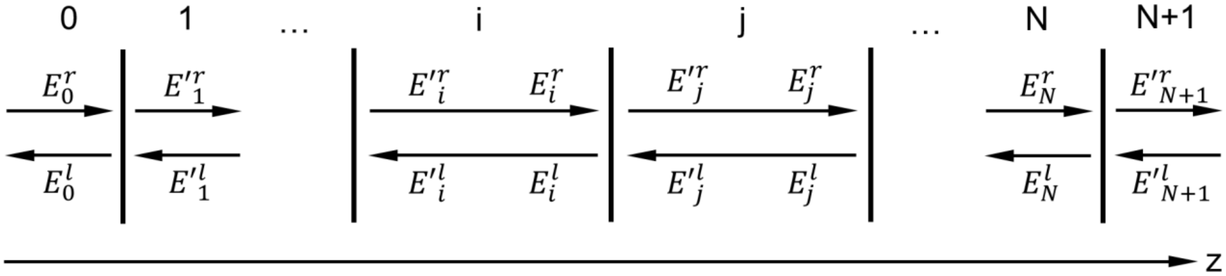

Fig. 3.2: Notation of the electric field amplitudes E_i within an arbitrary multilayer. The subscripts indicate the specific layer, the superscript distinguish between left- (l) and right-going (r) wave, respectively. A prime is used for waves at the right-hand side of an interface.

Left and right within the layer i the amplitude vectors differ by a phase φ_i, imposed by one traversal of light through the bulk material of the layer. It is determined by the z-component of the wave vector k_{zi} and the layer thickness d_i:

$$\varphi_i = k_{zi} d_i \tag{3.14}$$

This phase is taken into account by the propagation matrix $\mathbf{P}_i$:

$$\begin{pmatrix} E'^r_i \\ E'^l_i \end{pmatrix} = \begin{bmatrix} e^{-i\varphi_i} & 0 \\ 0 & e^{i\varphi_i} \end{bmatrix} \begin{pmatrix} E_i^r \\ E_i^l \end{pmatrix} = \mathbf{P}_i \begin{pmatrix} E_i^r \\ E_i^l \end{pmatrix} \tag{3.15}$$

Note that E and E’ refer to the electric fields in the left- and right-hand side of one layer. The repeated application of the transformations mentioned in Eq. 3.12 and 3.15 for N layers and N+1 interfaces leads to a final product of N+1 2x2 matrices:

$$\begin{pmatrix} E_0^r \\ E_0^l \end{pmatrix} = \mathbf{D}_{01} \prod_{i=1}^{N} \mathbf{P}_i \mathbf{D}_{i,i+1} \begin{pmatrix} E'^r_{N+1} \\ E'^l_{N+1} \end{pmatrix} = \begin{bmatrix} T_{11} & T_{12} \\ T_{21} & T_{22} \end{bmatrix} \begin{pmatrix} E'^r_{N+1} \\ E'^l_{N+1} \end{pmatrix} \tag{3.16}$$

Consequently, the total transfer matrix **T** of the layered system (so called system transfer matrix) results from the product of the individual phase and transition matrices. From this characteristic 2×2 matrix, reflection and transmission coefficients as well as propagation constants of guided waves can be calculated for any layered system. To calculate the reflection and transmission coefficients, one has to consider a wave with amplitude $\mathrm{E}_0^{\mathrm{r}}$ incident from the left half-space and a wave with amplitude equal to zero incident from the right half-space, i.e. $E'^l_{N+1} = 0$.

Accordingly, Eq. 3.16 yields the following relationships between the amplitudes of the left and right half-space:

$$E_0^r = T_{11}\, E'^r_{N+1} \qquad \text{and} \qquad E_0^l = T_{21}\, E'^r_{N+1} \tag{3.17}$$

The transmission and reflection coefficients of the total multilayer are given straightforward by their definitions in terms of the system transfer matrix elements:

$$t = \frac{E'^r_{N+1}}{E_0^r} = \frac{1}{T_{11}} \qquad \text{and} \qquad r = \frac{E_0^l}{E_0^r} = \frac{T_{21}}{T_{11}} \tag{3.18}$$

In particular, this matrix method is suitable to describe the resonance phenomena occurring from multiple reflections in stratified media. These resonances appear in the reflection and transmission spectra recorded in the course of experimental studies. For the transmission T and reflectivity R of a stacked system, the theoretical expression can be obtained from the matrix formalism as well:

$$T = |t|^2 = \left|\frac{1}{T_{11}}\right|^2 \qquad \text{and} \qquad R = |r|^2 = \left|\frac{T_{21}}{T_{11}}\right|^2 \tag{3.19}$$

T and R depend on the wavelength of the light and the optical parameters (layer thickness and complex refractive index) of the individual layers. By adapting the theoretical expression for T or R to measured transmission or reflection data, the layer thicknesses and refractive index of the layers can be determined as parameters of the best fit.

The application of the matrix method taken up in this work is presented in the course of the following chapter. Since this method is a long-term established tool for optical analysis, many programs were developed in the progression of the computer era. The presented theoretical date based on the transfer matrix method is calculated with the program “RefDex” that was developed in the group of Prof. Dr. Martina Schmid at the University of Duisburg-Essen [MYS14].

3.2 Optical Etalon with VO_2 NC Layer

One fascinating way to utilize the dielectric contrast between the two phases of VO_2 is the construction of a moderate-finesse etalon containing a sub-wavelength layer of VO_2 NCs. Two layouts, one with a fixed and the other one with a variable resonator length, are realized using broadband and highly reflective mirrors[22] ($R \approx 99\%$).

For the optical switching of the resonator's modes a layer of VO_2 NCs, embedded into fused silica, is glued to one of the cavity mirrors using UV-curing optical adhesive (Norland Optical Adhesive No. 61). Then, the surplus fused silica is lapped and polished to an overall thickness of ~10.2 µm. Finally, the second mirror is glued to the VO_2 NC sample to complete this stacking to a moderate-finesse etalon with a geometrical resonator length of ~12.4 µm. In contrast, an etalon with variable and precisely definable resonator length is built by mounting the second mirror on a mechanical translation stage. As a result, the spectral position of the transmission modes can be fine-tuned by altering the resonator length. Thereby, the thickness of the VO_2 NC sample limits the minimal gap in between the cavity mirrors and, therefore, limits the maximum spectral distancing between longitudinal modes of the resonator as well.

Going on to the experimental setup, partially depicted in Fig. 3.3, one has to distinguish between the two resonator layouts. The first etalon that is glued to a unit is located inside an aluminum block that is attached to a temperature-controlled oven (Covesion Oven PV10 and Controller OC1) (cf. Fig. 3.3(c)). It allows for operating temperatures between near-ambient values and 200°C and features a high thermal stability. This temperature range allows to completely cover the hysteresis of the VO_2 NCs (cf. Fig. 2.4). A mode-locked titanium-sapphire laser (Ti:Sa) is used as a broadband light source due to its large spectral tunability[23] and outstanding beam quality compared to an incoherent light source. It operates at a few hundred milliwatts of average output power and delivers a train of 50 fs pulses at a repetition rate of ~65 MHz. Only a few microwatts are used as probe beam in order to avoid any impact on the IMT or damage to the spectrometer unit (Avantes AvaSpec-2048).

The fully adjustable etalon is preferably used for optical excitation of the VO_2 NCs due to the reduced thermal contact originating from the air gap between the VO_2 sample and the second mirror (cf. Fig. 3.3(a)). Therefore, less laser power is needed to trigger the IMT and the phase transition occurs well below the damage threshold of the optical adhesive. The probe laser remains unchanged, whereas a solid state cw diode laser with a wavelength of 532 nm and an optical output power of 500 mW is utilized as excitation source for the IMT (Changchun New

---

[22] Specifically, the following mirrors are used: Glued resonator: Thorlabs BB05-E03. Variable resonator: Layertec Coating 115014. Both types of mirrors have a reflectivity of $R = 99{,}0\text{-}99{,}5\%$ for 700 nm to 1100 nm.

[23] A spectral range from 750 nm up to 1000 nm can be covered.

Industries MGL-H-532-500). Using a mechanical shutter, a half-wave-plate in combination with a polarizing beam splitter cube and a lens, a precisely adjustable portion of the pump laser beam (desired power density of up to ~8 kW/cm² for the IMT) is focused down to the NC layer and overlaps the low-power broadband Ti:Sa probe laser beam. Both beams feature a Gaussian shaped intensity profile in x- and y-direction and are aligned to illuminate concentric spots at the sample's surface. The spot diameter of the pump laser (~60 µm) is chosen to be three times larger than the probe laser spot (~20 µm) to illuminate the probed area with nearly homogenous pump intensity. Considering the excitation method regarding the variable etalon, one could also think about a thermally induced IMT by heating only the one mirror containing the VO_2 NC sample. This, at first glance, promising approach however leads to an unreproducible spectral shift of the modes due to an inhomogeneous thermal expansion of the whole mechanical stage.

Now both, heat deposition and optical excitation allow to actively control the optical properties of the resonator due to the substantial modification of the complex refractive index during the IMT. More precisely, a deviation in the real part n results in a spectral shift of the transmission peaks via a change of the optical path length δ inside the resonator (cf. Eq. 3.9). On the other hand, a rise of the imaginary part k is related to an increased linear absorptive index leading to a reduction of the resonator's finesse and peak transmission resulting in a broadening of the transmission peaks (cf. Eq. 3.8 and 3.10). The spectral data is recorded when the system has settled into thermal equilibrium at the probe spot.

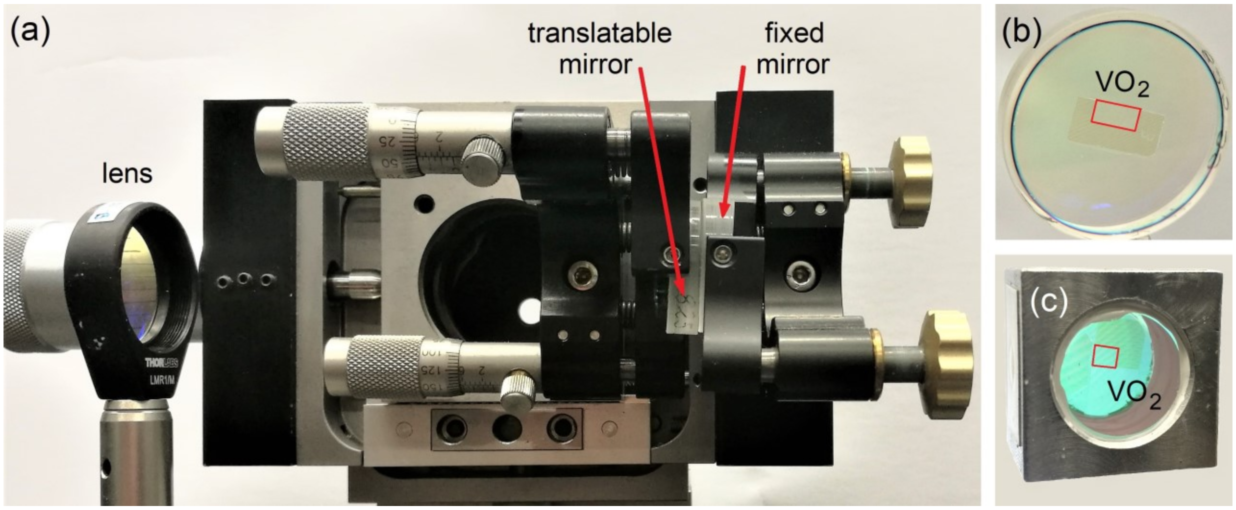

Fig. 3.3: Components of the Fabry-Pérot etalon containing a sub-wavelength layer of VO_2 NCs. (a) Etalon with variable resonator length. The tilt of the mirrors compensates for the refraction caused by the wedged mirrors (used to eliminate fringe patterns and cavity feedback due to the slightly tilted backside). (b) Resonator mirror from the variable resonator in panel (a). The glued VO_2 NC sample is located in the middle of the mirror. (c) Cavity with glued mirrors to each other and VO_2 NCs in between, mounted with thermal conduction paste inside an aluminum block for optimized thermal contact.

In the first step, an overview of the optical response of the glued moderate-finesse etalon containing a sub-wavelength layer of VO_2 NCs is provided. Fig. 3.4 (a) shows the etalon's transmission spectra of both crystallographic phases featuring several peaks of high transmissivity. The two spectra, the insulating phase shown in blue and the metallic phase in red, are acquired at the same temperature of 60°C. Note that the illustrated spectra in this section are not normalized to the incident light. From the spectral position of the transmission peaks in Fig. 3.4(a) and Eq. 2.8 the geometrical resonator length can be estimated to be ~12.4 µm. This value derives from the stacking of the resonator as listed in the following table. The thickness d and the real part n, as well as the imaginary part k of the complex refractive index are given exemplarily for a wavelength of 830 nm. The effective thickness d of the VO_2 NC layer can be estimated by averaging the spherically shaped NCs with a typical diameter of 100 nm and a lateral spacing of 60 nm (cf. Fig. 2.2(b)). Specifically, this configuration corresponds to an equivalent homogenous layer of approximately 25 nm thickness.

	material	d	n_{830nm}	k_{830nm}
1	HR mirror 99%	-	-	-
2	Norland Glue No. 61	~2.2µm	1.549	~0
3	VO_2 insulating / metallic	~25 nm	1.742 / 1.636	0.090 / 0.136
4	fused silica	~8.0 µm	1.453	~0
5	Norland Glue No. 61	~2.2 µm	1.549	~0
6	HR mirror 99%	-	-	-

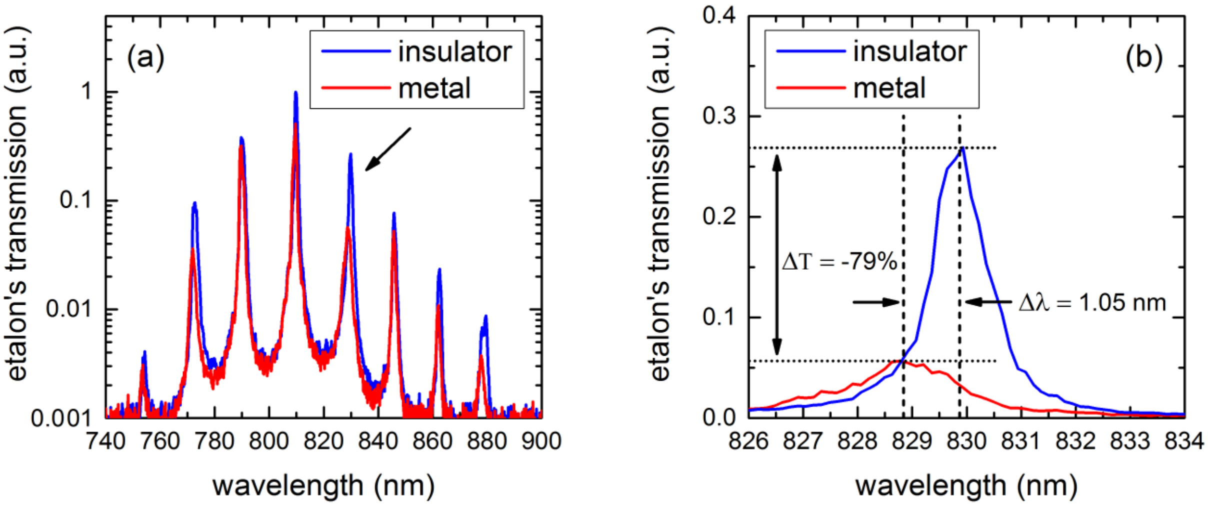

Fig. 3.4: (a) Resonator modes of a Fabry-Pérot etalon (geometrical cavity length: ~12.4 µm) containing a sub-wavelength layer of VO_2 NCs in the insulation (blue) and metallic (red) crystallographic phase. (b) Picture with higher resolution of the indicated resonator mode in panel (a). A transmission decrease of 79% accompanied by a spectral shift of 1.05 nm, caused by a substantial change of the complex refractive index during the IMT allows to actively switch the resonators modes.

For a quantitative analysis, the indicated resonator mode at ~830 nm wavelength in Fig. 3.4(a), featuring the most pronounced alteration in spectral position and amplitude, is shown with a higher resolution in panel (b). A reduction of the peak transmission by 79% and a spectral shift of the center wavelength by 1.05 nm can be extracted. This shift is comparable with the full width at half maximum (FWHM) of the mode in the insulating state. The reduction of the transmission, as expected from the Eq. 2.8, is strongly enhanced in comparison to a single pass through the VO_2 NC sample at ~830 nm wavelength (cf. Fig. 2.3 (b)). In combination, these two effects allow to actively switch the resonator modes via the IMT triggered by heat deposition.

So far, only two points of the hysteresis are compared to each other. In analogy to the data in Fig. 2.4, the spectral shift of the previously selected resonator mode at ~830 nm wavelength is recorded for the full thermal hysteresis. Fig. 3.5(a) shows this spectral shift including an additional linear offset due to the thermal linear expansion of the glued resonator. A correction for this linear offset reveals the spectral hysteresis originating only from the IMT as shown in Fig. 3.5(b). In comparison to the well-shaped hysteresis in Fig. 1(c), an additional modulation occurs. Internal reflections at the phase interfaces of the fused silica and VO_2 layer inside the cavity introduce additional low finesse cavities. Furthermore, the position of the nodes/anti-nodes of the standing waves in the resonator with respect to the position of the VO_2 layer defines the impact of the IMT to the resonator's modes. This "temperature-dependent" node/anti-node structure of the standing waves leads, in turn, to the well visible modulation, especially in the metallic state. Additional explanations will be provided later in this chapter.

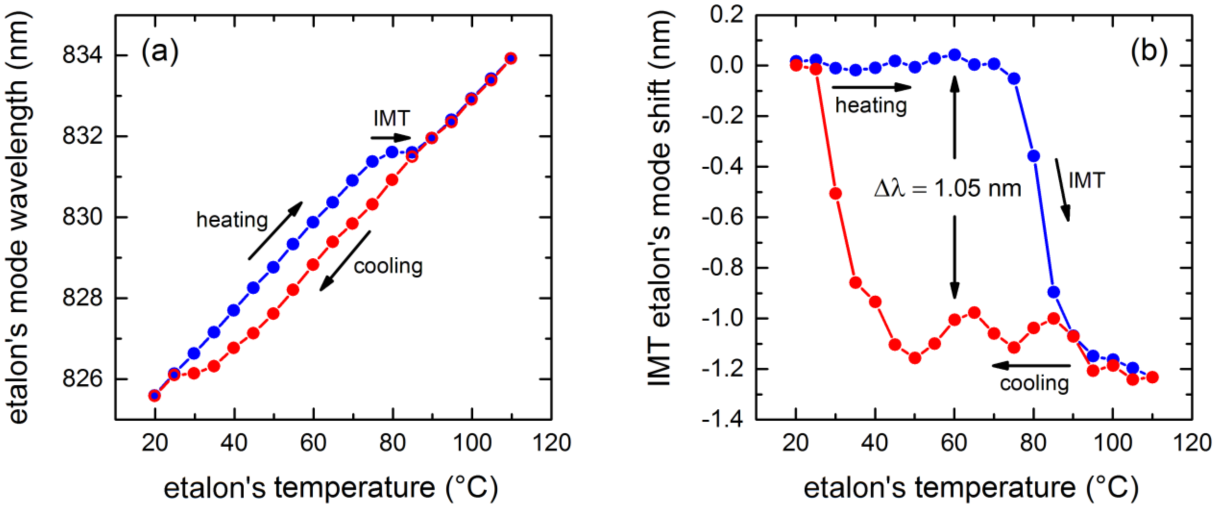

Fig. 3.5: (a) Spectral hysteresis of the indicated cavity mode in Fig. 3.4(a). In addition to the abrupt IMT, a linear thermal expansion disturbs the illustration of the hysteresis. (b) Pure thermal hysteresis extracted from panel (a). A modulation, especially in the metallic phase, occurs due to additional reflections at internal interfaces in combination with the altering node/anti-node pattern with respect to the VO_2 NC location in the thermally excited resonator.

Now the fully adjustable etalon where the IMT is triggered by optical excitation is in the focus of the analysis. Fig. 3.6(a) shows the etalon's broadband transmission spectra of both crystallographic phases, exhibiting a large amount of transmission peaks. The two spectra, the insulating phase shown again in blue and the metallic phase in red, are recorded at the same optical pump irradiance of ~2.3 kW/cm². In order to switch all VO_2 NCs in the metallic phase, a pump power density of ~8 kW/cm² is attained prior to the measurement of the metallic state. From the spectral position of the transmission peaks in Fig. 3.6(a) and Eq. 2.8 the selected geometrical resonator length can be estimated to be ~14.1 µm. For a quantitative analysis, the indicated peak at ~803 nm wavelength is shown with a higher spectral resolution in Fig. 3.6(b). Once again, this specific mode was selected due to its most pronounced change of the spectral position during the IMT. A reduction of the peak transmission by 74% and a spectral shift of the center wavelength by 0.45 nm become visible.

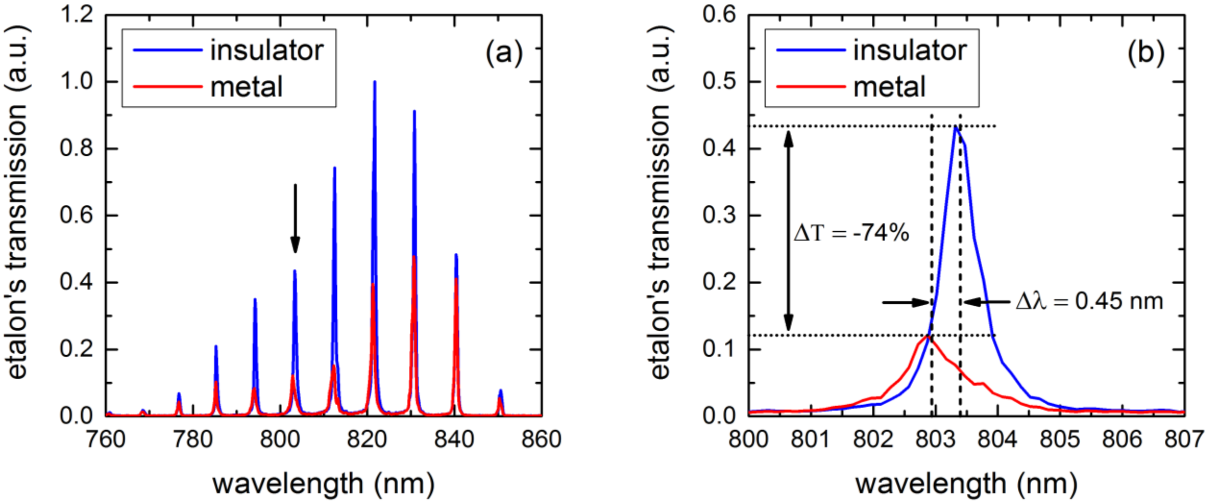

Fig. 3.6: (a) Resonator modes of a Fabry-Pérot etalon (geometrical cavity length: ~14.1 µm) containing a sub-wavelength layer of VO_2 NCs in the insulation (blue) and metallic (red) crystallographic phase. (b) Picture with higher resolution of the indicated resonator mode in panel (a). A transmission decrease of 74% accompanied by a spectral shift of 0.45 nm, caused by a substantial change of the complex refractive index during the IMT allows to actively switch the resonators modes.

In comparison to the spectral mode shift of the glued and thermally excited resonator (cf. Fig. 3.4(b)), this time the observed change of the peak's central wavelength is only half this size. Since the geometrical cavity length increased slightly by 13% (from 12.4 µm to 14.1 µm) the decrease of the spectral separation caused by the IMT is expected to be in the same order of magnitude[24]. However, this effect alone does not explain the observed reduced spectral shift. To

---

[24] Doubling the resonator length reduces the spectral separation of adjacent resonator modes by a factor of 2. In the same way, the spectral shift caused by the IMT is cut in half. This can be seen from Eq. 3.6 and 3.8.

account for the deviation of these two measurements, the amount of addressed NCs should be considered. Possibly, less crystals switch to and/or remain in the metallic state when the IMT is induced optically in the etalon's VO_2 sample and the transmission is recorded for equal pump irradiances. This effect is favored by the thermal coupling (optical adhesive) of the VO_2 NC layer to the mirror that serves as a heat sink. Recalling the final considerations from chapter 2.5, the optical excitation process was generalized as a "laser induced heating" of the VO_2 NCs for timescales that greatly exceed those of the two-step transition process (electronic and structural transition). Accordingly, increasing the sample temperature leads to less optical excitation that is needed for the phase transition [JZK14]. In the same way, cooling of the VO_2 NC layer by e.g. thermal coupling to a heat sink shifts the IMT hysteresis to higher pump irradiances.

In analogy to the measurement in chapter 2.5 an optically induced IMT hysteresis of the etalon's VO_2 NC sample is recorded and depicted in Fig. 3.7. Unlike the previous measurement where the sample's excitation area is practically suspended in free space (green curve), this time the sample is thermally coupled to one of the cavity mirrors at one surface (orange curve). This configuration results in a slight shift of the critical pump irradiance of the IMT to higher values and an additional distortion of the shape of the hysteresis. The latter is caused by the (inhomogeneous) cooling effect of the attached mirror. A pump irradiance of at least 8 kW/cm² is necessary to sufficiently heat up the probed spot on the sample and to switch all NCs to the metallic state. This threshold was reached when the experimental data from the variable and optically pumped resonator was recorded. Upon decreasing of the pump irradiance, the NCs gradually switch back to the insulating state without exhibiting such a pronounced plateau of a supercooled metallic state as observed beforehand. Furthermore, an additional weak interplay of the reflective surfaces of the mirror and the VO_2 sample that features an altering reflectance during the IMT contributes to the deformation of the hysteresis' appearance. In general, two points across the hysteresis loop, indicative of the same pump irradiance (e.g. at 2.3 kW/cm²), always refer to a transmission decrease slightly below the maximum value because not all crystals remain in the metallic state (from 8 kW/cm² to 2.3 kW/cm² the transmission increased again from 79% to 82%). Therefore the measured modal shift and transmission decrease of the etalon's modes, shown in Fig. 3.6(b), is somewhat reduced. Nevertheless, this detrimental effect is not expected to play a superior role since the transmission decrease in both resonator experiments reveal similar values. The strength of the two optical phenomena, the modal shift and the transmission decrease due to the IMT are related to each other. This limitation does not allow one phenomenon to occur without the other. In general, for similar resonator lengths, a switching of the VO_2 NCs by heat deposition shows a larger spectral shift compared to the results from an optically induced IMT using the present resonator setups. However, $\Delta\lambda$ is still in the order of the FWHM of the transmission peak in the insulating state that allows for an active switching of the resonators modes by optical excitation.

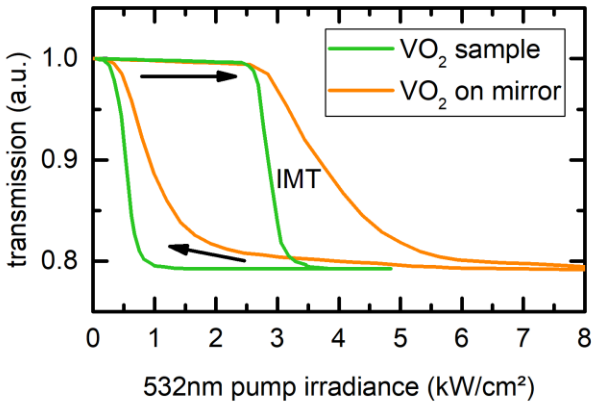

Fig. 3.7: Optically pumped hysteresis loop of a VO_2 NC sample suspended in free space (green curve) and thermally attached to one cavity mirror by optical adhesive (orange curve). Both feature the insulator-to-metal and reverse metal-to-insulator phase transition and are recorded by tracking a 1036 nm probe transmission for continuous change of the pump irradiance.

Most photonic devices require a well predictable and distinct switching of the optical properties, especially when they are based on nonlinear processes like the phase transition in VO_2. For this reason, the response of the etalon must be known, at least for all modes considered for optical application. The recorded transmission date of the present etalon, depicted in Fig. 3.6(a), permits to explore the spectral shift and transmission decrease of all individual cavity modes. Fig. 3.8(a) and (b) show the extracted modal shift and change in transmission, respectively. It is obvious from this data that the influence of the VO_2 NCs to the cavity modes strongly depends on the wavelength. More precisely in terms of the electromagnetic standing wave, the altering node/anti-node pattern of the electric field strength inside the cavity (cf. Fig. 3.1(b)) with respect to the VO_2 NC location defines the impact of the sub-wavelength thick VO_2 layer to the resonator modes. Domains inside the cavity where the electric field strength is low suffer from a weak light-matter interaction resulting in a small altering of the specific transmission mode. This explanation corresponds to the pronounced periodic modulation as seen in Fig. 3.8. From transmission data with more cavity modes this periodic modulation becomes even more obvious (data not shown). Considering any photonic application based on such a cavity, the knowledge of the node/anti-node pattern of the electric field with respect to the location of the VO_2 layer is crucial for a deterministic prediction of the modal shift and transmission decrease. This information must be provided by theoretical calculations and/or experimental experiments prior to the final application. Additional adjustments in a sophisticated range can only be guaranteed by an etalon with a variable resonator length and/or adjustable position of the VO_2 layer.

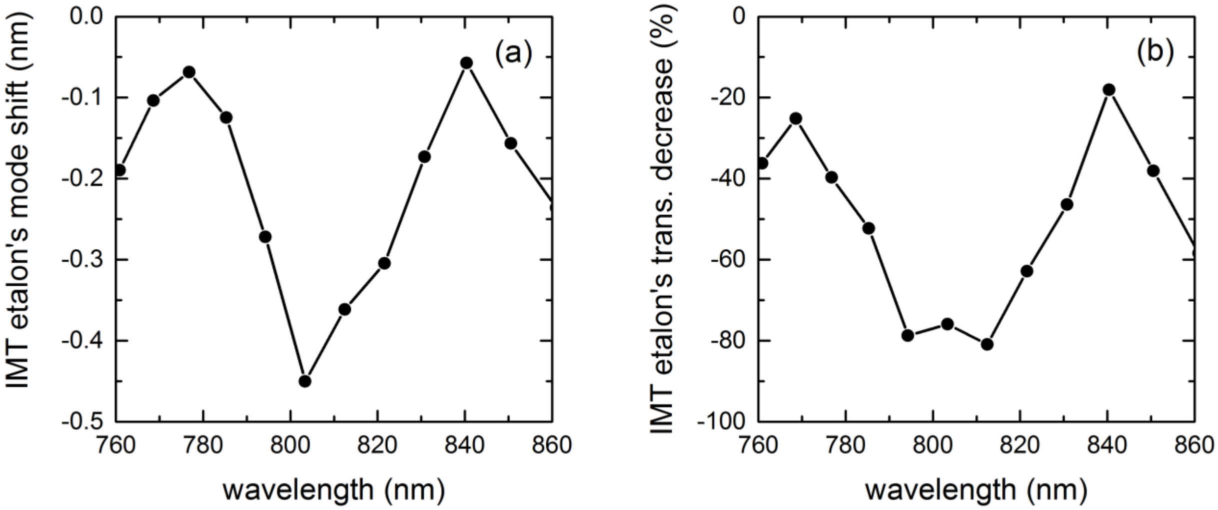

Fig. 3.8: Spectral shift (a) and change in transmission (b) of different cavity modes due to the IMT. The modulation is caused by the altering light matter interaction strength between the node/anti-node pattern of the electric field inside the cavity and the sub-wavelength layer of VO_2 NCs.

3.2.1 Simulation of the Etalon's Optical Response

From the theoretical point of view Eq. 2.3 describes the spectral response of the etalon. Thereby, the material composite in between the cavity mirrors is treated as a homogenous medium with average optical properties. All layers simply add up to a total optical path length δ with respect to their individual thickness d and refractive index n (cf. Eq. 3.9). Accordingly, additional internal multi-reflections at layer interfaces are neglected and do not contribute to the cavity losses or to spectral modulations originating from low-finesse cavities inside the main resonator. In general, losses can be attributed to the 99% reflectivity of the broadband cavity mirrors and to the absorption of the materials inside the resonator. Since the optical adhesive and the fused silica can be considered as transparent compared to the VO_2 in the near infrared spectral range, only the absorptive impact of the thin VO_2 NC layer is taken into account for the simulation. In particular, this makes sense, especially since only this specific layer changes its optical properties during the IMT. The linear absorption coefficient α of the VO_2 NC layer is calculated from the imaginary part k of the complex refractive index:

$$\alpha = \frac{4\pi k}{\lambda} \tag{3.20}$$

Considering the above listed stacking of the glued resonator with a total geometrical cavity length of 12.4 µm, the spectral response in the near infrared is simulated and depicted in Fig. 3.9(a). Note that all spectra in Fig. 3.9 are normalized to the maximum transmission signal with the VO_2 in the insulating state. The spectra in panel (a), showing the insulating phase in blue and the metallic phase in red, consist of several sharp transmission peaks with constant amplitude over the whole wavelength range. This appearance is expected, since the intensity of the initial wave is set to a constant value of one irrespective of the wavelength and the exact interaction of the modal structure of the standing wave inside the cavity and the sub-wavelength layer of VO_2 NCs is neglected in this model. For further, quantitative analysis the resonator mode at about 830 nm wavelength is selected and shown with a higher resolution in panel (b). A reduction of the peak transmission by only 42% and a spectral shift of the center wavelength by just 0.16 nm can be extracted. These numbers are, in fact, much smaller than the observed experimental changes shown in Fig. 3.4(b). Both effects, the transmission decrease and the modal shift, are based on the IMT and the related substantial change of the complex refractive index. However, a homogenous 25 nm thin layer of VO_2 does not lead to the observed mode shift of about one nanometer (roughly half a nanometer for the optically pumped resonator). A second simulation for a homogenous 200 nm VO_2 layer is performed and presented in Fig. 3.9(c) and (d). The optical path length δ of the resonator is kept at the same value by a slight decrease of the fused silica thickness in favor of the increased VO_2 layer thickness. Therefore the positions of the resonator's modes remain the same. This time the spectral mode shift introduced by the IMT is as large as 0.98 nm and, therefore, comparable to the experimental result shown in Fig. 3.4. Both approximations of the NC layer as an equivalent averaged and homogeneous plane layer deviate from the experimental findings. On the one hand the observed large mode shift cannot be covered by the simulation and on the other hand the assumed layer thickness of 200 nm is not supported by the TEM picture in Fig. 2.2(b). The reason for the significantly larger line shift recorded experimentally remains unclear. From the results in the context of Fig. 3.5 thermal expansion can definitely be excluded.

A more sophisticated way to theoretically calculate the optical response of the resonator is the transfer matrix method introduced in chapter 3.1.2. This formalism describes the propagation of electromagnetic waves through the layered components of the resonator. In this case, reflective surfaces, e.g. phase interfaces, within the cavity as well as the location of different (sub-wavelength thick) compounds with respect to the node/anti-node pattern of the standing wave are taken into account. Fig. 3.10 shows the results of the simulated resonator with the same geometrical properties as mentioned above but calculated using the transfer matrix method instead.

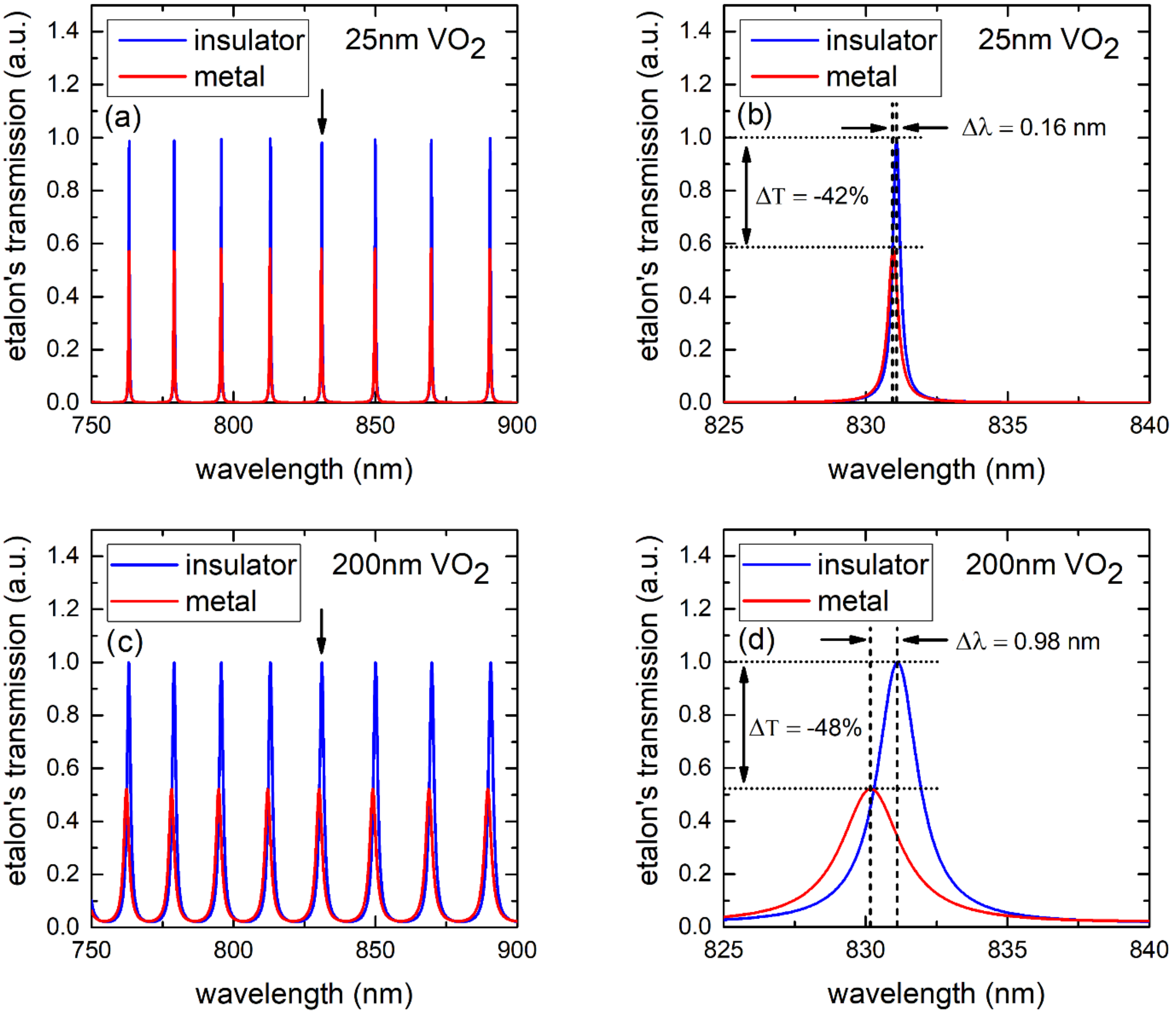

Fig. 3.9: Simulated resonator modes of a Fabry-Pérot etalon (geometrical cavity length: ~12.4 µm) containing a sub-wavelength layer of VO_2 NCs (25 nm and 200 nm) in the insulation (blue) and metallic (red) crystallographic phase. (b) and (c) Picture with higher resolution of the indicated resonator mode in panel (a) and (b), respectively. The transmission decrease and spectral shift, caused by a substantial change of the complex refractive index during the IMT, are indicated.

In comparison to the first simulation with simple resonator optics (cf. Fig. 3.9(a)), this time the spectra shown in panel (a) exhibit broader peaks that feature an additional modulation in intensity over the whole spectral range. The broadening is caused by added losses due to multi-reflections[25] on internal interfaces. The modulation, on one hand, is based on the same multi-reflections that introduce additional low-finesse cavities inside the main resonator. On the other

---

[25] Multi-reflections lead to destructive interference if the thicknesses of the different layers are not selected carefully to phase-match incoming and reflected waves at phase boundaries inside the cavity.

hand, this modulation originates from the complex interplay of the node/anti-node pattern of the standing wave with the sub-wavelength layer of VO_2 inside the resonator. Domains in the cavity where the electric field strength is low suffer from a weak light-matter interaction. Likewise, the spectral shift of the resonator modes, introduced by the IMT, is affected as well, resulting in a small altering of the specific transmission mode. Furthermore a so called stop-band, featuring low transmissivity, emerges in the middle of each transmission peak. It is introduced by the sub-wavelength thick layer of VO_2, featuring a higher refractive index as the surrounding material. This stop-band cannot be found in the experimental findings since the VO_2 NC layer consists of spherical particles. Thus, it is neither a homogenous nor a flat layer with parallel surfaces. The spherical shape of the small NCs scatters and deflects the incident light in various directions instead of partially reflecting it straight back perpendicular to the layer surface. Consequently, this stop-band is drastically disturbed and vanishes in the experimental findings. Additionally, the resolution of the spectrometer is expected to be too low to properly resolve a sharp stop-band. The resonator mode at about 830 nm wavelength is selected and shown with a higher resolution in panel (b) to further analyze the switching behavior by the IMT. A spectral shift of 0.17 nm is found. This value is in perfect agreement with the spectral shift extracted from the previous, simple resonator simulation (cf. Fig. 3.9(b)). A quantitative disclosure of the transmission decrease cannot be provided from the transfer matrix simulation since the stop-band drastically disturbs the transmission peak's appearance. Analogue to the results from the previous simulation, a homogenous 25 nm layer of VO_2 inside the resonator is not sufficient to accurately describe the experimentally observed spectral mode displacement due to the IMT. Paned (c) and (d) show a simulation using a 200 nm VO_2 layer inside a resonator that, again, features the same optical path length. From the picture of the single transmission peak at about 830 nm, shown in panel (d), a mode shift of 1.02 nm can be extracted. Again, this value stands in perfect agreement with the spectral shift extracted from the previous, simple resonator simulation (cf. Fig. 3.9(d)) and with the experimental findings presented in Fig. 3.4(b).

To sum up the findings of the theoretical studies on the etalon, the layer of spherical VO_2 NCs needs a more sophisticated description, accounting for the nanoscopic nature of the particles, to achieve a more accurate calculation of the optical response. Considering the VO_2 NCs as an equivalent homogeneous and plane layer of 25 nm average thickness for such a resonator geometry is a first approach to qualitatively describe the expected transmission behavior. However, a 200 nm layer is probably not a suitable replacement for this NC layer either. This becomes evident from the transmission electron micrograph in Fig. 2.2(b), showing the NC layer made up from spherical particles with a diameter of 100 nm and a lateral spacing of 60 nm. Nevertheless, the theoretical studies proof the principals of the switching performance of the etalon, indicative of a spectral mode shift accompanied by a transmission decrease of the specific cavity modes. Another aspect that can be seen from the data in panel (a) and (c) in Fig. 3.10 in combination with Fig. 3.8 is the modulation of the intensity of the transmission peaks itself and the modulation of the strength of the mode shift across the depicted spectral range. The complex interplay of the node/anti-node pattern of the standing wave with the sub-wavelength layer of VO_2 inside the resonator has a crucial impact on the light-matter interaction on the nanoscale. Further improved simulations must resolve this peculiarity with greater precision.

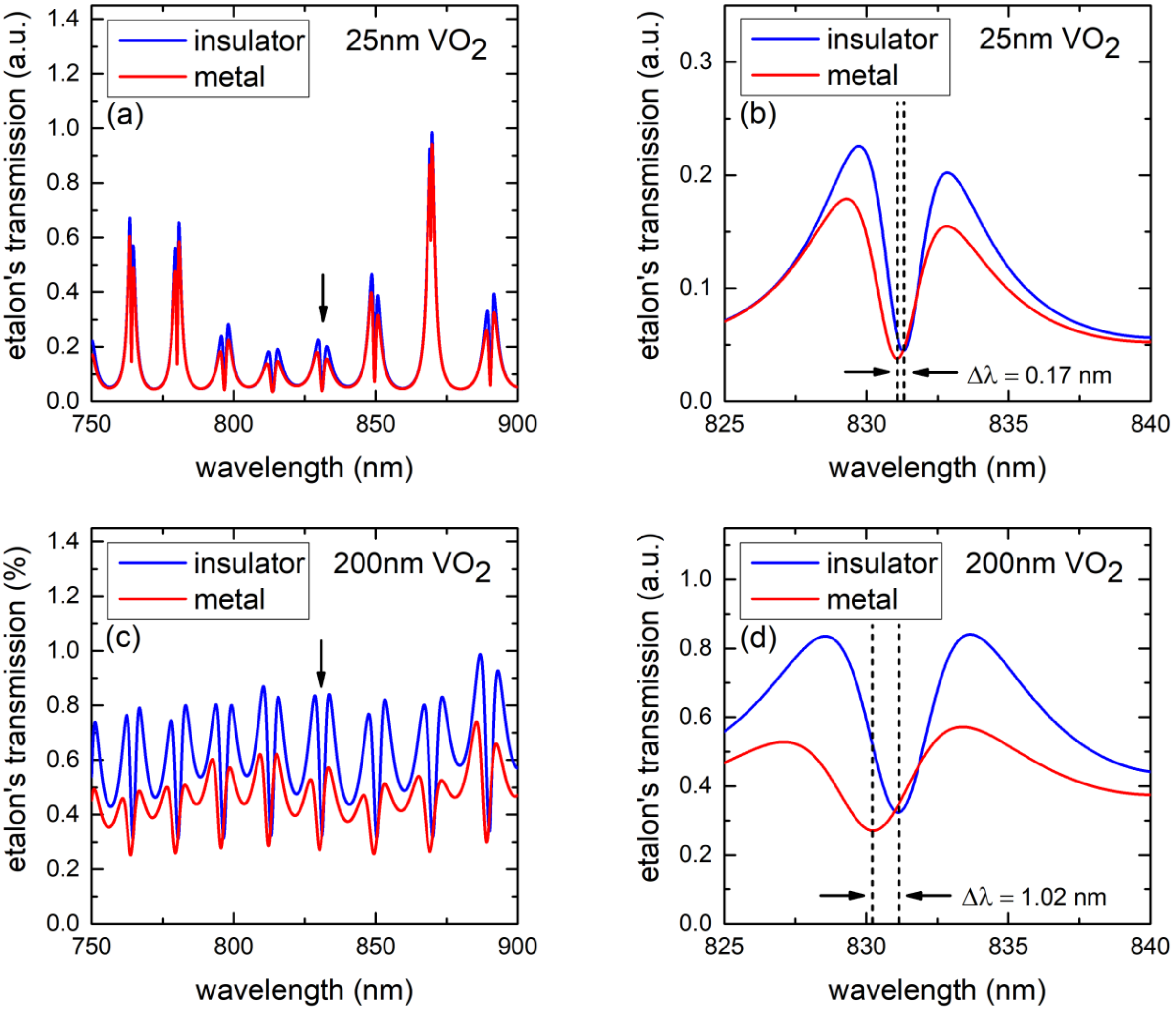

Fig. 3.10: Transfer matrix simulations of the optical response of a Fabry-Pérot etalon (geometrical cavity length: ~12.4 µm) containing a sub-wavelength layer of VO_2 NCs (25 nm and 200 nm) in the insulation (blue) and metallic (red) crystallographic phase. The transmission peaks feature an intensity-modulation and an additional stop-band in the middle. (b) and (c) Picture with higher resolution of the indicated resonator mode in panel (a) and (b), respectively. The spectral shift, caused by a substantial change of the complex refractive index during the IMT, is indicated.

Chapter 4

Optical Nonlinearities of the Two Individual Phases of VO_2 NCs

Vanadium dioxide (VO_2) exhibits an insulator-to-metal phase transition (IMT) near ambient temperatures. Upon heating, the material undergoes a structural change from a monoclinic to a rutile phase. It is accompanied by a substantial modification of the complex dielectric function and, closely related, a marked change of the complex refractive index. VO_2 nanocrystals (NCs) in their high-temperature phase feature near-infrared plasmonic resonances with properties depending on their size, shape and the host matrix material [LHB02]. The optical properties of the different solid phases[26] in bulk and nanoscopic VO_2 have been under intensive investigation for decades since F. J. Morin firstly reported the IMT in 1959 [Mor59].

Much less is known about the nonlinear optical properties of VO_2 beyond the established IMT. Z-scan experiments [SWV85] in bulk and nanoscale VO_2 have shown that effective nonlinear optical coefficients extracted for femtosecond pulses at 800 nm are mostly related to an optically induced phase transition rather than to an intrinsic optical nonlinearity of the two individual phases [LHF04]. This optical nonlinearity of the transition process is based on the abrupt change of the absorptive behavior and is often described as an "optical limiting".

In this chapter, the near-infrared optical nonlinearity of both the insulating and metallic state of VO_2 NCs of about 100 nm diameter embedded in fused silica is investigated. To this end, open aperture z-scans for a wide range of lattice temperatures and with the use of two complementary mode-locked fiber laser sources are performed. Such measurements provide direct insight into parameters such as effective saturation intensities[27] and/or effective nonlinear absorption coefficients, i.e., parameters for practical applications such as nonlinear absorbers. Parts of this chapter have already been published in Ref [MMK20].

---

[26] Beside the insulating (monoclinic) and the metallic (rutile) phases, several complex intermediate phases within the transition process are found and investigated [BLC15, MWR72, TBC16, GAF20, MCT14].

[27] The saturation intensity defines the incident optical power that is required for achieving a significant saturation of an absorber or a gain medium.

4.1 Open Aperture Z-Scan Technique

The z-scan technique, proposed and pioneered by van Stryland [SWV85] and Sheik-Bahae [SSW90] is an established measurement method for the experimental determination of the nonlinear refractive index n_2 (Kerr nonlinearity) as well as for the nonlinear (two-photon) absorption coefficient β via the “closed” and “open” aperture methods, respectively. Furthermore, the z-scan technique allows simultaneous measurements of various nonlinear optical parameters by means of a single measuring system and is applied to assess, e.g., the quality parameters of a laser beam by determining its characteristics (e.g. Gaussian distribution) [LLW03]. Due to its simplicity and high accuracy [SSW90], this method has proven to be one of the most convenient measurement techniques in nonlinear optics [SB98].

The experimental configuration of the z-scan technique is shown in Fig. 4.1. In general, z-scans are performed by translating the investigated sample through the beam waist of the focused laser beam along the optical z-axis[28] while measuring the total transmitted intensity for each sample position [SWV85, SSW90]. Because only the irradiance at the sample is changing upon translation, any (non-destructive) deviation in the total transmitted intensity must arise from nonlinear optical processes. The required translation range (scanning range) strongly depends on the experimental parameters (e.g. focal length, beam waist, laser power), the geometrical factors (e.g. sample thickness) and the strength of the nonlinear properties of the sample (e.g. nonlinear refractive index n_2 and nonlinear absorption coefficient β).

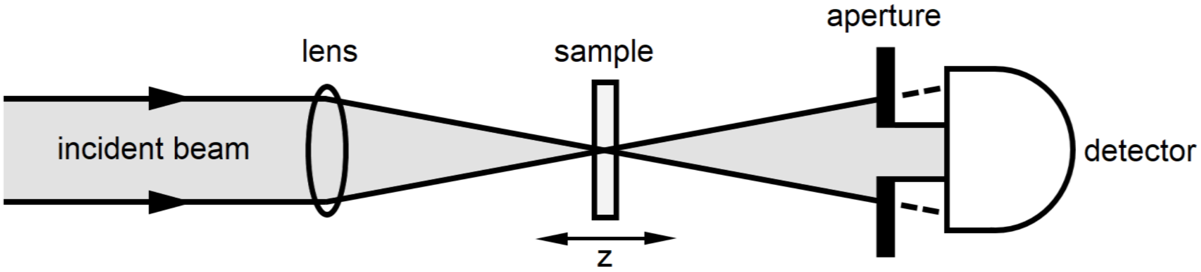

Fig. 4.1: Schematic illustration of the z-scan experimental apparatus. The incident beam is collimated and the sample is translated along the optical z-axis through the beam waist while recording the transmission signal. The aperture in the far field is used in the closed operation mode with finite inner diameter (as depicted here) to measure the nonlinear refractivity. The nonlinear absorption is determined by recording the total transmitted signal for an open aperture (dashed line).

---

[28] The translation direction is parallel to the optical axes (z-direction) giving rise to the unique name of this measurement method.

The z-scan setup is used in the closed-aperture form to measure the real part of the nonlinear refractive index n_2. Small beam distortions of the incident beam that originate from a weak intensity-dependent lensing effect of the nonlinear material can be easily detected using a far-field “closed” aperture (with finite inner diameter) in front of the detecting unit. The focusing power of this weak nonlinear lens is directly related to the nonlinear refractive index of the translated sample [Ras15]. The physical origin of this intensity-dependent lensing effect is based to the self-focusing phenomenon. The latter can be observed when a laser beam of non-uniform spatial intensity distribution, e.g. a Gaussian beam, travels through a medium with a nonlinear refractive index n_2, inducing an index gradient in the shape of the beam’s intensity distribution. A positive nonlinearity leads to a larger refractive index, and hence a more pronounced phase retardation in the on-axis center compared to the wings of the laser beam. The resulting nonlinear focusing, therefore, creates a positive ($n_2>0$) or negative ($n_2<0$) lens in the nonlinear medium that, finally, leads to a slight focusing or defocusing of the incident laser beam, respectively. Consequently, the translation of the sample through the focal plane causes changes in the transmitted intensity through the far-field aperture due to the induced change of the divergence of the beam. Finally, the index of nonlinear refraction n_2 can be extracted by analyzing the z-dependent transmission data acquired by the detector using an appropriate theory [SSW90].

The imaginary part of the nonlinear refractive index k_2 or the nonlinear absorption coefficient β can be extracted by using the “open” aperture z-scan technique. Therefore, the far-field aperture is removed (or completely “open”) and the whole signal is recorded by the detector. Small distortions of the beam by, e.g., a lensing effect become insignificant and any variations of the z-dependent signal strength are entirely due to the nonlinear absorption. Nonlinear (two-photon) absorption ($\beta>0$) will enhance the absorptive valley of the recorded z-scan trace at high irradiances around the focal point while a saturable absorption ($\beta<0$) will lead to the opposite effect.

In the original publication from Sheik-Bahae et al. a profound theoretical background was already provided and supported by experimental z-scan traces recorded for a zinc-selenide sample [SWV85]. The theory comes along with an expression for the open aperture z-scan transmission in terms of the peak irradiance in a summation form that is suitable for numerical analysis of the recorded data. It considers a general nonlinear absorption that can be, in some cases, reduced to the two-photon absorption. More specific expressions including the concurrence of different nonlinear absorption phenomena were developed later on [GZL05]. The open aperture z-scan analytical theory for simultaneous appearance of both saturable absorption and two photon absorption is developed by, e.g., Wang et al. using the Adomian decomposition method[29] [WGW10]. The resulting analytical expression stands in perfect agreement with the phenomenological model that is based on a nonlinear absorption coefficient and saturation intensity [GZL05].

For a quantitative analysis of the recorded open-aperture z-scan traces this phenomenological model is chosen since both nonlinear absorption processes are present in the VO_2 NC sample [ZZC15, WGW10, GZL05]. These composite nonlinear absorptions with opposite signs can be phenomenologically combined to a total nonlinear absorption coefficient:

$$\alpha(I) = \frac{\alpha_0}{1 + I/I_S} + \beta I \tag{4.1}$$

where α_0 is the linear absorption coefficient which is $\alpha_{\text{insulator}} = 1.05 \cdot 10^6\,\text{m}^{-1}$ and $\alpha_{\text{metal}} = 3.19 \cdot 10^6\,\text{m}^{-1}$ at 1036 nm and $\alpha_{\text{insulator}} = 5.08 \cdot 10^5\,\text{m}^{-1}$ and $\alpha_{\text{metal}} = 2.78 \cdot 10^6\,\text{m}^{-1}$ at 1550 nm, respectively. These values are calculated from the imaginary part k from the complex refractive index, cf. Fig. 2.3(b) and Eq. 3.20. β is the nonlinear absorption coefficient describing multi-photon absorption. I and I_S are the laser intensity and saturation intensity, respectively. In the limit where the nonlinear absorption is restricted to two-photon absorption, associated with the third order nonlinear susceptibility[30] $\chi^{(3)}$, the time-integrated transmitted intensity can be approximated by the following equation [SWV85, SSW90, ZZC15, WGW10, GZL05]:

$$T(z) = \sum_{m=0}^{\infty} \frac{\left[\left(\frac{-\alpha_0}{1 + I(z)/I_S} - \beta I(z)\right) L_{eff}\right]^m}{(m+1)^{3/2}} \tag{4.2}$$

$$I(z) = \frac{I_0}{1 + z^2/z_0^2} \qquad L_{eff} = (1 - e^{-\alpha_0 L})\alpha^{-1}$$

where β is the two-photon absorption coefficient, L_{eff} is the effective interaction length, z is the longitudinal coordinate with $z=0$ located at the focal plane, I_0 is the on-axis peak intensity and z_0 is the Rayleigh length. The sample length L can be estimated by averaging the spherically shaped NCs with an average diameter of 100 nm and a lateral spacing of about 60 nm. This configuration is estimated to correspond to a homogenous layer of approximately 25 nm thickness.

Despite the simple design of the optical z-scan system, obtaining reliable measurement results sometimes involves complex data analysis. Many factors affecting the z-scan results from both

---

[29] The Adomian decomposition method, developed from the 1970s to the 1990s by George Adomian, is a semi-analytical technique for solving ordinary and partial nonlinear differential equations. It makes use of "Adomian polynomials" which give the solution method more flexibility than a direct Taylor series expansion [Waz09].

[30] Further information about the nonlinear susceptibility are provided in 8.1.1.

experimental and theoretical points of view should be taken into account [CSH97]. Specifically, the original z-scan theory leads to inaccurate results, i.e. when the optical response of the nonlinear medium to the incident laser radiation is nonlocal in space. Thus, the nonlinear response from a specific point of the medium is not solely determined by the laser intensity at that point, but also depends on the laser intensity in the surrounding illuminated area [Ras13]. For the present sample this detrimental effect can be neglected since adjacent NCs are implanted into the fused silica host matrix and are unlikely to show a nonlocal nonlinear response. For instance, the optical field can cause a reorientation of dipoles when the nonlinear medium is dispersed in a dielectric solution leading to local changes of the electric field experienced by the nonlinear medium. Since nanoparticles and clusters are often dispersed in an aqueous solution [GZL05], this affecting factor should always be considered.

In the course of this thesis the open aperture z-scan technique is used to determine the nonlinear transmission characteristics of a layer of VO_2 NCs embedded into fused silica. The measurements are performed at wavelengths of 1036 nm as well as at 1550 nm and at various lattice temperatures corresponding to the different crystallographic phases of VO_2. The first laser source used is a commercial mode-locked Yb:fiber laser (Onefive, Origami HP-10) operating at 4.3 W of average output power. It delivers a train of linearly polarized, transform-limited 100 fs pulses at a repetition rate of 90 MHz and a central wavelength of 1036 nm (central photon energy of 1.20 eV). The second laser source is a commercial mode-locked Er:fiber laser (Toptica, FemtoFiber Scientific) operating at 280 mW of average output power. It delivers a train of linearly polarized, transform-limited 90 fs pulses at a repetition rate of 75 MHz and a central wavelength of 1550 nm (central photon energy of 0.80 eV). Using a half-wave-plate and a polarizing beam splitter cube, a portion of up to a few hundred milliwatts, propagating in the z-axis direction, is focused down to a beam waist of 12 µm (9 µm) using a lens with a focal length of 150 mm (75 mm) for the 1036 nm (1550 nm) pulses. These values correspond to the full width at half maximum and are measured with a commercial scanning-slit beam profiler (Thorlabs BP209-IR).

The VO_2 NC sample is located inside a temperature-controlled oven (Covesion Oven PV10 and Controller OC1) that provides operating temperatures between near-ambient values and 200°C with a high thermal stability. This oven is mounted on a computer-controlled translation stage that moves along the propagation path of the laser beam. Alternatively, the oven can be exchanged by a small vacuum chamber equipped with a Peltier element that allows to cool down the sample to -40°C. All temperatures given throughout this chapter are related to the SiO_2 substrate. Depending on the irradiance the temperature of the NCs is somewhat higher due to local photon absorption. One has to note, however, that the heat conduction into the SiO_2 substrate is much faster than for NCs in a liquid environment where heating, e.g., may lead to vapor generation [NUD13, FZN13].

4.2 Saturable and Reverse Saturable Absorption in VO_2 NCs

Nanoscopic materials provide a broad tunability of their optical properties by controlling the size and shape of the nanoparticles, giving rise to significantly modified properties superior to their bulk materials [LHB02]. The light-matter interaction at the nanoscale strongly depends on the confined electronic system (electrons or electron-hole pairs) that leads to localized surface plasmon resonance in metal and metal-like nanoparticles and an exciton[31] confinement in nanocrystals made from semiconductor material.

Saturable absorption and reverse saturable absorption have already been reported in a variety of different nanomaterials [LKM08, SN12]. Saturable absorber materials show a decrease in absorption while increasing the incident light intensity due to saturation of excited states or a bleaching of the ground state. In the case of reverse saturable absorbers the illuminated material transmits less with increased light intensity due to free carrier absorption or multi-photon absorption. In this chapter the nonlinear absorption response beyond the established IMT of a sub-wavelength thin layer of VO_2 NCs is examined using the open aperture z-scan technique at an excitation wavelength of 1036 nm and 1550 nm, respectively.

In the first step an overview of the rich phenomenology of nonlinear optical processes in VO_2 NCs is provided. Fig. 4.2(a) contains a large number of room temperature z-scan traces recorded for 1036 nm pulses of average powers ranging from 10 mW to 490 mW. The upper power limit is given by the threshold for permanent damage to the NCs occurring at higher power levels. Note that the sample is translated towards more positive z-values.

The findings can be grouped into three kinds of optical nonlinearities: (i) For power levels up to 30 mW only a weak positive peak is found around $z=0$, cf. enlarged z-scan traces in the top panel of Fig. 4.2(a). It is related to a saturable absorption in the insulating state. (ii) For larger power levels a pronounced dip with minimum transmission levels as low as 78% is seen. This behavior is readily explained by a light-induced IMT of VO_2. For somewhat larger powers, the traces become increasingly asymmetric around $z=0$. This asymmetry arises from the hysteresis of the NCs (cf. optically induced IMT shown in Fig. 2.5). At least a part of the excitation region remains in a supercooled metallic state in the $z>0$ section, eventually switching back in the low-fluence region. (iii) On top of the IMT-related drop of the transmission a marked positive peak is seen which arises from a pronounced saturable absorption of the metallic phase of VO_2. For the

---

[31] An exciton is an electron-hole pair that forms a bound state in a semiconductor. The bounding energy is given by the electrostatic Coulomb force, reduced by the relative permittivity and the small effective masses of the excited electron and hole.

largest power levels in Fig. 4.2(a), the transmissivity at z=0 is even almost restored to the values far away from z=0, i.e., in the low-fluence limit.

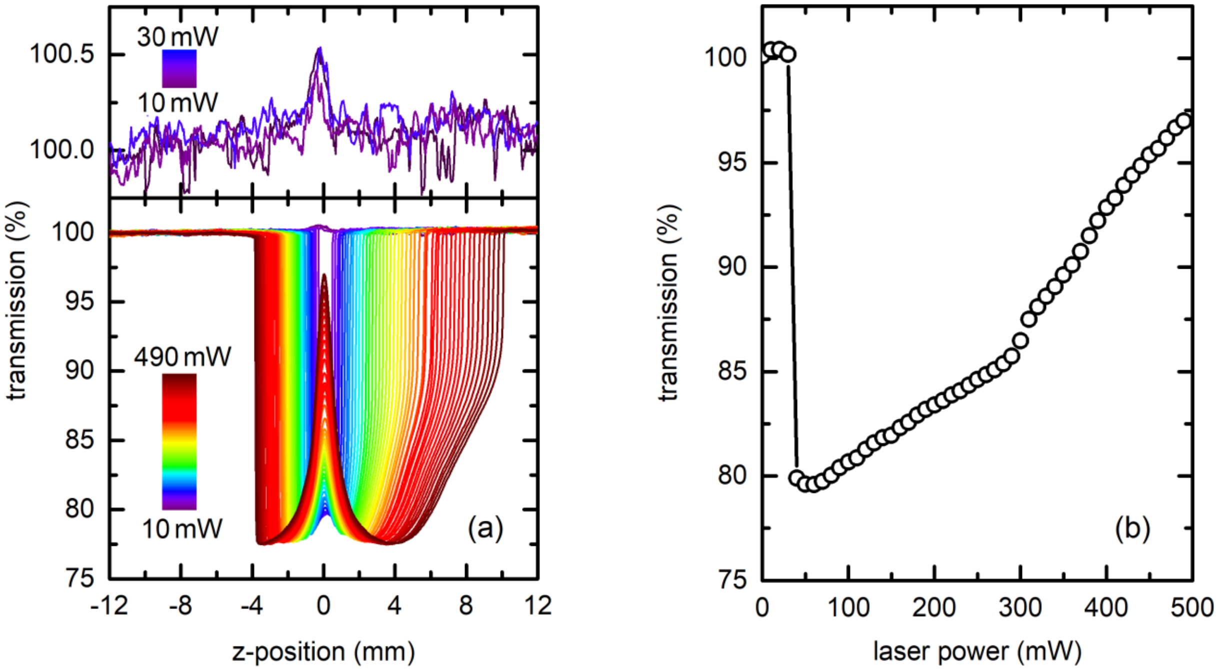

Fig. 4.2: (a) Series of room temperature z-scan traces recorded for 1036 nm pulses with translation direction to positive z-values. The top panel shows enlarged versions of three low-power z-scans for better visibility. (b) Transmissivity for various powers at the focal point z=0 extracted from Fig. 4.2(a). The spectral position of the laser wavelength of this particular measurement with respect to the NCs resonance is shown in Fig. 2.3(c).

The main focus of this section is a careful examination of the nonlinearities (i) and (iii). In contrast, the nonlinear IMT (ii) is very similar to earlier observations with 800 nm pulses [LHF04] and is not strongly emphasized in this chapter. The three different regimes are also evident from Fig. 4.2(b) where the transmissivities at the focal point z=0 are shown. When increasing the incident laser power level, a slight increase of the transmissivity is seen, i.e., a saturable absorption occurs. Then, a very sharp IMT-related drop of the transmission by ~20% is found. It is followed by an increasing transmission due to the saturable absorption of the metallic phase. Additionally, around power levels of 300 mW, a change of the slope is seen in Fig. 4.2(b). This finding is reproducible but, however, no explanation for the change of the nonlinearity can be offered to date.

Now the above findings are compared to the situation where the sample is translated through the beam waist of the 1550 nm pulse train. Fig. 4.3(a) displays z-scan traces for various power levels ranging from 20 mW to 265 mW. The transmissivity values at z=0 are again summarized in panel (b). For this wavelength the maximum power level is given by the available power of the mode-locked Er:fiber laser. To partially compensate for the lower power levels, a somewhat tighter focusing as quantified in the description of the experimental setup is used. The z-scan traces look drastically different from those in Fig. 4.2. For low power levels, a slight decrease of the transmissivity around the focal point at z=0 is seen. It arises from a reverse saturable absorption of the insulating state of VO_2. For elevated power levels, the traces are again dominated by the IMT-related sharp drop of the transmissivity. For 1550 nm pulses, the absorption of the metallic phase is slightly stronger when compared to the 1036 nm case. The result is also expected from the data in Fig. 2.3(c). On top of this nonlinearity, another drop of the transmissivity is observed for power levels >100 mW. It is related to reverse saturable absorption of the metallic state of VO_2. Remarkably, for the highest available powers the transmission at z=0 drops to values as low as 57% of the value for unfocused pulses.

The data in Fig. 4.3(b) show a marked change of their slope at about 160 mW. It is instructive to compare these results to Fig. 4.2(b). In both cases the change of the slope occurs at a power density of ~2.5 mW/µm^2 and point to a quantitative modification of the optical nonlinearity. Again, this effect is reproducible but still requires further investigation concerning the origin of the altering absorptive behavior.

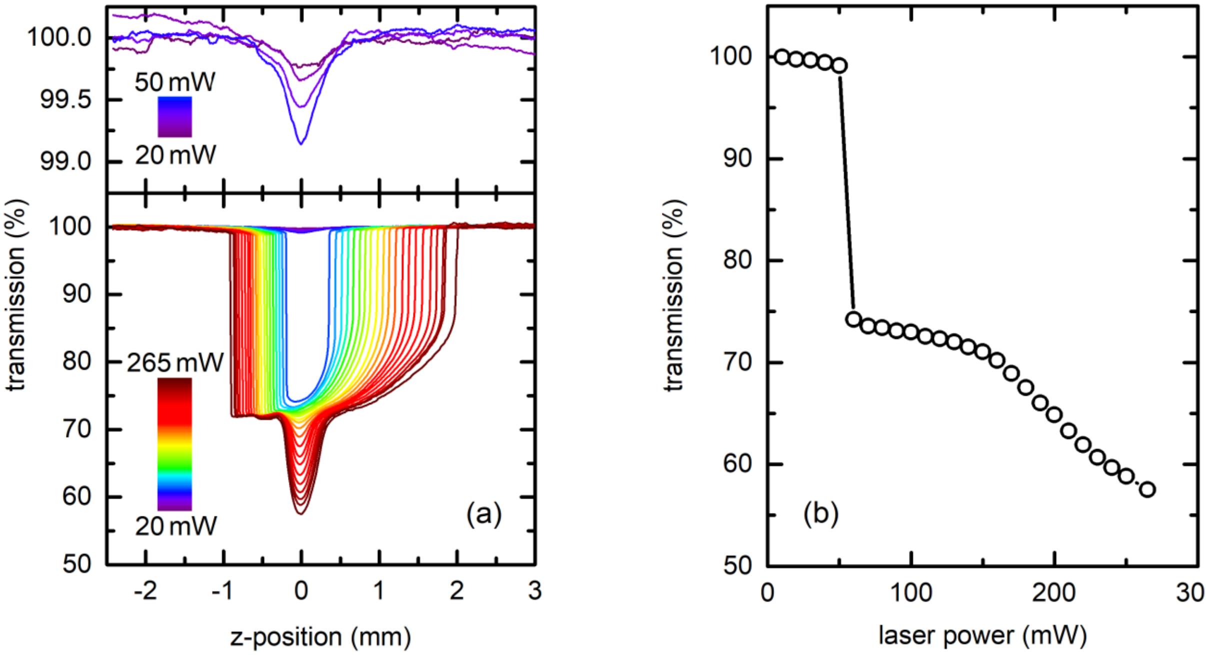

Fig. 4.3: (a) Series of room temperature z-scan traces recorded for 1550 nm pulses. The sample is translated towards positive z-values. The top panel shows enlarged versions of four low-power z-scans for better visibility. (b) Transmissivity values at z=0 for various power levels, as extracted from Fig. 4.3(a). The spectral position of the laser wavelength of this particular measurement with respect to the NCs resonance is shown in Fig. 2.3(c).

The results so far are related to a superposition of the IMT and the optical nonlinearity of both the metallic and insulating state. However, the central aspect of this chapter is the nonlinearity of the individual states of VO_2 NCs. To investigate the metallic state only, the sample is heated up to 100°C, i.e., well above the critical temperature of the phase transition T_C. Fig. 4.4(a) contains z-scan traces for the 1036 nm pulse train and the same power range as used for the data in Fig. 4.2(a). For all power levels, saturable absorption is found. For the highest irradiances the transmittance almost recovers to the value seen for the insulating state (cf. Fig. 4.2(a)). In a complex material such as VO_2 NCs, this saturable absorption is probably not related to a standard third-order nonlinearity. However, it is still instructive to extract, e.g., the saturation intensity I_S equivalent values from such traces. The extracted values for I_S according to Eq. 4.2 for the different power levels are summarized in Fig. 4.4(b) along with an example for such a fit to the data.

In the following these results are compared to the optical nonlinearity of the metallic state at 1550 nm. Fig. 4.4(c) contains z-scan traces for the 1550 nm pulse train and the same power range as used for the data in Fig. 4.3(a). It shows a transition from saturable absorption at low-to-moderate powers to reverse saturable absorption at elevated powers. This saturable absorption is not resolved in the data in Fig. 4.3(a) as it is probably hidden underneath the large response related to the IMT. The combined saturable and reverse saturable absorption is modeled according to Eq. 4.2 to yield equivalent I_S and β values. The extracted values for I_S and β for the different power levels are summarized in Fig. 4.4(d) along with an example for such a fit to the data. In direct comparison to Fig. 4.4(b), I_S takes values in the same order of magnitude. Also a decrease of I_S for increasing power levels is seen in both cases.

It is instructive to compare these values for I_S to those of other materials. The extracted values are comparable or somewhat smaller than the I_S of typical bulk semiconductors [GFC07]. However they are not as small as those of NCs made from noble metals [GZL05, HMN12]. In view of those results, the extracted values for the I_S of the present VO_2 NC sample seem reasonable as those NCs are made from a material of moderate metallic conductivity. Values of β can only be reliably extracted for 1550 nm pulses and power levels beyond 120 mW. They increase with the excitation power and are seen to take values as large as ~5000 cm/GW. As the typical two-photon absorption coefficient of, e.g., prototypical semiconductors such as GaAs, is in the range of 10 cm/GW [KMN73], the observed value for β is unlikely to arise from true two-photon absorption. In metallic systems, however, it is well known that very large values of the apparent two-photon absorption coefficients in z-scan traces can arise from thermal effects [RBF07]. In essence, the front part of the ultrashort laser pulse heats the electronic systems and, thereby, the absorption of the rear part is enhanced. Furthermore the overall power-dependent behavior of β suggests that higher orders of optical nonlinearities contribute to the observed absorption. Therefore Eq. 4.2 would have to be extended beyond the limit of a bare two-photon process for a more accurate description.

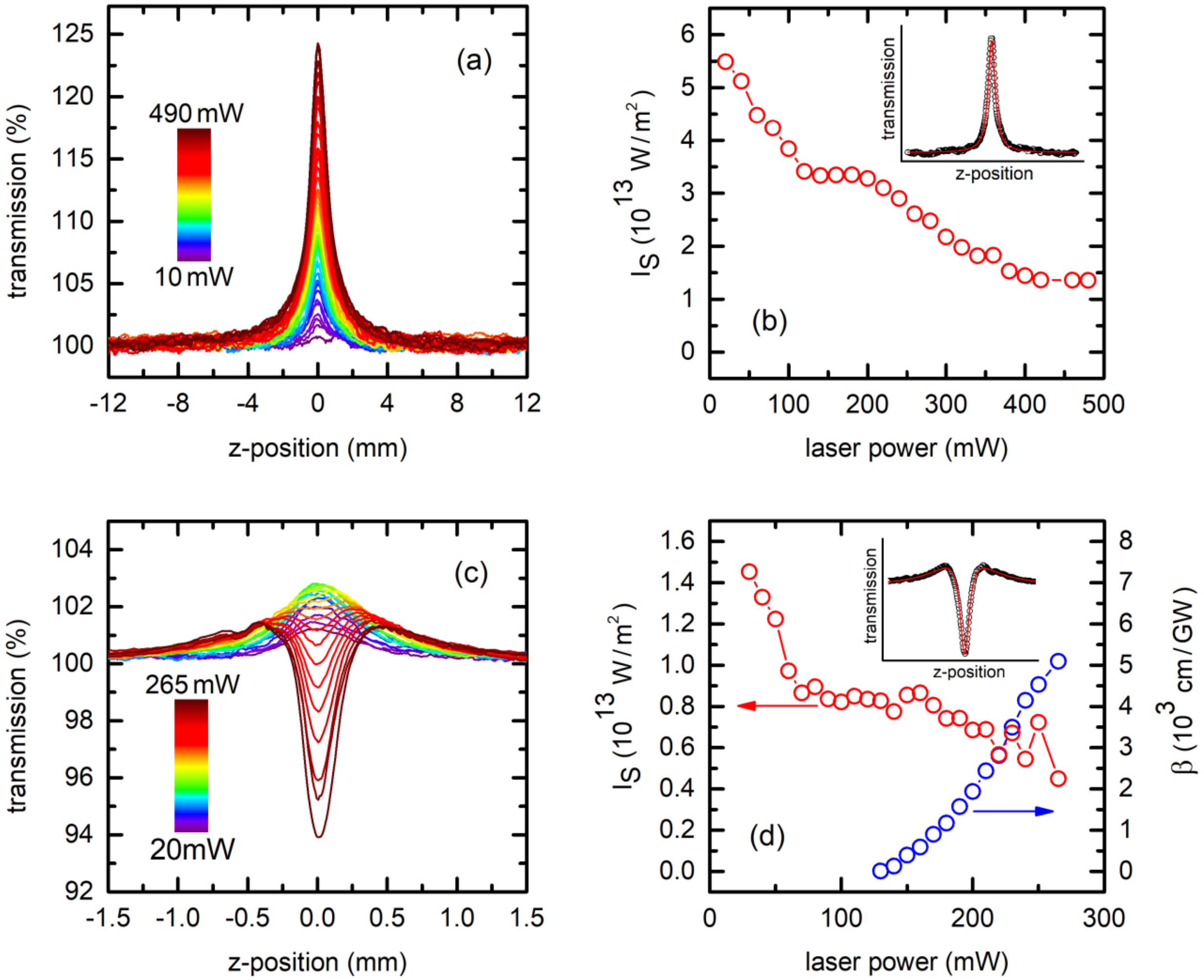

Fig. 4.4: (a) and (c) show series of high temperature ($T = 100°C > T_C$) z-scan traces recorded for (a) 1036 nm and (c) 1550 nm pulses with translation direction to positive z-values. (b) Saturation intensity I_S for VO_2 NCs in the metallic state and 1036 nm laser wavelength extracted from panel (a) using Eq. 4.2. (d) Saturation intensity I_S and two-photon absorption coefficient β for VO_2 NCs in the metallic state and 1550 nm laser wavelength extracted from panel (c) using Eq. 4.2.

At first glance the results presented in the panels 4(a) and 4(c) seem to be contradictory as a metallic system should behave similar irrespective of the exact photon energy in the near-infrared spectral domain. However, the different behavior can be directly related to the plasmonic resonance of the VO_2 NCs and its spectral profile for different temperatures. To this end, a white light transmission setup is used in combination with a high temperature oven (up to 1000°C) containing the VO_2 NC sample. For a variety of sample temperatures spectral transmission data is recorded. Fig. 4.5 shows the normalized difference between the metallic phase at different lattice temperatures when compared to the insulating state at room temperature. It shows a clear red-shift and broadening upon heating. This finding is well established, e.g., for gold nanoparticles [YBG13]. In short, the red-shift can be largely explained by the thermal expansion of the NCs while the broadening of the resonance is readily explained by enhanced electron-phonon scattering. Certainly the situation of an ultrashort interaction with the NCs is different in the sense that only the electron system is heated while the ~100 fs pulse is present and the timescale is too short for significant thermal expansion. As an example the 1550 nm Er:fiber laser's pulse energy is calculated to be $3.33 \cdot 10^{-9}$ J at an average laser power of 250 mW. The illuminated volume of pure VO_2 in the focal plane sums up to be ~1.6 μm^3 (c.f. last page of chapter 4.1). The rise of the electron temperature can now be estimated from the average kinetic energy taking into account an overall optical absorption of 42% of the laser's pulse energy (c.f. Fig. 4.3(a)). Consequently, for various values of the electron density in VO_2 found in literature [BVG66, Hen68, RHC09] the electron temperature ranges from several hundred Kelvin to a few ten thousand Kelvin above ambient temperature. The initial heating of the electronic system is followed by a lattice thermalization via electron-phonon scattering that occurs on timescales of picoseconds [MCT14, WFW13, KEH07]. Since the pulse-to-pulse time of the Er:fiber laser is 13,3 ns this thermalization process is expected to be mostly done before the next laser pulse arrives at the sample. A transient red-shift of the resonance readily explains the different observations in Figs. 4.4(a) and (c). As shown in the Fig. 4.5, such a red-shift moves the 1550 nm pulse towards the peak of the absorptive resonance. In contrast, the 1036 nm pulse is shifted away from the resonance explaining the reduced absorption for strong irradiance.

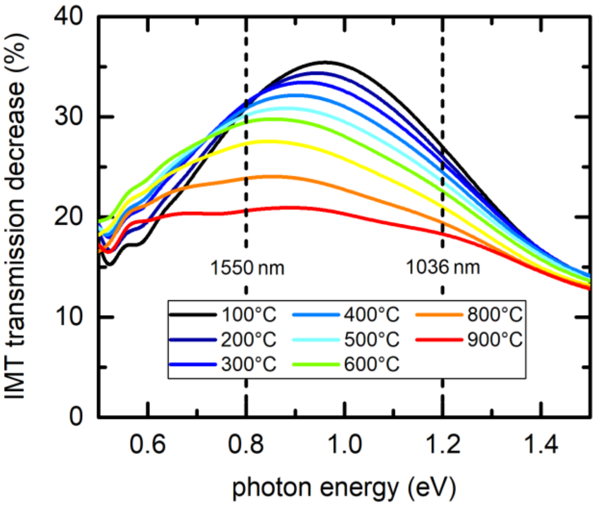

Fig. 4.5: Evolution of the IMT transmission decrease (normalized transmission difference between the metallic phase and the insulating state) at different lattice temperatures. The visible reduction of the resonance's amplitude partially occurs from a degeneration process of the hot sample in air environment. To partly compensate for this effect, a vertical offset aligns the traces outside the resonance. The sample investigated here originates from a different batch such that center energy, width and amplitude of the resonance slightly differ from the data shown in Fig. 2.3(c).

Finally the optical nonlinearity of the insulating state is addressed. To this end, the sample is cooled down to -35°C such that (in comparison with the data in Figs. 4.2 and 4.3) larger power levels can be used without triggering the IMT. To avoid any condensation and freezing of humidity on the sample's surface it is enclosed into a small vacuum container. At 1550 nm, power levels of up to 130 mW can be used before the IMT is photo-induced, cf. the dashed graph of Fig. 4.6(a) that shows the z-scan trace with an optically triggered IMT for a power of 140 mW. For all power levels a well-resolved reverse saturable absorption is found. However it is much weaker than the apparent nonlinearity related to the IMT at higher laser intensities. Nevertheless the z-scan trace for 130 mW power is indicative of an equivalent two-photon absorption coefficient as large as $\beta = 3510$ cm/GW.

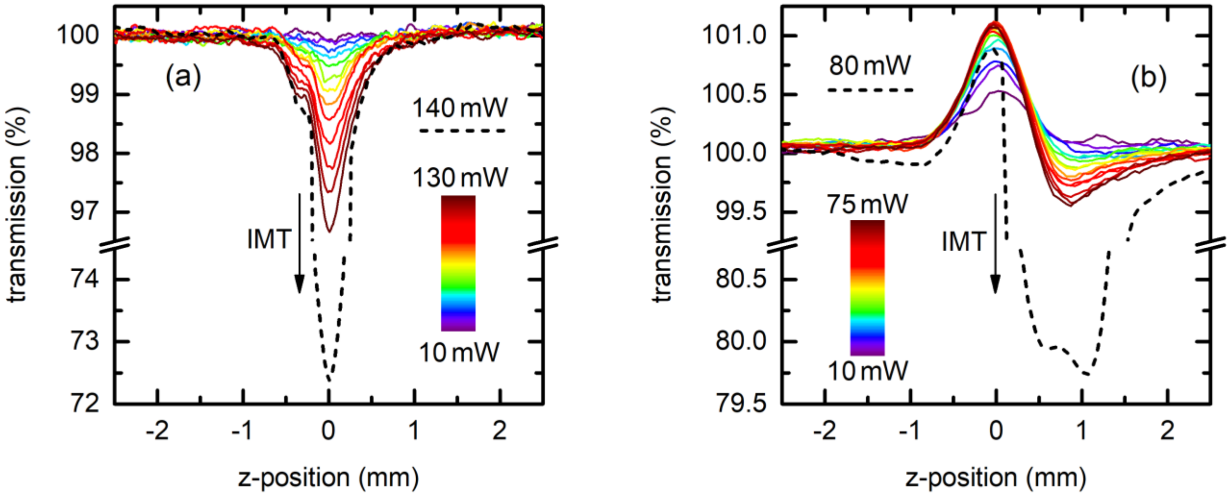

Fig. 4.6: (a) and (b) show series of low temperature ($T = -35°C < T_C$) z-scan traces recorded for (a) 1550 nm and (b) 1036 nm pulses with translation direction to positive z-values. The dashed graphs show z-scan traces with triggered IMT.

At 1036 nm, power levels up to 75 mW leave the sample in the insulating state, cf. the dashed graph of Fig. 4.6(b) that shows the z-scan trace with an optically triggered IMT for a power of 80 mW. The z-scan traces for lower power levels are indicative of rather weak optical nonlinearities with z-scan traces deviating from unity by 1% at most. Surprisingly, the traces exhibit dispersive features which are more likely to occur for closed-aperture z-scans. The traces are not related to, e.g., a lensing effect that could arise from the real part of the third-order optical nonlinearity. This was checked by an iris with variable inner diameter that, for fixed z-positions, induced changes of the total transmitted intensity only for aperture sizes way smaller than the photodiode. Thus, the total transmitted intensity is completely recorded by the detector. Instead the dispersive traces are related to some form of photo-induced modification of the NCs that exhibit a hysteretic behavior. Most likely this asymmetric graph originates from a slightly shifted overlap of a saturable absorption (symmetric around z=0) and an optically induced IMT with hysteretic behavior of only a few single nanocrystals ($z>0$). The latter can be estimated from the positive z-position of the induced phase transition at elevated laser power. In particular, the traces for a z-scan along the negative z-axes lead to traces that are mirrored around $z=0$. This fact clearly excludes a lensing effect and points to a hysteretic effect related to the nanocrystal's IMT. One has to note that this mirror-symmetry also holds true for z-scan traces where the IMT is photo-induced and the NCs remain in the supercooled metallic state (data not shown). Specifically the IMT always leads to asymmetric z-scan traces as shown in Fig. 4.2(a) or Fig. 4.3(a).

To sum up, marked differences in the nonlinear optical properties of VO_2 NC, investigated by the open aperture z-scan technique, are found for different laser photon energies spanning the telecom wavelength regime. The most striking observation for the metallic state is a pronounced saturable absorption for femtosecond pulses centered at a wavelength of 1036 nm, i.e. in the high-energy flank of the absorptive plasmonic resonance of the NCs. In marked contrast, a reverse saturable absorption for femtosecond pulses at a wavelength of 1550 nm, i.e., in the low-energy flank of the plasmonic resonance is found. Both results are readily understood as arising from a transient red-shift of the plasmonic resonance during the ultrashort light matter interaction window. Such a red-shift upon heating is well known from metallic nanoparticles [YBG13].

Chapter 5

Conclusions and Outlook Part I

Vanadium dioxide (VO_2) is one of the smart optical materials that feature an insulator-to-metal phase transition (IMT) in the near ambient temperature range. Upon heating, the material undergoes a structural change from a monoclinic to a rutile phase. This crystallographic transition is accompanied by a substantial modification of the complex dielectric function and, closely related, a marked change of the complex refractive index. VO_2 nanocrystals (NCs) feature near-infrared plasmonic resonances in their high-temperature phase with properties depending on their size, shape and the host matrix material.

In the first part of this thesis, VO_2 NCs embedded into a fused silica host matrix by ion-beam implantation are studied. In detail, the thermally induced IMT with its effect on the optical transmissivity is examined in a wide spectral range to sufficiently resolve the plasmonic resonance of the metallic spherical NCs. Specifically, a strong resonance centered around 1 eV photon energy in the telecom wavelength range is found featuring an absorption of up to 33% from a single layer of NCs. Additionally, the hysteresis of nanoscopic VO_2, induced by optical and thermal excitation, is investigated. Remarkably, the present sample is characterized by an exceptionally broad hysteresis, originating from the high crystal quality of the embedded NCs. Potential applications in memory and storage technology will benefit from this broad hysteresis as well as from the IMT-related substantial changes in the (optical) material properties. Furthermore, this type of linear optical characterization is a required basis for the creation of the switching etalon presented in the next chapter.

In the following section a novel optical functionality of VO_2 NCs which is mainly related to the change of the dielectric function during the IMT is demonstrated. In particular, a sub-wavelength layer of VO_2 NCs embedded into fused silica is introduced in an optical cavity creating a moderate-finesse etalon. When these NCs are driven through the IMT by either heating or optical excitation, a pronounced spectral shift as well as a transmission change of the near-infrared modes transmitted through the etalon is observed. These modifications are related to the substantial change of the complex refractive index connected to the structural phase transition. Both heat deposition and optical excitation permit to actively control the etalon's functionality. Remarkably, spectral shifts of about one linewidth can be achieved. In agreement with transfer matrix simulations these spectral shifts strongly depend on the thickness as well as on the location of the sub-wavelength thick VO_2 NC layer with respect to the node/anti-node pattern of the optical resonator. Quantitative deviations between the experimental findings and the theoretical simulations of the present etalons require further investigation. In general, a thicker layer of VO_2 NCs is required to accurately describe the optical response of the etalon by theoretical simulations. Nevertheless, this moderate-finesse etalon containing a sub-wavelength layer of VO_2 NCs is a proof of principal for an alternative active, fast and precise modulation of light. Instead of relying on mechanical components like a chopper or shutter, a tunable material changes its essential optical properties motionless and on demand by an external thermal or optical trigger.

Further improvements can be achieved by spectrally tuning the resonance to the desired operating wavelength via a change of the fabrication parameters (or vice versa). According to Fig. 2.3, the actual sample grants large spectral shifts at ~1.25 eV photon energy due to the pronounced change of the real part n of the complex refractive index during the IMT. On the other hand, at ~1 eV photon energy (in the center of the resonance) Δn becomes zero and the transmission peaks of the etalon are only subject to a change of the imaginary part k of the complex refractive index. This, in turn, leads to spectrally stable transmission peaks featuring a large change in transmission intensity during the phase transition. Additional considerations would include the layer thickness of the VO_2 NCs. Since the impact on the transmission modes depends the most on this crucial parameter, thicker layers might be considered. The other side of the coin is a reduced finesse of the etalon that leads to a spectral broadening of the peaks. Both must be considered prior to such an implementation of a layer of VO_2 into an etalon for optical application.

In the last chapter of part I the nonlinear optical response of a thin film of ion beam synthesized VO_2 nanocrystals is thoroughly investigated by the open aperture z-scan technique involving femtosecond near-infrared pulses. It is found that, beyond the established nonlinearity related to the insulator-metal phase transition of VO_2, the metallic state features a pronounced saturable absorption at $\lambda = 1036$ nm. In marked contrast, a pronounced reverse saturable absorption of the metallic state is found at $\lambda = 1550$ nm.

The insulating state is characterized by a substantial reverse saturable absorption at $\lambda = 1550$ nm and a weak optical nonlinearity at $\lambda = 1036$ nm. However, the increasing laser intensity eventually induces the IMT before large effects from these nonlinearities can be observed. Cooling the sample to liquid nitrogen or liquid helium temperatures may lead to a larger range of accessible transmission changes due to nonlinear (saturable) absorption.

In general, these two different nonlinearities are attributed to a transient red-shift of the plasmonic resonance of the NCs during the ultrafast light-matter interaction. This well-known red-shift for metal and metal-like nanoparticles is based on a thermal expansion of the NCs while the broadening of the resonance is readily explained by enhanced electron-phonon scattering.

A quantitative analysis of the different z-scan traces using a phenomenological model based on nonlinear and/or saturable absorption reveal high equivalent two-photon absorption coefficients of several thousand cm/GW and saturation intensities in the range of 1 kW/m^2. These nonlinearities are largely linked to the plasmonic resonances of metallic VO_2 NCs. As this resonance can be custom tailored by, e.g., the NCs' size and host material, the present results hold promise to achieve widely adjustable and large optical nonlinearities in the near-infrared, suitable for applications such as saturable absorbers to mode-locked lasers. Further samples may be custom-tailored to spectrally match the plasmonic resonance to these specific laser lines and/or optical applications.

However, the maximum impinging optical intensity is limited by the damage threshold of about 5 mW/µm^2 (for 1036 nm pulses). Exceeding this limit leads to a permanent imprint on the sample and degeneracy of the NCs from local heating (temperatures are expected to be in the order of the annealing temperature during the fabrication process). In accordance with the results presented in Fig. 4.2(a), a full restoring of the IMT-related transmission decrease by a saturable absorption is unlikely to be achieved without threatening the sample at its limits. Here, further improvements of the crystal quality and local heat distribution via the host matrix material may finally lead to a full and reversible transmission restoring by saturable absorption from high intensity laser radiation.

Part II

Hexagonal GaN/AlN Superlattice

Chapter 6

GaN/AlN Heterostructures

The III-V nitrides have attracted the world's attention rapidly in the last decades since they have long been viewed as a promising material system for semiconductor-based devices with application in the blue and ultraviolet wavelength range. Scientists, research groups and technology companies tried to tie in with the established arsenide and phosphide-based devices that successfully exploit the green, red and infrared spectral regime. Today, group III-nitrides are the typical material of choice for manifold device applications in optoelectronics and electronics like blue and UV light emitting diodes and laser diodes, high efficiency solar panels or as an alloy component in high-electron mobility transistors (HEMTs) [XAY19]. The spectral range in which these devices operate is determined by the semiconductor's bandgap. The available transition energies between valence and conduction band are, therefore, limited by the finite amount of available semiconductors and their alloys.

Owing to the huge band gaps reaching from 0.7 eV for InN to 3.4 eV for GaN and 6.2 eV for AlN, a large band discontinuity of e.g. ∼1.7 eV between AlN and GaN can be realized in quantum confined structures. Many novel nitride-based optical devices such as quantum cascade lasers [FCS94], photodetectors [MKS09] and modulators [MKS09] rely on intersubband transitions (ISBTs), i.e., optical transitions between confined discrete energy states of, e.g., a quantum well (QW). Since the initial discovery of ISBTs, intersubband physics has been mainly restricted to arsenide or antimonide materials, i.e., to mid- to far-infrared operation [WE85]. Owing to the extremely large conduction band offsets, modern GaN/AlN heterostructures offer ISBTs in the aspired 1.3-1.55 µm telecom window [MKS09, MNV16]. Since the positions of the discrete energy levels strongly depend on the dimension of the lateral confinement, transition energies between different subbands can be easily tailored during the fabrication process. This property is incredibly useful for any band engineering with regard to novel custom tailored QW devices. In particular, the central wavelength of the transition can range from ∼1 µm up to several tens of µm, covering a larger and continuously fine-tunable range than offered by inter-band transitions. [MKS09]. Furthermore, the group III-nitride family of semiconductors shows excellent characteristics concerning physical and chemical inertness as well as thermal and mechanical stability. Additionally, the superior electron saturation velocity and peak velocity, high breakdown voltage and good thermal conductivity are key factors for high-class optoelectronic and electronic devices [XAY19].

In the second half of this thesis a coupled multi quantum well (MQW) system based on an arrangement of 25 ultranarrow hexagonal AlN/GaN/AlN heterojunctions is investigated. The resulting structure is also referred as to an artificial superlattice featuring the periodicity of the layered stacking. Due to the spatial confinement of charge carriers in the potential landscape, discrete energy subbands emerge. Based on the coupling of adjacent wave functions and fluctuations during the growth process these subbands are energetically broadened and are usually referred as to minibands. The proper choice of the QW width combined with an extensive n-type doping of the AlN barrier layers results in the formation of a two-level system optimized for optical interaction in the telecom wavelength regime centered at $\sim 1.55\,\mu$m.

Several research groups have already reported on ISBTs in hexagonal GaN/AlGaN QWs and coupled QWs [TND06, MKS09, BGH06] providing systematic experimental and theoretical data for varying well and barrier thickness or different doping concentrations. What is new about the present sample is the record-high broadening of the inter-miniband transition that exceeds the results from previous studies [TND06, DFM07, MTS11]. The reason is a substantial coupling between adjacent wells caused by the fairly low barrier width of 5 nm. Many applications like single device photo detectors would certainly benefit from a broadened transition range since they could easily cover a wide spectral range at once.

In the context of chapter 6.2 the physical basics, outlined in the previous section 6.1, are used for simple simulations of the expected transition energies within a single QW. Monolayer fluctuations as well as the influence from doping or the polarization discontinuity in the hexagonal structure are discussed on a quantitative and/or qualitative level. In chapter 6.3 control measurements of the molecular beam epitaxy (MBE) growth process including X-ray diffraction and atomic force microscopy provide evidence of the overall good quality of the present GaN/AlN MQW sample. The ISBT is finally measured by optical means in a special waveguide structure and compared with the data from the simulations.

On the spectroscopic side, the regime of strongly driven intersubband transitions will be characterization with modern methods of femtosecond spectroscopy in chapter 7. Degenerate (single color) and non-degenerate (bi-color) time-resolved pump-probe spectroscopy in the near infrared wavelength regime is used to explore the properties of the ISBTs on the femtosecond timescale. In arsenide or antimonide based MQW structures ISBTs have to be analyzed in the fairly inconvenient THz region. In marked contrast, the GaN based MQW sample of the present thesis allows for studies in the near-infrared regime which offers better availability of femtosecond pulses and detectors. In addition, near-infrared laser pulses can be obtained with high peak powers and therefore easily permit to drive the ISBTs far beyond the regime of weak perturbations. The intersubband relaxation is governed by longitudinal optical phonon interaction that is estimated to be as fast as ∼100 fs in AlGaN/GaN QWs, i.e., ∼30 times faster than in InGaAs QWs [SI97, SI98]. The available laser source beats this theoretical relaxation time with a pulse duration of just 50 fs and thus allows a high time resolution. In general, nitride-based devices like quantum cascade lasers or modulators allow operation in the GHz and THz regime and benefit from this ultrafast electron relaxation [MKS09, MNV16].

A new direction in the research on the nonlinear optical properties associated with ISBT has opened up by combining ISBT with plasmonic nanostructures. In particular, metasurfaces with a record-high nonlinear response have been realized based on the resonant coupling of electromagnetic modes in plasmonic elements with quantum-engineered electronic ISBTs in semiconductor heterostructures [LTA14]. In the framework of this study the previously introduced GaN/AlN heterostructure is functionalized with an array of plasmonic rod antennas featuring cross-polarized resonances at near-infrared wavelengths and their second harmonic. Due to the local field enhancement at such plasmonic elements the optical nonlinearity is expected to massively enhance as well.

Experimentally, this concept will be demonstrated in chapter 8.4 for second harmonic generation (SHG) at a wavelength of about $\lambda_{SHG}=0.8\,\mu m$. In more detail, the present nonlinear metasurface allows for substantial SHG at normal incidence which is completely absent for an antenna array without the MQW structure underneath. While the second harmonic is originally radiated only into the plane of the QW, a proper geometrical arrangement of the plasmonic elements permits to redirect the second-harmonic light to free-space radiation, which is emitted perpendicular to the surface. Therefore, the proposed structure can act as an ultrathin highly nonlinear optical element that enables enhanced nonlinear optical frequency mixing. In order to characterize and improve the proposed concept, power and polarization dependent as well as spectrally resolved measurements are carried out.

This relatively young approach for a nonlinear optical metasurface is interesting for many researchers working in plasmonics, metamaterials and nonlinear optics since it has several advantages compared to the traditionally established nonlinear materials: (i) It is possible to engineer almost any element of the nonlinear susceptibility tensor of these structures. (ii) The magnitude of the (second-order) nonlinear response in optical metasurfaces is extremely large. (iii) Such a functional optical structures offers an extremely large spectral tunability. (iv) Reducing the dimensionality of a nonlinear material to practically two dimensions eliminates the requirement for sophisticated phase matching techniques as the thickness of such a metasurface is far below the coherence length.

6.1 Introduction to Quantum Wells

This section of the thesis provides a brief overview of the basic physics of quantum wells (QWs) and the formation of electronic energy states within such a well[32]. Furthermore, the transition to a MQW or superlattice with tunable inter-subband transitions is discussed. In the present case, a two-level-like mini-band system evolves from a GaN/AlN superlattice that is highly suitable for optical absorption and emission applications in the telecom wavelength range.

A QW is a potential well that restricts the freedom of motion of a particle (generally speaking of electrons and holes) in one dimension of space (z-direction)[33]. Consequently those particles are confined in a planar region (x,y-plane) within the potential barriers leading to the evolution of a quasi 2D particle-gas. Shrinking the width of the QW to values comparable to the de Broglie wavelength[34] of the carriers inside the QW subsequently leads to effects of quantum confinement. The width of the QW basically determines the quantum mechanical states that a particle can occupy. In particular, discrete energy levels (energy subbands) are formed, suitable for inter-subband transitions.

The theoretical concept of a QW was proposed in 1963 independently by H. Kroemer, Z. Alferov and R.F. Kazarinov [Kro63, AK63]. Based on this theory a wide variety of different electronic QW devices has been developed up to date. The most important application of QWs are laser diodes, light emitting diodes (LEDs), photo detectors and modulators. In general these devices are much faster and profit from a higher recombination probability and thus grant a higher efficiency. Due to the broad energetic/spectral tunability of the QW's response by altering the fabrication parameters, QW-based devices gained incredible importance to the technological and telecommunication industry. QW devices are currently replacing many conventional electrical components in a variety of industrial and home appliances [ON15].

Assuming an (idealized) infinitely high potential square well oriented in the z-direction and characterized by a width w, the potential landscape of the so called "particle-in-a-box" is given by $V(z)=0$ for $0<z<w$ and $V(z)=\infty$ elsewhere, cf. Fig. 6.1(a). The stationary Schrödinger equation for a particle in the potential box is:

$$-\frac{\hbar^2}{2m^*}\frac{\partial^2}{\partial z^2}\Psi(z) = E\,\Psi(z) \tag{6.1}$$

---

[32] More detailed information about the physics of quantum wells can be found in [Dav98].

[33] Usually the restriction is in the z-direction that, in general, equals the growth direction of the QW structure.

[34] All matter exhibits wave-like behavior and the associated de Broglie wavelength λ is defined as $\lambda=h/p=h/mv$ (with Planck constant h, particle momentum p and particle mass m). For electrons the QW width is in the order of 10 nm to show effects of quantum confinement.

where $\hbar$ is the reduced Planck constant, m* is the effective mass of the particle within the QW, Ψ(z) is the wave function and E is the energy of the system. In general the effective mass of a particle in its quantum environment strongly differs from the rest mass. Furthermore, the value of m* shows different values for different semiconductors and bands as it depends on the curvature of the band. Solving Eq. 6.1 results in the solution wave functions that are given by:

$$\Psi_n(z) = \sqrt{\frac{2}{w}} \sin(k_{z,n} z) = \sqrt{\frac{2}{w}} \sin\left(\frac{n\pi z}{w}\right) \tag{6.2}$$

Here, $k_{z,n}$ is the discrete wave vector in z-direction (cf. standing waves in Fig. 6.1(a)). The subscript n is the integer quantum number n>0, labeling the electronic subbands in the QW. Each wave vector is associated with a discrete eigenenergie of the quantized energy levels given by:

$$E_n = \frac{\hbar^2 k_{z,n}^2}{2m^*} = \frac{\hbar^2 \pi^2 n^2}{2m^* \, w^2} \tag{6.3}$$

All equations provided above describe the wave functions and eigenenergies with respect to the z-direction. Due to the confinement in the z-direction of the QW, electrons are still free to move in the x and y directions. A two-dimensional plane wave, characterized by the in-plane wave vector $k_\perp$ describes this in-plane part of the wave function. The corresponding total energy E(**k**) has to be extended by the in plane parabolic contribution as followed:

$$E(\boldsymbol{k}) = \frac{\hbar^2 k_{z,n}^2}{2m^*} + \frac{\hbar^2 k_\perp^2}{2m^*} \qquad \text{with} \qquad k_\perp^2 = k_x^2 + k_y^2 \tag{6.4}$$

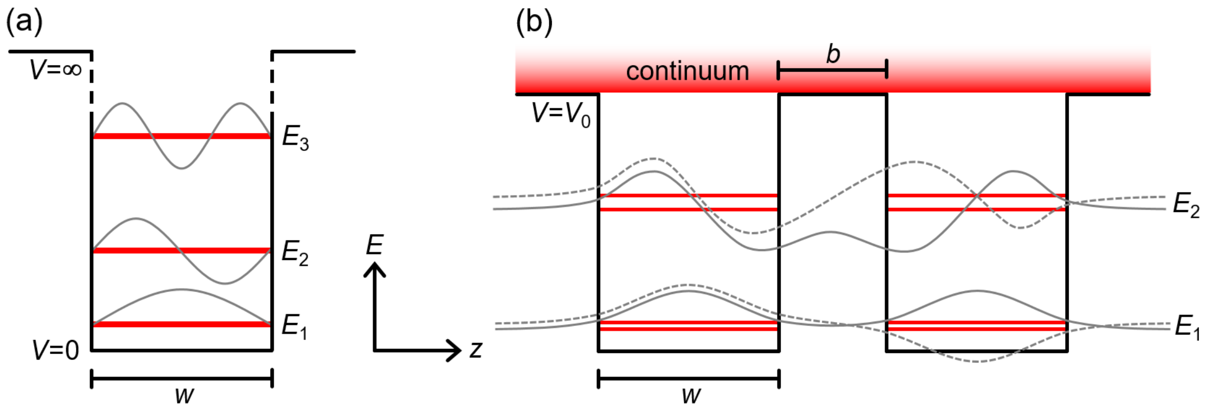

Fig. 6.1: Schematic illustration of the potential landscape V(z) of (a) a single QW with infinitely high potential barriers and (b) a double QW with finite barrier height. Energy levels E_n of the electronic subbands within the well are depicted by red lines and the corresponding wave-functions are shown by grey lines. (b) Due to quantum coupling of the adjacent wells with finite barrier width, two solutions for the wave function (symmetric and antisymmetric) exist. The corresponding energy levels are non-degenerate and the subband splits up.

The infinite well approximation provides a helpful model to understand the basic properties of a quantum confined 2D electron gas in a type I aligned[35] QW structure. Since the energy levels E_n are inverse proportional to the square of the width of the QW, transition energies between different subbands can be easily tailored during the fabrication process. This property is incredibly useful for any band-gap engineering with regard to novel custom tailored QW devices. Furthermore the energy levels are inversely proportional to the effective mass of the charge carriers. Consequently, electrons, heavy holes and light holes[36] have different energy states within the well.

As the walls of real QWs are finite and show “relatively” small values in the order of $V_0 \approx 1\,\mathrm{eV}$, the infinite well model predicts many more energy states than really exist. Electronic levels above V_0 are not localized anymore and are considered as continuum (states). Consequently, the wave functions do not vanish at the boundaries of the finite well but exponentially decay into the potential barriers due to quantum tunneling.

If two finite QWs are lined up far enough apart, the wave functions do not overlap and a simple double QW structure is formed. When the barriers between adjacent QWs are sufficiently thin the wave functions actually overlap. Consequently, tunnel coupling between the neighboring QWs sets in and electrons from bound states in one well can tunnel into the adjacent

---

[35] For a type I band alignment, the conduction band of the second semiconductor is lower and the valence band is higher than the corresponding conduction/valence band of the first semiconductor (cf. Fig. 6.1).

[36] The light and heavy hole valence bands are formed as a consequence of the spin-orbit angular momentum interaction of the atomic states involved, resulting in a splitting of the states. The triple degeneracy of the valence band leads to the formation of the additional split-off band.

well. The theory for a single (finite) QW is no longer sufficiently accurate, but a more sophisticated analytical solution for the coupled system is required. In this case, the stationary Schrödinger equation is solved by a symmetric and an anti-symmetric wave function with two different eigenenergies (cf. Fig. 6.1(b)). Accordingly, each subband splits into two non-degenerate energetic states leading to a higher amount of available inter-subband transitions. Since the tunnel coupling becomes stronger for a decreasing barrier width, the resulting splitting of the subband increases.

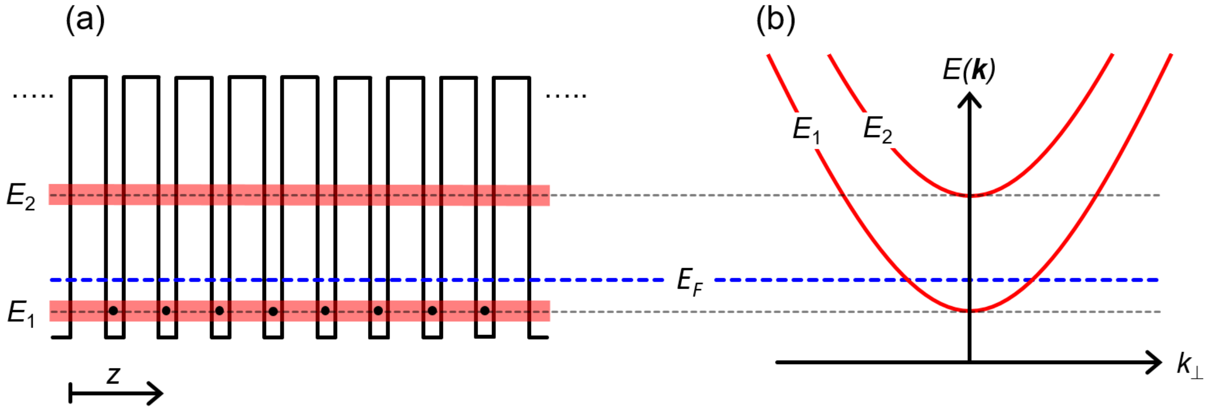

Fig. 6.2: (a) Schematic illustration of the potential landscape of a superlattice. Energetically broadened mini-bands, shown in red, evolve from strong interwell coupling. Due to strong n-doping the Fermi energy (dashed blue line) is raised and the energy level E_1 is populated by electrons. (b) Shows the central energies of the electronic mini-bands with respect to the $k_\perp$-vector. The quantum confinement in z-direction leads to the offset of the bands and the parabolic behavior originates from a free in-plane movement of the electrons.

When the number N of coupled QWs is further raised, a MQW is formed and each subband subsequently splits into N energy levels. For an increasing number N, the energy splitting between the lowest and the highest energy level becomes larger and the range of possible inter-subband transition energies is further broadened. A periodic structure composed of a large one-dimensional array of coupled QWs, schematically depicted in Fig. 6.2 (a), is called a "superlattice". The term originates from the second level of periodicity of the QW array that is made from different, first level periodic lattices. In general, both expressions (MQW and superlattice) are used synonymously since no clear distinction based on the number of QWs exists but the term superlattice often highlights a stronger coupling of adjacent, periodically arranged QWs. In the case of the present superlattice with N = 25 strongly coupled[37] QWs, the subband splitting is fairly broad. Additionally, the natural line width of each energy level in

---

[37] From the ratio of the well width w = 1.8 and the barrier width b = 5nm a fairly strong coupling of the QWs is expected.

combination with thermal broadening and scattering processes in grown samples form a practically continuous “mini-band” composed of the individual 25 subbands. The resulting inter-miniband transitions are, therefore, expected to be greatly enlarged in a superlattice structure classified by a high N and low barrier width.

The superlattice structure can also be seen as a resonant tunneling system. The transmission of electrons through the periodic structure is either near unity, if the electron occupies a miniband, or zero otherwise. Another theoretical approach is the Kronig-Penney model which describes the motion of electrons in a one-dimensional periodic square-well potential. The solving wave function is composed of a plane wave in growth direction multiplied with a periodic Bloch function that incorporates the second level of periodicity of the superlattice. The resulting band structure shows energetic gaps due to the periodic arrangement of the wells.

Since the carrier density of an intrinsic semiconductor is fairly low, doping with small amounts of intentionally introduced impurities can dramatically increase the conductivity of the material. Barrier-doped or well-doped superlattices may gain metal-like characters due to their partially filled energy bands. For the present sample, modulation doping[38] of the AlN barriers with a silicon (Si) concentration of $n \sim 10^{19}\,\mathrm{cm}^{-3}$ gives rise to a two-dimensional electron gas. The Fermi energy is lifted above the minimum of the first subband (E_1) that behaves as a strongly populated ground state. In combination with an empty upper state (E_2), this system resembles a two-level system. Both mini-bands show a parabolic energy dispersion, well-known from a semiconductor’s conduction band structure (cf. Fig. 6.2(b)).

The resulting two-level inter-miniband system from an ultranarrow GaN/AlN heterostructure offers transitions in the telecom-range suitable for applications based on absorption and spontaneous or stimulated emission. As the theoretical introduction showed, energetic/spectral tunability is accessible by the fabrication parameters. Various epitaxial growth techniques are used to create such QW structures with specifically designed transition energies. In the next section the growing process of the investigated superlattice sample and the first control measurements are outlined.

---

[38] Modulation doped semiconductors have very high carrier mobilities since the free charge carriers are spatially separated from the donors, thus eliminating scattering.

6.2 Fabrication Process and Energy Levels of the GaN/AlN Superlattice

Gallium nitride (GaN) and aluminum nitride (AlN) are group III-V direct semiconductors consisting of gallium or aluminum and nitrogen. Both GaN and AlN show a large band gap at the Γ-point, corresponding to interband transition wavelengths in the UV range. The following table provides some important structural and electronic parameters of both semiconductors at 300K (room temperature) [LRS01, LRS03, LTS96]. The effective mass is given in proportion of the electron rest mass m_0.

	α-GaN	α-AlN
lattice constant a_0 / c_0 (Å)	3.189 / 5.185	3.112 / 4.982
band gap at Γ-point (eV)	3.39-3.51	6.03-6.30
effective electron mass (m_0)	0.2	0.3-0.4
effective light hole mass k_z / k_x (m_0)	1.1/ 0.15	3.53 / 0.24
effective heavy hole mass k_z / k_x (m_0)	1.1 / 1.6	3.53 / 10.42

GaN and AlN crystallize preferentially in the hexagonal (wurtzite) structure (α-GaN/α-AlN), whereas the cubic (zincblende) structure (c-GaN/c-AlN) is not stable. However, both semiconductors can be forced to grow in this metastable lattice structure by using, e.g., cubic silicon carbide (3C-SiC)[39] as a substrate layer. 3C-SiC in its (001) orientation nearly matches the lattice constant of the c-AlN [SPA07, As09, Wec13, WHF15]. Nevertheless, thick layers of cubic GaN/AlN tend to become increasingly unstable and, eventually, switch to the hexagonal structure during the growth process. In contrast to the rectangular potential landscape of a cubic GaN/AlN MQW, the hexagonal heterostructure is characterized by a triangular band structure (cf. Fig. 6.3(b)) with strong bendings at the band edges [NJC06]. The confinement of charge carriers in the triangular potential wells and the resulting spatial separation of electrons and holes along the growth axis are undesirable due to the reduced transition probabilities. Consequently, the lack of spatial overlap of the electron- and hole-wave functions limits the efficiency of optical devices. This carrier localization in the triangular potentials leads to spontaneous and piezo-electric polarizations in the hexagonal lattice along the c-axis that are not present in the cubic crystal structure [BFV97, YDA99]. The resulting internal electric fields orientated along the growth direction have a negative effect on the electron mobility. The properties of c-GaN/c-AlN

---

[39] The number 3 in 3C-SIC refers to the three-bilayer periodicity of the layer stacking (ABCABC…) and the letter C denotes the cubic symmetry of the crystal.

would have been beneficial for the design and efficiency of electro-optical devices but in the course of this thesis, the growth of high quality c-GaN-based heterostructures turned out to be more challenging than expected. Therefore, the investigated samples are grown in the hexagonal lattice structure that will be simply referred as to GaN/AlN in the further course of this thesis.

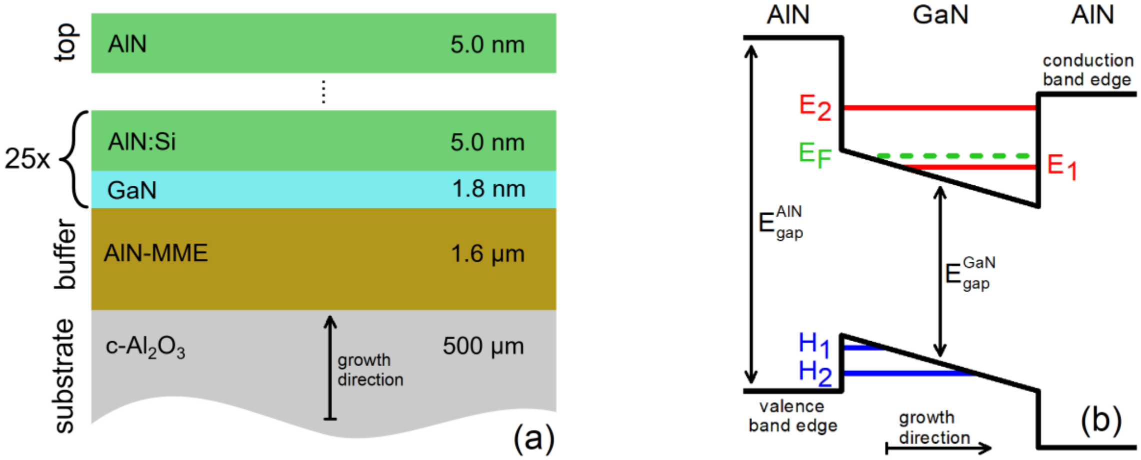

Fig. 6.3: (a) Layer sequence of the hexagonal GaN/AlN superlattice grown by molecular beam epitaxy. (b) Sketch of the type I band alignment in the hexagonal AlN/GaN/AlN heterojunction. Due to the quantum confinement of charge carriers discrete subbands emerge within the potential landscape of the QW (H_i=hole states, E_i=electron states (subbands), E_F=Fermi energy).

The superlattice heterostructure of this study, schematically depicted in Fig. 6.3(a), was fabricated by Valentin Jmerik and Sergey Ivanov from the Ioffe Institute in St. Petersburg, Russia. It was grown by plasma-assisted molecular beam epitaxy (MBE Compact21T, Riber) on a double-side polished c-sapphire wafer[40] (c-Al_2O_3). During this process, crystalline layers of the desired material compounds were grown using gas phase deposition of the evaporated source elements. Growth temperature, evaporation ratio, flux rate, growth rate and other growth parameters show a crucial impact on the crystal quality and have to be selected carefully. Initially, a 1.6 µm thick AlN buffer layer was grown using two-stage metal-modulated epitaxy to reduce the threading dislocation density to mid-10^9 cm^{-2} and to achieve an atomically smooth surface, as detailed in [NKR20]. Then, 25 GaN QWs with a thickness of 1.8 nm (equal to 7 monolayers), separated by 5 nm thick AlN barrier layers, were formed using the sub-monolayer digital alloying method described in [JNT18]. A fluctuation in the order of ±1 monolayer for the present narrow well is realistic, whereas fluctuations in the layer thickness of more than one monolayer cannot be excluded for larger layer/well widths. In general, near-stoichiometric conditions are used for

---

[40] The letter c specifies the surface orientation of the cut through the monocrystalline Al_2O_3 wafer. Specifically, it defines the (0001) plane in the hexagonal crystal. An intentionally c-plane off-angle toward the m-axis of 0.3 degrees reduces the mismatch between the substrate and the AlN.

many of the growing processes. Here, GaN and AlN are grown at metal-rich conditions to improve the smoothness of the structure. Meanwhile the unintentional formation of undesired Al droplets had to be avoided. While the GaN QWs are nominally undoped, the AlN barriers were grown with an n-type Si-doping with a concentration of $n = 1.5 \cdot 10^{19}\,\mathrm{cm}^{-3}$. The doping gives rise to a two-dimensional electron gas (2DEG) with an expected carrier density of $n = 4 \cdot 10^{12}\,\mathrm{cm}^{-3}$, corresponding to a calculated Fermi energy of $E_F = (\pi\hbar^2/m^*) \cdot n = 90\,\mathrm{meV}$ above the minimum of the first subband. Finally, the MQW structure was capped and protected by a 5 nm AlN layer. As a result, these growth and doping parameters lead to the formation of a high-mobility 2DEG with low sheet resistance. Furthermore, this superlattice structure offers a large density of states for resonant ISBTs centered at ~0.8 eV. A previous study on a nominally almost identical, cubic, heterostructure showed that QWs of the present width exhibit ISBTs around 0.8 eV [JWR15]. This experimental finding is consistent with band structure simulations performed with the commercial nextnano simulation package [Nex22]. In addition, basic simulations of the energy levels of a single finite QW have been carried out for the current hexagonal GaN/AlN sample. In the next section a short introduction to the crucial parameters of the simulation and the results for the ISB transition energy for a variation of the well width are outlined. The successful theoretical prediction of the quantized energy levels is a key to achieve the desired inter-miniband (IMB) transition energy in further samples.

Recalling the short overview of quantum well physics in chapter 6.1, a confined electron in a potential well, whose width is comparable to the de Broglie wavelength of the electron, experiences energetic quantization effects. Discrete energy states are formed within the QW that are allowed to be occupied by the charge carriers. For a better understanding and verification of the experimental results theoretical calculations of the mini bands in the superlattice structure have to be performed. For this purpose the Schrödinger-, Poisson- and the current continuity equation for electrons and holes have to be solved. In order to keep the simulation as simple as possible, a one dimensional band structure and transition energy calculation based on an effective mass model is applied to a single QW. Within a close approximation the values obtained by this simulation refer to the center of the energetically broadened mini bands in the superlattice, thus defining the central IMB transition energy. The most important parameter involved in the estimation of the heterostructure's energy levels is the band offset that characterizes the band discontinuity. For the present GaN/AlN QW the type I band alignment is described by the conduction band offsets (CBO) and valance band offset (VBO), respectively. Both parameters reflect how the bandgap difference of the involved semiconductor materials is portioned between the discontinuities of the bands. A rule of thumb for this kind of group III-V materials is a 2:1 ratio [MSE98]. Thereby the CBO defines the depth of the potential well. Extensive experimental and computational research has revealed the band offsets between various semiconductor heterojunctions and alloys[41]. Nevertheless, a broad range of CBO values in hexagonal GaN/AlN systems between 1.4 eV and 2.3 eV has been reported in literature so far [WG96, VMR01, AR00, WN03, BMK94]. However, the most stated CBO values for hexagonal GaN/AlN MQWs cover the span between 1.7eV and 1.9eV. Subsequently, the energetic position of the confined states and the resulting IMB transition energy strongly depends on the choice of the CBO. The respective VBO is found to be 0.8±0.3 eV [MSB98].

Looking back at the table of the structural and electronic parameters, the difference between the lattice constants of both semiconductor alloys is small but not negligible. The AlN layers are tensile strained to the GaN due to the smaller lattice and vice versa. A modification of the band gap energy due to strain caused by the misfit of the lattice parameters can be calculated using the deformation potential and the elastic constants of both materials. As a result, the band gap energy of the GaN (AlN) is slightly increased (decreased). The total change of both gap energies sums up to roughly 0.2 eV [CDS10]. As a result the CBO and VBO decrease in total by this value. Since the given range of CBOs exceeds this value, the effect of strain will not be included in this simulation. Nevertheless, it should be noted that a strain induced reduction of the CBO in a GaN/AlN QW leads to a somewhat red shifted ISB transition.

The hexagonal phase of GaN and AlN is characterized by strong internal piezoelectric and pyroelectric fields along the c-axis leading to a triangular potential landscape (cf. Fig. 6.3(b)). In general, theses detrimental effects are undesirable for many optoelectronic applications, complicate the theoretical design and limit the tunability of the transition energies. For wide wells made from polar group III-nitrides, the transition energy is observed to be almost independent of the well width due to the confinement of carriers in the triangular potential. Above 2 nm well thickness, the first two states are completely confined by the triangular-shaped potential in the well. The transition energy is therefore governed by the magnitude of the internal electric field. The narrower the well, the more the influence of the tilted potential can be neglected. To be more specific, the IMB transmission wavelength is somewhat blue-shifted compared to the results calculated without built-in electric field. Simplified, this can be explained as follows: The effective width of the strongly tilted (triangular) potential well is reduced compared to a rectangular potential landscape. In agreement with Eq. 6.2 the emerging subbands are subsequently pushed to somewhat higher energies. Additionally, the built-in electric field breaks the potential symmetry and allows ISB transitions from the ground state E_1 to the second excited state E_3 [HSH02]. Furthermore, bound-to-continuum transitions are energetically benefited to one side of the asymmetric QW (cf. Fig. 6.3(b)). It is found that the built-in electric field within the QW is 2-3 MV/cm [SIK03] up to 8-10 MV/cm [HTL03]. For the sake of simplicity, the nominally 1.8 nm narrow biased well will be approximated by a square potential landscape.

---

[41] The conduction band offset can be obtained from intersubband spectroscopy and model calculations based on, e.g., density functional theory using the proper material parameters.

Heavy doping of the GaN/AlN QW leads to a systematical blue shift of the ISB transition energy in n-doped samples, with respect to a nominally identical undoped sample. The exchange interaction is found to be the dominant contribution of this many-body effect. This way, a doping concentration of $n = 1 \cdot 10^{19}\,\text{cm}^{-3}$ can introduce a blue shift of the ISB transition by as much as 80 meV in a 1.8 nm wide QW [HTL03]. Actually, the effect of strong doping is not taken into account in the simulation, but should be considered qualitatively.

For an even more sophisticated outcome of the simulation the enhancement of the effective masses due to non-parabolicity effects and the energy dependency of the effective electron mass would have to be taken into account [Kan57].

In Fig. 6.4 the calculated energy levels within the GaN/AlN QW and the associated intersubband transition energies are compared. CBO values of 1.7 eV (a-c) and 1.9 eV (d-f) are used for the different simulations. To account for a possible uncertainty in the growth process a well width variation of ±1 ML is included. In particular, a variation by one monolayer in the QW thickness leads to a larger change in the transition energy for thinner QWs and should therefore be considered in the actual case of a nominally 1.8 nm wide well. On the other hand, strain results only in a small shift of the ISB transition energy in the order of 10 meV and is negligible in this first approximation compared to the effect of a monolayer fluctuation that easily shifts the ISB transition by 100 meV. Expected from theory, the general trend observed in the simulation shows that the narrower and deeper the well, the further the IMB transition is shifted to higher photon energies/shorter wavelengths. To anticipate the experimental results outlined in the next chapter, a QW consisting of only 6 MLs can be ruled out because the ISB transition energies are way too high above the desired 0.8 eV photon energy. A QW width of 7 to 8 MLs leads to a more accurate match with the experimentally observed ISB transition energy of 760 meV (cf. Fig. 6.6(c)) while remaining within the range of growth uncertainty (panels b, c, d, f).

In an experimental and theoretical study performed by Helman et al. ISB spectroscopy of similar doped and undoped GaN/AlN QWs grown by MBE on a sapphire (0001) substrate reveal ISB transition energies between 0.67 eV and 0.85 eV depending on the width of the QW and the doping concentration, respectively [HTL03]. Specifically, an effectively 1.87 nm wide well featuring a doping concentration of $n = 1 \cdot 10^{19}\,\text{cm}^{-3}$ shows an experimentally observed ISB transition energy of 740 meV. This value stands in agreement with their provided theoretical simulations based on an energy-dependent effective-mass approach including a depolarization shift, doping and the GaN conduction band nonparabolicity[42]. Exemplarily, a nominally 1.8 nm wide QW shows ISB transitions centered at 750 mV ($n = 1 \cdot 10^{19}\,\text{cm}^{-3}$) and 780 mV ($n = 2 \cdot 10^{19}\,\text{cm}^{-3}$). The nominally 1.8 nm and highly doped ($n = 1.5 \cdot 10^{19}\,\text{cm}^{-3}$) QW sample that is investigated in this thesis fits perfectly between these given values and shows ISB transition energies centered around 760 mV (cf. Fig. 6.6(c)).

---

[42] A conduction-band offset (CBO) of 1.78 eV and a polarization discontinuity at the interface of $\Delta P/\varepsilon = 8\,\text{MV/cm}$ are used for the simulation [HTL03].

To sum up, the theoretical study of the fabricated MQW sample supports the results of the experimental ISB transition investigations performed in the next chapter that, in turn, verify the successful growth of the intended superlattice sample featuring ISB transitions in the telecom wavelength range. Incorporating further material properties in the theoretical calculations will lead to more sophisticated simulations of the superlattice structure. For the growth of further samples theoretical predictions using, e.g., the nextnano simulation package are recommended since the simple approximation of a single rectangular QW without the impact of strain, internal electric fields or doping shows too much inaccuracy.

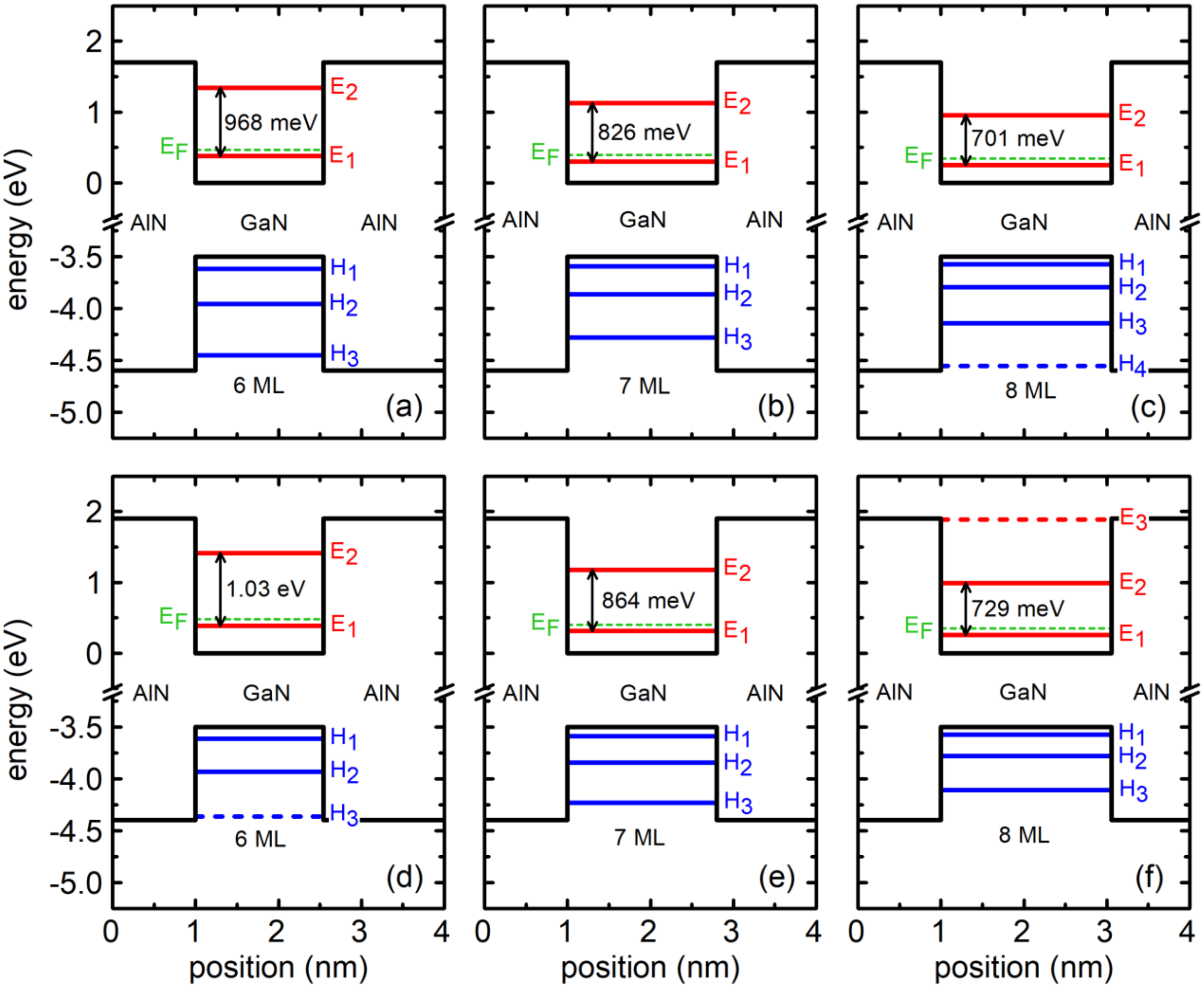

Fig. 6.4: Simulation of the energy levels in a single GaN/AlN QW for varying QW thickness and CBO, including ISB transition energies (arrows). (H_i=hole states, E_i=electron states, E_F=Fermi energy). The impact of strain, an internal electric fields or doping is not taken into account. The dashed red and blue lines indicate discrete energy levels just slightly below the band edge.

6.3 Control Measurements of the Fabrication Process

In order to characterize the material and optical properties of the grown GaN/AlN superlattice sample and to further validate the preceding simulation, several control measurements were performed. The results of these measurements contribute to the general estimation of the sample's quality and suitability for the scheduled experiments in the telecom wavelength regime.

High-Resolution X-ray Diffraction (HRXRD[43]) measurements of the (0002) reflection of the GaN/AlN superlattice, performed by Michael Deppe from the group of Prof. Dr. Donat As at the University of Paderborn, confirm the well grown superlattice with good quality interfaces by the presence of many pronounced satellite peaks in the 2θ-diffraction graph, as depicted in Fig. 6.5(a). The number and width of the satellite reflection peaks is generally accepted as a first estimation of the structural quality of the heterostructure, since an intensity decrease and broadening of the peaks is induced by threading and mixed dislocations of the layers [Ina14, PWZ99]. Here, the full width at half maximum (FWHM) of the satellite peaks (from "0" to "-4") are 375, 515, 685, 862 and 994 arcsec characterizing interfaces with some little roughness but overall satisfying smoothness for a MQW structure with roughly 50 internal interfaces [Kan08].

Furthermore, atomic force microscope (AFM[44]) measurements are performed by Michael Deppe on a $10\,\mu\text{m} \times 10\,\mu\text{m}$ area on the sample revealing a relatively smooth but slightly grainy surface (~500 nm grain size) characterized by an overall low root mean square height of 0.9 nm. The recorded image of the surface is shown in Fig. 6.5(b). The small undulations may arise from little stacking faults, monolayer fluctuations but mainly from aluminum micro-droplets in the AlN layers. Consequently, the deviation from the ideal layer sequence somewhat alters the inter-subband transition energies and slightly affects their width [KVM15]. Systematically performed scanning electron microscope (SEM[45]) measurements by the growth team at the Ioffe institute reveal a surface roughness gradient from the slightly grainy center area to the somewhat flatter edge of the waver. This gradient originates from a radial non-uniformity of the plasma density and substrate heating during the fabrication process.

---

[43] XRD/HRXRD is a general purpose technique that refers to the diffraction of X-rays on crystals and quasi-crystalline materials for structural analysis. The basic idea of this analytical method is the angle-dependent detection of reflected X-rays (angle of incidence equals angle of reflection). More information in Ref. [Ina14].

[44] The AFM is a scanning probe microscope used to mechanically scan surfaces by measuring the atomic force at the nanometer scale.

[45] The SEM produces images of a (electrically conductive) sample by scanning the surface with a focused beam of electrons and measuring the scattered and secondary electrons for topographical and material information.

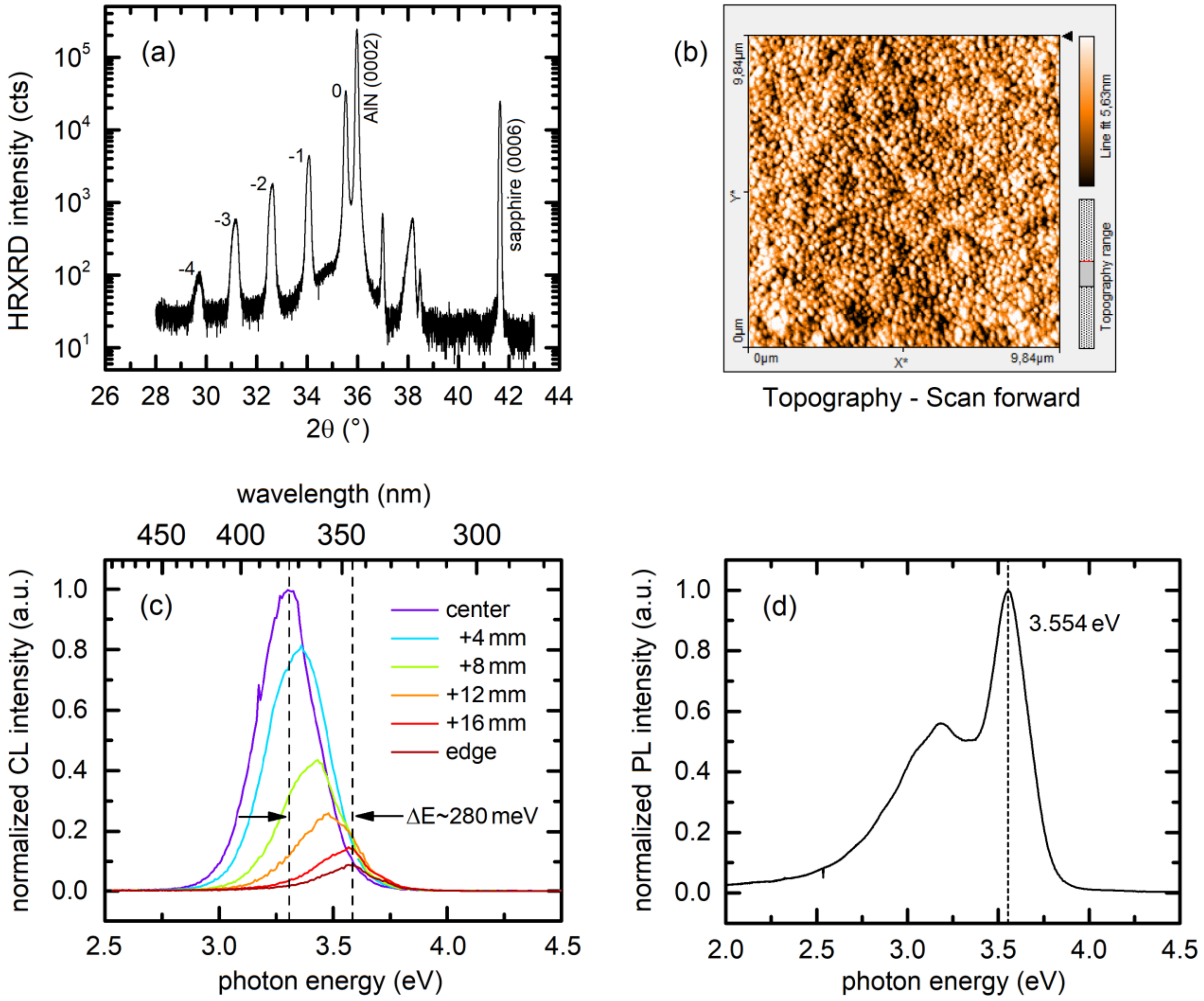

Fig.6.5: (a) HRXRD θ-2θ scan of the (0002) reflection of the GaN/AlN superlattice with several pronounced satellite peaks ("0" to "-4") indicating an overall good quality layer structure. (b) AFM image of the superlattice showing a slightly grainy surface morphology due to the formation of aluminum droplets in the AlN layers. (c) Room-temperature CL spectra from the superlattice. (d) Room-temperature PL spectra of the superlattice showing the interband transition at 3.554 eV.

The additional optical characterization by room-temperature cathodoluminescence (CL[46]) is performed by the fabrication team from the Ioffe insitute using an accelerating voltage of 10 keV for optimized emitted CL by the MQW region. The results, depicted in Fig. 6.5(c), show that the CL spectra are dominated by the band edge emission between 3.31 eV and 3.59 eV. This span of 280 meV originates again from the radial non-uniformity of the plasma density and substrate heating during the fabrication process resulting in a spatial intensity gradient and spectral blue-

---

[46] In Cl spectroscopy an electron beam impinges on a solid sample and cause the emission of characteristic photons with energies referring to the involved transition processes.

shift of the CL intensity from the center region towards the edge of the wafer. One possible explanation is the formation of some potential relief in the center of the substrate that leads to a localization effect on the charge carriers in local potential minima resulting in suppression of their lateral transport and decrease of the CL energy. This assumption corresponds to the observed slightly rougher surface morphology in the center of the sample.

Moreover, photoluminescence (PL[47]) measurements are performed by Michael Deppe to determine the energetically lowest inter-band transition energy from the first heavy-hole band H_1 to the mini-band E_1 within the QW (cf. Fig. 6.3(b)). Depicted in Fig. 6.5(d), the spectrally resolved, room-temperature and time-integrated PL-intensity of a sample piece near the edge region of the wafer shows a peak at 3.554 eV corresponding to the inter-band transition energy.

Due to quantization effects within the well, the PL and CL energies are expected to be slightly above the band gap energy $E_{gap} \approx 3.5\,\mathrm{eV}$ as the recoded photon energy refers to $E_\gamma = E_1 - H_1 > E_{gap}$. However in hexagonal GaN/AlN QWs the internal electric field tilts the QW and charge carriers are confined in the triangular potential (at their respective quantization levels, cf. Fig. 6.3(b)). The increase of the interband transition energy is, therefore, to some extent compensated by the tilt of the potential. Yet the spatial separation of the charge carriers leads to reduced transition probabilities.

In order to obtain comparable and reliable information, all subsequent measurements involving the GaN/AlN superlattice are carried out with the same sample piece taken from the center region of the same wafer (unless otherwise specified).

To complete the control measures of the growth process, the inter-miniband (IMB) transition between the two energy levels E_1 and E_2 is investigated by linear transmission measurements at room temperature. The goal of this optical analysis is to quantify the central energy and width of the IMB transition. For this purpose, the transmission of a broadband near infrared light source through the superlattice structure is analyzed.

The measurement of the IMB absorption benefits from a polarization selectivity that originates from the orientation of the IMB dipole moment along the growth direction of the superlattice. Therefore, electric field components E_z (TM - transverse magnetic, p-polarized) need to be present in the incident light beam to drive the IMB transition (see Ref. [Dav98] p. 316ff). In-plane components E_x and E_y (TE - transverse electric, s-polarized) interact only with the plane-wave part of the electron's wave function and do not contribute to the IMB transition (cf. Fig. 6.6(a,b)). Therefore, the maximum light-IMB interaction can be observed for TM polarized light propagating parallel to the layered superlattice structure whereas TE polarized light results in no IMB absorption. Impinging light with normal incidence to the superlattice generally leads

---

[47] In PL spectroscopy the investigated sample is optically excited (here 266 nm/4.66 eV continuous wave laser) and electrons are lifted into higher states, eventually returning to energetically lower states by spontaneous photon emission. The emitted light from the recombining electron-hole pairs is detected and provides information about the electronic levels involved in the transition.

to no IMB absorption since the electric field components are always normal to the growth direction. Accordingly, the experimental approach has to deal with the different polarizations/electric field components in order to distinguish between the TM and TE contributions to the overall absorption and, eventually, to determine the IMB absorption.

To enhance the light-IMB interaction length, a rectangular piece of the sample is processed into a trapezoidal waveguide geometry (bottom length of the substrate is 7.7 mm) which takes advantage of a multi-pass through the superlattice layer (cf. Fig. 6.6(a)). To this end, both side facets of the waveguide are tilted by 65° with respect to the top surface. When the focused broadband emission of a stable tungsten light source is coupled into the waveguide through one of the facets it undergoes multiple internal total reflections at the top and bottom air boundaries before leaving the sample through the opposite facet. Assuming normal incidence at the incoupling facet this geometry corresponds to ≈3 reflections at the superlattice/air interface, i.e. light traverses the superlattice layer ≈6 times[48]. Due to the refraction at the internal Al_2O_3-AlN interface the confined light passes the superlattice under an interaction angle of $\varphi \approx 45°$ (cf. Fig. 6.6(a,b)). Consequently, the residual electric field component E_z of the TM polarized light that addresses the IMB transition is reduced by the sine of the interaction angle $E_z = \sin(\varphi) E$. At the outcoupling facet the transmitted light is collected with an optical fiber and spectrally resolved in a monochromator unit (Andor Shamrock 193i, grating: 150 lines/mm) together with an extended-range InGaAs photodiode (Thorlabs DET05D). Lock-in detection is performed to increase the signal to noise ratio (Standford Research 830 and Thorlabs mechanical chopper). To quantify the IMB transition, polarization dependent measurements are done since the light-IMB interaction is expected only for TM polarized light. For this purpose a broadband near-infrared liner polarizer is inserted in the experimental setup. Subsequently, the difference between the TE and TM polarized transmission signals reveals the IMB absorption. In order to eliminate any detrimental effects on the transmission due to the birefringence of the Al_2O_3 the measurement is performed on a geometrically identical reference sample as well that is made only from the sapphire substrate. A more sophisticated reference sample would contain a thick (no quantum confinement) epilayer of GaN and/or AlN on the top side. By this means the differences in the transmissivity introduced by the altering reflective behavior at the various internal interfaces for the two polarization states could be further eliminated. Finally, the IMB absorption spectrum is calculated from the relative difference of the TM and TE raw transmission through the superlattice (SL) normalized by the respective reference sample's data (Ref) as followed:

$$\left(\frac{\mathrm{SL_{TE}}}{\mathrm{Ref_{TE}}} - \frac{\mathrm{QW_{TM}}}{\mathrm{Ref_{TM}}}\right) \cdot \left(\frac{\mathrm{Ref_{TE}}}{\mathrm{SL_{TE}}}\right) \tag{6.5}$$

---

[48] Due to the angular distribution of the impinging focused light beam the number of total internal reflections is subject to a certain degree of uncertainty. Since the focusing is performed with a MgF lens with 50 mm focal length the angular distributions is expected to be ±10°.

Although a reference sample is used for the normalization of the sample's transmission data, the resulting IMB absorption spectrum is hampered by strong Fabry-Pérot interferences and residual distortion from the substrate's birefringence. In order to partly overcome this detrimental effects, the angle of the incident light beam with respect to the incoupling facet is gradually altered by up to ±20°. Consequently, the oscillations will spectrally shift depending on the angle of incidence. Since the spectral position and (in a certain range) the width of the IMB absorption are not subject to the changing angle of interaction, averaging the calculated IMB absorption spectra for various impinging beam angles eventually results in a less disturbed graph. The other side of the coin is the loss of reliable information about the absorption strength[49] since the number of passes through the superlattice structure becomes uncertain.

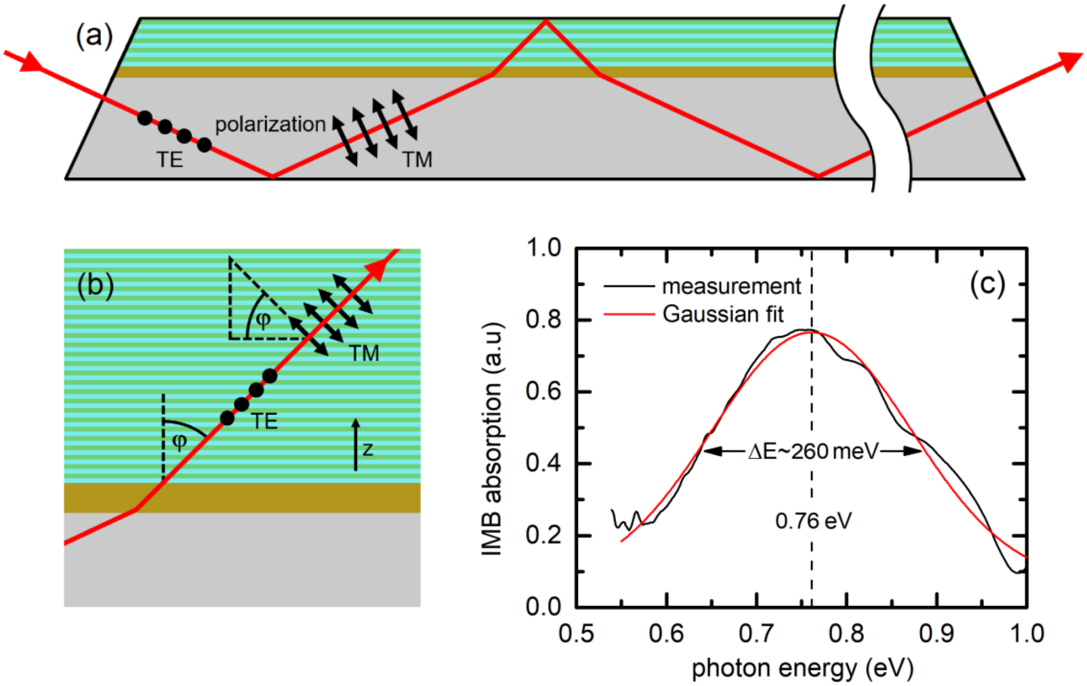

Fig. 6.6: (a) Schematic illustration of the waveguide geometry that benefits from a multipass through the superlattice layer to enhance the light-IMB absorption length. Total internal reflections at the air boundaries guide the confined broadband light through the sample. (b) Scheme of the polarization states in the superlattice region: TM light with a finite interaction angle $\varphi>0$ is required to address the IMB transition with an electric field component $E_z \parallel z$ parallel to the growth direction. (c) Spectrally resolved IMB absorption of the hexagonal GaN/AlN superlattice with nominally 1.8 nm wide QWs separated by 5 nm wide barriers.

---

[49] The number of passes through the superlattice layer as well as the interaction angle will change as the incident light beam is tilted out of normal with respect to the incoupling facet.

Fig. 6.6(c) displays the results for the IMB absorption spectrum for photon energies between 0.5 eV (detector limit) and 1.0 eV. Specifically, this graph illustrates the average of many spectra recorded for different angles of up to ±20° away from perpendicular incidence on the incoupling facet. As supposed, a broad absorption centered at 0.76 eV is found. Most strikingly, the width of the IMB absorption that is determined by extracting the full width at half maximum (FWHM) of a Gaussian fit to the data, is as large as 260 meV. Previous experimental studies on similar hexagonal Al(Ga)N/GaN superlattices found typical IMB transition widths between 100 meV and 240 meV [TND06, HTL03, LHJ07, LBA15, LBA16]. Remarkably, the transition width of the present sample slightly exceeds this range. On the one hand, this increase can be attributed to a strong tunnel coupling between adjacent wells due to the narrow AlN barriers. Consequently, the energetic level splitting is increased and the resulting minibands are substantially broadened (cf. fundamentals of MQWs in chapter 6.1). On the other hand, a slightly grainy surface morphology is observed in AFM measurements (cf. Fig. 6.5(b)). This gives reason to assume that internal interfaces also suffer from roughness due to dislocations[50] and Al droplets that formed during the metal rich growth process. In turn, this condition leads to an increased scattering at internal interfaces that, again, causes a broadening of the IMB transition [Khu08, SBB16]. Furthermore, spatial fluctuations of the QW width by ±1 monolayer are expected to occur during the growth process. According to Eq. 6.2 the variation of the well thickness changes the energy levels within the QW and, therefore, shifts the central IMB transition energy. The total optical response of these spatial microscopic inhomogeneities is intrinsically recorded in the utilized macroscopic waveguide structure and, finally, leads to an increased inhomogeneously broadened absorption spectrum [KVM15].

The result from the experimental control measurements in combination with the simulation of a single QW validate the assumption of an inter-miniband transition with a central energy at ~760 meV in the present sample. The energetically lowest inter-band transition is to some extent reproduced by the CL and PL measurements. Optimized samples can be designed based on these results and eventually be grown for further analysis and application. More sophisticated simulations that incorporate proper material parameters (strain and built-in electric fields) may lead to more accurate estimations of the IMB transition energies prior to the fabrication.

---

[50] Although reflection high energy electron diffraction (RHEED) demonstrates rather streaky patterns during the growth of the AlN/GaN superlattice structure (indicating two-dimensional growth), these patterns are not homogeneous and, therefore, the superlattice has no perfect morphology.

Chapter 7

Ultrafast (Inter Miniband) Carrier Dynamics in a GaN/AlN Superlattice

Ultrafast optical applications based on electro-optical or all-optical devices are now widespread technology. The successful design of such devices, which are, e.g., based on inter-miniband (IMB) transitions in semiconductor heterostructures, requires the knowledge of the ultrafast nonlinear electronical and optical behavior. The speed and efficiency of potential applications is intrinsically connected to the timescales of the electron dynamics. Time-resolved spectroscopy provides an important insight to these electron dynamics of the involved transitions and, in addition, reveals electron relaxation times that are characteristic for specific scattering processes in the structure. By this means, the time-resolved spectroscopy technique grants information about the microscopic interactions, which are not readily observable. In general, the signatures of transient signals from the time resolved changes of the electronic system are a key to the substantial characterization of semiconductor heterostructures. Furthermore, it allows conclusions to be drawn about the quality and potential improvements of the manufacturing process.

In order to classify the present hexagonal GaN/AlN superlattice in the mentioned aspects, the ultrafast and nonlinear dynamical response of the quasi two-level inter-miniband (IMB) transition in the near infrared spectral range is analyzed in this chapter. For this purpose time-resolved, degenerate (single color) and non-degenerate (bi-color) pump-probe measurements are performed. The recorded transient signals for different laser wavelengths and light polarizations are analyzed and discussed. The focus is on the change of the transmission signal strength with respect to the wavelength and polarization combination of the pump- and probe beams. Furthermore, the lifetime of the optically excited electrons (from lower subband E_1 to upper subband E_2) in the upper subband E_2 are determined. The non-degenerate measurement using 800 nm pump-wavelength and resonant IMB probe-wavelength aims to identify the relaxation process from continuum “states” back to the quantified levels within the QWs of the superlattice. In the following chapter the principles of the time resolved pump-probe measurement technique are introduced and the experimental setup is outlined.

7.1 Time-resolved Pump-Probe Spectroscopy and Experimental Setup

While linear experiments provide only "static" information, the pump-probe measurement technique is one of the most important tools to investigate processes that occur on pico- and femtosecond time scales [Wei09]. The heart of a pump-probe experiment is a laser operating in pulsed mode. Mode-locked lasers are by far the most common source of ultrashort pulses, especially in the deep femtosecond regime, offering ultrafast time-resolved spectroscopy. One step further, attosecond physics already established itself in the ultrafast sciences and promises to advance a wide range of scientific time-resolved disciplines. Currently available laser sources cover a broad spectral range from soft X-ray up to the terahertz regime, granting access to a multitude of resonant and off-resonant excitation energies.

The central idea of the pump-probe measurement is to induce ("pump") a physical effect (non-equilibrium state) within the sample's electronic system and, subsequently, probe its temporal evolution. In the simplest case of such an experiment, the laser output is split and guided to the sample along two different paths without further modification. At the sample position, both beams[51] are spatially superimposed. The path length covered by one of the two pulse trains is variable, so that a precisely definable time delay $\Delta\tau$ can be set between the arrival of pulse A and pulse B. The first arriving intense "pump" pulse causes a change in the electronical and optical properties of the excited sample material. The second, much weaker "probe" pulse is used to detect this momentary pump-induced change. By varying the time delay $\Delta\tau$ between pulse A and B, a time-resolved signal is obtained. In many cases, the transient transmission, absorption or reflection are measured. However, other properties such as the refractive index or the polarization angle can be investigated in this way as well.

In the current situation of a GaN/AlN superlattice, the electron dynamics are analyzed by an optically induced change in the quasi two-level IMB electronic system leading to an altered light-matter interaction. The strength of the absorption in such a two-level system that resonantly interacts with photons is determined by the carrier occupation of the levels. Consequently, a higher transmission of the probe beam is directly related to the pump-induced carrier excitation from subband E_1 to E_2.

---

[51] In this context, the term "beam" refers to the train of ultrashort pulses emitted at high repetition rate, thus giving the impression of a solid beam.

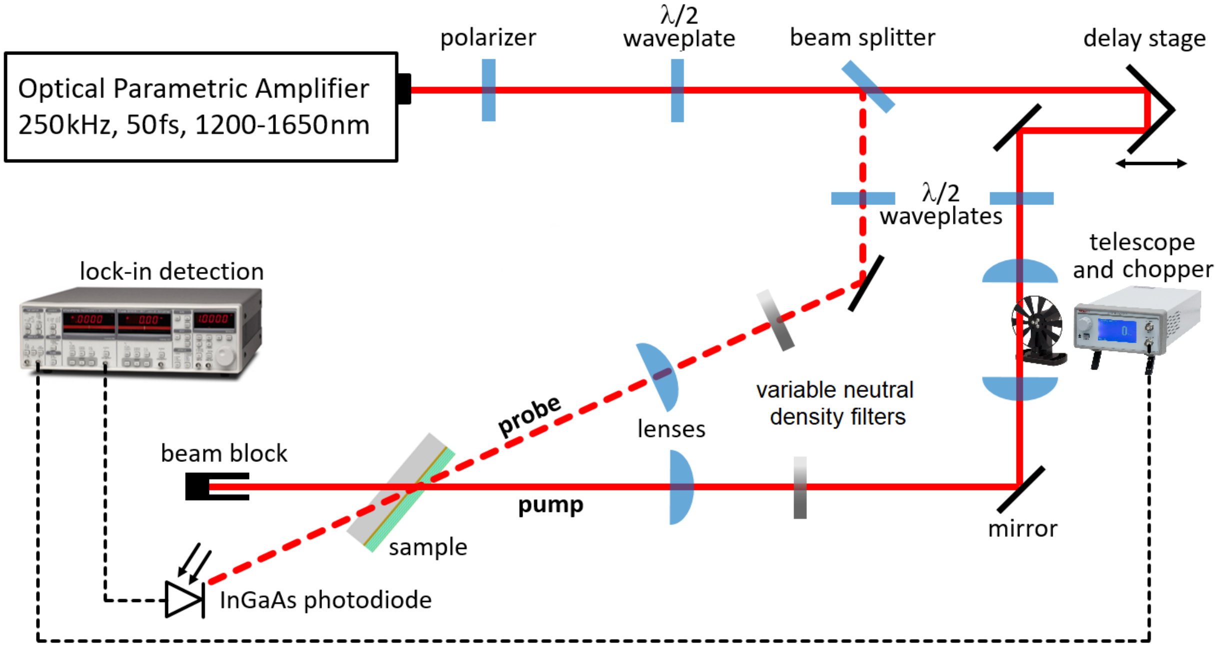

Fig. 7.1: Scheme of the optical pump-probe setup used for the time resolved measurement in single pass geometry. The pulsed output of the optical parametric amplifier is split and guided along the pump and probe arm until they are superimposed on the sample. The time delay is tuned by a motorized delay stage. Polarization optics allow to set the polarization state in each arm individually. The transient signal is recorded using lock-in detecting referenced with the pump modulation.

The heart of the experimental setup, schematically illustrated in Fig. 7.1, is a commercially available ultrashort pulse laser system. It relies on an optical parametric amplifier[52] (Coherent OPA 9850) that is seeded by an amplified titanium-sapphire laser[53] (Coherent RegA 9040). The OPA allows to tune the wavelength in a range from 1200 nm to roughly 1650 nm, whereby the upper limit matches the center of the IMB resonance (cf. Fig. 6.6(c)). One has to note that only the signal beam featuring the mentioned wavelength range is used, whereas the cross-polarized idler is blocked by a broadband linear polarizer. Depending on the selected wavelength, the average output power is in the order of a few tens of milliwatts. The OPA emits nearly transform-

---

[52] A portion of the input beam is used to generate a white-light continuum in a sapphire crystal which is then superimposed with the residual input beam in a beta barium borate (BBO) crystal. Spectral components that fulfill the phase matching condition contribute to the nonlinear frequency mixing. Taking into account the conservation of energy, two photons (signal and idler) are generated from the input photon.

[53] Passive modelocking is achieved using the optical Kerr effect: The laser beam experiences intensity-dependent focusing in the active medium, a titanium-doped sapphire crystal. An appropriate arrangement of the focusing optics in the resonator grants low losses for high-intensity components. Thus, the laser favors the gain of ultrashort pulses with high peak intensities [HW10].

limited[54] ≈50 fs (FWHM) and linearly polarized pulses at a repetition rate of $f_{\text{rep}} = 250\,\text{kHz}$. Typical timescales for carrier dynamics in semiconductors range from ≤100 fs (carrier-phonon and carrier-carrier scattering, cf. [Sha99] p.11 and p.135) to several ns (radiative inter-band recombination, cf. [Kli06] p.639). Within the repetition period of the laser system

$$T_{\text{rep}} = \frac{1}{f_{\text{rep}}} = 4\mu\text{s}\cdot \tag{7.1}$$

the investigated IMB transition is, therefore, expected to relax completely until the next pump pulse of the pulse train excites the sample again. This way, the pump-probe technique allows to average individual data points over an elevated period of time. The use of optical beam modulation (mechanical chopper, electro- or acousto-optic modulators) together with the lock-in amplification technique offers superior noise suppression, which makes pump-probe spectroscopy the method of choice for many time-resolved optical experiments featuring low signal strength. Typical lock-in integration times range from milliseconds to seconds. This leads to the beneficial lack of any necessity to meticulously resolve the pulse duration and repetition rate. A possible disadvantage concerning the investigation of long-term sustaining effects is the limitation of the maximum usable time delay by the repetition period of the selected laser.

In the case of the degenerate measurement, both pump and probe beams originate from the linearly polarized OPA output. To this end, a polarizing beam splitter cube (PBSC) divides this fundamental beam into the high-power pump and a low-power probe arm. The power ratio between both beams can be adjusted with a prefixed half-wave plate that tilts the linear polarization axis of the fundamental beam in front of the PBSC. The polarization states of each arm is set by an additional half-wave plate individually. Graduated neutral density (ND) filters allow to fine adjust both beams average power.

For the non-degenerate pump-probe measurement an additional beam splitter is installed in front of the OPA. This bypassed pulse train features a few hundred milliwatts of average power at the fundamental wavelength of 800 nm and serves as a new pump beam. In order to guarantee a high temporal stability without noise from timing jitter, i.e., the fluctuations of temporal pulse positions of consecutive laser pulses, one initial laser pulse from the regenerative amplifier is split into two fractions. In one arm the pulse undergoes a spectral tuning by the OPA while the other fundamental pulse remains unchanged. Finally, both beams are spatially superimposed at the sample.

To study the temporal evolution of the electronic excitation and relaxing process of the IMB transition, a motorized mechanical linear translation stage (Newport UTS50PP), hosting a pair of

---

[54] The minimum pulse width (so called “transform limited”) is inversely proportional to the spectral width as evident from the Fourier transform of a Gaussian wave packet.

orthogonal mirrors, is inserted in the pump beam path. Consequently, the time delay $\Delta\tau$ depends on the change of the optical path length Δx and is determined by the finite speed of light c:

$$\Delta\tau = \frac{\Delta x n}{c} \tag{7.2}$$

The time delay $\Delta\tau$ is defined in such a way that the pump pulse precedes the probe pulse for positive $\Delta\tau$ values. As all pump-probe experiments in this thesis are carried out in ambient conditions, the impact of dispersion is negligible ($n_{air} \approx 1$). Since the minimum incremental step size of the translation stage is in the order of one micrometer, the corresponding time delay features only a few femtoseconds. Consequently, the temporal resolution of this measurement technique is generally limited by the finite pulse duration, given by the laser system. As an example, the temporal resolution for two pulses with equal pulse duration t and a Gaussian shape in the time domain is determined by the convolution of both pulses that equals the $\sqrt{2}t$ at FWHM. Experimentally this time interval can be determined by a two-photon absorption measurement. The simplicity of the experimental setup combined with the high temporal resolution are a major advantage over other time-resolved measuring methods like, e.g., streak cameras based on elaborate and expensive electronics.

In order to adjust the beam diameter, the pump beam subsequently passes a pair of two convex lenses that form a telescope. It is favorable to adjust the spot sizes of both beams in such a way that the pump spot is at least twice as large as the probe spot. This way the area illuminated by the probe beam experiences nearly spatially homogenous pump intensity. Furthermore a small relative shift of both beams does not lead to a crucial decrease of the overlap integral. For the experiments presented in this part of the thesis, the spot sizes in the sample plane are adjusted to be roughly 30 µm for the probe and 60 µm for the pump beam (FWHM, measured with a commercial scanning slit beam profiler Thorlabs BP104-IR). Both beams are superimposed on the sample with a relative angle of ≈20°. (cf. Fig. 7.1). The beam configuration is chosen to be in a single pass geometry since the spatial and temporal overlap of both focused beams cannot be maintained properly in a waveguide structure. To achieve a large angle of interaction, the sample is tilted out of perpendicular incidence (angle of incidence[55]: $\varphi_{probe}=65°$ and $\varphi_{pump}=45°$), thus addressing the IMB transition for TM polarized light. Due to the strong refraction at the air-superlattice interface ($n_{GaN/AlN} \approx 2.2$ in the near infrared), the internal angle of interaction is reduced ($\varphi_{probe}=24°$ and $\varphi_{pump}=19°$). A signal contribution from the Al_2O_3 substrate originating from e.g. multi photon absorption is unlikely to disturb the investigated IMB electron dynamic since sapphire is a fairly transparent material offering a broad bandgap of 8.7 eV [PAP10].

---

[55] The Brewster angle of the given air-GaN/AlN interface is $\varphi_B \approx 65°$, referring to minimized reflection for p-polarized light (in this setup p-polarization corresponds to the TM polarization state).

After passing through the sample, the probe beam is again collimated and focused onto a biased InGaAs photodiode, while the residual pump beam is blocked. The photodiode's signal is monitored with a lock-in amplifier (Standford Research 830) utilizing two mechanical optical choppers (Thorlabs optical chopper) to modulate the pump or probe beam individually. In a first step, the pump beam is blocked and the modulated probe transmission signal T is recorded. Afterwards, the first chopper is switched off and only the pump beam is modulated with the second chopper. By detecting the probe signal referenced with the frequency of the chopper in the pump beam, it is then possible to observe pump-induced transmission changes ΔT of the probe beam. It is instructive to modulate beams at the highest applicable frequency as several sources of noise decrease with higher frequencies. Therefore, the mechanical chopper blade is installed in the focal plane of the telescope, allowing for a minimal slit size of the chopper blade and, thus, a higher chopping frequency[56]. Finally the normalized pump-induced transmission change ΔT/T is calculated and used for the evaluation process.

7.2 Degenerate Pump-Probe Spectroscopy

The pump-probe measurement is a widely used technique to investigate the temporal evolution of an excited system back to the equilibrium. The ultrafast and nonlinear optical response of the present GaN/AlN superlattice grants insight to the inter-miniband (IMB) electron dynamics that are crucially important for the design of optoelectronic devices like, e.g., artificial superlattice structures for quantum cascade lasers [GCS01]. The recorded transient transmission signals reveal the characteristic time scales of the relaxation processes. Both, an introduction to ultrafast pump-probe spectroscopy and to the utilized experimental setup are provided in the previous chapter.

In this section the IMB relaxation dynamics of electrons in the GaN/AlN superlattice are investigated by degenerate (single color) pump probe experiments using a pulsed laser system that emits spectrally tunable femtosecond laser pulses. The strength of the pump-induced alteration of the transmission signal that depends on the pump intensity, the wavelength and the polarization state of both beams is analyzed. In all of these experiments, an instant bleaching of the IMB transition is observed followed by a fast relaxation back to the equilibrium. The time-constants that are extracted from the recorded transient signals range in the 70fs regime.

---

[56] The modulation frequency must remain much smaller than the laser repetition rate.

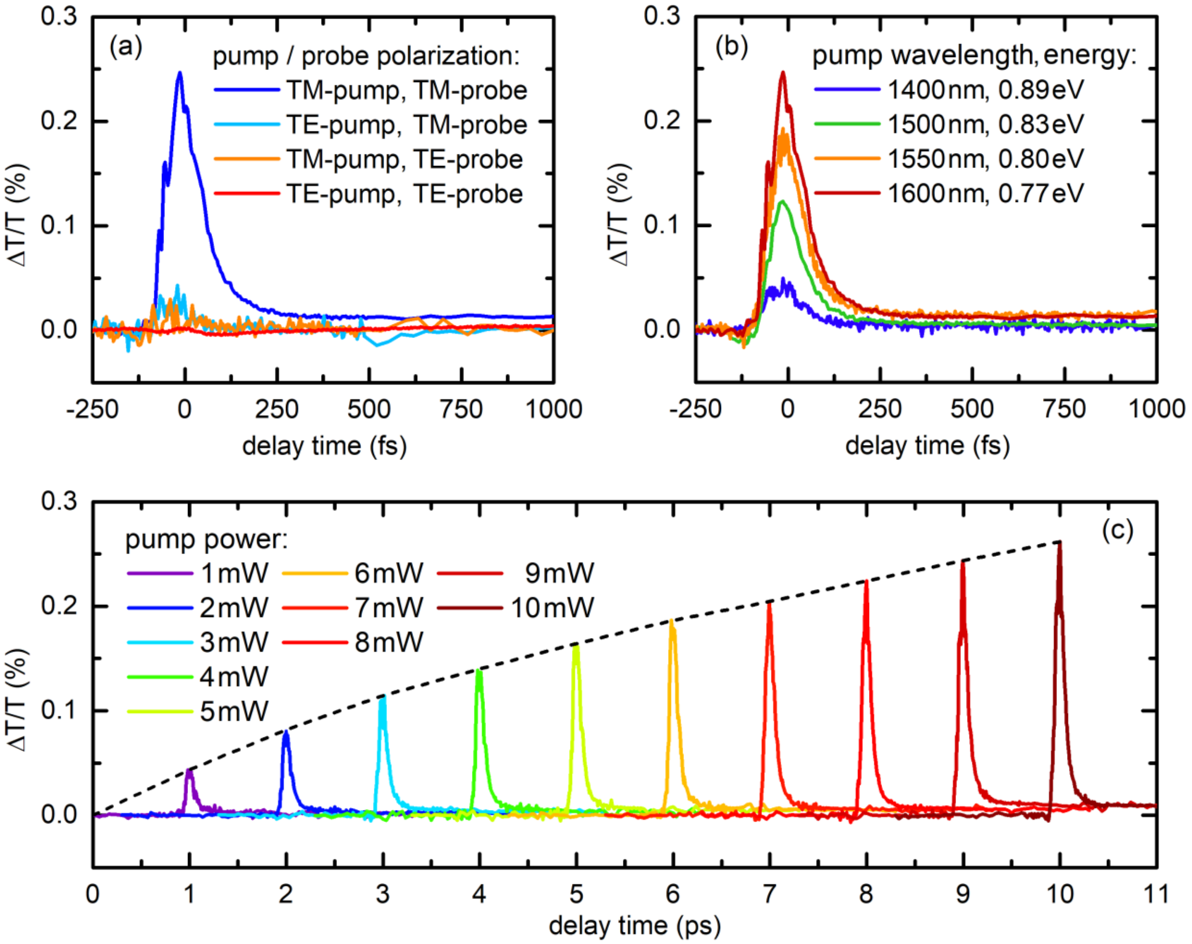

Fig. 7.2: Degenerate pump-probe transients for different configurations: Pump-induced change of the optical transmission $\Delta T/T$ through the superlattice (angle of incidence: $\varphi_{\text{probe}}=65°$ and $\varphi_{\text{pump}}=45°$). (a) Transient signals $\Delta T/T$ for all four polarization combinations of pump and probe beams at 1600 nm wavelength and constant 10 mW of average pump power (equivalent to 27 GW/cm² peak irradiance (pulse power)). (b) Transient signals $\Delta T/T$ for an altered TM polarized laser wavelength/photon energy and constant 10 mW of average pump power. (c) Evolution of the transient signal $\Delta T/T$ for increasing pump power and a constant TM polarized laser wavelength of 1600 nm (the recorded signals are shifted to the right by 1 ps each with respect to the previous data).

The recorded degenerate pump-probe transient signals are illustrated for different optical configurations in Fig. 7.2. The results for a polarization dependent measurement performed at the resonant excitation wavelength of 1600 nm[57] and 10 mW of average laser power (equivalent to 27 GW/cm² peak irradiance (pulse power)) are shown in panel (a). It is clearly visible from the

---

[57] The central wavelength of the Gaussian shaped OPA spectrum is 1600 nm referring to a central photon energy of 775 meV. The FWHM is ~90 nm (the bandwidth of a transform limited 50 fs Gaussian shaped pulse at 1600 nm calculated from the time-bandwidth product is 75 nm).

maximum height of all four curves that the IMB transition is addressed appropriately for TM polarized pump and probe beams only (dark blue curve). Mixed configurations of TE and TM polarized light beams lead to simply small but still visible signals. The same is valid when both beams are in the TE polarization state. The reason for this can be explained as followed: Scattering and refraction at surface roughness and undulated layers cause a fraction of the incident TE polarized beam to change its polarization angle. Therefore, a parasitic part of the electric light field is again oriented along the dipole moment of the IMB transition leading to the small but measurable light-matter interaction. Furthermore roughness partially permits otherwise forbidden transitions since the optical selection rules are somewhat relaxed [KVM15].

Regardless of the mentioned detrimental effect on the polarization due to sample imperfections, beams at normal incidence lead to only insignificantly small transient signals independent of the polarization states, as the amount of parasitic TM light addressing the IMB transition dipole becomes nearly negligible (data not shown).

When both TM polarized beams impinge out of normal incidence and the IMB transition is properly addressed (dark blue curve in panel (a)) the observed maximum relative transmission increase of $\Delta T/T=0.25\%$ can be attributed to a substantial Pauli[58] blocking of the probe transmission in the quasi two-level IMB system. Pauli blocking is often also referred to as saturation/bleaching of the absorption/transition, which is expressed as a reduced absorption coefficient with increasing light intensity (cf. Ref. [Men01] p. 514). The optical transmission of a resonantly excited two-level system is directly related to the electronic occupation of both states. Resonant optical pumping of the IMB transition by intense photon absorption leads to a strong depopulation of carriers in the lower miniband E_1 and, consequently, to a strong population in the upper miniband E_2. Subsequently, the absorption of additional probe photons is hampered due to the lack of occupied initial states in E_1 and free final states in E_2.

Taken together, all these findings from the polarization dependent measurement confirm the pump-probe transient signal to originate from the IMB transition in the GaN/AlN superlattice. The appropriate addressing of the IMB dipole moment that is oriented along the growth direction of the superlattice by TM polarized light is mandatory in order to profit from a strong light-matter interaction.

Furthermore, the knowledge of the spectrally resolved optical response of potential devices based on IMB transitions is a critical key for the overall performance and suitability. Therefore, the spectral dependence of the transient signal is analyzed to elaborate the electron dynamics for altered photon energies within the IMB transition range. For this purpose, the OPA is tuned

---

[58] Pauli blocking is a direct consequence of the Pauli exclusion principle that forbids indistinguishable fermions to occupy the same quantum mechanical state. Consequently, at least one relevant quantity (in semiconductors: energy, wave vector and spin) has do differ. The transition rate given in Fermi's golden rule is proportional to the density of initial (occupied) states in the lower level and the density of final (free) states in the upper level.

to several different wavelengths[59]. The experimental settings such as the TM polarization state, the angle of incidence and the average pump power of 10 mW remain unchanged to effectively drive the IMB transition. Systematically performed intensity autocorrelation measurements of the utilized laser system, conducted in previous studies, reveal negligible variations of the pulse duration by only a few femtoseconds over the whole spectral tuning range of the signal beam. Fig. 7.2(b) displays the transient pump-probe signals for different laser wavelength. As the photon energies move closer to the center of the IMB transition energy (~760 meV equivalent to ~1630 nm wavelength) the signal strength increases, strictly following the spectral dependence of the IMB absorption strength. The consistency of both, the linear absorption measurement (cf. Fig. 6.6(c)) and the nonlinear pump-probe experiment, confirm the presence of a wide IMB transition at telecom wavelengths in the actual superlattice structure. The extracted exponential decay times of the fast relaxation process do not show any significant fluctuations and range around 70 fs. This finding indicates fairly universal electron dynamics of the IMB transition within the investigated spectral range. A more detailed analysis of the decay process is outlined at the end of this chapter.

In a third series of measurements the pump power dependence of the probe absorption is investigated. For this purpose pump-probe transient signals are recorded for varying pump power and constant laser wavelength of 1600 nm. The results are shown in Fig. 7.2(c). Note that the evolution of the transient signal with increasing pump power is plotted using a continuous x-axis in such a way that the individual signals are shifted to the right by 1 ps compared to the previous data. The maximum height of the peaks is highlighted by the dashed envelope curve. Within the investigated pump power range this curve shows a distinct saturation behavior which indicates self-saturation of the pump beam. In other words, the absorption of pump photons from the trailing part of the laser pulse is hampered due to Pauli blocking generated by the leading part of the pulse. Consequently, the relative transmission of the single pump beam (I_{in}/I_{out}) is not constant but increases with the beam's power, eventually leading to the self-saturation phenomena. The pump-probe process is, therefore, not restricted to a third order nonlinear effect[60] but shifts to higher order nonlinearities. This light-induced nonlinearity is used in optical devices such as all-optical switches or saturable absorbers.

In addition to the above findings, the altered pump power does not have any significant influence on the electron relaxation dynamics/times or the overall temporal shape of the transients indicating a fairly universal IMB transition process.

---

[59] The spectral range of the OPA's signal beam does not cover the entire IMB-transition depicted in Fig. 7.5(c). The idler beam is not considered for the experimental study due to an insufficient beam quality.

[60] The optical response of a specific material is characterized by the light-induced polarization which is expressed as a power series of the electric field strength times the n-th order susceptibility tensor. Additional information are provided in chapter 8.1.1.

The application of the femtosecond pump-probe technology provides a fundamental understanding for the ultrafast electron dynamics in real time. The temporal evolution of the transient transmission change grants insight to the IMB electron transition processes and their respective time scales. For this purpose, the transient signal with maximum amplitude from Fig. 7.2(a), illustrated as dark blue curve is plotted again in Fig. 7.3, but in a semi-logarithmic scale. In addition to the main data, the intensity autocorrelation of pump and probe beam in a thin intrinsic GaAs waver is included (red dotted line). This signal originates from two-photon absorption and indicates the temporal convolution of both beams (cf. Ref. [Kli06] p. 710). The width of this signal provides the time resolution of the setup which is ~70 fs (FWHM). For this reason, sophisticated statements about the IMB electron dynamics and their respective decay constants have to exclude this nonlinear interaction phase of pump and probe during the time overlap. It is evident from the asymmetric transient that for delay times beyond 100fs a significant pump-induced change of the transmission remains present. This way the corresponding relaxation time constants can be determined confidently. The quantitative investigation of the decay process will, therefore, exclusively use the experimental results for $\Delta\tau > 100$ fs that can be clearly associated with changes in the electronic band occupation.

The pump induced transmission change begins to increase at $\Delta\tau \approx -100$ fs. At zero time delay (maximum temporal overlap) a pronounced peak value of $\Delta T/T = 0.25\%$ is reached. For positive time delays the signal starts to decrease exponentially and, eventually, vanishes almost completely for $\Delta\tau > 250$ fs. The exponential decay is governed by the rapid relaxation of electrons back into the lower miniband E_1. For a quantitative analysis, electron decay times are extracted from the decaying transient signal using a multi-component exponential decay fit function[61]

$$F(t, t_0) = \sum_i a_i e^{-(t-t_0)/\tau_i} \tag{7.3}$$

where a_i and τ_i correspond to the signal amplitude and lifetime of the i-th decay process, respectively. The extracted characteristic time constant of the fast electron relaxation of $\tau_1 \approx 70$fs is found to be below values reported in literature (130-370 fs) for similar GaN/Al(Ga)N MQW structures featuring ISB transition energies between 700 meV and 800 meV [GFN01, HGN02, IKS04, HMK04, NTJ06]. Theoretical predictions for the ISB electron relaxation calculate electron scattering times with longitudinal optical (LO) phonons of ~100 fs [SI98, GFN01, HGN02]. This is the dominant relaxation channel in (quasi) two-dimensional heterostructures. As a reminder, this value is some orders of magnitude smaller than that of band relaxation processes. On one hand the present experimental setup profits from an improved temporal resolution due to the fairly

---

[61] In general the whole observed signal is approximated by the convolution between the pump-probe correlation and the decay function [LYZ04]. To simplify the data processing, however, only the decay function is fitted to the transient signal using data points outside the temporal autocorrelation range.

low pulse duration of only ~50 fs. On the other hand, scattering at internal layer roughness may enhance the carrier relaxation process (cf. chapter 6.3). Both effects lead to a somewhat reduced electron decay time compared to literature data. Nevertheless, the ultrafast electron relaxation in the present GaN/AlN superlattice has reached the limit of the temporal resolution and further research has to overcome this boundary. But nevertheless, much smaller relaxation times are not expected to be found since the LO-phonon scattering remains the dominant decay channel.

After the excitation, the carriers rapidly relax and the transient signal returns practically to the baseline level. For delay times beyond 250 fs the semi-logarithmic representation of the data reveals an additional decay channel of the residual signal. The extracted time constant of $\tau_2 \approx 15$ps can be attributed to the thermalization of the excited electron ensemble, generally occurring on picosecond timescales [GFN01, HGN02]. To distinguish between both decay channels, the IMB transition has to be reconsidered in the **k**-space (cf. Fig. 6.2(b)). The leading fast decay channel represents IMB relaxations with equal $k_\perp$ in the initial und final state (vertical transition in the **k**-space). The following slow decay process involves an additional interaction with a phonon to compensate for deviating wave vectors in both states. In this picture, the thermalization of the system describes the relaxation of carriers to the Γ-point. The recombination of electrons and holes across the IMB gap finally returns the system to its initial thermal equilibrium state.

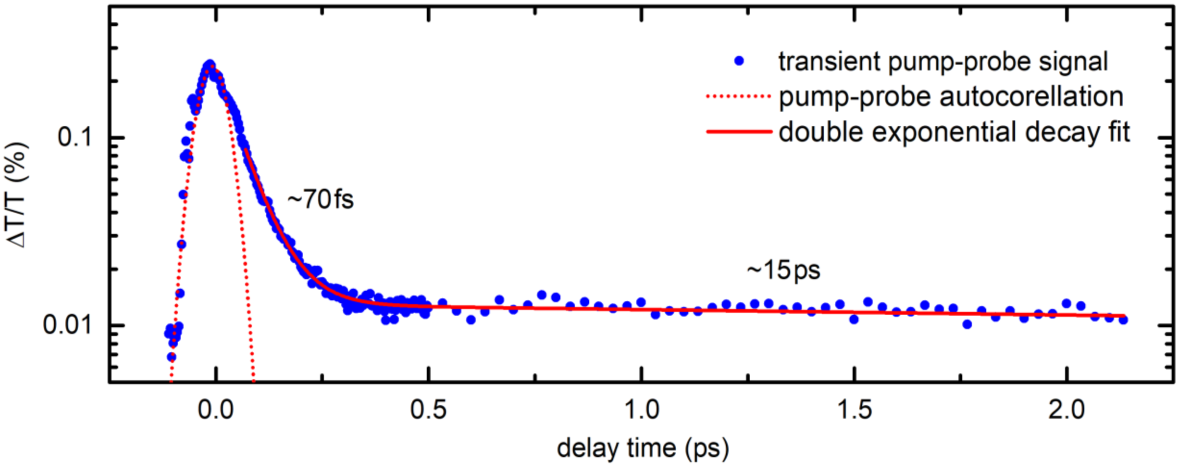

Fig. 7.3: Pump-probe transient signal ΔT/T for TM polarized laser wavelength of 1600 nm and 10 mW of average pump power (blue dots). The red line illustrates a double-exponential decay fit to the data. The red dotted line shows an intensity autocorrelation of pump and probe beam in a micrometer thin intrinsic GaAs waver that indicates the temporal overlap (convolution) of pump and probe beam.

7.3 Non-Degenerate Pump-Probe Spectroscopy

The ultrafast pump-probe measurement technique correlates the electronic properties of a material with its characteristic optical response. In addition to a single color measurement, non-degenerate (bi-color) pump-probe spectroscopy can provide supplementary information about the carrier flow between different energy states. As already described in chapter 7.1, the experimental setup has to undergo a small adjustment to be used in the non-degenerate measurement scheme. In order to achieve a high temporal stability without noise from timing jitter, the fundamental pulse train from the regenerative amplifier is split and guided to the sample on two different paths. In one arm of the setup the probe pulse undergoes a spectral tuning by the optical parametric amplifier (OPA) while the other fundamental pump pulse remains unchanged at ~800 nm central wavelength / 1.55 eV central photon energy. This excitation energy greatly exceeds the IMB transition energy and even addresses continuum states outside the QW confinement (cf. Fig. 6.1(b) and Fig. 6.3(b)). Furthermore, bound-to-continuum transitions are energetically benefited to one side of the asymmetric QW (cf. Fig. 6.3(b)). The transition of electrons into the continuum is always accompanied by electronic excitation into the first subband E_2 at a higher k vector, thus the excitation density is not very well known. Additionally, the built-in electric field breaks the potential symmetry and somewhat allows ISB transitions from the ground state E_1 to the second excited state E_3 (assuming this is present in the current QW) [HSH02]. In general, the dipole moment features only vanishingly small oscillator strength for an E_1 to E_3 intersubband transition. Interband transitions involving excitations from hole states in the valance band to electron states in the conduction band require even larger photon energies (>3.5 eV) and are, therefore, not addressed at all. This also applies to interband two photon absorption. Just as a reminder for the time-resolved measurements, both beams feature a ~50 fs pulse duration so that the time resolution of the setup is still ~70 fs. All other experimental settings remain unchanged.

The investigation is performed in analogy to the previous chapter involving single color pump probe measurements. It is recommended to get at least a quick overview of chapter 7.2 before proceeding with the non-degenerate study, if not already done. As before, the pump pulse strongly perturbs the system from equilibrium and the time-delayed weak and spectrally tunable probe pulse measures the photo-induced change in the transmission through the sample.

The recorded non-degenerate pump-probe transient signals are illustrated for different optical configurations in Fig. 7.4, 7.5 and 7.6. Panel (a) in Fig. 7.4 shows the results for a polarization dependent measurement performed at 800 nm pump wavelength and 100 mW of average pump laser power (equivalent to 270 GW/cm² peak irradiance (pulse power)). The transmission change ΔT/T is probed at the resonant IMB transition wavelength of 1600 nm. The proper addressing of the IMB transition dipole is again restricted to TM polarized probe light (blue curves). In this case a high pump-induced change in the probed transmission of up to ΔT/T = 1.5% is observed. The intense pumping of the electronic system leads to a strong depopulation of carriers in the lower miniband E_1. Consequently, the absorption of additional probe photons is hampered due to the lack of occupied initial states in E_1 leading to an increased probe transmission. On the other hand, a TE polarized probe only leads to small detectable transient signals that originate from a minor portion of parasitic TM light introduced by sample imperfections due to roughness and undulated layers (orange and red curve). The maximum strength of these two signals in turn is more or less independent of the pump polarization state. This can be explained as follows: In comparison to the previously performed degenerate measurements at telecom wavelengths, the higher pump photon energy allows carriers to be excited to continuum states above the confined energy levels of the QW (cf. Fig. 6.1(b)). In this picture the continuum can be considered as a continuous above-barrier band featuring a parabolic 3D energy dispersion. These bound-to-continuum transitions show, in contrast to the restrictive bound-to-bound IMB transitions, way more relaxed selection rules. This fact makes the excitation of the electrons into the continuum much more independent of the pump polarization. Also, this circumstance legitimates, at a first glance, the fairly strong transient signal strength for a TE pump in combination with a scanning TM probe beam at IMB resonance (light blue curve).

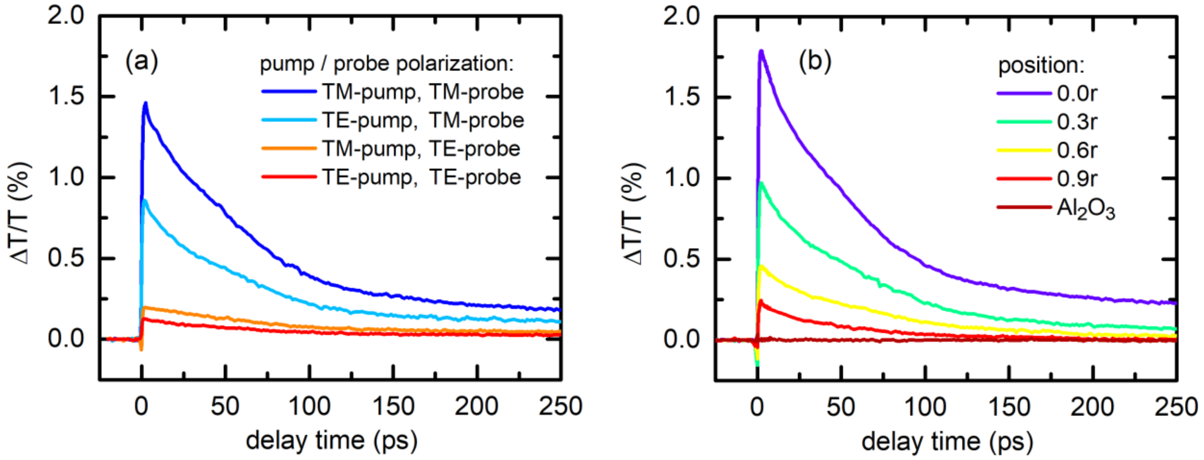

Fig. 7.4: Non-degenerate pump-induced (800 nm) change of the optical probe (1600 nm) transmission ΔT/T: (a) Transient signals for all four polarization combinations of pump and probe beams at constant 100 mW of average pump power (27 GW/cm² peak irradiance). (b) Transient signals for different investigated positions on the 2 inch Al_2O_3 wafer (0.0 r equals the center of the wafer). Both beams are TM polarized and the average pump power is set to 100 mW.

The intensity of the recorded time-resolved signals can provide further information about the quality of the superlattice. Here, the term quality refers to the accuracy of the growth process regarding sample imperfections as well as deviations from the geometrical target values of the QWs. Therefore, in addition to the measurements carried out in the previous chapter, transient signals are recorded for different TM-polarized laser spot positions on the 2 inch substrate wafer carrying the superlattice. This spatially resolved analysis is illustrated in Fig. 7.4(b) and shows a strong dependence of the signal strength on the radial position (0.0 r equals zero radial displacement from the center). The signal intensity continuously decreases when the investigated position approaches the edge of the wafer. Finally, the transient signal vanishes completely at the outer area on the wafer that does not contain any superlattice because it was covered by a clamping holder during the molecular beam epitaxy process. This excluded zone refers to the Al_2O_3 substrate only, which does not show any significant nonlinear optical response. Consequently, the strong transient signals (especially in the center region) can be clearly attributed to an altered occupation of the electronic system in the superlattice structure. The observation correlates with the results from room-temperature cathode luminescence (CL) measurements where an equivalent spatial gradient of the signal strength is present. The cause can be attributed to a radial non-uniformity of the plasma density and substrate heating during the fabrication process (cf. Fig. 6.5(c)). According to this findings one has to assume a certain deviation of the MQW's structure with far-reaching impact on the electronic system over the whole wafer. Beside a deviation from the intended geometrical parameters of the QW, that shifts the ISB transition energy, roughness, dislocations and the formation of aluminum droplets show an impact on the absorption strength. As all previous measurements involve only the center position on the wafer, the further experimental analysis is also carried out at this position.

In the next step of the investigation, the spectrally resolved optical response of the highly excited GaN/AlN superlattice is analyzed. For this reason the wavelength of the probe beam is gradually tuned using the entire spectral range offered by the OPA's signal beam. Fig. 7.5(a) shows the recorded transient signals. In agreement with the degenerate measurement the signal drops significantly as the probe wavelength is tuned away from the center of the IMB resonance. This behavior is illustrated in panel (b) which shows the maximum $\Delta T/T$ depending on the probe beam's photon energy. The obtained data points nicely cover one wing of the IMB resonance that is depicted as a Gaussian fit featuring a central photon energy of 760 meV and a width of 260 meV (FWHM). These values are taken from the experimentally determined IMB resonance depicted in Fig. 6.6(c). One last remark about the slight discrepancy regarding the maximum observed $\Delta T/T$ compared to the previous measurement in this chapter: Small deviations between sets of measurements typically originate from (minor) lateral shifts of the laser spot positions. Sample imperfections and sweet spots featuring distinctive optical responses can certainly cause a $\pm 10\%$ change of the transient signal strength. Definitely, the proper spatial overlap of the pump and probe beams is ensured in all measurements.

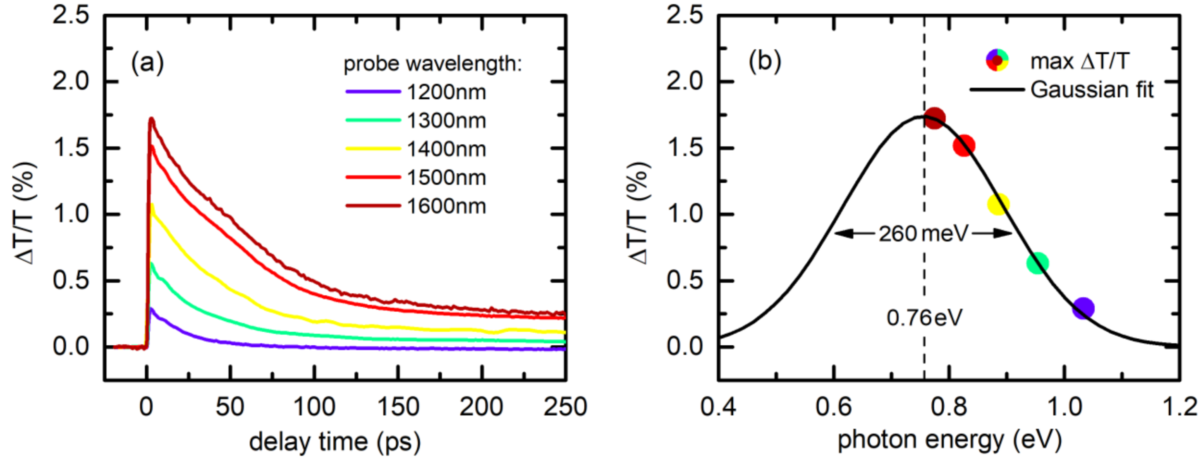

Fig. 7.5: Non-degenerate TM pump-induced (800 nm) change of the optical TM probe transmission ΔT/T: (a) Transient signals for altered probe laser wavelength and constant 100 mW of average pump power. (b) Maximum ΔT/T for each probe wavelength/phone energy, extracted from panel (a). The central energy and width of the Gaussian fit are taken from the experimental findings in Fig. 6.5(c).

In another series of measurements the nonlinear light-matter interaction is analyzed by a variation of the pump power. Transient signals are recorded for average laser powers between 1 mW and 100 mW and are illustrated in Fig. 7.6(a). The probing occurs at 1600 nm, i.e., resonant to IMB transition. The maximum transmission change of each curve (at approximately zero time delay) is extracted and plotted versus the pump power in panel (b). Within the investigated power range the data points follow a linear fit to the data without any sign of saturation. In comparison to the resonant IMB excitation (cf. Fig. 7.2(c)) the transition into the continuum offers a wider range of final states within the 3D parabolic energy band. Self-saturation of the pump beam due to Pauli blocking is, therefore, not observed to this extent here. Irrespective of these findings, in both series of experiments the maximum transient signal strength ΔT/T at 10 mW pump power reaches similar values of 0.25% for the degenerate and 0.22% for the non-degenerate measurement, respectively. The amount of excited charge carriers is therefore comparable, whereas the resonant IMBT is still beneficial at least at low pump powers.

In contrast to the measurements presented in chapter 7.2, however, the transient signals now exhibit a change in curvature at a time delay of ~50 ps, which is particularly visible at elevated pump powers (cf. Fig. 7.6(a)). This observation is an indication of a more complex multi-stage relaxation process upon extensive pumping. Above the threshold of 50 mW the observed perturbation is no longer negligible concerning the quantitative analysis based on the multi-exponential decay with equal τ_0 introduced in Eq. 7.3. On the other hand, a back-reflection of the pump beam eventually exciting the sample again at ~50 ps time delay can be excluded since the fingerprint of such a disturbing back-reflection is a weak copy of the initial peak at zero delay time but temporarily shifted to the decaying branch. Such a sharp spike is not observed at all.

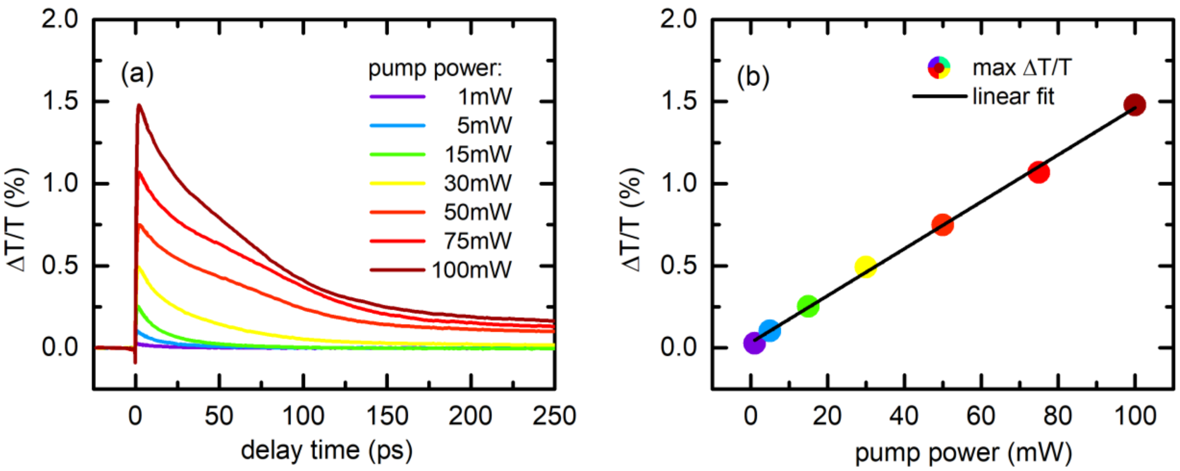

Fig. 7.6: Degenerate TM pump-induced (800 nm) change of the optical TM probe (1600 nm) transmission ΔT/T: (a) Transient signals for altered pump laser power. (b) Maximum ΔT/T depending on the pump power, extracted from panel (a).

In order to fully benefit from the time-resolved measurement technique, the recorded transient signals that are shown in Fig. 7.6(a) are now analyzed in the time domain and the individual decay times are extracted. The goal is to get an insight into the electron relaxation process occurring upon the bound-to-continuum photoexcitation. The transient signals for different pump powers are recorded using the full travel range of the mechanical delay stage. Fig. 7.7(a) illustrates a part of the dataset in a semi-logarithmic diagram including the determined relaxation constants τ_1 (left) and τ_2 (right), respectively. They are presented separately in panel (b) and (c). As stated before, above 50 mW of average pump power the transient signals exhibit a clearly visible change of the curvature at around 50 ps delay time. Therefore, the recorded signals deviate from a pure bi-exponential decay scheme and are not considered for the quantitative analysis. However, the question of the origin of this observation remains since no conclusive explanation can be given at this time.

Taking a closer look at the extracted electron decay times in panel (a) and (b) a plateau in the lower pump power regime featuring approximately constant $\tau_1 \approx 8$ ps and $\tau_2 \approx 30$ ps times becomes visible. It is followed by an eye-catching (exponential) increase of the relaxation times originating from an alteration of the electron decay process at elevated pump powers. The question that arises now is two-fold: (i) What is the background to the significantly increased relaxation times occurring at higher excitation photon energies and (ii) what is the reason for the drastic change in electron dynamics at elevated pump powers? In the following section of the evaluation the electron dynamics of the relaxation process are discussed and potential descriptions for the observations are provided. However, a proper explanation cannot be provided up to date and the explanations are more of a prototypical nature.

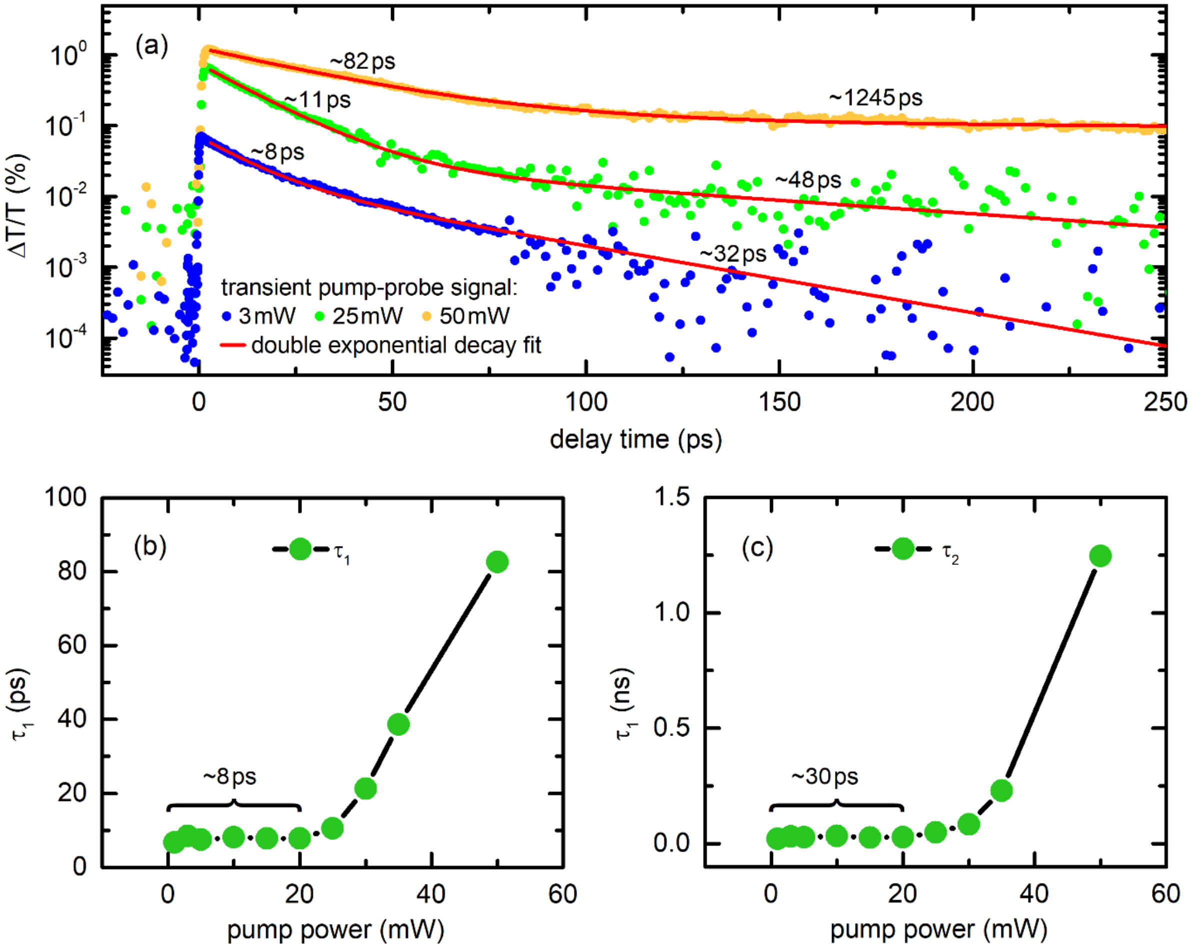

Fig. 7.7: (a) Degenerate pump-probe transient signal ΔT/T for TM polarized 800 nm pump and 1600 nm probe laser wavelength for three different average pump powers. The red lines illustrates double-exponential decay fits to the data. (b) and (c) illustrate the extracted electron relaxation times τ_1 and τ_2 from panel (a).

Excited carriers in the continuum above the barrier edge are eventually captured into the bound states within the QW by a combination of several competing relaxation processes [MHL97]. The decay channels include electron-electron or Auger collisions. This scattering channels refer to a thermalizing process on (sub-)picosecond timescales that do not contribute to a net energy loss of the excited electron gas, leading to extended overall decay times. The final capture into a quantum-confined state is typically mediated by the emission of longitudinal optical (LO) phonons [AFB12, EWP18]. It is an energy-loss mechanism that occurs on sub-picosecond time scales. On the other hand, potential relaxation via acoustic phonon scattering happens on timescales of several hundred picoseconds.

Usually the hot electron relaxes by LO phonon scattering into a low k vector continuum state. From here, it can be scattered efficiently into the confined ground state via the interaction with an acoustic or LO phonon. The direct scattering from the continuum state at k=0 into the confined E_1-level by a LO phonon is, in general, not allowed considering energy and momentum conservation laws [AFB12]. Due to this circumstance, the relaxation pathway is at least a two-step decay process that may be hampered by the absence of resonant phonon modes. Inhibiting the relaxation processes between the involved energy levels lengthens the time scale for the thermalization to many picoseconds and even nanoseconds. The result is a long sustaining hot electron distribution with extended decay times compared to the fast IMB transition. The phenomenon can be classified as the so called phonon bottleneck[62] [AFB12, EWP18].

Additionally, optically excited electrons in the 3D energy dispersion of the continuum may be scattered into other above-barrier continuum states with different lower or higher k-wave vectors via interaction with a phonon. This way the coupling with the surrounding continuum may lead to a finite escape probability of the excited electrons from the non-localized energy states above the QW (thermal escape) [AFB12] eventually leading to strongly increased relaxation times. Moreover a net current flow along the tilted potential landscape of the superlattice is possible. This might not only happen above the barrier level but also via a cascade transfer to adjacent QWs [GCS01]. This is basically how a quantum cascade laser works: The quantized energy levels of adjacent QWs are aligned with each other in such a way that electrons can tunnel from a low energy level of one QW to a high energy level in another neighboring QW. Then the energy difference between the high and low energy levels can be emitted in the form of photons and the process repeats.

Another rather delicate consideration regarding the addressing of states in the continuum should be mentioned here: The so called bound states in the continuum (BSIC) are spatially confined states with infinite lifetime spectrally overlapping with lossy states in the continuum [Bas84, PW93, WP94, VG05, AFB12]. Typically these bound or quasi-bound states are embedded in the energetically higher continuous part of the spectrum above the confinement of exotic potentials. The relatively long relaxation lifetime results from the absence of coupling between the excited state and the surrounding continuum in addition with a temperature-dependent escape probability (thermal scattering). Recent studies show that quasi-bound states exist not only for exotic / complex quantum systems, but also for typical (rectangular) potential landscapes [VG05]. The existence of BICS above different types of quantum structures has been discussed for decades along with their implementation in photonics systems. Still the fundamental nature of this unusual and robust type of solutions is unanswered.

To sum up briefly, electron-electron or Auger collisions are most likely to sustain a hot electron distribution that eventually relaxes by a multi-stage phonon scattering process which in turn might be hampered by a phonon bottleneck, thermal and cascade-type escape.

---

[62] In general, a phonon bottleneck describes the existence of a non-equilibrium phonon distribution, typically exhibiting a large imbalance in the density of optical and acoustic phonons. It inhibits the dissipation of LO phonons leading to the re-absorption of LO phonons which, in turn, facilitates a sustaining hot carrier distribution [EWP18].

Chapter 8

A Nonlinear Metasurface Based on a Superlattice and Plasmonic Antennas

Frequency conversion processes such as second-harmonic generation (SHG) are integral to nonlinear optics, which is the bedrock of modern photonic science and technology. The wide field of application covers e.g. the generation of coherent ultraviolet light [MTV16], supercontinuum light generation [KGW16], nonlinear spectroscopy [GBS12], the generation of entangled photon pairs[63] [BCZ10] and many more. Specifically, SHG has found extensive everyday applications from handheld laser pointers to spectroscopic and microscopic analysis techniques. The nonlinear response of naturally occurring materials is inherently weak such that, e.g., phase-matching techniques [ST12, Boy20] are required to realize a significant nonlinear response. Therefore researchers are currently targeting the synthesis of novel materials that generate a substantial nonlinear response even from thin layers [Khu14, ZYS16, LTA14]. This approach would eliminate the requirement for sophisticated phase matching techniques as the necessary crystal thickness shrinks below the coherence length (intrinsic length of phase matching, c.f. Eq. 8.3). Additionally, plasmonic metasurfaces offer a large potential for nonlinear optical interactions. They combine deep-subwavelength thickness with the possibility to engineer the shape of these structures to resonantly enhance the light-matter interaction at certain frequencies. It is strongly desirable to combine plasmonic structures with semiconductor-based materials to further enhance the nonlinear susceptibilities [LTA14, NZ16]. Doped quantum well (QW) [NTJ06] and doped multi-quantum well (MQW) structures [YLZ14] are particularly suited to tailor the nonlinear optical response in the infrared wavelength range. By proper choice of the material combinations and well widths, intersubband transitions (ISBTs) can be quantum-engineered to match certain desired optical frequencies in the telecom regime. At the same time, MQW structures can feature a broken inversion symmetry required for SHG [KTA18]. However,

---

[63] Quantum entanglement occurs when particles (e.g. photons) are generated, interact, or share spatial proximity such that a common description of the unified quantum state of this group of particles is necessary.

the excitation of ISBTs requires vertical (z-polarized) electric field components that are absent, e.g., for free-space illumination at normal incidence (consult chapter 6.3 and especially Fig. 6.6 for further information). Therefore, a combination with plasmonic structures that partially convert normally impinging light into such z-polarized components in the MQW volume is particularly beneficial. The local field enhancement at plasmonic elements of up to 10^3 [BSF15], corresponding to a local intensity increase of six orders of magnitude, favors the observation of nonlinear optical effects. Lee et al. [LTA14] have demonstrated record-high levels of SHG efficiencies at such ISBTs by functionalizing AlGaAs/GaAs heterostructures with antenna arrays featuring resonances for both fundamental (ω) and second harmonic (2ω) frequencies. Tuning this concept to the more practical near-infrared regime requires the use of compounds with larger band offsets and narrower QWs. Group III-nitrides are a good platform to meet these requirements as a GaN/AlN heterojunction offers a conduction band offset (CBO) of ~2 eV [MBR96]. Wolf et al. [WAM15] have demonstrated enhanced SHG efficiencies for fundamental radiation around 3.5 µm based on this material system in combination with resonant plasmonic resonators. However, tuning to shorter wavelengths is hampered by the finite depth of the potential in the conduction band. A strong confinement in ultranarrow GaN/AlN QWs can partially compensate the lack of high CBOs of available heterojunctions and finally shift the ISBTs to telecom wavelengths.

In this part of the thesis, a nonlinear metasurface based on ISBTs in ultranarrow GaN/AlN MQWs operating with resonant plasmonic antennas in the telecom range is investigated. The GaN/AlN superlattice was already introduced in the previous chapters and the ISBT was extensively analyzed by optical means. Taking advantage of a waveguide structure, linear transmission measurements reveal a broad ISB absorption centered at 0.76 eV. Remarkably, the width of the absorption is as large as 260 meV (FWHM) offering a huge potential for resonant plasmonic interaction (cf. Fig. 6.6). Subsequently the superlattice is functionalized with an array of plasmonic antennas featuring cross-polarized resonances at near-infrared wavelengths and their second harmonic. This kind of nonlinear metasurface allows for substantial second harmonic generation at normal incidence which is completely absent for an antenna array without the heterostructure underneath. While the second harmonic is originally radiated only into the plane of the QWs, a proper geometrical arrangement of the plasmonic elements permits to redirect the second harmonic to free-space radiation, which is emitted perpendicular to the surface.

In the next chapter a brief introduction to nonlinear optics and plasmonics is provided. It is followed by a presentation of the investigated metasurface including the sample preparation process and basic characterizations of the plasmonic elements with optical and computational means. Chapter 8.4 discusses the nonlinear response of the metasurface based on optical harmonic generation. The main focus is on the observation of SHG and its critical dependence on the antenna spacing. Parts of chapter 8 have already been published in Ref. [MSJ21].

8.1 Introduction to Nonlinear Optics and Nanoplasmonics

8.1.1 Nonlinear Optics

The current chapter provides a brief introduction to the fundamentals of nonlinear optics. The focus lies on one of the most important and prominent nonlinear optical phenomena: the generation of the second harmonic (SHG). SHG was first demonstrated by the research group around Peter Franken at the University of Michigan in 1961 [FHP61]. The observation[64] was made possible shortly after the invention of the laser, which was necessary to create the required high intensity coherent light. The zoo of nonlinear optical effects can be roughly divided into two groups: frequency-mixing processes and other nonlinear processes that rely on the nonlinear response of material properties such as the refractive index (Kerr effect). All these various nonlinearities have led to a large number of developments of novel laser light sources and measurement techniques [HW84, Sha77]. In particular, SHG is forbidden for bulk media with inversion symmetry via the leading order electric dipole contribution (in contrast to the third harmonic generation[65] (THG)). In turn, the broken symmetry at surfaces and interfaces allows for SHG and discriminates against signals from the bulk material. Therefore, SHG and also sum frequency generation are implicitly referred to as surface-specific analysis techniques (for inversion-symmetric materials). The pump-probe technique presented in the previous chapters is another example of nonlinear light-matter interaction since the pump-induced change of the material properties subsequently alters the probe-matter interaction.

From the linear wave equation, one can see that the interaction between the light and the medium is given by the electric light field $\boldsymbol{E}$ and the dielectric polarization density $\boldsymbol{P}$. The polarization generated in the medium can be seen as a response to a light field:

$$\boldsymbol{P} = \varepsilon_0 \chi \boldsymbol{E} = \varepsilon_0 (\varepsilon - 1) \boldsymbol{E} \tag{8.1}$$

Here, ε_0 is the vacuum permittivity and the (scalar) susceptibility χ, which also refers to as dielectric function, describes the strength of the interaction. This linear expression is only valid for weak light intensities where the properties of the material remain unchanged. This holds true

---

[64] Unfortunately the copy editor of the journal mistook the dim SHG spot (at 347 nm) on the photographic paper as a speck of dirt and removed it from the publication in Physical Review Letters [FHP61].

[65] THG is a volumetric process but can be enhanced at interfaces [CX02].

for everyday phenomena like absorption/transmission or reflection that depend on the frequency and polarization of the incident light irrespective of the (weak) intensity. For strong light fields (typically in the range of the atomic electric fields around 10^8 V/m), this relation must be described by a nonlinear rapidly converging Taylor series expansion

$$\boldsymbol{P} = \epsilon_0 \sum_{n=1}^{\infty} \chi^{(n)} \boldsymbol{E}^n \tag{8.2}$$

where the coefficients $\chi^{(n)}$ are the n-th order susceptibility tensors of the medium [Sut03]. The presence of such a term is generally expressed as an n-th order nonlinearity. Since the susceptibilities drop drastically with increasing order, strong light fields are required to observe higher order nonlinear processes. Typically, the second-order susceptibility takes values around 10^{-10} cm/V, whereas the third order susceptibility can be found at around 10^{-17} cm²/V² [Web03]. For example, SHG is a $\chi^{(2)}$ process, since the power of the generated second harmonic depends quadratically on the fundamental input power. THG, Self-focusing and two photon absorption (TPA) are related to the third order nonlinearity. TPA describes the simultaneous absorption of two photons with identical (degenerate) or different (non-degenerate) photon energies. The TPA excitation probability from a ground state to a higher energy state is proportional to the square of the light intensity. Typically the absorption cross section of TPA is several orders of magnitude smaller compared to the one-photon absorption cross section.

Considering only the leading nonlinear term of the polarization (so called second-order polarization) of Eq. 8.2, the presence of two different electric fields with the frequencies ω_1 and ω_2 leads to an expression that contains, among others, contributions with the sum frequency $\omega_{SFG}=\omega_1+\omega_2$, as well as a difference frequency $\omega_{DFG}=\omega_1-\omega_2$. For the case of two equal incident frequencies the sum frequency becomes the second harmonic $\omega_{SFG}=\omega_{SHG}$. For the generation and annihilation of photons conservation of energy and momentum must be ensured. The most challenging part is the realization of the phase matching (momentum), since dispersion in the medium causes a phase mismatch $\Delta k \neq 0$ due to the wavelength-dependent refractive index. The fulfilment of the perfect phase matching condition $\Delta k=0$ means that the electric field strengths and the nonlinear polarizations have a persistent phase relation while propagating through the medium. Consequently the SHG power is growing in proportion to the square of the propagation distance. To achieve phase matching condition to some extent, several methods like birefringent phase matching[66] or quasi-phase matching[67] technique [ST91] are implemented in many light

---

[66] The tuning range of the three-wave process is further restricted from the transparency range of the nonlinear medium to the range of phase matching by birefringence. Due to the walk-off effect, the increasing spatial separation of the beams leads to a lower conversion efficiency.

[67] In quasi-phase matching, the relative phase of the waves can be corrected by a periodical structuring of the crystal in the form of antiparallel polar domains, while avoiding the disadvantages of birefringent phase matching.

conversion setups. Without proper phase matching the efficiently usable length of the nonlinear crystal thus shrinks to the size of the coherence length:

$$l_{\text{koh}} = \lambda_{\omega}/4|n_{2\omega} - n_{\omega}| \tag{8.3}$$

For the present GaN/AlN MQW system at $\lambda_{\omega}=1600\,\text{nm}$ the coherence length ranges somewhat between $10\,\mu\text{m}$ and $65\,\mu\text{m}$ with respect to the different refractive indices and the birefringent character of the material. Reducing the dimensionality of a nonlinear media thus eliminates the requirement for a sophisticated phase matching technique as the crystal thickness remains below the coherence length.

Furthermore, due to the finite time-bandwidth product a broadband spectrum occurs as the pulses duration decreases [DR06]. Consequently, an optimal phase matching for all spectral components in thick bulk material cannot be achieved. For short pulses in the femtosecond range, group velocity dispersion (GVD) also plays an important role since the temporal and spatial overlap of the individual pulses is affected by the different group velocities. From this considerations 2D materials provide an intrinsic benefit over bulk material systems.

As next-generation optoelectronic devices demand for high efficient and small volume nonlinear media, two dimensional MQW structures functionalized with plasmonic antennas become an ideal candidate for such optimized nonlinear metasurfaces. Therefore, a brief introduction to nanoplasmonics is given in the following chapter.

8.1.2 Nanoplasmonics

In this chapter of the thesis an introduction to nanoplasmonics is provided. Since the entire synopsis of past, present and future research in the field of plasmonics would go beyond the scope of this chapter the interested reader is encouraged to consult a focused editorial in Nature Photonics and the references within [SPR12]. As plasmonic structures share most of the physical properties of high-frequency antennas, they are often referred to as optical antennas. In general, they are (mostly) metallic nanostructures that feature a resonant behavior at certain optical frequencies. The specific resonances can be custom-engineered by a variation of the geometry at the nanoscale (shape and length), the material and the dielectric environment. Due to this sensitivity plasmonic structures are a promising tool for, e.g., sensor devices [BSF15]. The excitation of localized plasma oscillations[68] results in a spatially limited and strongly enhanced electromagnetic near-field. Therefore, plasmonic structures serve as converting elements

---

[68] A plasma oscillation is a periodic oscillation of the charge density in a medium (e.g. plasma or metal). The quasiparticle that emerges from the quantization of these oscillations is the plasmon.

between near-field distribution and far-field radiation. In this way, electromagnetic radiation can be concentrated below the diffraction limit and thus significantly enhance the radiation coupling of molecules and nanoemitters (e.g. quantum dots) [BHH12]. It is obvious that many applications based on plasmonic structures have evolved covering near-field microscopy [FEP07], fluorescence amplification [TMS07], spectroscopy [AMY07] and nonlinear optics [DSF17]. The reason for this wide range of practical implementations is, on the one hand, the durability of the metallic nanostructures, as well as the highly precise fabrication by electron beam lithography. On the other hand, different plasmonic structures can be coupled via their electromagnetic near-fields resulting in hybrid systems that may feature completely new optical properties compared to those of the individual plasmonic elements. The following section provides the theoretical fundamentals of the light-matter interaction at the nanoscale. Beginning with the concept of the classical antenna and the dielectric properties of metals, light scattering at nanoparticles is outlined further on.

Antennas are the converting compounds between bound and freely moving electromagnetic fields. The electric field is maximum at the interface and decays exponentially within the first tenth of nanometers (skin depth) in the metal. Depending on the kind of application and the resulting requirements, different antenna types have been established [Bal05]. The elementary rod antenna can be explained in analogy to the Hertzian dipole that describes an ideal and infinitesimally small radiation source: A periodic movement of free charge carriers along an open resonant circuit, e.g. a rod antenna, generates a propagating current wave which is reflected at each end forming a standing wave within the antenna [SKH03]. The acoustic everyday analogue is a guitar string that is plucked. The interference of incoming and returning current waves results in the generation of a continuously oscillating electromagnetic field around the antenna. In the resonant situation the effective wavelength λ_{eff} in the antenna is defined by its length L:

$$L = n\lambda_{\mathrm{eff}}/2 \tag{8.4}$$

Here, n is the resonant order, i.e. n=1 corresponds to a half-wave antenna. The resonance wavelength in this kind of traditional macroscopic wire antenna is almost equal to its radiation wavelength [ST81]. Consequently the ratio Λ of the effective wavelength of the rod antenna to the incident wavelength is approximately 1. At this point it should already be mentioned that the effective wavelength of an optical rod antenna is greatly shorter than the radiation wavelength resulting in much smaller Λ-ratios[69] [ZZ10]. The radiation of a half-wave dipole is omnidirectional and maximum in the plane perpendicular to the antenna and drops to zero at both ends. In three dimensions the radiation pattern shows a toroid (doughnut shape) symmetric around the

---

[69] For an incident plane wave with λ=850nm, a rood antenna embedded in the vacuum featuring a diameter of 10nm and a length of L=63nm, the resonant order n=1 leads to an effective wavelength of λ_{eff}=125nm and a resulting ratio Λ=0.147 [ZZ10].

antenna. The radiation pattern of the half-wave dipole is comparable to the ideal dipole whereas higher resonant orders show more complex directivity functions (see e.g. Ref. [ZZ10] for a graphical illustration). For microscopic antennas with low length-to-width-ratio, the radiative pattern becomes even more complex. Comparable to their macroscopic counterparts, optical antennas show a polarization dependence [MEM05] and a length-scaling resonance behavior [Nov07]. Therefore, slab or rod antennas feature strong characteristic resonances along their symmetry axis. Based on this consideration, the optical excitation of the applied rectangular plasmonic slab antennas is performed with longitudinal polarized (parallel to the long axis) fundamental light in the telecom wavelength range to properly address the antenna's main resonance. The cross-polarized resonance is optimized to match the second harmonic of the excitation wavelength.

The second section of the chapter is dedicated to the fundamentals of plasmonics: The dielectric properties of the different metals at optical frequencies. Since the choice of the proper material is crucial for the performance of the optical element the optical properties of metals will be discussed in the following section.

The band structure of metals is characterized by a partially occupied conduction band offering many free electronic states for a continuous excitation energy. This partial filling of the band with electrons is responsible for the high electric conductivity and is also referred to as electron gas or electron plasma surrounding the bound nuclei. The optical properties of metals and highly doped semiconductors are determined by interband transitions, electron-phonon interactions, and the excitation of the electron plasma by electromagnetic waves. The latter is the leading part in the low photon energy regime until the impact of electronic transitions becomes dominant for higher energies. Based on Maxwell's equations the dielectric function of a metal can be calculated according to Drude and Lorentz [Dru04, Mai07]. The model describes the interaction of an external electric field with (weakly) bound electrons in a dielectric media. The impinging field excites the electron gas to perform collective spatial oscillations. Therefore, the resulting polarization of the material is based on light-induced dipole moments that can be treated as damped harmonic oscillators. Neglecting the Lorentz (interband) absorptions the complex dielectric function of a metal can be modelled realistically for a large spectral range including the telecom wavelength regime:

$$\varepsilon(\omega) = \varepsilon - \frac{\omega_{\mathrm{p}}^2}{\omega^2 + i\gamma\omega} \qquad \text{with} \qquad \omega_p = \sqrt{\frac{ne^2}{\varepsilon_0 m^*}} \tag{8.5}$$

It depends on the dielectric constant ε of the surrounding material, the plasma frequency ω_p, which is proportional to the square root of the free charge carrier density n and the Drude damping constant γ. The latter is in the order of $\gamma \approx 10\text{-}100\,\mathrm{THz}$ at room temperature. The plasma constant for gold is $\hbar\omega_p \approx 9\,\mathrm{eV}$. Below this energy (so called plasma edge) the reflectivity increases strongly. For higher frequencies, however, the free electron gas becomes practically transparent. The optical properties are then determined by interband transitions of the bound electrons. For gold, however, d-band transitions start to set in at 2 eV and the conduction band electrons cannot be considered as quasi-free above this energy threshold. Consequently this is the upper photon energy for efficient gold-based plasmonic elements as well as for reflective coatings.

The quasiparticle that emerges from the quantization of the collective spatial charge density oscillations is the plasmon. Depending on the system, a distinction is made between volume, surface and particle plasmons. As the names suggest, volume plasmons occur in an extended 3D body, surface plasmons at a boundary layer and particle plasmons in confined nanoobjects. While a surface plasmon can spread along the 2D interface (similar to water waves on a water surface), sometimes over several tens of micrometers, particles are laterally very limited. Particle plasmons can be seen as a special case of surface plasmons and are often referred to as localized surface plasmon polaritons (LSPP). The volumetric restriction leads to discrete energy levels with different wave functions or charge density distributions within the confined object. This principle appears in analogy to the quantum mechanical particle in the box. However, particle plasmons are not a quantum phenomenon, but can also be described classically within certain limits.

As already mentioned, the wavelength of the absorbed/radiated light is typically much larger than the nanoobject itself, which means that the driving electric field can be assumed to be locally constant. Excited by the electromagnetic alternating field, the conduction band electrons oscillate coherently with the excitation wave. The polarization of the material, i.e. the displacement of the free charge carriers against the ion cores in the confined structure, leads to a Coulombic restoring force which, in addition to the plasma frequency of the material, determines the resonance frequency of the nanoobject [BHH12]. As a consequence, resonators at the nanoscale are formed, that can be tuned via the particle size, geometry, the material or the environment. Additionally, the vicinity of neighboring antennas causes a coupling of their respective particle plasmon resonance. The resulting reduction of the restoring force due to strong coupling leads to a spectral red shift at longitudinal excitation [RHL03]. Bearing in mind the quite large lateral distances (350 nm to 500 nm) between individual plasmonic elements of the antenna pattern used later in this thesis, no significant red shift due to a Coulomb attenuation is to be expected.

If the dimensions of a metallic object reach the nanometer scale, additional effects such as optical elastic scattering must be taken into account[70]. For spherical, metallic subwavelength particles, analytical formulas for the scattering and absorption cross-section can be derived on the basis of Maxwell's equations and Mie-theory (see Ref. [Men01] p. 145). Specifically, the Mie

---

[70] Inelastic scattering processes, such as Raman or Brillouin scattering, should not be discussed here.

solutions take the form of an infinite series of spherical multipole partial waves respecting the boundary conditions of the spherical surface of the particles (cf. chapter 2.3).

By means of a Fabry-Pérot model, simple cylindrical rod nanoantennas can be approximated as short plasmonic waveguides featuring a standing surface plasmon wave [BHH12]. For more complex structures and even for a more detailed understanding of rectangular rod antennas on a dielectric substrate, simulations of the near-field and charge distribution are necessary, using algorithms for time- and spatially-resolved field calculations based on Maxwell's equations.

To sum up the general characteristics and main purpose of the plasmonic elements applied on the nonlinear GaN/AlN superlattice the popular synonym "optical antennas" can be seen as guiding principle. The optical excitation of LSPP in the plasmonic structures results in a spatially limited and strongly enhanced electromagnetic near-field, especially at the ends, tips and areas of tight curvature. Therefore, the plasmonic antennas serve as converting elements between far-field radiation and near-field distribution. In this way, electromagnetic radiation can be concentrated below the diffraction limit and thus significantly enhance the nonlinear light-matter interaction in the underlying nonlinear material.

In the next chapter the functionalization process of the heterostructure with a nominally inversion-symmetric antenna array is outlined. Furthermore, basic characterizations of the plasmonic elements with optical and computational means provide evidence of the aspired resonance behavior.

8.2 Preparation and Linear Optical Properties of the Metasurface

The GaN/AlN superlattice of this study, introduced and characterized in chapter 6 and schematically depicted in Fig. 8.1(a), is grown by plasma-assisted molecular beam epitaxy on a double-side polished c-sapphire wafer (c-Al_2O_3). It features 25 GaN QWs with a thickness of 1.8 nm, separated by 5 nm thick Si-doped AlN barrier layers. As a result, the structure offers a large density of states for resonant ISBTs centered at 0.76 eV. This finding is consistent with band structure simulations and confirmed experimentally by linear transmission measurements (cf. chapter 6.3) and nonlinear time-resolved, degenerate and non-degenerate pump-probe measurements (cf. chapter 7.2 and 7.3). The latter reveal strong transient signals for TM polarized light centered around 1630 nm wavelength.

MQW structures can feature a broken inversion symmetry required for SHG [KTA18]. Hexagonal GaN-based heterostructures exhibit both a crystalline inversion asymmetry and a structural inversion asymmetry arising, e.g., from internal polarization fields and therefore allow for SHG. While the first intersubband transition is centered at 0.76 eV in the QWs, any potential second harmonic is resonant to bound-to-continuum transitions.

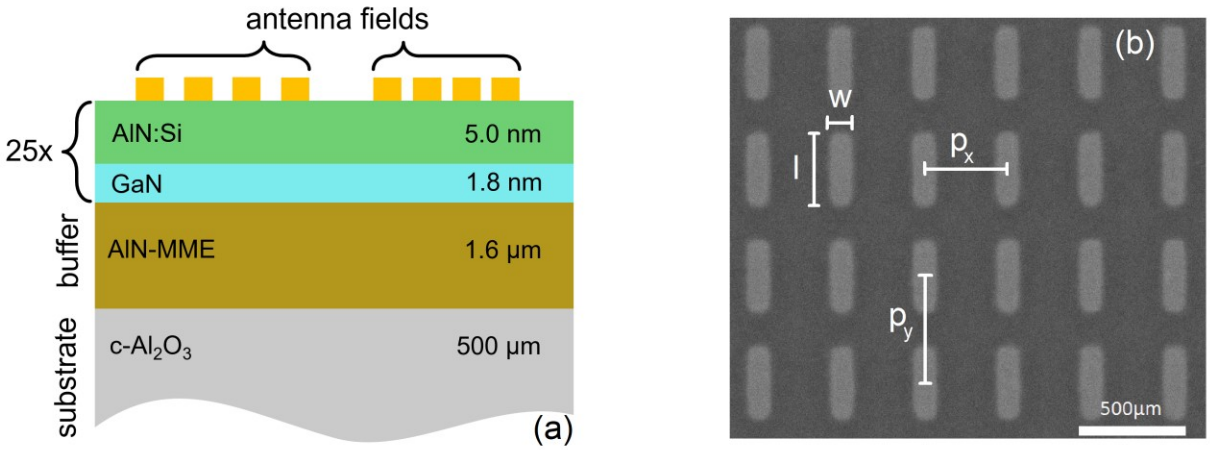

Fig. 8.1: (a) Schematic illustration of the semiconductor heterostructure functionalized with a nominally inversion-symmetric antenna array: The AlN buffer layer and 25 GaN/AlN QWs are grown on a double-side polished sapphire substrate. The antenna arrays are fabricated on top of the heterostructure by electron-beam lithography. (b) Top view image of an exemplary plasmonic antenna array taken on a scanning electron microscope. The width (w), length (l) and spacings in x- and y-direction (p_x and p_y) are included.

In the next preparation step the heterostructure is functionalized with a nominally inversion-symmetric antenna array. Fig. 8.1(a) and (b) illustrate the plasmonic elements deposited on top of the GaN/AlN heterostructure by standard electron-beam lithography. They are made of gold and fabricated by Florian Spreyer from the group of Prof. Dr. Thomas Zentgraf at the University of Paderborn. After the lithography process, the Polymethylmethacrylat (PMMA) photoresist is developed and 30 nm of gold is deposited by electron beam evaporation onto the sample. In the last step, the plasmonic structures are laid bare via a lift-off process where the PMMA mask is removed. Specifically, a periodic array of rod antennas with their length and width chosen to support cross-polarized plasmonic resonances at the driving fundamental wavelength and its second harmonic is used. In detail, an antenna length of $l=300$ nm up to $l=350$ nm is found to best match the profile of the ISBT and the available femtosecond pulses from the optical parametric amplifier (OPA) source in the near infrared. The nonlinear response of shorter as well as longer antennas is found to decrease gradually as expected since their resonance shifts away from the laser spectrum and/or the ISBTs.

Furthermore, several other antenna structures and lengths have been studied including a Y-shaped structure with threefold symmetry, a U-shaped split ring and i-shaped antennas. In a series of comparative measurements using an additional reference sample without the underlying MQW structure, nonlinear signals (SHG and THG) of similar magnitude are recorded. Considering the inversion asymmetric structure of the antenna types listed above this observation indicates a weak interaction between plasmonic antennas and the MQW but rather points to an intrinsic nonlinear light conversion originating from the plasmonic elements. Since the focus of this thesis is the investigation of a nonlinear metasurface consisting of a MQW structure functionalized with plasmonic antennas, the above mentioned structures are not considered any further. Nevertheless, these standard structures remain essential for other plasmonic applications as their resonances and locally enhanced near-fields are beneficial for e.g. radiation coupling [BHH12] and the manipulation or controlling of the phase of light [CLC18].

Fig. 8.2(b) shows a top view image of the plasmonic antennas taken on a scanning electron microscope by Florian Spreyer. The picture contains the notation for the dimensions of the antennas. They have a height of $h=30$ nm and a width of $w=80$ nm. While the separation along the y-axis is set to a constant value of $p_y=500$ nm, the lateral distance p_x is systematically varied between 350 nm and 500 nm. Fields of 100 µm x 100 µm are filled with a periodic array of antennas with fixed p_x. The panel (a) in Fig. 8.2 shows the calculated transmission spectra for different periods p_x of plasmonic antenna arrays on an AlN-substrate. These simulations are performed by Florian Spreyer using a plane wave excitation with y-polarized light implemented with the commercial CST Studio Suite from 3DS Dassault Systèmes. Furthermore, the z-components of the calculated electric field close to the antenna are extracted and illustrated in panel (b). It is shown, that strong near-fields are coupled into the MQW region of the stacked AlN/GaN layers, especially at the tips of the square rod antenna. In this way the electric field from free-space illumination at normal incidence is partially converted into z-polarized components that are necessary for substantial SHG in the MQW. The panels (c) and (d) of Fig. 8.2 display the linear transmission spectra of several arrays for y-polarized (longitudinal) light in the near-infrared as well as for x-polarized (transversal) light in the visible range. They are indicative of plasmonic resonances at ~1.6 µm and its second harmonic at ~800 nm wavelength. The measured resonances at the fundamental wavelength in panel (c) are in line with the corresponding design wavelengths shown in panel (a). Details of the spectra such as the widths of the resonances depend on the lateral distance p_x which indicates a coupling to some extent between adjacent antennas [UZP11, PWG19]. The present plasmonic array shows a slight redshift for increasing p_x.

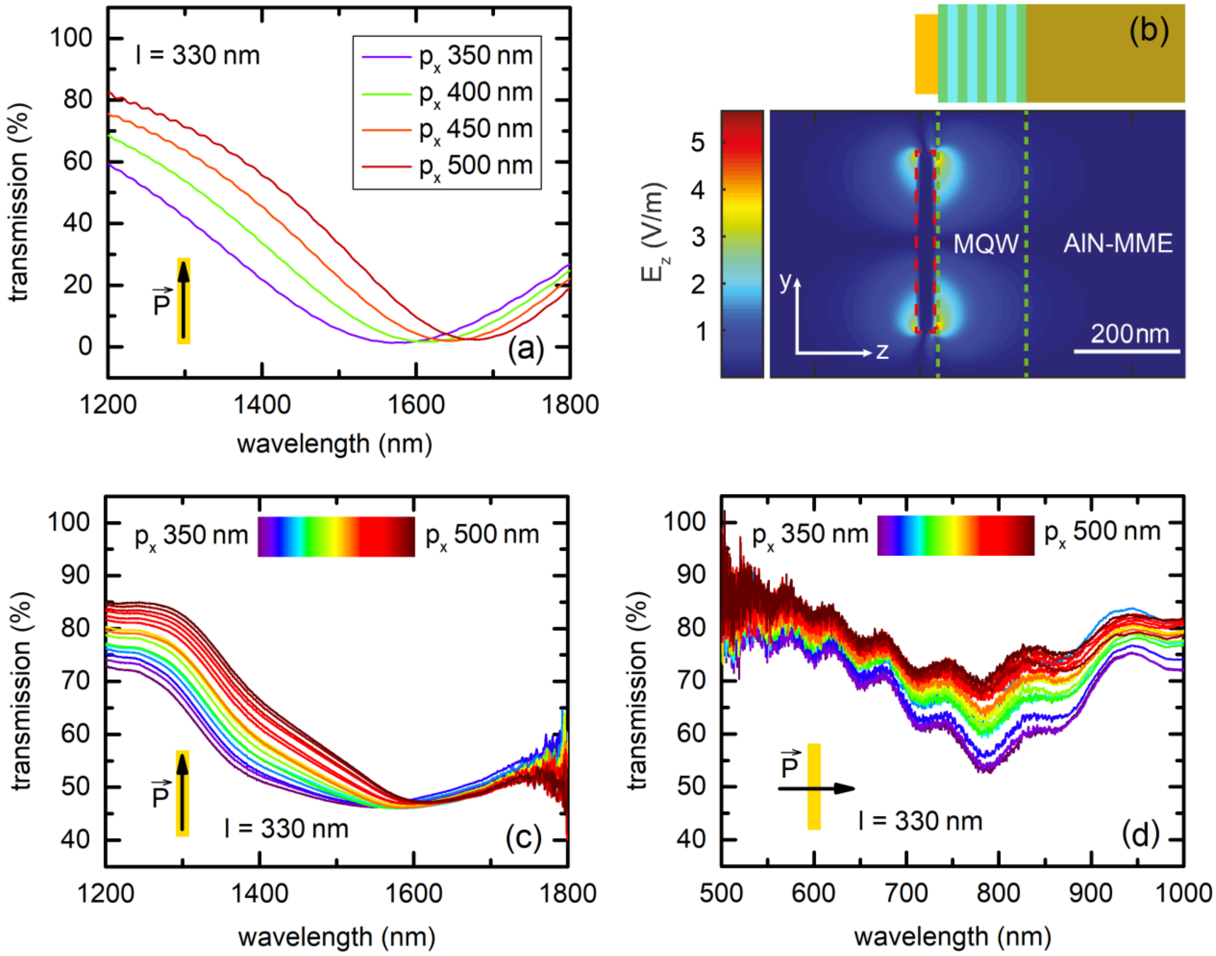

Fig. 8.2: (a) Calculated transmission spectra for different periods p_x of plasmonic antenna arrays on an AlN-substrate. (b) Calculated electric field close to the antenna. The antenna is indicated by a dashed red line and the MQW area is located between the two dashed green lines. (c) Transmission spectra of several arrays for y-polarized (longitudinal) incident light in the near-infrared. (d) Transmission spectra of the corresponding antenna arrays for x-polarized (transversal) incident light in the visible (SHG) range.

8.3 Experimental Approach for SHG/THG

Before moving to the demonstration of the generation of optical harmonics from the metasurface, the setup used for most of the experiments in the following chapter is presented. The experimental setup, schematically shown in Fig. 8.3, is designed for polarization-resolved transmission measurements. The main focus of the experiment is the detection and spectral analysis of the second and third harmonic signals generated in transmission geometry. A modelocked amplified laser system (Coherent RegA 9040) in combination with an OPA (Coherent OPA 9850) is used as a pump source. It delivers a train of linearly polarized, nearly transform-limited ~50 fs pulses at a repetition rate of 250 kHz. While this source is somewhat tunable, a fixed center wavelength of 1550 nm is chosen such that the pulses have a good spectral overlap with the ISBTs and the antennas' resonance (cf. Fig. 6.6(c) and Fig. 8.2(c)). If not stated otherwise, the measurements are performed in a single pass geometry with perpendicular incidence and longitudinal light polarization with respect to the orientation of the antennas. The sample is clamped to a tiltable holder and illuminated from the backside. Using a half-wave-plate and a polarizing beam splitter cube, a portion of up to a few hundred microwatts is focused down to a beam waist of approximately 30 µm using a lens with a focal length of 50 mm. This value corresponds to the full with at half maximum and is measured with a commercial scanning-slit beam profiler (Thorlabs BP209-IR). The detection unit for the nonlinear signals consists of a cooled sensitive camera (Atik 414EX, for imaging purposes) and a monochromator with a cooled CCD array (Andor Cornerstone, DU420-0E, for spectrally resolved measurements). The additional use of a suitable short-pass filter with high transmissivity at the second and third harmonic wavelength ensures the suppression of the fundamental pump beam. A linear polarizer and an achromatic half-wave-plate in front of the detection unit allow for polarization-resolved measurements.

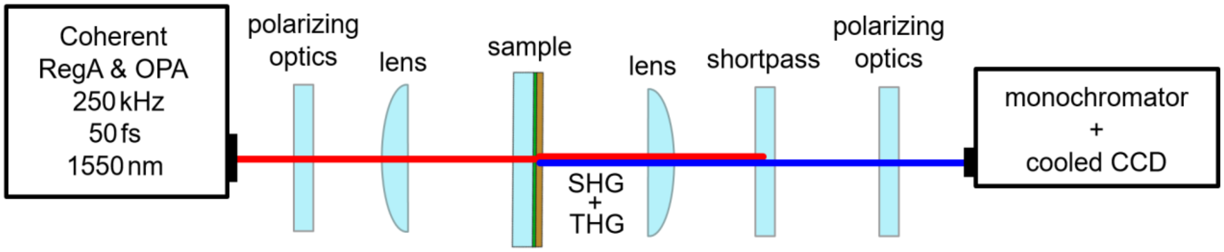

Fig. 8.3: Sketch of the experimental setup. The fundamental laser beam is focused down to the antenna arrays, passing the sample from the backside. An additional short-pass filter and polarization optics allow for spectrally and polarization-resolved measurements using a monochromator with a cooled CCD array.

8.4 Characterization of the Nonlinear Response from the Metasurface

The central section of chapter 8 presents the nonlinear optical response of the metasurface. This structure is based on an ultranarrow GaN/AlN MQW functionalized with a plasmonic rod antenna array made from gold and designed for resonant excitation in the telecom wavelength regime. SHG and THG are strongly supported by the near-field enhancement of these plasmonic structures. In the case of intense excitation with longitudinal polarized femtosecond laser pulses, the emission of the second and third optical harmonic can be observed in the far-field using either a sensitive camera for imaging purpose or the cooled spectrometer unit for spectral analysis. In addition, the system is powerful enough to spectroscopically analyze the emitted radiation in terms of its nonlinear power dependence.

8.4.1 Power Dependence

In the first step, an example of the nonlinear optical response to 1550 nm femtosecond pulses impinging on the metasurface is presented. Already with the naked eye the faint green glimmering of the THG is visible in the darkness. With the help of the sensitive camera and proper illumination of the sample, the nonlinear response is recorded photographically. Fig. 8.4(a) shows a monochrome picture detail featuring a white spot (SHG + THG) on the rectangular antenna array. This nonlinear response from the metasurface is dominated by the bright THG. The fundamental beam (its position is indicated by a green circle) is blocked by an appropriate filter and therefore not recorded/measured at all. This becomes clear from the picture presented in panel (b) where the fundamental laser spot has been moved in between two antenna arrays targeting the MQW solely. In this area and under the current illuminative situation no significant light, neither from the fundamental beam nor from any optical harmonics is visible. Further quantitative information about individual contributions of the MQW and the antenna array independently of each other are provided in the course of the current chapter.

Since plasmonic nanoantennas are fragile in terms of optical damage, the threshold for permanent damage is determined in a first quantitative measurement. Fig. 8.4(c) shows the pump power dependency of the THG intensity. Minor deviations from the cubic power law indicate saturation whereas negative gradients in the upper pump power regime clearly point to irreversible damage to the metasurface. Further data points recorded at the exact same position thus lead to strongly reduced nonlinear signals. It can be assumed that permanent damage to the plasmonic antennas occurs somewhat above 3 mW, referring to a peak power density of 420 W/cm². Consequently, the upper power limit for all further experiments is chosen to be greatly smaller than this particular threshold.

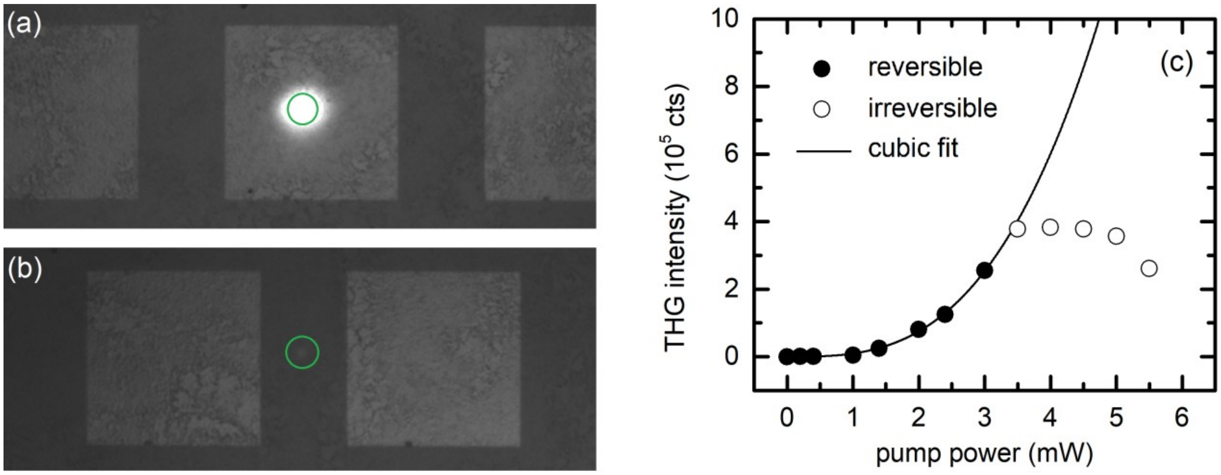

Fig. 8.4: (a) and (b) show monochrome photographs taken from the illuminated metasurface with several rectangular antenna arrays. Nonlinear emission is manifested by a white spot in panel (a). The fundamental beam is indicated by a green circle. (c) Pump power dependency of the THG intensity. Deviations from the theoretical cubic behavior indicate saturation and/or damage to the sample.

In the next step a series of pump power dependent measurements is performed to identify THG and SHG according to their power laws. Fig. 8.5(a) and (b) contain several spectra recorded for 1550 nm fundamental pulses of average powers ranging from 50 µW to 400 µW. The length of the antennas is l = 330 nm and the separation in the x-direction is p_x = 400 nm. A more detailed discussion of the p_x significance is carried out in chapter 8.4.3. Under these conditions, substantial SHG is observed (cf. panel (b)). It is almost as strong as the THG signal shown in panel (a). While THG is expected for the C2 symmetry of the antennas, the observation of substantial SHG cannot arise from the antenna array solely. The spectrum of the SHG shows an unexpected structure with two peaks. It arises from the modal structure of the AlN buffer layer and will be discussed later in chapter 8.4.3. Fig. 8.5(c) and (d) show the quantitative analysis of SHG and THG as a function of the fundamental pump power. The pump power dependence of the THG reveals a cubic behavior, as expected for this nonlinear process. For the SHG a power law fit for the power dependence is used. A scaling of $\sim x^{1.62}$ (red curve) is found to best match the experimental data points. The deviation of the SHG intensity from the expected quadratic one (green curve) arises from saturation effects in the regime of strongly driven ISBTs. In comparison to similar measurements on MQWs found in literature [VCP97, LTA14], a less pronounced saturation of SHG intensity is visible here. This finding can be attributed to the rather strong doping. For a Fermi energy of 90 meV, depletion of the lowest subband is hard to achieve.

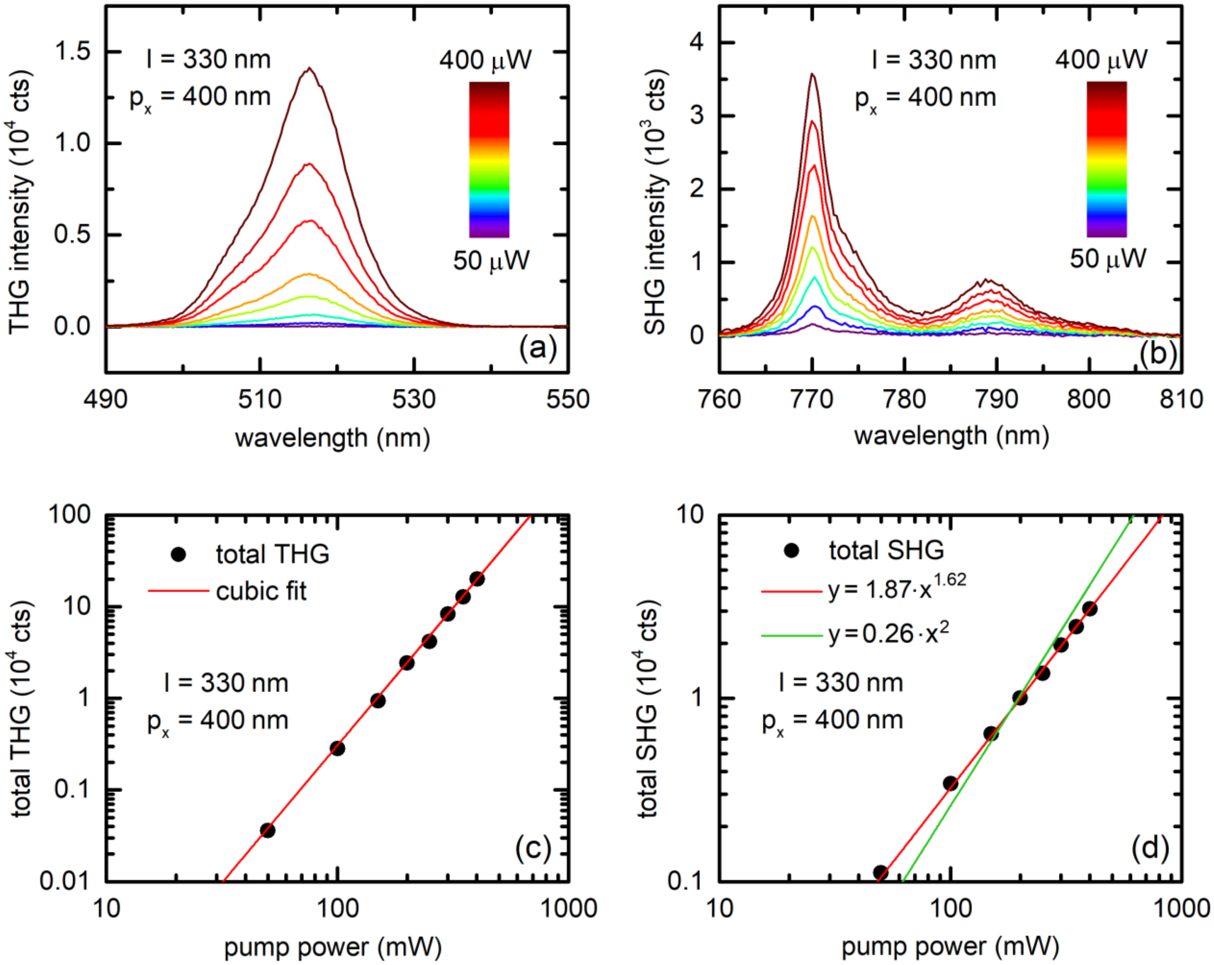

Fig. 8.5: (a) THG and (b) SHG spectra for various fundamental pump powers. The antenna array on top of the GaN/AlN MQW is characterized by l = 330 nm and p_x = 400 nm. (c) and (d) show the results for the spectrally integrated THG and SHG intensity ("total") together with a cubic and exponential/parabola fit, respectively.

In the remainder of this thesis, a comprehensive evidence should be provided that the unexpected SHG arises from an interplay between the ISBTs and the antenna array. As a first aspect of such evidence, it is verified that none of the two ingredients alone allow for substantial SHG. To this end, a reference sample where no MQW is present, i.e., the antenna arrays are deposited onto the sapphire substrate[71], is investigated. In this case, the SHG signal is below the detection limit of the setup. This holds true for all antenna arrays irrespective of the value of p_x and the antenna length[72]. An exemplary dataset featuring the same l and p_x values as used for

---

[71] A more sophisticated reference sample might contain a non-quantum layer of GaN/AlN below the antennas.

[72] The set of measurements includes values from p_x = 350 nm up to p_x = 500 nm. The antenna length varies between l = 320 nm and l = 340 nm, featuring strong resonances matching the ISBT in the telecom wavelength range.

the previous measurement is illustrated in Fig. 8.6. THG from this reference sample is about one order of magnitude smaller compared to the results shown in Fig. 8.5. Admittedly, the absolute intensity varies with respect to the antenna's dimensions and corresponding resonance. Since the C2 symmetry of the plasmonic rod antennas allows for THG this somewhat reduced nonlinear response is expected. Nevertheless, significant coupling between the resonantly driven antennas and the underlying nonlinear superlattice seems to be responsible for the substantial THG signal emitted from the metasurface. Furthermore, SHG/THG emission from a bare GaN/AlN heterostructure without any plasmonic structures on top is investigated. Again, any emitted SHG signal is, if at all, barely above the spectrometer's noise limit as can be seen in Fig. 8.6 (b). Most likely, the broken symmetry at the surface and the internal interfaces in the MQW allow for some SHG and discriminate against THG signals from the bulk material. In turn, THG is reduced by two orders of magnitude when compared to the results in Fig. 8.5. The spectral structure with a triple peak results again from the modal structure of the AlN buffer layer. In summary, on can conclude that the SHG of this nonlinear metasurface is based on the interplay of ISBTs in the GaN/AlN MQWs with the spectrally matched plasmonic antenna arrays. The absence and/or mismatch of one component leads to the practically complete disappearance of the SHG signal.

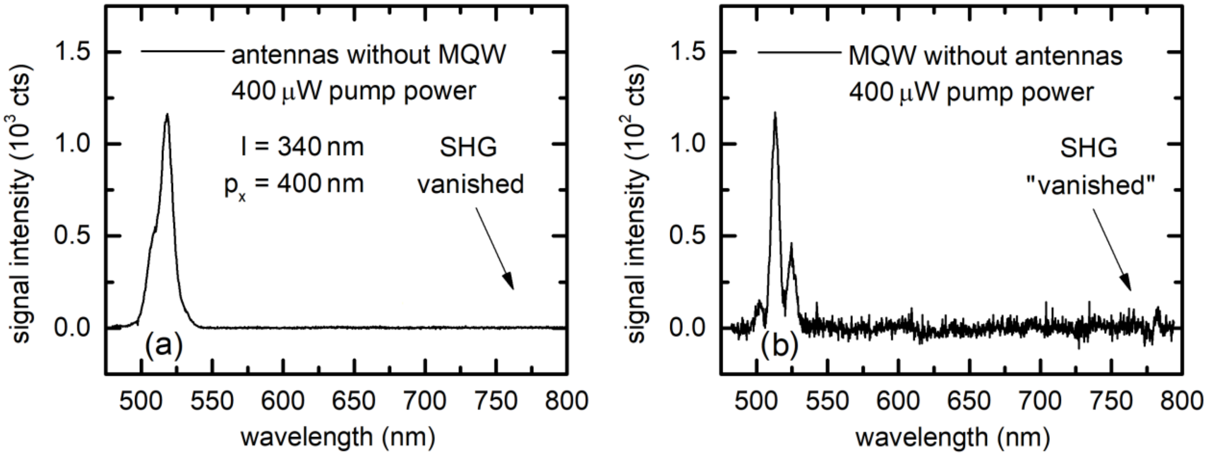

Fig. 8.6: Emission spectra including the THG and SHG range from (a) a reference sample with plasmonic antennas fabricated directly on a sapphire substrate and (b) the MQW sample without any plasmonic antennas. The length of the antennas and thus the spectral resonance was slightly adjusted with respect to the changed dielectric environment to match the laser wavelength again.

One of the most interesting aspects is the true output power of the second harmonic radiation from the nonlinear metasurface. The measurable value strongly depends on the choice of the plasmonic elements that permit conversion of the second harmonic light to free-space radiation. The emission is measured perpendicular to the surface in the far-field using the CCD array from the spectrometer. For calibration purpose, a thin BBO crystal is used at the original position of the sample. This allows second-harmonic power measurements with ordinary commercial devices leading to an accurate power-per-count calibration. The most intense second harmonic output for a constant pump power of 400 µW is observed for antennas with $l = 340\,\text{nm}$ and $p_x = 420\,\text{nm}$ and equals about 10 fW. The calculated power conversion efficiency $\eta_{SHG} = P_{SHG}/P_{Pump}$ is therefore $2.5 \cdot 10^{-11}$. It is quite possible that the actual conversion efficiency is larger to some extent. The experiment is designed to detect the second harmonic generated at the excitation spot with a microscope objective with a numerical aperture of 0.25. Due to the spectrally wide pump beam (full width at half maximum is $\Delta\lambda \approx 80\,\text{nm}$ at 1550 nm central wavelength) the spectral components of the SHG, converted into transmission geometry from the antenna arrays, are emitted into slightly different directions with respect to the surface normal. With a numerical aperture of 0.25, most of them will still be collected. However, as discussed in detail in the context of Fig. 8.8, the second harmonic is originally radiated into the heterostructure plane. As a result, second harmonic emission occurs over the entire antenna field of 100 µm x 100 µm size and even from adjacent patterns. It seems quite possible that second harmonic components are guided even further through the AlN layer. Consequently, the collimation of the SHG radiation using a microscope objective with a numerical aperture of 0.25 and the measurement in the far-field using the CCD in the spectrometer certainly does not collect all the SHG of the metasurface. Furthermore, the SHG might not completely couple back to the far-field in transmission geometry by the antenna array but is further guided in the AlN slab (see mode discussion below in the context of Fig. 8.9). This assumption is supported by the optical impression of the green THG light, visible to the naked eye, when looking onto the side facets of the sample, indicating good guidance inside the AlN waveguide. This leads to an underestimation of the SHG signal strength. In comparison to different realizations of metasurfaces found in literature, the introduced nonlinear metasurface reveals a power conversion efficiency above hybrid structures based on transition metal dichalcogenides (TMDCs) and plasmonic antennas ($\eta_{SHG} = 10^{-13}$) [SZH20] or plasmonic metalens ($\eta_{SHG} = 10^{-12}$) [SWR18]. Nevertheless, metasurfaces with, e.g., optimized plasmonic three-arm trapezoidal silver antennas reach a power conversion efficiency as high as $\eta_{SHG} = 10^{-9}$ [ANR12].

8.4.2 Polarization Dependence

As plasmonic structures share most of the physical properties of standard macroscopic high-frequency antennas, they feature a specific polarization dependence corresponding to their geometrical shape [MEM05]. In general, microscopic antennas with low length-to-width-ratio, exhibit a complex radiative pattern. Nevertheless, slab or rod antennas show strong characteristic resonances along their symmetry axis (cf. Fig. 8.2). The point of interest is now directed towards polarization-dependent measurements at a fixed pump power. For this purpose a half-wave plate is inserted in front of the sample. It allows for continuous rotation of the linear polarization of the fundamental laser beam. For longitudinal polarization (polarization parallel to the long axes of the antennas) the strongest SHG signal is observed, cf. Fig. 8.7(a). In the case of transverse polarization (polarization axes perpendicular to the long axes of the antennas) practically no SHG takes place. It is important to note that the data in Fig. 8.7(a) is recorded for non-polarized detection. This observation stands in perfect agreement with the antennas' resonances originating from their geometrical shape and dimensions (cf. Fig. 8.2(c) and (d)). Only in the case of roughly 1550 nm wavelength and longitudinal light polarization, a significant amount of the fundamental laser light is converted into z-polarized field components in the MQW, thereby allowing for SHG. In the case of transversal polarization, the antennas do not exhibit any resonance around ~1550 nm. A similar dependence on the polarization of the fundamental beam is also seen for THG. Since the third harmonic is mainly generated from the plasmonic elements any impinging light with transverse polarization cannot properly address the resonance of the antennas in the telecom wavelength range. Consequently, maintaining the correct polarization axis of the plasmonic elements is essential for a high nonlinear conversion efficiency.

In the final step of this short section the polarization state of the SHG and THG for longitudinally polarized fundamental light is investigated. To this end, a polarizer is inserted into the detection beam path. As depicted in Fig. 8.7(b) the second harmonic light is cross-polarized with respect to the fundamental. This finding can be attributed to the cross-polarized resonances of the antennas for fundamental and second harmonic light seen in Fig. 8.2. In contrast, the THG is polarized parallel to the fundamental light, as expected for the rod antennas.

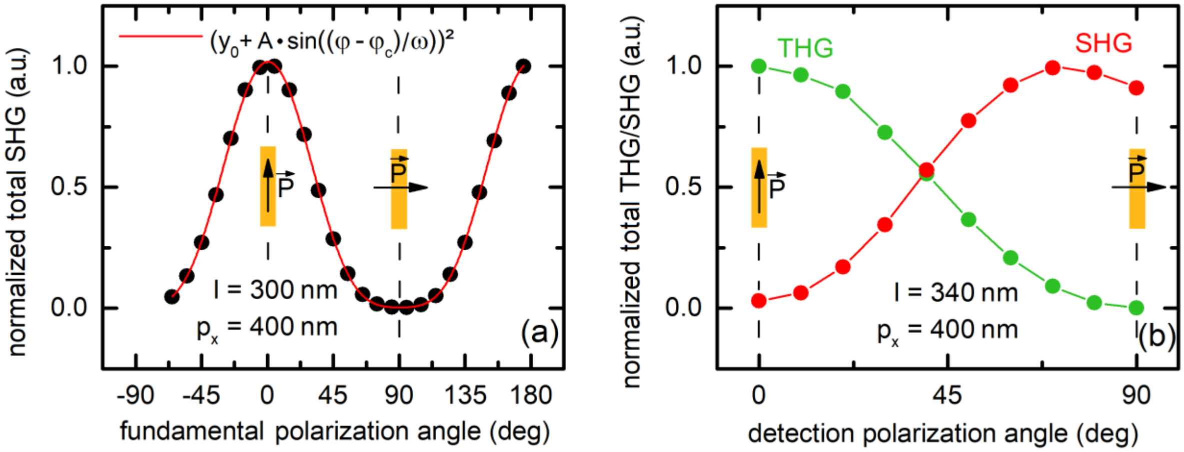

Fig. 8.7: (a) SHG signal as a function of the polarization angle of the fundamental light beam (0° longitudinal, 90° transversal) for non-polarized detection. The red line visualizes a fit to the data. (b) Normalized spectrally integrated SHG and THG intensity ("total") for change of the detection polarization angle (0° longitudinal, 90° transversal) for a longitudinal polarized fundamental beam.

8.4.3 Influence of the Antenna Periodicity

The generation and emission of second harmonic light from the metasurface is the result of a complex interplay between the plasmonic structures and the nonlinear GaN/AlN superlattice. Specifically, an electric field component $E_z \| z$ parallel to the growth direction (z-direction) of the GaN/AlN superlattice is required to properly address the IMB transition dipole (cf. Fig. 6.6). As evident from the electric near-field distribution of the plasmonic rod antenna (cf. Fig. 8.2(b)) such essential and moreover drastically enhanced field components are present. While the second harmonic is originally radiated only into the plane of the QWs, a proper geometrical arrangement of the plasmonic elements permits to redirect the second harmonic to free-space radiation, which is eventually emitted perpendicular to the surface. This, at first glance unforeseen aspect is now under a more detailed investigation.

The observation of substantial SHG is restricted to a fairly small range of lateral antenna spacings p_x. Also, the visual appearance of the second harmonic emission drastically depends on the p_x. To illustrate this aspect, an exemplary set of pictures taken for $l=340\,\text{nm}$ and p_x-values ranging from 300 nm up to 500 nm is shown in the upper section of Fig. 8.8 (note that these pictures are rotated by 90° in comparison to the SEM picture in Fig. 8.1(b)). The recorded THG and SHG spectra including additional antenna lengths are located below the corresponding image. For better visibility, some sets of graphs are shown with enlarged amplitude and the respecting magnification factors are included. In general, the visual appearance is dominated by the bright THG emission, whose intensity is at least one order of magnitude higher than that of the SHG. For increasing p_x values the THG intensity increases slightly. This observation will be discussed more briefly in the context of Fig. 8.9. Nevertheless, compared to the SHG intensity it shows a fairly monotonous behavior. For $p_x=300\,\text{nm}$ and $p_x=500\,\text{nm}$, some weaker second harmonic emission occurs at the excitation spot (green circle). In marked contrast, the emission spot for $p_x=350\,\text{nm}$, $p_x=400\,\text{nm}$ and $p_x=450\,\text{nm}$ appears to be much wider and somewhat brighter. With respect to the corresponding THG and SHG spectra this increase in brightness can be clearly attributed to the intensification of the SHG emission. Additionally, light seems to be emitted even from the adjacent antenna patterns (pattern size: $100\,\mu\text{m} \times 100\,\mu\text{m}$) which are located perpendicular to the polarization direction of the fundamental light beam. The only explanation for this finding is that the second harmonic is radiated into the plane of the QWs and then converted into free-space radiation by the periodic arrangements of antennas. In particular, the plasmonic elements of the heterostructure partially convert the impinging light into z-polarized components in the MQWs. These components are aligned along the dipole moment of the ISBTs and can, therefore, be converted into the second optical harmonic when the ISBTs are strongly driven. Also, the diffraction by 90° is not completely unexpected: the second harmonic radiation has a wavelength of ~400 nm inside the heterostructure since the vacuum wavelength is ~775 nm and the refractive index is ~2. Details and the precise mode index depend on the AlN buffer layer underneath the MQWs which mostly guides the second-harmonic radiation. This guiding effect seems to be pronounced as the light even reaches adjacent antenna patterns (indicated by blue squares), where the SHG is also scattered back into the z-direction.

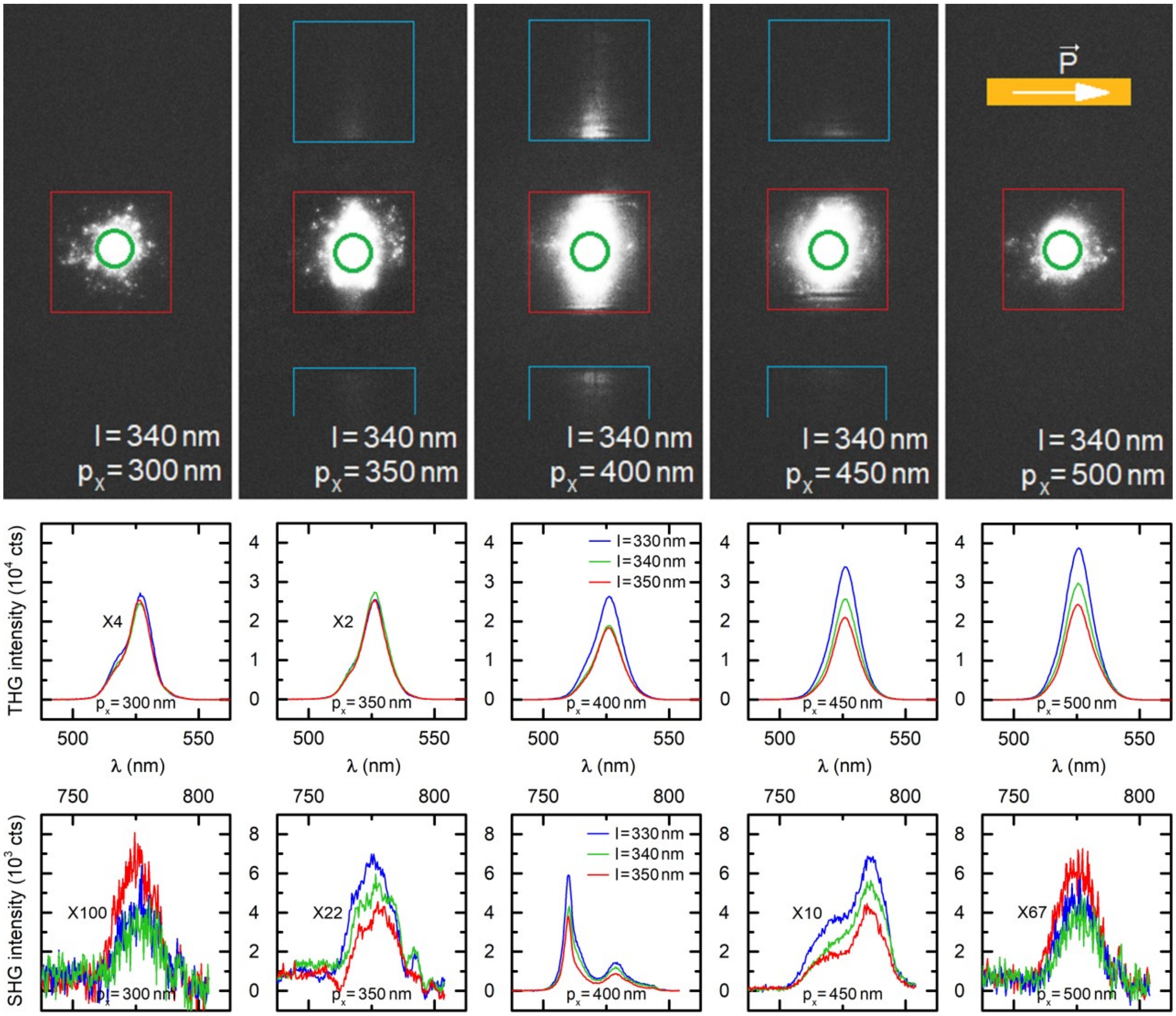

Fig. 8.8: Pictures taken from different illuminated antenna arrays (red boxes, array size: 100 µm x 100 µm) on top of the MQW. The longitudinally polarized pump laser (the spot on the sample is indicated by a green circle) is filtered out by a suitable shortpass thus only THG and SHG contribute to the illuminated areas. Substantial SHG can be observed for p_x=350-450 nm with in-plane emission to adjacent antenna patterns (blue boxes). For better illustration the pictures are rotated by 90 degrees with respect to the SEM picture of the sample in Fig. 1(b). The corresponding THG and SHG spectra including additional antenna lengths are located below the referring picture. Magnification factors are included. In accordance with the pictures, substantial SHG can be observed for p_x=350 nm to p_x=450 nm.

Next, the p_x-dependence of the emitted second and third harmonic spectra will be elaborated. Fig. 8.9(a) displays a false-color plot of the emitted third harmonic spectrum for various p_x. While the intensity is seen to increase slightly with p_x, no significant changes to the spectrum are observed. The increase of the intensity with p_x is somewhat surprising as the areal density of the antennas decreases with p_x and fewer antennas contribute to the nonlinear optical emission. This observation points to a coupling of the antennas even for distances as large as p_x=500 nm. However, for increasing p_x values the optical resonances become somewhat narrower[73] (cf. Fig. 8.2 panel (a) and (c)) supporting the observed small increase in third harmonic emission to some extent. The constant spectrum points to the THG of the antenna array itself with no major impact on the optical mode structure of the semiconductor underneath.

In stark contrast, the spectrum of the emitted second harmonic in Fig. 8.9(b) massively depends on p_x (note that the false-color plot in panel (b) uses a logarithmic scale to enhance the visibility of smaller side-peaks). For a fixed p_x, the emission into a few optical modes with a spectral separation of ~20 nm is typically observed (cf. also SHG spectra in Fig. 8.5(b)). This finding reflects the modal structure of the ~1.6 µm thick semiconductor layer on top of the sapphire substrate. It also accounts for the observed lateral guidance of the generated harmonic light underneath the antenna array to the edges of the sample. Due to the relatively large thickness of the AlN layer, several higher-order modes can be excited by the periodic antenna arrays. Hereby the mode dispersion shifts the spectral coupling with varying p_x. Because the wavelength range of the SHG is restricted by the fundamental laser bandwidth, as well as by the IMB transition and antenna resonance, an enhanced SHG signal can be observed if the generated light matches one of the TM modes of the guiding slab. The higher-order TM-mode dispersion indicated by red lines in Fig. 8.9(b) are calculated by Florian Spreyer. The coupling of the localized plasmon resonances of the antennas along the short axis together with the stronger grating effect leads to the strong coupling for the TM modes. On the other hand, the TE modes of the slab cannot couple to the plasmon resonance and no enhanced SHG emission is observed for these modes.

Finally, the dependence of the spectrally integrated second and third harmonic on the lateral spacing p_x is investigated. The total THG intensity is illustrated in Fig. 8.9(c) and the total SHG intensity is shown in paned (d). The data points are obtained from the above panels (a) and (b), respectively. As already observed and explained in the context of Fig. 8.8 the THG intensity is seen to increase with expanding antenna spacings. In marked contrast the total SHG shows a pronounced maximum for p_x=420 nm. The efficiency of the nonlinear optical process decreases fairly rapidly for both smaller and larger separations. To exclude a substantial influence of the optical mode structure, additional data sets have also been recorded for the spectrally integrated SHG at different small tilt angles (data not shown). They reveal practically identical dependence

---

[73] In particular, this spectral narrowing of the resonance for increasing lateral spacings p_x becomes obvious when looking at a set of resonance spectra of the reference sample for various p_x (data not shown).

of the integrated SHG on p_x. Even the somewhat reduced THG and SHG signal for p_x=410 nm is present in this additional data set which is related to minor imperfections of the specific antenna array. They can be attributed to residues from the cleaning process resulting in a partially incomplete lift-off process during the fabrication. Apparently, lateral separations around p_x=420 nm are best suited for SHG in the plane of the heterostructure and its conversion into free-space radiation emitted perpendicular to the surface. At this period/wavelength combination, the best mode matching to the guide modes in the AlN film for coupling perpendicular to the free-space radiation is obtained.

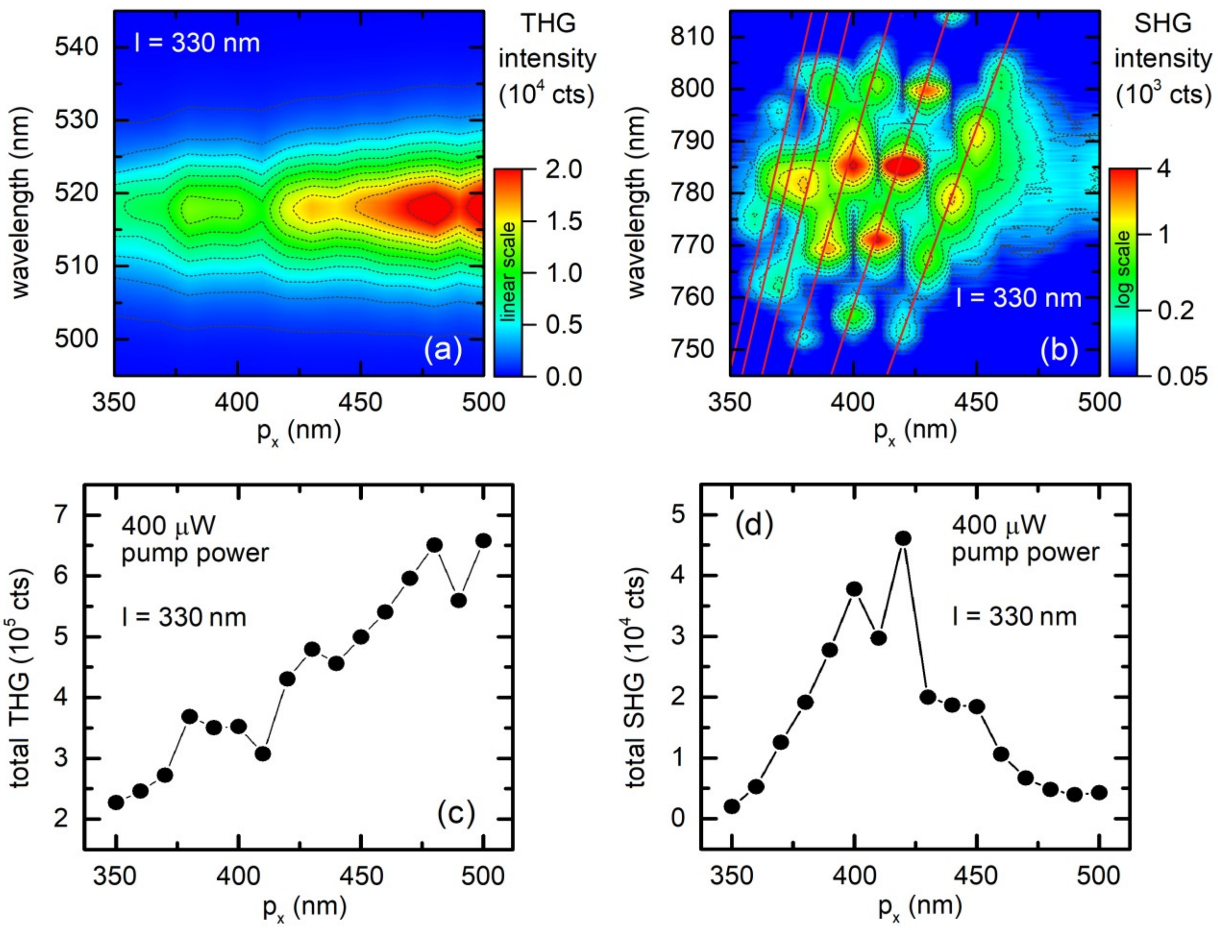

Fig. 8.9: (a), (b) False-color representations of the spectra of the emitted third harmonic (panel (a), linear scale) and second harmonic (panel (b), logarithmic scale) for different lateral periodicities p_x of the antennas. The red lines indicate calculated higher-order TM-modes. (c) Spectrally integrated THG extracted from the data in panel (a). (d) Spectrally integrated SHG extracted from the data in panel (b).

Last but not least, to further illustrate the impact of these optical guide modes in the AlN film a small tilt of the sample is introduced. Fig. 8.10 contains third and second harmonic spectra for a fixed period of $p_x = 420$ nm but varying angle of incidence. Note that the sample is rotated around the longitudinal axes of the antennas. Within this small range of angles, changes of the effective lateral periodicity are practically negligible. Since the generation of the third harmonic is practically restricted to the antennas solely without major impact on the optical mode structure of the semiconductor underneath, the recorded spectra remain constant over a range of 10 degrees of tilt. On the other hand, the second harmonic spectra show a more complex intensity pattern while the angle of incidence is changed. Fundamental light, now impinging off normal incidence, provides additional in-plane momentum for the coupling of second harmonic light into the optical modes of the semiconductor heterostructure. In line with this reasoning, the modes of the emitted spectrum exhibit a linear shift when the angle of incidence is changed. This shift is illustrated by the dashed lines.

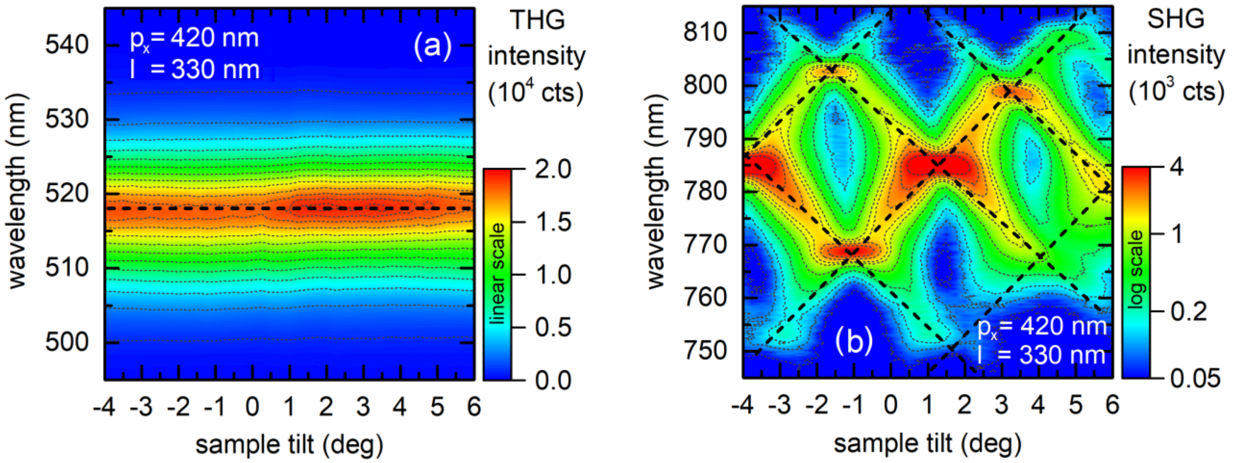

Fig. 8.10: False-color representation of (a) the third harmonic (linear scale) and (b) the second harmonic (logarithmic scale) spectra for different tilt angles of the sample with respect to the incident fundamental beam. An angle of zero degrees refers to normal incidence. The tilt occurs along the long axes of the antennas. The dotted lines visualize the observed spectral modes originating from the tilting of the sample.

Chapter 9

Conclusions and Outlook Part II

The spatial confinement of charge carriers in the GaN/AlN superlattice leads to the generation of a quasi-two-level system with fabrication-tailored inter-miniband transition energies. Compared to the commonly established arsenide or antimonide materials the GaN/AlN structure benefits from a high conduction band offset around 2 eV offering operation in the fiber-optics telecommunication wavelength regime (1.3-1.55 µm). The investigated hexagonal GaN/AlN structure features ultranarrow 1.8 nm quantum wells (QWs) separated by 5 nm barriers. While the wells are nominally undoped, the high n-type Si-doping of the barriers gives rise to a two-dimensional electron gas such that the first subband is strongly populated. In the framework of chapter 6.3 the linear optical properties of the IMB transition are determined. A broad absorption centered at 0.76 eV is found. Most strikingly, the full width at half maximum of the IMB absorption is as large as 260 meV. As elaborated in the context of the fundamental quantum well physics in chapter 6.2, the extraordinary broadening can be attributed to (i) the tunneling-induced coupling of wavefunctions across the narrow AlN barriers, (ii) the scattering at interface roughness and (iii) monolayer fluctuations of the QW thickness. Considering potential applications, a broad IMB transition is beneficial especially for, e.g., single unit detector devices or broadband nonlinear frequency conversions. Additionally, basic simulations of the inter-subband transition energy agree with the experimental data, if the GaN QW thickness is assumed to be seven to eight monolayers. More sophisticated predictions may include internal electric fields, strain and coupling between adjacent QWs.

The ultrafast electron dynamics in the hexagonal GaN/AlN superlattice are studied employing time-resolved degenerate (chapter 7.2) and non-degenerate (chapter 7.3) pump-probe spectroscopy. For a resonant excitation and a resonant probe by TM polarized beams, that properly address the IMB transition dipole, a maximum relative transmission increase of $\Delta T/T=0.25\%$ is observed. It can be attributed to a substantial Pauli blocking of the probe transmission in the quasi two-level IMB system. Spectrally resolved and polarization dependent measurements confirm the nonlinear optical response to originate from the saturation of the IMB absorption. The present experimental setup profits from an improved temporal resolution due to the fairly low pulse duration of only ~50 fs. The fast IMB relaxation time is found to be ∼70 fs, which indicates electron scattering with longitudinal optical (LO) phonons. Nevertheless the experimental system has reached the limit of the temporal resolution and further research has to overcome this limit. Since theoretical predictions for the ISB electron relaxation calculate electron scattering times with LO phonons of ~100 fs [SI98, GFN01, HGN02], major deviations from the experimentally determined value are not expected. An additional slow decay channel reveals a time constant of ∼15 ps that can be attributed to the thermalization of the 2D electron gas. In the second set of measurements non-degenerate pump-probe spectroscopy using 1.55 eV excitation energy is performed. This excitation energy greatly exceeds the IMB transition energy and even addresses continuum states outside the QW confinement. The spectrally resolved optical response of the highly excited GaN/AlN superlattice stands in agreement with the results from the degenerate measurement. The signal drops significantly as the probe wavelength is tuned away from the center of the IMB resonance. The obtained data points nicely cover one wing of the IMB resonance obtained by linear transmission measurements. In the field of polarization-dependent experiments, there are slight deviations to the previously performed measurements that can be attributed to the relaxed selection rules for bound-to-continuum transitions. Nevertheless, TM-polarized pump and probe beams that properly address the IMB transition still lead to the maximum transient signal strength. In comparison to the degenerate pump-probe investigation, non-degenerate power-dependent measurements do not show any sign of saturation within the covered power range since the transition into the continuum offers a wider range of final states within the 3D parabolic energy band. Self-saturation of the pump beam due to Pauli blocking is, therefore, not observed to this extent. In great contrast, the non-degenerate pump-probe spectroscopy based on bound-to-continuum photoexcitation reveals electron relaxation times in the picosecond regime. These extended decay times are most likely due to electron-electron or Auger collisions that sustain a hot electron distribution. The excited system eventually relaxes by a multi-stage phonon scattering process which in turn might be hampered by a phonon bottleneck, thermal and cascade-type escape. Nevertheless, further experimental and theoretical analysis is inevitably needed to explain the electron dynamics more precisely.

Further research might aim to enlarge the resonant nonlinearity associated with the ISBTs in GaN/Al(Ga)N heterostructures. This can be achieved by stronger doping and growth of structures with spectrally narrower inter subband resonances. The extensive knowledge obtained in the course of the past research period about the molecular beam epitaxy (MBE) fabrication of n-doped heterostructures with near-infrared intersubband transitions (especially in the telecom window of 1.3 - 1.55 µm wavelength) will be beneficial for the growth of future optimized samples.

In chapter 8.2 a nonlinear metasurface based on the previously investigated superlattice and plasmonic antennas is introduced. This artificial material composition takes advantage of ISBTs in the ultranarrow n-doped GaN/AlN MQWs and plasmonic elements designed to be in resonance with these ISBTs to massively enhance the optical nonlinearity. Specifically, the heterostructure is functionalized with an array of plasmonic gold antennas featuring cross-polarized resonances at these near-infrared wavelengths and their second harmonic. This kind of nonlinear metasurface allows for substantial second-harmonic generation at normal incidence which is completely absent for an antenna array without the MQW structure underneath. In a nutshell, the antennas partially convert light impinging at normal incidence into field components polarized vertically to the heterostructure's plane. These fields strongly drive the ISBTs and give rise to SHG initially radiated into the plane of the QWs. By an appropriate choice of the lateral spacings within the periodic antenna array, the second harmonic is redirected into a transmission geometry with respect to the incident driving pulse. Owing to the large conduction band offsets in the GaN/AlN material system, this metasurface exhibits SHG for fundamental pulses in the telecom window which is hard to realize in any other established semiconductor family. Remarkably, this concept allows for SHG in a nominally inversion-symmetric metasurface with a power conversion efficiency of $\eta_{SHG}=2.5\cdot10^{-11}$ in the far-field. An increase in efficiency is envisioned for an optimized out-coupling of the SHG and, thereby, associated with an improved antenna geometry, making an outlook to future research.

In contrast, corresponding investigations on cubic III-nitrides have been scarce. However, due to the higher crystal symmetry of zinc-blende III-nitrides polarization effects and large internal electrical fields, typical of hexagonal nitrides, are avoided. Additionally, strong band bendings even in narrow QWs, which may result in depletion layers or 2D electron gases do not have to be taken into account in the cubic system. Therefore, the proper choice of the material's crystal structure can ease the design and quality of the electronic, linear and nonlinear optical properties. These superior characteristics of the cubic GaN/AlN would have been beneficial for the design and efficiency of electro-optical devices. Nevertheless, thick layers of cubic GaN/AlN tend to become increasingly unstable and, eventually, switch to the hexagonal structure during the growth process. Optimized metasurfaces based on cubic GaN/AlN would subsequently pave the way for potential applications with enhanced performance.

Bibliography

[ABC12] J. M. Atkin, S. Berweger, E. K. Chavez, M. B. Raschke, J. Cao, W. Fan and J. Wu, "Strain and temperature dependence of the insulating phases of VO_2 near the metal-insulator transition," Physical Review B **85**, 020101 (2012)

[AFB12] Asaf Albo, D. Fekete and G. Bahir, "Electronic bound states in the continuum above (Ga,In)(As,N)/(Al,Ga)As quantum wells," Physical Review B **85**, 115307 (2012)

[AGF91] M. Abbate, F. M. F. de Groot, J. C. Fuggle, Y. J. Ma, C. T. Chen, F. Sette, A. Fujimori, Y. Ueda and K. Kosuge, "Soft-x-ray-absorption studies of the electronic-structure changes through the VO_2 phase transition," Physical Review B **43**, 7263 (1991)

[AGG17] A.G. Ardakani, Z. Ghasemi and M. M. Golshan, "A new transfer matrix for investigation of surface plasmon modes in multilayer structures containing anisotropic graphene layers," European Physical Journal Plus **132**, 206 (2017)

[Agr10] G.P. Agrawal, *Fiber-Optic Communication Systems*, 4th edition, John Wiley & Sons, Inc, Hoboken, New Jersey (2010)

[AK63] Z. I. Alferov and R. F. Kazarinov, Inventor's Certificate No. 181737 [in Russian], Application No. 950840, priority as of March 30, 1963; H. Kroemer, Proc. IEEE **51**, 1782 (1963)

[ALS12] K. Appavoo, D. Y. Lei, Y. Sonnefraud, B. Wang, S. T. Pantelides, S. A. Maier and R. F. Haglund Jr., "Role of Defects in the Phase Transition of VO_2 Nanoparticles Probed by Plasmon Resonance Spectroscopy," Nano Letters **12**, 780-786 (2012)

[AMY07] A. V. Akimov, A. Mukherjee, C. L. Yu, D. E. Chang, A. S. Zibrov, P. R. Hemmer, H. Park and M. D. Lukin, "Generation of single optical plasmons in metallic nanowires coupled to quantum dots," Nature **450**, 402 (2007)

[ANR12] H. Aouani, M. Navarro-Cia, M. Rahmani, T. Sidiropoulos, M. Hong, R. Oulton and S. Maier, “Multiresonant Broadband Optical Antennas as Efficient Tunable Nanosources of Second Harmonic Light,” Nano Letters **12**, 4997-5002 (2012)

[AR00] A. D. Andreev and E. P. O’Reilly, “Theory of the electronic structure of GaN/AlN hexagonal quantum dots,” Physical Review B **62**(23), 15851 (2000)

[As09] D. J. As, “Cubic group-III nitride-based nanostructures - basics and applications in optoelectronics,” Microelectronics Journal **40**, 204-209 (2009)

[Bal05] C. J. Balanis, *Antenna theory, analysis and design*, third edition, Wiley (2005)

[Bas84] G. Bastard, “Quantum-size effects in the continuum states of semiconductor quantum wells,” Physical Review B **30**(6), 3547-3549 (1984)

[BAT20] S. Bayda, M. Adeel, T. Tuccinardi, M. Cordani and F. Rizzolio, “The History of Nanoscience and Nanotechnology: From Chemical-Physical Applications to Nanomedicine,” Molecules **25**(1), 112 (2020)

[BCZ10] S. Barz, G. Cronenberg, A. Zeilinger and P. Walther, “Heralded generation of entangled photon pairs,” Nature Photonics **4**, 553-556 (2010)

[BBW96] M. F. Becker, A. B. Buckmann, R. M. Walser, T. Lepine, P. Georges and A. Brun, “Femtosecond laser excitation dynamics of the semiconductor-metal phase transition in VO_2,” Journal of Applied Physics **79**, 2404-2408 (1996)

[BCF02] W. Burkhardt, T. Christmann, S. Franke, W. Kriegseis, D. Meister, B. K. Meyer, W. Niessner, D. Schalch and A. Scharmann, “Tungsten and fluorine co-doping of VO_2 films,” Thin Solid Films **402**(1), 226-231 (2002)

[BFV97] F. Bernardini, V. Fiorentini and D. Vanderbilt, “Spontaneous polarization and piezoelectric constants of III-V nitrides,” Physical Review B **56**, 10024 (1997)

[BGH06] E. Baumann, F. R. Giorgetta, D. Hofstetter, S. Golka, W. Schrenk, G. Strasser, L. Kirste, S. Nicolay, E. Feltin, J. F. Carlin and N. Grandjean, “Near infrared absorption and room temperature photovoltaic response in AlN⁄GaN superlattices grown by metal-organic vapor-phase epitaxy,” Applied Physics Letters **89**, 041106 (2006)

[BGK00] L. A. Boyarsky, S. P. Gabuda and S. G. Kozlova, “Unusual magnetic behavior of vanadium dioxide: NMR ^{51}V study,” Physica B: Condensed Matter **284**, 1454-1455 (2000)

[BHH12] P. Biagioni, J.-S. Huang and B. Hecht, “Nanoantennas for visible and infrared radiation,” Reports on Progress in Physics **75**, 024402 (2012)

[BLC15] L. Bai, Q. Li, S. A. Corr, Y. Meng, C. Park, S. V. Sinogeikin, C. Ko, J. Wu and G. Shen, "Pressure-induced phase transitions and metallization in VO_2," Physical Review B **91**, 104110 (2015)

[BMK94] J. Baur, K. Maier, M. Kunzer, U. Kaufmann and J. Schneider, "Determination of the GaN/AlN band offset via the (-/0) acceptor level of iron, Applied Physics Letters **65**, 2211 (1994)

[Boy20] R.W. Boyd, *Nonlinear Optics*, fourth edition, Academic Press (2020)

[BPB09] C. S. Blackman, C. Piccirillo, R. Binions and Ivan P. Parkin, "Atmospheric pressure chemical vapour deposition of thermochromic tungsten doped vanadium dioxide thin films for use in architectural glazing," Thin Solid Films **51**7(16), 4565-4570 (2009)

[BPL05] S. Biermann, A. Poteryaev, A. I. Lichtenstein and A. Georges, "Dynamical Singlets and Correlation-Assisted Peierls Transition in VO_2," Physical Review Letters **94**, 026404 (2005)

[BR82] G. Binnig, H. Rohrer, "Scanning Tunneling Microscope," 4343993A, U.S. Patent, August 10 (1982)

[BSF15] L. Baldassarre, E. Sakat, J. Frigerio, A. Samarelli, K. Gallacher, E. Calandrini, G. Isella, D. J. Paul, M. Ortolani and P. Biagioni, "Midinfrared Plasmon-Enhanced Spectroscopy with Germanium Antennas on Silicon Substrates," Nano Letters **15**, 7225 (2015)

[BVG66] A. S. Barker, Jr., H. W. Verleur and H. J. Guggenheim, "Infrared Optical Properties of Vanadium Dioxide Above and Below the Transition Temperature," Physical Review Letters **17**, 1286 (1966)

[BYZ07] P. Baum, D.-S. Yang and A. H. Zewail, "4D Visualization of Transitional Structures in Phase Transformations by Electron Diffraction," Science **318**, 788-792 (2007)

[CCH07] G. Chen, H. Chen, M. Haurylau, N. A. Nelson, D. H. Albonesi, P. M. Fauchet and E. G. Friedman, "Predictions of CMOS compatible on-chip optical interconnect," Integration, the VLSI Journal **40**, 434-446 (2007)

[CD10] H. J. Caulfield and S. Dolev, "Why future supercomputing requires optics," Nature Photonics **4**, 261-263 (2010)

[CDC04] A. Cavalleri, Th. Dekorsy, H. H. W. Chong, J. C. Kieffer and R. W. Schoenlein, "Evidence for a structurally-driven insulator-to-metal transition in VO_2: A view from the ultrafast timescale," Physical Review B **70**, 161102 (2004)

[CDS10] X. Y. Cui, B. Delley and C. Stampfl, “Band gap engineering of wurtzite and zincblende GaN/AlN superlattices from first principles,” Journal of Applied Physics **108**, 103701 (2010)

[CFN96] T. Christmann, B. Felde, W. Niessner, D. Schalch and A. Scharmann, “Thermochromic VO_2 thin films studied by photoelectron spectroscopy,” Thin Solid Films **287**, 134-138 (1996)

[CGF10] J. Cao, Y. Gu, W. Fan, L. Q. Chen, D. F. Ogletree, K. Chen, N. Tamura, M. Kunz, C. Barrett, J. Seidel and J. Wu, “Extended Mapping and Exploration of the Vanadium Dioxide Stress-Temperature Phase Diagram,” Nano Letters **10**, 2667-2673 (2010)

[CJH15] B. T. O’Callahan, A. C. Jones, J. Hyung Park, D. H. Cobden, J. M. Atkin and M. B. Raschke, “Inhomogeneity of the ultrafast insulator-to-metal transition dynamics of VO_2,” Nature Communications **6**, (2015)

[CJL19] X. Cao, P. Jin and H. Luo, *Nanotechnology in Eco-efficient Construction*, second edition, Woodhead Publishing, Duxford, Cambridge, Kidlington (2019)

[CKK11] S. B. Choi, J. S. Kyoung, H. S. Kim, H. R. Park, D. J. Park, B.-J. Kim, Y. H. Ahn, F. Rotermund, H.-T. Kim, K. J. Ahn and D. S. Kim, “Nanopattern enabled terahertz all-optical switching on vanadium dioxide thin film,” Applied Physics Letters **98**, 071105 (2011)

[CLC18] S. Chen, G. Li, K. W. Cheah, T. Zentgraf and S. Zhang, “Controlling the phase of optical nonlinearity with plasmonic metasurfaces,” Nanophotonics **7**(6), 1013-1024 (2018)

[CRS06] A. Cavalleri, M. Rini and R. W. Schoenlein, “Ultra-Broadband Femtosecond Measurements of the Photo-Induced Phase Transition in VO_2: From the Mid-IR to the Hard X-rays,” Journal of the Physical Society of Japan **75**, 011004 (2006)

[CSH97] P. B. Chapple, J. Staromlynska, J. A. Hermann, T. J. Mckay and R. G. Mcduff, “Single-Beam Z-Scan: Measurement Techniques and Analysis,” Journal of Nonlinear Optical Physics & Materials **6**(3), 251-293 (1997)

[CTS01] A. Cavalleri, C. Toth, C. W. Siders and J. A. Squier, “Femtosecond Structural Dynamics in VO_2 during an Ultrafast Solid-Solid Phase Transition,” Physical Review Letters **87**, 237401 (2001)

[CWD19] M. Currie, V. D. Wheeler, B. Downey, N. Nepal, S. B. Qadri, J. A. Wollmershauser, J. Avila and L. Nyakiti, “Asymmetric hysteresis in vanadium dioxide thin films,” Optical Materials Express **9**, 3717-3728 (2019)

[CX02] J. Cheng and X. Xie, “Green’s function formulation for third-harmonic generation microscopy,” Journal of the Optical Society of America B **19**, 1604 (2002)

[Dav98] J.H. Davies, *The Physics of Low-Dimensional Semiconductors: An Introduction*, first edition, Cambridge University Press (1998)

[DFM07] E. A. De Cuir, E. Fred, M. O. Manasreh, J. Schörmann, D. J. As and K. Lischka, “Near-infrared intersubband absorption in nonpolar GaN/AlN superlattices,” Applied Physics Letters **91**, 041991 (2007)

[DKC09] T. Driscoll, H.-T. Kim, B.-G. Chae, B.-J. Kim, Y.-W. Lee, N. M. Jokerst, S. Palit, D. R. Smith, M. Di Ventra and D. N. Basov, “Memory Metamaterials,” Science **325**, 1518-1521 (2009)

[DLF09] E. U. Donev, R. Lopez, L. C. Feldman and R. F. Haglund, “Confocal Raman Microscopy across the Metal-Insulator Transition of Single Vanadium Dioxide Nanoparticles,” Nano Letters **9**, 702-706 (2009)

[DNJ96] Y. Dachuan, X. Niankan, Z. Jingyu and Z. Xiulin, “Vanadium dioxide films with good electrical switching property,” Journal of Physics D: Appl. Phys. **29,** 1051-1057 (1996)

[DR06] J.-C. Diels and W. Rudolph, *Ultrashort Laser Pulse Phenomena: Fundamentals, Techniques, and Applications on a Femtosecond Time Scale*, Academic Press, (2006)

[Dre86] K. E. Drexler, *Engines of creation - The Coming Era of Nanotechnology*, first edition, Anchor Press/Doubleday, New York, USA (1986)

[Dru04] P. Drude, “Optische Eigenschaften und Elektronentheorie, ” Annalen der Physik **319**(10), 936 (1904)

[DSF17] G. Deka, C.-K. Sun, K. Fujita and S.-W. Chu, “Nonlinear plasmonic imaging techniques and their biological applications,” Nanophotonics **6**, 31 (2017)

[Eye02] V. Eyert, “The metal-insulator transitions of VO_2: A band theoretical approach,” Annalen der Physik **11**, 650-702 (2002)

[EWP18] H. Esmaielpour, V. R. Whiteside, H. P. Piyathilaka et al., “Enhanced hot electron lifetimes in quantum wells with inhibited phonon coupling.” Scientific Reports **8**, 12473 (2018)

[FCS94] J. Faist, F. Capasso, D. L. Sivco, C. Sirtori, A. L. Hutchinson and A. Y. Cho, “Quantum Cascade Laser,” Science **264**, 553-556 (1994)

[FEP07] J. N. Farahani, H.-J. Eisler, D. W. Pohl, M. Pavius, P. Flückiger, P. Gasser and B. Hecht, "Bow-tie optical antenna probes for single-emitter scanning near-field optical microscopy," Nanotechnology **18**, 125506 (2007)

[Fey60] R. P. Feynman, "There's Plenty of Room at the Bottom," Engineering and Science **23**(5), 22-36 (1960)

[FHP61] P. A. Franken, A. E. Hill, C. W. Peters and G. Weinreich, "Generation of Optical Harmonics," Physical Review Letters **7**, 118 (1961)

[FZN13] Z. Fang, Y.-R. Zhen, O. Neumann, A. Polman, F. J. G. de Abajo, P. Nordlander and N. J. Halas, "Evolution of light-induced vapor generation at a liquid-immersed metallic nanoparticle," Nano Letters **13**, 1736 (2013)

[GAF20] F. Grandi, A. Amaricci and M. Fabrizio, "Unraveling the Mott-Peierls intrigue in Vanadium dioxide," Physical Revview Research **2**, 013298 (2020)

[GB96] L. A. Gea and L. A. Boatnera, "Optical switching of coherent VO_2 precipitates formed in sapphire by ion implantation and annealing, Applied Physics Letters **68**, 3081 (1996)

[GB97] J. M. Gregg and R. M. Bowman, "The effect of applied strain on the resistance of VO_2 thin films," Applied Physics Letters **71**, 3649-3651 (1997)

[GBB99] L. Gea, J. Budai and L. Boatner, "Formation and phase transition of VO_2 precipitates embedded in sapphire," Materials Research Society **14**, 2602 (1999)

[GBS12] M. Geissbuehler, L. Bonacina, V. Shcheslavskiy, N. L. Bocchio, S. Geissbuehler, M. Leutenegger, I. Märki, J.-P. Wolf and T. Lasser, "Nonlinear Correlation Spectroscopy (NLCS)," Nano Letters **12**(3), 1668-1672 (2012)

[GCS01] C. Gmachl, F. Capasso, D. L. Sivco and A. Y. Cho, "Recent progress in quantum cascade lasers and applications," Reports on Progress in Physics **64**, 1533 (2001)

[GFC07] B. Gu, Y.-X. Fan, J. Chen, H.-T. Wang, J. He and W. Ji, "Z-scan theory of two-photon absorption saturation and experimental evidence," Journal of Applied Physics **102**, 083101 (2007)

[GFE77] Michèle Gupta, A. J. Freeman and D. E. Ellis, "Electronic structure and lattice instability of metallic VO_2," Physical Review B **16**, 3338 (1977)

[GFN01] C. Gmachl, S. V. Frolov, H. M. Ng, S. N. G. Chu and A. Y. Cho, "Sub-picosecond electron scattering time for $\lambda = 1.55\mu m$ intersubband transitions in GaN/AlGaN multiple quantum wells," Electronics Letters **3**7, 378-380 (2001)

[Gra16] C. G. Granqvist, “Recent progress in thermochromics and electrochromics: A brief survey,” Thin Solid Films, (2016)

[Goo71] J. B. Goodenough, “The two components of the crystallographic transition in VO_2,” Journal of Solid State Chemistry **3**, 490-500 (1971)

[GZL05] Y. Gao, X. Zhang, Y. Li, H. Liu, Y. Wang, Q. Chang, W. Jiao and Y. Song, “Saturable absorption and reverse saturable absorption in platinum nanoparticles,” Optics Communications **251**(4-6), 429-433 (2005)

[HCS15] W.-K. Hong, S. N. Cha, J. I. Sohn and J. M. Kim, “Metal-Insulator Phase Transition in Quasi-One-Dimensional VO_2 Structures,” Journal of Nanomaterials **2015**, 538954 (2015)

[Hea73] C. Hearn, “The anomalous thermal expansion of VO_2 crystal with the rutile structure,” Solid State Communications **13**, 1139-1141 (1973)

[Hen68] D. H. Hensler, “Transport Properties of Sputtered Vanadium Dioxide Thin Films,” Journal of Applied Physics **39**, 2354-2360 (1968)

[HGN02] J. D. Heber, C. Gmachl, H. M. Ng and A. Y. Cho, “Comparative study of ultrafast intersubband electron scattering times at 1.55µm wavelength in GaN/AlGaN heterostructures,” Applied Physics Letters **8**1, 1237-1239 (2002)

[HHT05] M. W. Haverkort, Z. Hu, A. Tanaka, W. Reichelt, S. V. Streltsov, M. A. Korotin, V. I. Anisimov, H. H. Hsieh, H.-J. Lin, C. T. Chen, D. I. Khomskii and L. H. Tjeng, “Orbital-Assisted Metal-Insulator Transition in VO_2,” Physical Review Letters **95**, 196404 (2005)

[HMK04] J. Hamazaki, S. Matsui, H. Kunugita, K. Ema, H. Kanazawa, T. Tachibana, A. Kikuchi and K. Kishino, “Ultrafast intersubband relaxation and nonlinear susceptibility at 1.55µm in GaN/AlN multiple-quantum wells,” Applied Physics Letters **84**, 1102-1104 (2004)

[HMN12] M. Hari, S. Mathew, B. Nithyaja, S. A. Joseph, V. P. N. Nampoori and P. Radhakrishnan, “Saturable and reverse saturable absorption in aqueous silver nanoparticles at off-resonant wavelength,” Optical and Quantum Electronics **43**, 49-58 (2012)

[HSH02] K. Hoshino, T. Someya, K. Hirakaw and Y. Arakawa. “Observation of intersubband transition from the first to the third subband (e_1e_3) in GaN/AlGaN quantum wells,” Physica Status Solidi **192**(1), 27-32 (2002)

[HTL03] A. Helman, M. Tchernycheva, A. Lusson, E. Warde, F. H. Julien, Kh. Moumanis, G. Fishman, E. Monroy, B. Daudin, D. Le Si Dang, E. Bellet-Amalric and D. Jalabert, "Intersubband spectroscopy of doped and undoped GaN/AlN quantum wells grown by molecular-beam epitaxy," Applied Physics Letters **83**, 5196-5198 (2003)

[HW10] S. Hooker and C. Webb, "*Laser Physics*," Oxford University Press, Oxford, (2010)

[HW84] J. Herrmann and B. Wilhelmi, *Laser für ultrakurze Lichtimpulse*, Physik-Verlag, Weinheim (1984)

[IKS04] N. Iizuka, K. Kaneko and N. Suzuki, "Sub-picosecond modulation by intersubband transition in ridge waveguide with GaN/AlN quantum wells," Electronics Letters **40**, 962-963 (2004)

[Ina14] K. Inaba, "Special Feature: GaN for Opto- and Power-electronic Applications (2) Characterization of GaN-related materials using high-resolution XRD," Rigaku Journal **30**(1), (2014)

[Int22] Intel Technology Roadmaps and Milestones, last access 25 march 2022, URL: https://www.intel.com/content/www/us/en/newsroom/news/intel-technology-roadmaps-milestones.html

[JKS13] A. Joushaghani, B. A. Kruger, S. Paradis, D. Alain, S. J. Aitchison and J. K. S. Poon, "Sub-volt broadband hybrid plasmonic-vanadium dioxide switches," Applied Physics Letters **102** (2013)

[JMZ16] T. Jostmeier, M. Mangold, J. Zimmer, H. Karl, H. J. Krenner, C. Ruppert and M. Betz, "Thermochromic modulation of surface plasmon polaritons in vanadium dioxide nanocomposites," Optics Express **24**, 17321-17331 (2016)

[JNT18] V. N. Jmerik, D. V. Nechaev, A. A. Toropov, E. A. Evropeitsev, V. I. Kozlovsky, V. P. Martovitsky, S. Rouvimov and S. V. Ivanov, "High-efficiency electron-beam-pumped sub-240-nm ultraviolet emitters based on ultra-thin GaN/AlN multiple quantum wells grown by plasma-assisted molecular-beam epitaxy on c-Al_2O_3, Applied Physics Express **11**, 091003 (2018)

[JWR15] T. Jostmeier, T. Wecker, D. Reuter, D. J. As and M. Betz, "Ultrafast carrier dynamics and resonant inter-miniband nonlinearity of a cubic GaN/AlN superlattice", Applied Physics Letters **107**, 211101 (2015)

[JZK14] T. Jostmeier, J. Zimmer, H. Karl, H. J. Krenner and M. Betz, "Optically imprinted reconfigurable photonic elements in a VO_2 nanocomposite," Applied Physics Letters **105**, 071107 (2014)

[Kan08] P. K. Kandaswamy et al., “GaN/AlN short-period superlattices for intersubband optoelectronics: A systematic study of their epitaxial growth, design, and performance,” Journal of applied physics **104**, 093501 (2008)

[Kan57] E. O. Kane, “Band structure of indium antimonide,” Journal of Physics and Chemistry of Solids **1**, 249 (1957)

[KAP15] A. F. Koenderink, A. Alu and A. Polman, “Nanophotonics: shrinking light-based technology,” Science **348**, 516 (2015)

[KDS09] H. Karl, J. Dreher and B. Stritzker, “Semiconductor-metal Phase Transition in Doped Ion Beam Synthesized VO_2 Nanoclusters,” MRS Proceedings **1174**, 1174-V06-35 (2009)

[KEH07] C. Kübler, H. Ehrke, R. Huber, R. Lopez, A. Halabica, R. F. Haglund and A. Leitenstorfer, “Coherent Structural Dynamics and Electronic Correlations during an Ultrafast Insulator-to-Metal Phase Transition in VO_2,” Physical Review Letters **99**, 116401 (2007)

[KGW16] A.V. Krasavin, P. Ginzburg, G.A. Wurtz and A.V Zayats, “Nonlocality-driven supercontinuum white light generation in plasmonic nanostructures,” Nature Communication **7**, 11497 (2016)

[Khu08] J. B. Khurgin, “Inhomogeneous origin of the interface roughness broadening of intersubband transitions,” Applied Physics Letters **93**, 091104 (2008)

[Khu14] J. B. Khurgin, “Graphene - A rather ordinary nonlinear optical material,” Applied Physics Letters **104**, 161116 (2014)

[KJN07] H. Kakiuchida, P. Jin, S. Nakao and M. Tazawa, “Optical Properties of Vanadium Dioxide Film during Semiconductive-Metallic Phase Transition,” Japanese Journal of Applied Physics **46**, L113 (2007)

[KL64] A. H. Kahn and A. J. Leyendecker, “Electronic Energy Bands in Strontium Titanate,” Physical Review **135**, A1321 (1964)

[Kli06] C. F. Klingshirn, *Semiconductor Optics*, 3rd edition, Springer, Berlin (2006)

[KMN73] D. A. Kleinman, R. C. Miller and W. A. Nordland, “Two-photon absorption of Nd laser radiation in GaAs,” Applied Physics Letters **23**, 243 (1973)

[KN79] D. Kucharczyk and T. Niklewski, “Accurate X-ray determination of the lattice parameters and the thermal expansion coefficients of VO_2 near the transition temperature,” Journal of Applied Crystallography **12**, 370-373 (1979)

[KNZ20] S. Kabir, S. Nirantar, L. Zhu, C. Ton-That, S. K. Jain, A. Bin Ahmad Kayani, B. J. Murdoch, S. Sriram, S. Walia and M. Bhaskaran, “Phase change vanadium dioxide light sensors,” Applied Materials Today **21**, 100833 (2020)

[Kro63] H. Kroemer, “A proposed class of hetero-junction injection lasers,” Proceedings of the IEEE **51**(12), 1782-1783 (1963)

[KS02] C. C. Katsidis and D. I. Siapkas, “General transfer-matrix method for optical multilayer systems with coherent, partially coherent, and incoherent interference,” Applied Optics **41**, 3978-3987 (2002)

[KSP17] K. H. Kim, A. Späh, H. Pathak, F. Perakis, D. Mariedahl and K. Amann, “Maxima in the thermodynamic response and correlation functions of deeply supercooled water,” Science **358**(6370), 1589-1593 (2017)

[KTA18] A. Krasnok, M. Tymchenko and A. Alù, “Nonlinear metasurfaces: a paradigm shift in nonlinear optics,” Materials Today **21**(1d), 8-21 (2018)

[KVM15] R. M. Kemper, P. Veit, C. Mietze, A. Dempewolf, T. Wecker, F. Bertram, J. Christen, J. K. N. Lindner and D. J. As, “STEM-CL investigations on the influence of stacking faults on the optical emission of cubic GaN epilayers and cubic GaN/AlN multi-quantum wells,” physica status solidi (c) **12**, 469-472 (2015)

[Lau80] R. Laughlin, “Optical absorption edge of SiO_2,” Physical Review B **22**, 3021-3029 (1980)

[LBA15] C. B. Lim, M. Beeler, A. Ajay, J. Lähnemann, E. Bellet-Amalric, C. Bougerol and E. Monroy, “Intersubband transitions in nonpolar GaN/Al(Ga)N heterostructures in the short- and mid-wavelength infrared regions,” Journal of Applied Physics **118**, (2015)

[LBA16] C. B. Lim, M. Beeler, A. Ajay, J. Lähnemann, E. Bellet-Amalric, C. Bougerol, J. Schörmann, M. Eickhoff and E. Monroy, “Short-wavelength, mid- and far-infrared intersubband absorption in nonpolar GaN/Al(Ga)N heterostructures,” Japanese Journal of Applied Physics **55**, 05FG05 (2016)

[LBH02] R. López, L. A. Boatner, T.E. Haynes, L. C. Feldman and R. F. Haglund, Jr., “Synthesis and characterization of size-controlled vanadium dioxide nanocrystals in a fused silica matrix,” Journal of Applied Physics **92**, 4031-4036 (2002)

[LFH04] R. López, L. C. Feldmann and R. F. Haglund, Jr., Size-Dependent Optical Properties of VO_2 Nanoparticle Arrays, Physical Review Letters **93**(17), 177403 (2004)

[LHB02] R. López, T. E. Haynes and L. A. Boatner, "Size effects in the structural phase transition of VO_2 nanoparticles," Physical Review B **65**, 224113 (2002)

[LHF04] R. López, R. F. Haglund, Jr. and L. C. Feldman, "Optical nonlinearities in VO_2 nanoparticles and thin films," Applied Physics Letters **85**(22), 5191-5193 (2004)

[LHJ07] X. Y. Liu, P. Holmström, P. Jänes, L. Thylén and T. G. Andersson, "Intersubband absorption at 1.5–3.5 µm in GaN/AlN multiple quantum wells grown by molecular beam epitaxy on sapphire," physica status solidi (b) **244**, 2892-2905 (2007)

[LKM08] A. D. Lad, P. P. Kiran, D. More, G. R. Kumar and S. Mahamuni, "Two-photon absorption in ZnSe and ZnSe⁄ZnS core/shell quantum structures," Applied Physics Letters **92**, 043126 (2008)

[LLW03] S. J. Lee, Y. L. Lee, S. Y. Woo et al., "Simple method for determining Gaussian beam waist using lens Z-scan," The 5th Pacific Rim Conference on Lasers and Electro-Optics (IEEE Cat. No.03TH8671) **1**, 246 (2003)

[LMH19] J. Lappalainen, J. Mizsei and M. Huotari, "Neuromorphic thermal-electric circuits based on phase-change VO_2 thin-film memristor elements," Journal of Applied Physics **125**, 044501 (2019)

[LNG10] S.-Y. Li, G. A. Niklasson and C. G. Granqvist, "Nanothermochromics: Calculations for VO_2 nanoparticles in dielectric hosts show much improved luminous transmittance and solar energy transmittance modulation," Journal of Applied Physics **108**, 063525 (2010)

[LRS01] M. E. Levinshtein, S. L. Rumyantsev and M. S. Shur, *Properties of Advanced Semiconductor Materials: GaN, AlN, InN, BN, SiC, SiGe*, John Wiley & Sons, New York (2001)

[LRS03] M. E. Levinshtein, S. L. Rumyantsev and M. S. Shur, *Material properties of nitrides - Summary*, Solid State Electronics Division, The Ioffe Physical-Technical Institute of Russian Academy of Sciences, 194021, St. Petersburg, Russia (2003)

[LTA14] J. Lee, M. Tymchenko, C. Argyropoulos, P.-Y. Chen, F. Lu, F. Demmerle, G. Boehm, M.-C. Amann, A. Alù and M. A. Belkin, "Giant nonlinear response from plasmonic metasurfaces coupled to intersubband transitions," Nature **511**, 65-69 (2014)

[LTS96] M. Leszczynski, H. Teisseyre, T. Suski, I. Grzegory, M. Bockowski, J. Jun, S. Porowski, K. Pakula, J. M. Baranowski, C.T. Foxon and T. S. Cheng, "Lattice parameters of gallium nitride," Applied Physics Letters **69**(1), 73-75 (1996)

[LYZ04] H. Liu, S. Yin, J. Zhang, B. Jiang, L. Wang and N. Lou, "Data analysis for pump-probe experiment with femtosecond pulses," Chemistry, (2004)

[Mai07] S. Maier, *Plasmonics - Fundamentals and Applications*, Springer, New York (2007)

[Mat79] R. A. Matula, "Electrical resistivity of copper, gold, palladium and silver," Journal of Physical and Chemical Reference Data **8**, 1147 (1979)

[MBR96] G. Martin, A. Botchkarev, A. Rockett and H. Morkoc, "Valence-band discontinuities of wurtzite GaN, AlN, and InN heterojunctions measured by x-ray photoemission spectroscopy," Applied Physics Letters **68**(18), 2541-2543 (1996)

[MCT14] V. R. Morrison, R. P. Chatelain, K. L. Tiwari, A. Hendaoui, A. Bruhács, M. Chaker and B. J. Siwick, "A photoinduced metal-like phase of monoclinic VO_2 revealed by ultrafast electron diffraction," Science **24**, 445-448 (2014)

[MEM05] P. Mühlschlegel, H.-J. Eisler, O. J. F. Martin, B. Hecht and D. W. Pohl, "Resonant optical antennas," Science **308**(5728), 1607-1609 (2005)

[Men01] R. Menzel, *Photonics - Linear and Nonlinear Interactions of Laser Light and Matter*, first edition, Springer, Berlin (2001)

[MHL97] B. Murdin, W. Heiss, C. Langerak, S.-C. Lee, I. Galbraith, G. Strasser, E. Gornik, M. Helm and C. R. Pidgeon, "Direct observation of the LO phonon bottleneck in wide GaAs/$Al_xGa_{1-x}As$ quantum wells," Physical Review B **55**, 5171 (1997)

[MJD05] M. Maksimovic, Z. Jaksic and N. Dalarsson, "Transmission Properties of Gradient Index Metamaterial Slabs," iCEST 2005 Conference Paper Collection, 191-194 (2005)

[MKS09] H. Machhadani, P. Kandaswamy, S. Sakr, A. Vardi, A. Wirtmüller, L. Nevou, F. Guillot, G. Pozzovivo, M. Tchernycheva, A. Lupu, L. Vivien, P. Crozat, E. Warde, C. Bougerol, S. Schacham, G. Strasser, G. Bahir, E. Monroy and F. H. Julien, "GaN/AlGaN intersubband optoelectronic devices," New Journal of Physics **11**, 125023 (2009)

[MKK20] J. Mundry, H. J. Krenner, H. Karl and M. Betz, "Near-infrared saturable and reverse saturable absorption of ion beam synthesized VO_2 nanocrystals," Optical Materials Express **10**, 1630-1640 (2020)

[MNV16] L. Monteagudo-Lerma, F. B. Naranjo, S. Valdueza-Felip, M. Jiménez-Rodríguez, E. Monroy, P. A. Postigo, P. Corredera and M. González-Herráez, "III-nitride-based waveguides for ultrafast all-optical signal processing at 1.55 µm," physica status solidi (a) **213**, 1269-1275 (2016)

[Moo98] G. E. Moore, “Cramming More Components Onto Integrated Circuits,” Proceedings of the IEEE **86**, 82-85 (1998)

[Mor59] F. J. Morin, “Oxides Which Show a Metal-to-Insulator Transition at the Neel Temperature,” Physical Review Letters **3**, 34-36 (1959)

[MPB05] T. D. Manning, I. P. Parkin, C. Blackman and U. Qureshi, “APCVD of thermochromic vanadium dioxide thin films - solid solutions $V_{2-x}M_xO_2$ (M=Mo, Nb) or composites VO_2: SnO_2,” Journal of Materials Chemistry **15**(42), 4560-4566 (2005)

[Mol21] Molecular Technology (MolTech) GmbH, Berlin, Germany. Table of main properties of synthetic sapphire, last access 26 march 2021, URL: http://www.mt-berlin.com/frames_cryst/descriptions/sapphire.htm

[MSE98] G. Martin, S. Strite, A. Botchkarev, et al., “Valence-band discontinuity between GaN and AlN measured by x-ray photoemission spectroscopy,” Applied Physics Letters **65**, 610 (1994)

[MSJ21] J. Mundry, F. Spreyer, V. Jmerik, S. Ivanov, T. Zentgraf and M. Betz, “Nonlinear metasurface combining telecom-range intersubband transitions in GaN/AlN quantum wells with resonant plasmonic antenna arrays,” Optical Materials Express **11**, 2134-2144 (2021)

[MTS11] H. Machhadani, M. Tchernycheva, S. Sakr, L. Rigutti, R. Colombelli, E. Warde, C. Mietze, D. J. As and F. H. Julien, “Intersubband absorption of cubic GaN/Al(Ga)N quantum wells in the near-infrared to terahertz spectral range,” Physical Review B **83**, 075313 (2011)

[MTV16] S. V. Makarov, A. N. Tsypkin, T. A. Voytova, V. A. Milichko, I. S. Mukhin, A. V. Yulin, S. E. Putilin, M. A. Baranov, A. E. Krasnok, I. A. Morozov and P. A. Belov, “Self-adjusted all-dielectric metasurfaces for deep ultraviolet femtosecond pulse generation,” Nanoscale **8**(41), 17809-17814 (2016)

[MUH02] Y. Muraoka, Y. Ueda and Z. Hiroi, “Large modification of the metal-insulator transition temperature in strained VO_2 films grown on TiO_2 substrates,” Journal of Physics and Chemistry of Solids **63**, 965-967 (2002)

[MWR72] M. Marezio, D. B. McWhan, J. P. Remeika and P. D. Dernier, “Structural Aspects of the Metal-Insulator Transitions in Cr-Doped VO_2,” Physical Review B **5**, 2541-2551 (1972)

[MYS14] P. Manley, G. Yin, M. Schmid "A method for calculating the complex refractive index of inhomogeneous thin films" Journal of Physics D: Applied Physics **47**(20), 205301 (2014)

[Nex22] nextnano GmbH, last access 03 march 2022, URL: https://www.nextnano.de/

[NH12] L. Novotny and B. Hecht, *Principles of nano-optics*, Cambridge University Press (2012)

[NHH89] J. F. D. Natale, P. J. Hood and A. B. Harker, "Formation and characterization of grain-oriented VO_2 thin films," Journal of Applied Physics **66**, 5844-5850 (1989)

[NJC06] L. Nevou, F. H. Julien, R. Colombelli, F. Guillot, E. Monroy, "Room-temperature intersubband emission of GaN/AlN quantum wells at λ=2.3 µm," Electronics Letters **42**(22), 1308–1309 (2006)

[NKR20] D. V. Nechaev, O. A. Koshelev, V. V. Ratnikov, P. N. Brunkov, A. V. Myasoedov, A. A. Sitnikova, S. V. Ivanov and V. N. Jmerik, "Effect of stoichiometric conditions and growth mode on threading dislocations filtering in AlN/c-Al_2O_3 templates grown by PA MBE," Superlattices and Microstructures **138**, 106368 (2020)

[Nov07] L. Novotny, "Effective Wavelength Scaling for Optical Antennas," Physical Review Letters **98**(26), 266802 (2007)

[NTJ06] L. Nevou, M. Tchernycheva, F. Julien, M. Raybaut, A. Godard, E. Rosencher, F. Guillot and E. Monroy, "Intersubband resonant enhancement of second-harmonic generation in GaN/AlN quantum wells," Applied Physics Letters **89**, 151101 (2006)

[NUD13] O. Neumann, A. S. Urban, J. Day, S. Lal, P. Nordlander and N. J. Halas, "Solar Vapor Generation Enabled by Nanoparticles," ACS Nano **7**(42) (2013)

[NZ16] N. Nouri and M. Zavvari, "Second-Harmonic Generation in III-Nitride Quantum Wells Enhanced by Metamaterials," Photonics Technology Letters **28**(20), 2199-2202 (2016)

[ON15] E. O. Odoh and A. S. Njapba, "A Review of Semiconductor Quantum Well Devices," Advances in Physics Theories and Applications **46**, 26-32 (2015)

[PCK13] J. H. Park, J. M. Coy, T. S. Kasirga, C. Huang, Z. Fei, S. Hunter and D. H. Cobden, "Measurement of a solid-state triple point at the metal-insulator transition in VO_2," Nature **500**(7463), 431-434 (2013)

[Pee00] P. S. Peercy, "The drive to miniaturization," Nature **406**, 1023-1026 (2000)

[PKE11] A. Pashkin, C. Kübler, H. Ehrke, R. Lopez, A. Halabica, R. F. Haglund, R. Huber and A. Leitenstorfer, "Ultrafast insulator-metal phase transition in VO_2 studied by multiterahertz spectroscopy," Physical Review B **83**, 195120 (2011)

[PL80] D. Paquet and P. Leroux-Hugon, "Electron correlations and electron-lattice interactions in the metal-insulator, ferroelastic transition in VO_2: A thermodynamical study," Physical Review B **22**, 5284-5301 (1980)

[PSP10] V. A. Pustovarova, V. S. Alievb, T. V. Perevalovb, V. A. Gritsenkob and A. P. Eliseev, "Electronic Structure of an Oxygen Vacancy in Al_2O_3 from the Results of Ab Initio Quantum-Chemical Calculations and Photoluminescence Experiments," Journal of Experimental and Theoretical Physics **111**(6), 989 (2010)

[PW93] D. L. Pursey and T. A. Weber, "Bound quantum states with no classical turning points," Physical Review A **52**(5), 4255-4258 (1993)

[PWG19] M. Protte, N. Weber, C. Golla, T. Zentgraf and C. Meier, "Strong nonlinear optical response from ZnO by coupled and lattice-matched nanoantennas," Journal of Applied Physics **125**, 193104 (2019)

[PWZ99] Z. Pan, Y. T. Wang, Y. Zhuang, Y. W. Lin, Z. Q. Zhou, L. H. Li, R. H. Wu, and Q. M. Wang, "Investigation of periodicity fluctuations in strained $(GaNAs)_1(GaAs)_m$ superlattices by the kinematical simulation of x-ray diffraction", Applied Physics Letters **75**, 223 (1999)

[QBC07] M. M. Qazilbash, M. Brehm, B.-G. Chae, P.-C. Ho, G. O. Andreev, Bong-Jun Kim, Sun Jin Yun, A. V. Balatsky, M. B. Maple, F. Keilmann, H.-T. Kim and D. N. Basov, "Mott Transition in VO_2 Revealed by Infrared Spectroscopy and Nano-Imaging," Science **318**, 1750-1753 (2007)

[Ram16] J. Ramsden, *Nanotechnology - An Introduction*, 2nd edition, Elsevier Science/William Andrew (2016)

[Ras13] M. R. Rashidian Vaziri, "Z-scan theory for nonlocal nonlinear media with simultaneous nonlinear refraction and nonlinear absorption," Applied Optics **52**(20), 4843 (2013)

[Ras15] M. R. Rashidian Vaziri, Comment on "Nonlinear refraction measurements of materials using the moiré deflectometry", Optics Communications **357**, 200-201 (2015)

[RBF07] N. Rotenberg, A. D. Bristow, M. Pfeiffer, M. Betz and H. M. van Driel, “Nonlinear absorption in Au films: Role of thermal effects,” Physical Review B **75**, 155426 (2007)

[RCS05] M. Rini, A. Cavalleri, R. W. Schoenlein, R. López, L. C. Feldman, R. F. Haglund Jr., L. A. Boatner and T. E. Haynes, “Photoinduced phase transition in VO_2 nanocrystals: ultrafast control of surface-plasmon resonance,” Optics Letters **30**, 558-560 (2005)

[RFN13] D. J. Richardson, J. M. Fini and L. E. Nelson, “Space-division multiplexing in optical fibres,” Nature Photonics **7**, 354-362 (2013)

[RHC09] D. Ruzmetov, D. Heiman, B. B. Claflin, V. Narayanamurti and S. Ramanathan, “Hall carrier density and magnetoresistance measurements in thin film vanadium dioxide across the metal-insulator transition,” Physical Review B **79**, 153107 (2009)

[RHL03] W. Rechberger, A. Hohenau, A. Leitner, J. R. Krenn, B. Lamprecht, and F. R. Aussenegg, “Optical properties of two interacting gold nanoparticles,” Optics Communications **220**, 137-141 (2003)

[RKM03] R.T. Rajendra Kumar, B. Karunagaran, D. Mangalaraj, S. K. Narayandass, P. Manoravi, M. Joseph and Vishnu Gopal, “Pulsed laser deposited vanadium oxide thin films for uncooled infrared detectors,” Sensors and Actuators A: Physical **107**, 62-67 (2003)

[RLP94] T. M. Rice, H. Launois and J. P. Pouget, “Comment on "VO_2: Peierls or Mott-Hubbard? A View from Band Theory",” Physical Review Letters **73**(22), 3042 (1994)

[Roa71] W. R. Roach, “Holographic Storage in VO_2,” Applied Physics Letters **19**, 453-455 (1971)

[RRH20] A. Rashidi, S. Roshan Entezar and A. Hatef, “Tunable Multispectral Near-Infrared Absorption with a Phase Transition of VO_2 Nanoparticles Hybridized with 1D Photonic Crystals,” Nanotechnology **10**(1088), 1361-6528 (2020)

[SB98] E. W. Van Stryland and M. Sheik-Bahae, *Characterization Techniques and Tabulations for Organic Nonlinear Optical Materials*, first edition, Routledge, New York (1989)

[SBB16] A. Y. Song, R. Bhat, P. Bouzi, C.-E. Zah and C. F. Gmachl, "Three-Dimensional Interface Roughness in Layered Semiconductor Structures and Its Effects on Intersubband Transitions," Physical Reviev B **94**, 165307 (2016)

[SBV14] T. V. Son, C. O. F. Ba, R. Vallée and A. Haché, "Nanometer-thick flat lens with adjustable focus," Applied Physics Letters **105**, 231120 (2014)

[SE04] U. Schwingenschlögl and V. Eyert, „The vanadium Magneli phases V_nO_{2n-1}," Annalen der Physik (Leipzig) **13**(9), 475-510 (2004)

[Sea14] R. P. Sear, "Quantitative Studies of Crystal Nucleation at Constant Supersaturation: Experimental Data and Models". CrystEngComm. **16**(29): 6506-6522 (2014)

[Sef31] N. G. Sefstöm, "Über das Vanadin, ein neues Metall, gefunden im Stangeneisen von Eckersholm, einer Eisenhütte, die ihr Erz von Taberg in Småland bezieht", Annalen der Physik **97**, 1-4 (1831)

[Sha77] S. L. Shapiro, *Ultrashort Light Pulses*, Topics in Applied Physics 18, Springer, Berlin, Heiderlberg, New York (1977)

[Sha99] J. Shah, *Ultrafast Spectroscopy of Semiconductors and Semiconductor Nanostructures*, 2nd edition, Springer, Berlin (1999)

[SKH03] G. Schider, J. R. Krenn, A. Hohenau, H. Ditlbacher, A. Leitner and F. R. Aussenegg, "Plasmon dispersion relation of Au and Ag nanowires," Physical Review B **68**, 155427 (2003)

[SI97] N. Suzuki and N. Iizuka, "Feasibility Study on Ultrafast Nonlinear Optical Properties of 1.55-µm Intersubband Transition in AlGaN/GaN Quantum Wells," Japanese Journal of Applied Physics **36**, L1006 (1997)

[SI98] N. Suzuki and N. Iizuka, "Electron Scattering Rates in AlGaN/GaN Quantum Wells for 1.55µm Inter-Subband Transition," Japanese Journal of Applied Physics **37**, L369 (1998)

[SIK03] N. Suzuki, N. Iizuka and K. Kaneko, "Calculation of Near-Infrared Intersubband Absorption Spectra in GaN/AlN Quantum Wells," Japanese Journal of Applied Physics **42**, 132 (2003)

[SKL12] G. Seo, B.-J. Kim, Y. W. Lee and H.-T. Kim, "Photo-assisted bistable switching using Mott transition in two-terminal VO_2 device," Applied Physics Letters **100**, 011908 (2012)

[SLF04] J. Y. Suh, R. Lopez, L. C. Feldman and R. F. Haglund, "Semiconductor to metal phase transition in the nucleation and growth of VO_2 nanoparticles and thin films," Journal of Applied Physics **96**, 1209-1213 (2004)

[SLK09] E. Strelcov, Y. Lilach and A. Kolmakov, "Gas Sensor Based on Metal-Insulator Transition in VO_2 Nanowire Thermistor," Nano Letters **9**, 2322–2326 (2009)

[Smi73] A. W. Smith, "Optical storage in VO_2 films," Applied Physics Letters **23**, 437-438 (1973)

[SN12] H. Sekhar and D. Narayana Rao, "Preparation, characterization and nonlinear absorption studies of cuprous oxide nanoclusters, micro-cubes and micro-particles," Journal of Nanoparticle Research **14**, 976 (2012)

[SPA07] J. Schörmann, S. Potthast, D. J. As and K. Lischka, "In situ growth regime characterization of cubic GaN using reflection high energy electron diffraction," Applied Physics Letters **90**, 041918 (2007)

[SPR12] Editorial, "Surface plasmon resurrection," Nature Photonics **6** (2012)

[SST90] S. Shin, S. Suga, M. Taniguchi, M. Fujisawa, H. Kanzaki, A. Fujimori, H. Daimon, Y. Ueda, K. Kosuge and S. Kachi, "Vacuum-ultraviolet reflectance and photoemission study of the metal-insulator phase transitions in VO_2, V_6O_{13}, and V_2O_3" Physical Review B **41**, 4993 (1990)

[SSW90] M. Sheik-Bahae, A. A. Said, T. H. Wei, D. J. Hagan and E. W. Van Stryland, "Sensitive measurement of optical nonlinearities using a single beam," IEEE Journal of Quantum Electronics **26**, 760-769 (1990)

[ST12] B. E. A. Saleh and M. C. Teich, *Fundamentals of Photonics*, second edition, John Wiley & Sons, Inc., New York, Chichester, Brisbane, Toronto, Singapore (2012)

[ST81] W. L. Stutzman and G. A. Thiele, *Antenna theory and design*, John Wiley & Sons, Inc. (1981)

[ST91] B. E. A. Saleh and M. C. Teich, *Fundamentals of Photonics*, John Wiley & Sons, Inc., New York, Chichester, Brisbane, Toronto, Singapore (1991)

[STA15] N. Shukla, A. V. Thathachary, A. Agrawal, H. Paik, A. Aziz, D. G. Schlom, S. K. Gupta, R. Engel-Herbert and S. Datta, "A steep-slope transistor based on abrupt electronic phase transition," Nature Communications **6**, (2015)

[Str98] D. Stroud, "The effective medium approximations: Some recent developments," Superlattices and Microstructures **23**, 567-573 (1998)

[Sut03] R. L. Sutherland, *Handbook of Nonlinear Optics*, Marcel Dekker Inc., New York, Basel (2003)

[SWR18] C. Schlickriede, N. Waterman, B. Reineke, P. Georgi, G. Li, S. Zhang and T. Zentgraf, "Imaging through Nonlinear Metalens Using Second Harmonic Generation," Advanced Materials **2018**(30), 1703843 (2018)

[SWV85] E. W. Van Stryland, M. A. Woodall, H. Vanherzeele and M. J. Soileau, "Energy band-gap dependence of two-photon absorption," Optics Letters **10**, 490-492 (1985)

[SZB14] T. V. Son , K. Zongo, C. Ba, G. Beydaghyan and A. Haché, "Pure optical phase control in vanadium dioxide thin films," Optics Communications **320**, 151-155 (2014)

[SZH20] F. Spreyer, R. Zhao, L. Huang and T. Zentgraf, "Second harmonic imaging of plasmonic Pancharatnam-Berry phase metasurfaces coupled to monolayers of WS_2," Nanophotonics **9**(2), 351-360 (2020)

[SZM14] J. Sakai, M. Zaghrioui, M. Matsushima, H. Funakubo and K. Okimura, "Impact of thermal expansion of substrates on phase transition temperature of VO_2 films," Journal of Applied Physics **116**, 123510 (2014)

[TAK74] N. Taniguchi, C. Arakawa, T. Kobayashi, "On the basic concept of nano-technology," Proceedings of the International Conference on Production Engineering, Tokyo, Japan, 26-29 August (1974)

[TBC16] V. Théry, A. Boulle, A. Crunteanu, J. C. Orlianges, A. Beaumont, R. Mayet, A. Mennai, F. Cosset, A. Bessaudou and M. Fabert, "Role of thermal strain in the metal-insulator and structural phase transition of epitaxial VO_2 films," Physical Review B **93**, 184106 (2016)

[TBM22] The British Museum, Object: The Lycurgus Cup, last access 25 march 2022, URL: https://www.britishmuseum.org/collection/object/H_1958-1202-1

[TCW16] Y. Tan, L. Chen, D. Wang et al, "Tunable Picosecond Laser Pulses via the Contrast of Two Reverse Saturable Absorption Phases in a Waveguide Platform," Scientific Reports **6**, 26176 (2016)

[TJT98] M. Tazawa, P. Jin and S. Tanemura, "Optical constants of $V_{1-x}W_xO_2$ Films," Applied Optics **37**, 1858-1861 (1998)

[TKU10] H. Takami, T. Kanki, S. Ueda, K. Kobayashi and H. Tanaka, "Electronic Structure of W-Doped VO_2 Thin Films with Giant Metal–Insulator Transition Investigated by Hard X-ray Core-Level Photoemission Spectroscopy," Applied Physics Express **3**(6), 063201 (2010)

[TMS07] T. H. Taminiau, R. J. Moerland, F. B. Segerink, L. Kuipers and N. F. van Hulst, "$\lambda/4$ Resonance of an Optical Monopole Antenna Probed by Single Molecule Fluorescence," Nano Letters **7**, 28 (2007)

[TND06] M. Tchernycheva, L. Nevou, L. Doyennette, et al., "Systematic experimental and theoretical investigation of intersubband absorption in GaN/AlN quantum wells," Physical Review B **73**, 125347 (2006)

[Tow07] C.H. Townes, "Theodore H. Maiman (1927-2007)," Nature **447**, 654 (2007)

[UZP11] T. Utikal, T. Zentgraf, T. Paul, C. Rockstuhl, F. Lederer, M. Lippitz and H. Giessen, "Towards the Origin of the Nonlinear Response in Hybrid Plasmonic Systems," Physical Review Letters **106**, 133901 (2011)

[VBB68] H.W. Verleur, A. S. Barker, Jr. and C. N. Berglund, "Optical properties of VO_2 between 0.25 and 5eV," Physical Review Online Archive (Prola) **172**, 788-798 (1968)

[VCP97] K. L. Vodopyanov, V. Chazapis, C. C. Phillips, B. Sung and J. S. Harris Jr., "Intersubband absorption saturation study of narrow III-V multiple quantumwells in the λ=2.8-9µm spectral range," Semiconductor Science and Technology **12**, 708-714 (1997)

[VCZ19] T. D. Vu, Z. Chen, X. Zeng, M. Jiang, S. Liu, Y. Gao and Y. Long, "Physical vapour deposition of vanadium dioxide for thermochromic smart window applications," Journal of Materials Chemistry C **7**, 2121-2145 (2019)

[VG05] S.J. Vlaev and V. M. Gonzales-Robles, "Mean lifetimes of quasi-bound electronic states in single rectangular quantum wells," Physica Status Solidi (c) **2**(10), 3653-3656 (2005)

[VMR01] I. Vurgaftman, J. R. Meyer and L. R. Ram-Mohan, Journal of Applied Physics **89**, 5815 (2001)

[WAM15] O. Wolf, A. A. Allerman, X. Ma, J. R. Wendt, A. Y. Song, E. A. Shaner and I. Brener, "Enhanced optical nonlinearities in the near-infrared using III-nitride heterostructures coupled to metamaterials," Applied Physics Letters **107**, 151108 (2015)

[Waz09] A.-M. Wazwaz, *Partial Differential Equations and Solitary Waves Theory*, Higher Education Press, (2009)

[WE85] L. C. West and S. J. Eglash, “First observation of an extremely large-dipole infrared transition within the conduction band of a GaAs quantum well,” Applied Physics Letters **46**, 1156 (1985)

[Web03] M. J. Weber, *Handbook of Optical Materials*, CRC Press LLC, Florida (2003)

[Wec13] T. Wecker, “Herstellung und Charakterisierung von symmetrischen und asymmetrischen Doppel Quantum Wells,” master thesis, University of Paderborn (2013)

[Wei09] A.M. Weiner, *Ultrafast Optics*, John Wiley & Sons, Inc., Hoboken, New Jersy, 2009.

[WFW13] S. Wall, L. Foglia, D. Wegkamp, K. Appavoo, J. Nag, R. F. Haglund, J. Stähler and M. Wolf, “Tracking the evolution of electronic and structural properties of VO_2 during the ultrafast photoinduced insulator-metal transition,” Physical Review B **87**, 115126 (2013)

[WG96] J. R. Waldrop and R. W. Grant, “Measurement of AlN/GaN (0001) heterojunction band offsets by x-ray photoemission spectroscopy,” Applied Physics Letters **68**, 2879 (1996)

[WGW10] J. Wang, B. Gu, H.-T. Wang, and X.-W. Ni, “Z-scan analytical theory for material with saturable absorption and two-photon absorption,” Optics Communications **283**(18), 3525-3528 (2010)

[WHF15] T. Wecker, F. Hörich, M. Feneberg, R. Goldhahn, D. Reuter and D. J. As, “Structural and optical properties of MBE-grown asymmetric cubic GaN/$Al_xGa_{1-x}N$ double quantum wells,” physica status solidi (b) **252**, 873-878 (2015)

[WHX14] D. Wegkamp, M. Herzog, L. Xian, et al., “Instantaneous Band Gap Collapse in Photoexcited Monoclinic VO_2 due to Photocarrier Doping,” Physical Review Letters **113**, 216401 (2014)

[WLK16] S. Wang, M. Liu, L. Kong, Y. Long, X. Jiang and A. Yu, “Recent progress in VO_2 smart coatings: Strategies to improve the thermochromic properties,” Progress in Materials Science **81**, 1-54 (2016)

[WMY99] Z. P. Wu, A. Miyashita, S. Yamamoto, et al., “Molybdenum substitutional doping and its effects on phase transition properties in single crystalline vanadium dioxide thin film,” Journal of Applied Physics **86**(9) 5311-5313, (1999)

[WN03] C. G. Van de Walle and J. Neugebauer, “Universal alignment of hydrogen levels in semiconductors, insulators and solutions,” Nature **423** (2003)

[WP94] T. A. Weber and D. L. Pursey, “Continuum bound states,” Physical Review A **50**(6), 4478-4487 (1994)

[WRH12] C. Weber, D. O’Regan, N. Hine, M. Payne, G. Kotliar and P. Littlewood, “Vanadium Dioxide: A Peierls-Mott Insulator Stable against Disorder,” Physical Review Letters **108**(25) 256402 (2012)

[WSA94] R. M. Wentzcovitch, W. W. Schulz and P. B. Allen, “VO_2: Peierls or Mott-Hubbard? A view from band theory,” Physical Review Letters **72**, 3389-3392 (1994)

[WTS22] F. Wu, H. Tian, Y. Shen et al., “Vertical MoS_2 transistors with sub-1-nm gate lengths,” Nature **603**, 259-264 (2022)

[WWC09] J. Wei, Z. Wang, W. Chen and D. H. Cobden, “New aspects of the metal-insulator transition in single-domain vanadium dioxide nanobeams,” Nature Nanotechnology **4**, 420-424 (2009)

[WYC16] X. Wang, C. Yin and Z. Cao, “Transfer Matrix Method and the Graded-Index Waveguide, Part of the Springer Tracts in Modern Physics book series (STMP) volume **266**, (2016)

[XAY19] H. Xin Jing, C. A. C. Abdullah, M. Z. M. Yusoff, A. Mahyuddin, Z. Hassan, “Structural and optical properties of AlN/GaN and AlN/AlGaN/GaN thin films on silicon substrate prepared by plasma assisted molecular beam epitaxy (MBE),” Results in Physics **12**, 1177-1181 (2019)

[YBG13] O. A. Yeshchenko, I. S. Bondarchuk, V. S. Gurin, I. M. Dimitruk and A. V. Kotko, “Temperature dependence of the surface plasmon resonance in gold nanoparticles,” Surface Science **608**, 275-281 (2013)

[YDA99] E. T. Yu, X. Z. Dang, P. M. Asbeck, S. S. Lau and G. J. Sullivan, “Spontaneous and piezoelectric polarization effects in III-V nitride heterostructures,” Journal of Vacuum Science & Technology B **17**, 1742-1749 (1999)

[Yeh88] P. Yeh, *Optical Waves in Layered Media*, first edition, John Wiley & Sons, New York (1988)

[YLZ14] M.-H. Yuan, H. Li, J.-H. Zeng, H.-H. Fan, Q.-F. Dai, S. Lan and S.-T. Li, “Efficient blue light emission from $In_{0.16}Ga_{0.84}N$/GaN multiple quantum wells excited by 2.48 µm femtosecond laser pulses,” Optics Letters **39**(12), 3555 (2014)

[ZCX20] W. Zeng, N. Chen and W. Xie, “Research progress on the preparation methods for VO_2 nanoparticles and their application in smart windows,” CrystEngComm **22**(5), 851-869 (2020)

[ZM75] A. Zylbersztejn and N. F. Mott, “Metal-insulator transition in vanadium dioxide,” Physical Review B 11, 4383–4395 (1975)

[ZS15] Y. Zhou and S. Ramanathan, “Mott Memory and Neuromorphic Devices,” Proceedings of the IEEE **103**, 1289–1310 (2015)

[ZWK12] J. Zimmer, A. Wixforth, H. Karl and H. J. Krenner, “Ion beam synthesis of nanothermochromic diffraction gratings with giant switching contrast at telecom wavelengths,” Applied Physics Letters **100**, 231911 (2012)

[ZWW14] H. Zhang, Z. Wu, X. Wu, W. Yang and Y. Jiang, “Transversal grain size effect on the phase-transition hysteresis width of vanadium dioxide films comprising spheroidal nanoparticles,” Vacuum **104**, 47-50 (2014)

[ZYS16] M. Zhao, Z. Ye, R. Suzuki, et al., “Atomically phase-matched second-harmonic generation in a 2D crystal,” Light: Science and Application **5,** e16131 (2016)

[ZZ10] C. Zhao and J. Zhang, “The extraordinary radiation pattern of an optical rod antenna,” arXiv:1007.2314 [physics.optics] (2010)

[ZZC15] X. Zheng, Y. Zhang, R. Chen, X. Cheng, Z. Xu and T. Jiang, “Z-scan measurement of the nonlinear refractive index of monolayer WS_2,” Optics Express **23**(12), 15616-15623 (2015)

Publications

J. Mundry, F. Spreyer, V. Jmerik, S. Ivanov, T. Zentgraf and M. Betz, "Nonlinear metasurface combining telecom-range intersubband transitions in GaN/AlN quantum wells with resonant plasmonic antenna arrays", Optical Materials Express 11, 2134-2144 (2021)

J. Mundry, H. J. Krenner, H. Karl and M. Betz, "Near-infrared saturable and reverse saturable absorption of ion beam synthesized VO2 nanocrystals", Optical Materials Express 10, 1630-1640 (2020)

Conference Contributions

September 2020, Regular Talk, "Optical inter-subband nonlinearities in hexagonal GaN/AlN multi-quantum wells", 7th Internal Workshop of SFB/TRR142, Bad Sassendorf, DE

September 2019, Regular Talk, "Optical inter-subband nonlinearities in hexagonal GaN/AlN multi-quantum wells", 6th Internal Workshop of SFB/TRR142, Bad Sassendorf, DE

October 2018, Poster presentation, "Nonlinear Optics and coherent intersubband physics of c-GaN/Al(Ga)N heterostructures" and "Optical Properties of GaN/Al(Ga)N and VO_2-based Nanostructures", 5th Internal Workshop of SFB/TRR142, Bad Sassendorf, DE

January 2018, Regular talk, "Nonlinear optical functionalities of VO_2 nanocomposites", SPIE Photonics West 2018, San Francisco, USA

February 2017, Poster presentation, "Nonlinear optics and coherent intersubband physics of c-GaN/Al(Ga)N heterostructures", 4th Internal Workshop of SFB/TRR142, Bad Sassendorf, DE

Acknowledgements

At this point, I would like to thank all the people who have contributed to the creation of this thesis, whether directly, indirectly or through their pleasant company during my graduation time. I would like to express my gratitude to the following people in particular:

First and foremost my advisor Prof. Dr. Markus Betz for supervising my work, for his ideas and thoughts on new experiments and his theoretical as well as experimental guidance on the research.

Prof. Dr. Donat As, Dr. Tobias Wecker, Dr. Michael Deppe and Mario Littmann from the University of Paderborn for the fantastic teamwork during the study of the GaN/AlN-based heterostructures.

Prof. Dr. Thomas Zentgraf and Florian Spreyer for the productive joint work in the context of nonlinear metasurfaces based on GaN/AlN heterostructures.

Dr. Valentin Jmerik and Dr. Sergey Ivanov from Ioffe Institute in St. Petersburg for the supply of a series of GaN/AlN superlattices.

Prof. Dr. Hubert Krenner and Prof. Dr. Helmut Karl from the University of Augsburg for providing ion beam synthesized VO_2 nanocrystal samples.

Dr. Claudia Ruppert, Dr. Sergiu Anghel, Dr. Thorben Jostmeier and Dr. Jan Lorenz for the introduction to focused but creative laboratory work.

All former and current members of E2 for a pleasant overall atmosphere full of helpful physical discussions, pep talks and a lot of fun outside-of-work activities.

Gisela Pike and Dirk Schemionek for the accurate sample preparation and many technical advises.

Lars Wieschollek and the members of the mechanical and electrical workshop for technical assistance.

Michaela Wäscher, Nina Collette and Katharina Sparka for administrative paperwork and the many procurements.

Laura Krauß-Kodytek for being the perfect office/lab companion and a reliable honey supplier.

My whole family for all kind of assistance and unconditional support.

Sabine for her unconditional and heartening support accompanied with an infinite forbearance and patience.